Spatiotemporal analysis of coherent structures in confined environments via time-resolved and tomographic PIV : case of internal combustion engine aerodynamics

Petra Daher

THÈSE

Pour obtenir le diplôme de doctorat

Spécialité Energétique

Préparée au sein de l'Université de Rouen Normandie

Spatiotemporal Analysis of Coherent Structures in Confined Environments via Time-Resolved and Tomographic PIV: Case of Internal Combustion Engine Aerodynamics

Présentée et soutenue par

Petra DAHER

Thèse soutenue publiquement le 12 décembre 2018 devant le jury composé de		
M. Laurent DAVID	Professeur des Universités, Institut Pprime, ENSMA, Poitiers	Rapporteur
M. Xavier TAUZIA	Maître de Conférences, HDR, LHEEA, Nantes	Rapporteur
M. Jacques BOREE	Professeur des Universités, Institut Pprime, ENSMA, Poitiers	Examinateur
M. Pietro Matteo PINAZZI	Docteur, Ingénieur Innovation Combustion, Groupe PSA	Examinateur
M. Innocent MUTABAZI	Professeur des Universités, LOMC, Le Havre	Examinateur
M. Bertrand LECORDIER	Chargé de Recherche CNRS, CORIA, Rouen	Co-encadrant de thèse
Mme Corine LACOUR	Maître de Conférences, CORIA, Rouen	Co-encadrante de thèse
Mme Armelle CESSOU	Directrice de Recherche CNRS, CORIA, Rouen	Directrice de thèse

Thèse dirigée par Armelle CESSOU, Directrice de Recherche CNRS, Université de Rouen, CORIA

UNIVERSITÉ DE ROUEN NORMANDIE

ED PSIME

coria UMR 6614

I would like to dedicate this thesis to my beloved parents

“He who does everything in its proper time, He is wise.”

- Ovid

Acknowledgments

I would like to thank my advisors, Dr. Bertrand Lecordier and Dr. Corine Lacour for their guidance throughout my years as a PhD student, for allowing me to learn from their experience and for answering my many questions.
I would also like to thank Dr. Armelle Cessou for her continuous support and for agreeing to supervise my project.

I am very thankful to Pr. Laurent David and Assistant Pr. Xavier Tauzia for agreeing to review my manuscript, Pr. Jacques Borée, Pr. Innocent Mutabazi and Dr. Pierto Pinazzi for agreeing to be on my defence jury. I am most honoured. Your thoughts and comments on my dissertation proposal have been invaluable guides.

I have had the privilege of being a member of the Coria laboratory for the past few years. This warm place has been the source of many instructive discussions on engine research and optical diagnostic techniques as well as a friendly and nurturing environment.

I would particularly like to thank the workshop personnel for helping me build parts of my experiment and the metrology team for always tackling laser complications in the shortest delays. Special thanks to Franck Lefebvre for helping me run the engine test bench and Carole Gobin for helping along the path, the optical one that is.

I would also like to thank my officemates along the years, Julien Lemetayer, Irfan Mulla and Florestan Guichard. Our discussions are ones of the most marking memories I have from my time in Coria.
It has also been a pleasure sharing laughs, meals and good times with:
Abou, Javier, Hassan, Michael, Anirudh, Teddy, Fakhry, Edouard, Nelson, Yacine, Victor, Eliot, Eden, Hélène and Lilivet. You made my time in Rouen very nice.

I am immeasurably grateful to my best friend and companion, Pete,
for crossing seas to be by my side, for being my anchor through the storms and for bringing music to my life.

My family - my parents, my brothers, Francesca and Myriam - has been a constant source of love and encouragement through my time as a PhD student, as always.
Thank you!

Résumé

Les mécanismes d'évolution spatio-temporelle des structures turbulentes instationnaires tridimensionnelles, et en particulier ceux rencontrés aux plus grandes échelles sont encore mal connus. Ils sont pourtant à l'origine de phénomènes d'instabilité dans les écoulements ce qui conduit très souvent à une diminution de la performance des systèmes énergétiques. Malgré les progrès substantiels réalisés par la simulation numérique en mécanique des fluides au cours des deux dernières décennies pour capter ces instationnarités dans les écoulements 3D, les approches expérimentales demeurent essentielles pour l'analyse physique et la compréhension des phénomènes dans l'espace réel. Néanmoins, les bancs d'essais font souvent face à un grand nombre de contraintes qui doivent être surmontées afin d'assurer la bonne précision des mesures. Dans ce travail de thèse, on s'intéresse à l'analyse spatio-temporelle des structures à grandes échelles dans la chambre de combustion d'un moteur automobile qui vont amplement influencer la qualité du mélange air/carburant et donc la qualité et les produits de la combustion. Cette étude est effectuée en s'appuyant sur les développements les plus récents en vélocimétrie par image de particules (PIV) et les méthodes de traitement du signal associées. Ainsi, la PIV haute cadence (TR-PIV) et la PIV tomographique (Tomo-PIV) ont été appliquées et adaptées au banc moteur optique du laboratoire CORIA. Trois conditions d'admission et deux vitesses de rotation ont été considérées. La TR-PIV a permis d'abord d'obtenir un suivi temporel de l'écoulement dans le cylindre durant un même cycle moteur ainsi qu'identifier ces variations cycliques en fonction des conditions de fonctionnement du moteur. La décomposition propre orthogonale (POD) a été employée afin de séparer les différentes échelles dans l'écoulement et le critère Γ a permis d'identifier le positionnement spatiotemporel des plus grandes structures (tumble) durant les cycles moteur. La Tomo-PIV a permis ensuite d'étendre les données mesurées vers l'espace tridimensionnel et de fournir un complément d'information au mesure TR-PIV. Dans ce travail, la Tomo-PIV, faisant intervenir quatre caméras en position angulaire, a été adaptée et appliquée à un environnement de géométrie complexe ayant un accès optique restreint et introduisant des déformations optiques importantes. Notamment, le processus de calibration des modèles de caméras a fait l'objet d'une attention particulière pour faire face au confinement de la chambre de combustion. Pour cela des procédures originales de calibration Tomo-PIV ont été développées et validées pour les environnements confinés à fortes déformations optiques tels que le moteur. La complémentarité des résultats 2D et 3D a montré le rôle fondamental que joue la combinaison banc moteur optique - PIV dans l'amélioration des compréhensions des phénomènes physiques et en conséquence les potentiels de cette approche pour l'amélioration et la validation des modèles industriels.

Contents

Abbreviations and Acronyms

2D	Two-dimensional
3D	Three-dimensional
BDC	Bottom dead centre
CCV	Cycle-to-cycle variations
CAD	Crank angle degree
CPIV	Classical particle image velocimetry
DF	Laser flash-lamp delay
DISI	Direct injection spark ignition
DQ	Laser Q-switch delay
ICE	Internal combustion engine
KE	Kinetic energy
PIV	Particle image velocimetry
POD	Proper orthogonal decomposition
RMS	Root mean square
RPM	Round per minute
SNR	Signal to noise ratio
TDC	Top dead centre
TKE	Turbulent kinetic energy
Tomo-PIV	Tomographic PIV
TR-PIV	Time-resolved PIV

Γ	Gamma function
ρ	density
t	Time period
f	Frequency
u,v,w	Velocity components
u,v,w	Velocity vectors
$\bar{u}$, $\bar{v}$, $\bar{w}$	Ensemble averaged velocity components
<u>,<v>,<w>	Spatial averaged velocity component
<$\bar{u}$>,<$\bar{v}$>,<$\bar{w}$>	Ensemble average of spatial averaged velocity component
u',v',w'	Magnitude of velocity fluctuations
$\overline{u'}$, $\overline{v'}$,$\overline{w'}$	Ensemble average velocity fluctuations
<u'>,<v'>,<w'>	Spatial averaged velocity component
<$\overline{u'}$>,<$\overline{v'}$>,<$\overline{w'}$>	Ensemble averaged of spatial averaged velocity fluctuations
|V|	Velocity magnitude
|V'|	Velocity fluctuations
X,Y,Z	Spatial coordinates
x_r,y_r	Real planar coordinates
x_p,y_p	Image pixel coordinates

Introduction

Nine out of ten people around the globe live in areas where the air pollution rate exceeds official health limits – Statement of the World Health Organisation.

The dominant cause for this alarming statement is the burning of fossil fuels that are still indispensable in today's industrial world. Particularly, the automotive industry stands as a major source of pollution with thermal vehicles, i.e. Internal Combustion (IC) engines, producing more than 20% of the world's CO_2 emissions in addition to other harmful pollutant particles such as sulphates, NOx and CO which makes the transport sector a main contributor to global warming (tsp-data-portal). And with the increasing gravity of global warming, emissions regulations are becoming more and more sever. In November 2016, a two degree warming scenario (2DS) was agreed upon by the international community and is being avidly pursued today. It translates into implementing deep cuts in all sectors emissions, as much as 70% by 2050. For the automotive industry, this translates into 60% emission reduction (International Energy Agency).

Urgent actions are therefore required in order to improve efficiency and engine emissions, to reduce pollution levels and limit from global warming. In this context, alternative fuels and electric technologies are witnessing great progress. Their current potential is still however limited and until alternative methods are mature enough, IC engines will remain to occupy the major share of the market, exceeding 70% in 2030 and 60% in 2050 (ADEME). Consequently, 'greener' IC engines are continuously in the making and while aiming for reduced emissions on one hand, on the other hand lies the automakers requirements to ensure high engine performance which also depends on the combustion quality and its efficiency.

Hence, the engine's combustion process needs to be optimised.

In this context, IC engines are characterised with a very short duration of the combustion process. Therefore, optimising the combustion's progress after ignition is not easily controllable and it proves easier to control the initial conditions of the reaction in order to guide its products. Amongst many factors, the combustion's initial conditions relate to the aerodynamic structure of the air-fuel mixture at the end of the compression stroke. This structure undergoes large-scale variations on a cyclic basis which can cause

an increase in pollutant emissions, knock or even misfire. This directly and drastically affects the engine's efficiency on a cyclic basis and therefore needs to be controlled.

Consequently, identifying in-cylinder aerodynamics at the moment of ignition is key to understanding and directing the cyclic phenomena. Additionally, a spatiotemporal analysis of the cyclic flow evolution is essential to achieve a better understanding of engine operation since this evolution is correlated to cyclic fluctuations of energetic efficiency. In order to carry out the spatiotemporal analysis, the need arises to visualize and interpret the complex aerodynamic processes taking place within the engine's cylinder. Researchers are thus continuously working to develop and improve the catalogue of numerical and experimental tools aiming to achieve the best modelling and understanding of the occurring phenomena. The efforts of this study lies in this category.

Experimental measurements are a requirement to validate any numerical modelling of a physical process. The combination of commercially available optical diagnostic techniques and optically accessible IC engines provides the mean to perform instantaneous measurements of real life operation condition, i.e. production engines operation. Despite the numerous advancements witnessed in these areas, one remaining challenge is the extent to which can a measurement technique provide information with the desired accuracy and spatial and temporal resolutions. Particularly in the context of IC engines, many constraints arise regarding the engine's geometry and the optical access into the confined cylindrical combustion chamber, especially when two-dimensional or three-dimensional measurements are required.

In this study, the evolution of internal aerodynamics in a direct-injection spark-ignition engine is analysed during intake and compression strokes. We aim in particular to provide insight on the cyclic variability of large-scale coherent structures that largely influence the air/fuel mixture and could limit the engine's operating range. Thus, understanding and controlling cycle-to-cycle variabilities (CCV) in the combustion chamber is fundamental to optimize engine performance while meeting imposed emission standards. Moreover, having encountered harsh conditions for 3D measurements in engines, an adapted experimental procedure is introduced.

- **Manuscript plan**

In the first chapter, a brief bibliographic review presents the role played by optical engines and emerging laser diagnostic techniques in furthering our understanding of in-cylinder phenomena. This review focuses on particle image velocimetry (PIV) techniques that allow us today to obtain instantaneous velocity measurements with high spatial and temporal resolutions in relatively large continuous investigation domains inside the engine's combustion chamber.

Then the two PIV experimental setups used in the course of this study are presented in the second chapter. Part one describes the high speed PIV setup that allows us to obtain the cyclic evolution of in-cylinder flow. Part two treats the tomographic PIV setup allowing us to obtain the three-dimensional flow field. A bespoke calibration procedure is developed and validated for the application of tomographic PIV in confined environments with restricted optical access.

The third chapter then presents the results of in-cylinder flow variations with respect to different engine conditions, i.e. three inlet flows and two realistic engine speeds, and their effect on cycle-to-cycle fluctuations. The 2D time-resolved measurements are completed with the 3D phase-locked results providing additional information otherwise missed in planar measurements.

Finally in the last chapter, the conclusions of this study are summarized, future steps are suggested and perspectives are presented.

1 IC engines and optical diagnostics: bibliographic study

This chapter is divided into three main parts. The first part describes the in-cylinder flow dynamics and presents an overview of the optical diagnostic techniques used to visualise it. The second addresses particularly the particle image velocimetry technique used in the course of this study and its application on IC engines. The advancements it allowed for in-cylinder measurements are relayed as well as the challenges it faces especially when three-dimensional measurements are desired. The third part finally summarises the chapter's review allowing thus to define the thesis objectives.

1.1 Overview

Along the decades, engines have been classified according to their different operating characteristics ranging from the type of ignition, to the type of fuel, the mixture preparation, the number of strokes per cycle, and many others. However, all internal combustion engines share the fundamental principal of cyclic operation converting chemical energy into mechanical energy within the confinement of a cylinder. Nowadays, the most common engine cycle consists of 4 strokes. The efficiency of the engine highly depends on the efficiency of the occurring combustion process during that cycle, which in turn is affected by a number of variables. Particularly, in-cylinder aerodynamics dictates the combustion's initial conditions. Therefore, understanding the underlying processes is crucial for the production of more efficient engines. In order to do so, researchers seek to visualise the flow by developing the corresponding optical diagnostic techniques on the one hand and by adapting their use to the engine configuration on the other hand. In this section, the engine operation mode and the main characteristics of in-cylinder aerodynamics are first described in §1.1.1. Then, an overview of the laser based diagnostic techniques used for in-cylinder flow visualisation are relayed in §1.1.2.

1.1.1 The engine cycle and in-cylinder aerodynamics

The recurrent engine cycle denotes two crank shaft revolutions, i.e. 720 crank angle degrees (CAD), accompanied by four translational movements of the piston along its cylinder liner. Four strokes hence take place and form the engine's cycle illustrated in Figure 1-1.

The first phase of the cycle is called the intake stroke in which the intake valves open and air is drawn into the cylinder with high speed and large Reynolds number, i.e. the flow is highly turbulent. This intake flow then develops toward the bottom dead centre (BDC) in the confined environment of the cylinder with inter-jet interactions and jet-wall interactions.

The second phase of the cycle is the compression stroke in which the valves close and the inlet charge motion induced by the intake flow stops. The piston pushes the flow towards the TDC in a highly confined environment thus creating an extreme alteration of the flow's structures. Large vortices break into small vortices and kinetic energy is dissipated into heat which causes a decrease in turbulence at the end of the compression stroke.

The third phase is the power stroke, i.e. where combustion takes place and the burning gases expand pushing the piston back to the BDC. Naturally, the efficiency of this stroke is highly dependent on the preceding one, i.e. compression stroke, which will dictate its initial conditions and influence its evolution. Finally, the forth phase of the engine's cycle is the exhaust stroke in which exhaust valves open and burned gases are forced out of the cylinder.

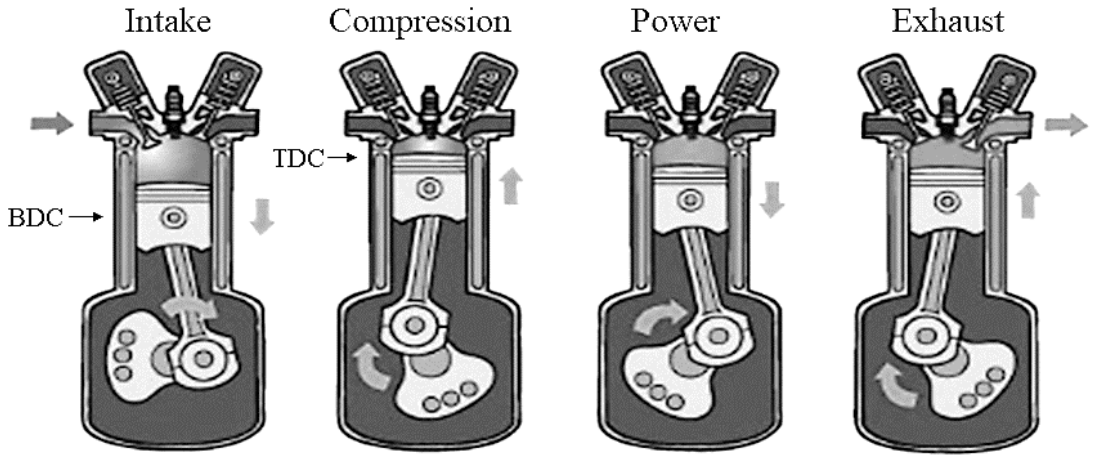

Figure 1-1 Four strokes of an engine cycle (BDC: bottom dead centre, TDC: top dead centre)

The cyclic engine operation can then be illustrated by the in-cylinder pressure evolution throughout the four strokes as well as the piston's position with respect to the top dead centre (TDC) as the example shown in Figure 1-2. Even though the working principle is a relatively simple one, yet each phase is influenced by a large number of parameters affecting the efficiency and sustainability of engine operation (Heywood, 1988) (Müller, 2012).

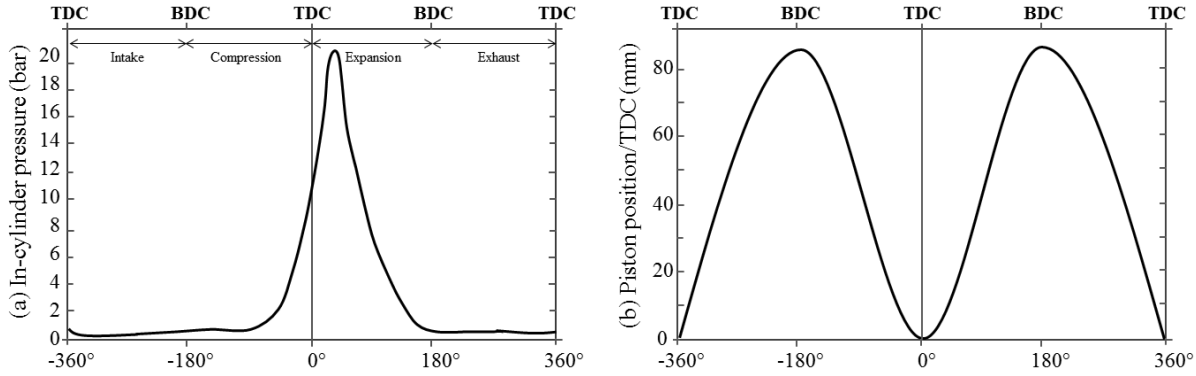

Figure 1-2 Example of (a) in-cylinder pressure evolution and (b) piston position with respect to top dead centre versus the crank angle degree of a 4 strokes engine.

In fact, the in-cylinder flow is non-stationary, complex and turbulent. Understanding the evolution of different scale structures during the engine's cycle is crucial for researchers and engine designers who mainly seek to control and optimise the combustion process. This is possible by mastering the generation of turbulent motions capable of optimising the initiation and propagation of the flame (Buschbeck et al, 2012) (Pera et al, 2015) (Zentgraf et al, 2016). Creating this small-scale turbulence is particularly done by addressing the storage of momentum and energy in large scale structures that are less dissipative than the former and conserve their kinetic energy longer during the engine's cycle.

The creation of large scale structures is usually ensured by the intake manifold's shape, by the number and the position of the valves as well as by the geometry of the combustion chamber (Baby, 2000). Two main rotational structures can then be identified: tumble and swirl. Tumble has an axis of rotation perpendicular to the cylinder axis and swirl has an axis aligned with the cylinder axis (Figure 1-3).

Momentum and energy are stored in these motions hence providing the means to manipulate in-cylinder dynamics during the engine cycle whether by forcing the breakdown of their coherent structure, thereby releasing its energy into turbulence, or by driving the generation of new structures that can aid the fuel transport process (Borée & Miles, 2012).

Particularly in spark ignition engines, the increase of turbulent kinetic energy is due to tumble breakdown taking place near the end of the compression stroke. Their energy transfers thus to the small scale turbulence that are sought. However, this energy also transfers in part to cycle-to-cycle variabilities that can cause undesired instabilities.

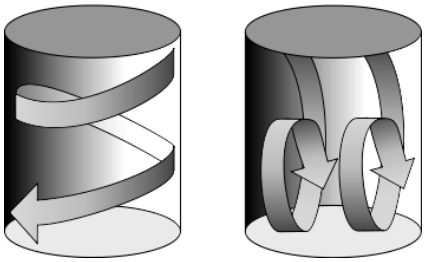

(a) (b)

Figure 1-3 In-cylinder (a) swirl and (b) tumble rotational motions.

In fact, a major challenge for engine designers is understanding, modelling and controlling the cycle-to-cycle variations (CCV) which can cause severe irregularities in the engine operation, excessive noise, higher emissions, and potentially lead to engine damage (Goryntsev et al, 2009). The non-reproducibility of consecutive engine cycles is mainly caused by the temporal and spatial randomness of the velocity field on the one hand and by the instability of the periodic movement of the piston and the valves on the other hand (Lengyel, 1995). Large scale cyclic fluctuations hence occur and coexist with small scale turbulence. Their corresponding fluctuations are both accounted into the total kinetic energy of the combustion chamber and should therefore be separated to avoid overestimating the flow's turbulence level (Floch, 1990) (Voisine et al, 2010).

Many factors have been shown to create CCV, such as the mixture preparation process, the fuel composition, the combustion kinetics, the spark plug characteristics, the heat transfers, and the evolution of in-cylinder aerodynamics (Enaux, 2010). The consequences of CCV can be described as the variation of the in-cylinder maximal pressure from one cycle to the following caused by the fluctuating movement of large scales structures, or the low frequencies, i.e. coherent structures. Particularly in spark ignition engines, CCV can be observed in the fluctuations of the tumble centre's location from one cycle to another.

Despite the numerous existing studies, the cause and effect chain of CCV is still not fully unravelled. It has been shown for example in an experimental study that the cyclic-fluctuations increase during the compression process. At the end of compression nevertheless, the authors reached a level of fluctuation similar to what was obtained at the beginning of the intake process (Druault et al, 2005). In another study, CCV of the in-cylinder flow structures were linked to the CCV in the intake manifold (Justham et al, 2006). And in a similar context, CCV were linked to variations in valve lift (Liu et al, 2012). These studies, and many others that coupled the measurement of cyclic fluctuations with the varying of engine parameters, showed that the presence and the management of

strong coherent structures can lower the CCV of in-cylinder aerodynamics and therefore improve the stability of engine operation.

Motivated to better understand the complexity of the engine's in-cylinder flow, researchers have looked for ways to visualise and quantify the occurring processes. Particularly in recent years, there has been a dramatic increase in available experimental data thanks to the progress witnessed by optical engines on the one hand and laser diagnostics on the other hand, which has been allowing throughout the years a better conception of more environmentally friendly and more efficient engines. A brief overview of optical engines history and their coupling to optical diagnostics is presented in the following.

1.1.2 In-cylinder flow visualization and historical background

For more than a century, optical engines have been playing a fundamental role in furthering our understanding of the complex physical phenomena having place in the engine's combustion chamber. It is indeed essential to visualize the in-cylinder mixing process and the ensuing combustion in order to comprehend the operation of an engine and its ancillary devices and improve its efficiency and emissions. Moreover, with the arrival of numerical simulations, optical engines assumed the additional role of producing quantitative databases over a large unobstructed spatial domain with high crank-angle degree resolution in order to validate and enhance the conception of various engine systems.

One of the first experimental concepts to visualise the in-cylinder aerodynamics goes back to the 1800s and consisted on using smoke from cigarettes drawn into a thin transparent cylinder to track in-cylinder motions. Several models where then derived from that concept in the aim of visualising the mixing process in a more realistic engine cylinder and study the role of in-cylinder aerodynamics in the ensuing combustion. These models were then classified as optical engines (Kashdan & Thirouard, 2011)(Miles, 2015).

At the beginning, optical engines witnessed many alterations to the IC engine's initial geometry in order to allow further optical access. Small transparent windows were implemented on the combustion chamber and side-valves were used making it possible to record the exact ignition timing and the flame propagation speed by stroboscopic measurements (Ricardo et al, 1927) (Marvin and Best, 1932). Many variables were also examined for the first time such as fuel-air ratio, compression pressure and the impact of residual gases on slowing the flame. Small windows were then replaced with one rectangular quartz plate, fitted on the head of the combustion chamber and coupled with a

specifically developed camera thus introducing temporal measurements into account (Withrow & Rassweiler, 1931). After that, the quartz windows were inserted to the cylinder's walls to enable further optical access (Watts & Lloyd-Evans, 1934) and the use of a liner consisting of larger quartz plates rapidly followed (Rassweiler and Withrow, 1936).

Naturally after that, researchers were motivated to extend the optical access to a full transparent cylinder on the one hand and to develop high speed cameras in order to refine recordings and the experimental data on the other hand. Figure 1-4 shows one of the first reported full optically-accessible engines where a 12.7 mm thick glass liner is supported by a steel casting (Lee, 1939). Having this extended access, the means to visualise the aerodynamic flow structures were sought and one of the first tracer particles used to study the interaction between the flow and the spray consisted of chopped goose feathers and individual feathers whose displacement provided a quantitative measure of the velocity at a fixed crank angle.

The next breakthrough in the optical engine industry was the extension of the piston-cylinder assembly to allow the insertion of a 45° inclined mirror (Bowditch, 1961). This allowed the combustion chamber to be viewed with a larger degree of optical access ensured by the mirror and the quartz piston head eliminating thus the need to alter the combustion's chamber geometry (Figure 1-5). Major advancements and discoveries were then made possible by optical engines such as the effect of different inlet ports, different piston heads, different injection mechanisms and the impact of exhaust gas recirculation on the combustion process.

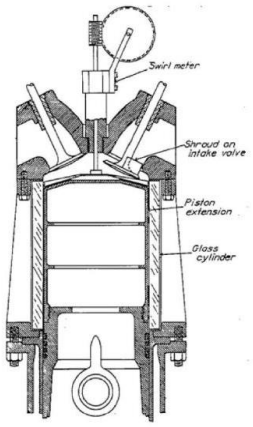

Figure 1-4 Optically accessible engine equipped with a full quartz cylinder (Lee, 1939)

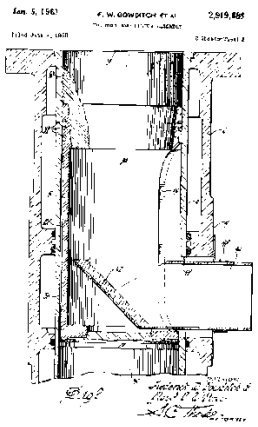

Figure 1-5 Bowditch optical cylinder design (Bowditch, 1961)

The number of studies conducted in optical engines continued to increase significantly with the commercial availability of lasers in the 1970s. This is mainly due to

the appeal of laser based optical diagnostics for fluid flow measurements due to their non-intrusive nature. In other terms, it was now possible to observe the changes in the flow and record them at the same time that they occur, without compromising the flow's nature. Possible in-cylinder measurements then included continuous-wave laser Raman spectroscopy for fuel and air concentrations, pulsed laser Raman spectroscopy for density fluctuations, high-speed cinematography for flow visualization, and laser Doppler velocimetry (LDV) for one point or multiple points measurements of velocities and turbulence intensities (Rask, 1979) (Johnston et al, 1979) (Floch, 1990). Particularly, LDV has been widely used since it can be easily adapted to study flows in hard to reach geometries such as the valve exit flow or the bumping clearance (Arcoumanis & Whitelaw, 1985).

Along to advancements in optical diagnostics, optical engines continued witnessing progress and higher compression ratios and rotational speeds were reached and operation conditions were closer to real life production engines (Steinberger et al, 1979). For instance, the square piston emerged with two opposed cylinder walls made of quartz followed by making all four cylinder walls from quartz plates (Maly et al, 1990). A CR of 10:1 was achieved and an engine speed of 2500 rpm allowed the examination of turbulent combustion models and the application of optical diagnostics such as Laser Induced Fluorescence (LIF) for fuel-air mixing studies and Particle Image Velocimetry (PIV) for flame rates studies. Moreover, coupled measurements using LDV and PIV provided complementary information about the motion of tumble during compression (Marc et al, 1997).

The full cylindrical transparent liner found increasing interest amongst researchers (Arcoumanis, 1982). Shortly after the squared piston, the use of transparent cylinder engines followed and only motored conditions where possible (Richman & Reynolds, 1984) (Marko et al, 1986) (Regan et al, 1987) (Bates, 1988). Using a form of particle tracking velocimetry, low-speed flow visualization, and flame imaging studies, earlier observations of intake jet flapping and significant cycle-to-cycle variability in the combustion development were confirmed. Moreover, the attained realistic operation conditions and extended optical access allowed taking a greater step in validating numerical simulations (Kuo and Reuss, 1995).

Another profitable feature introduced to the optical engine was the incorporation of a separating cylinder liner that permits rapid cleaning of the windows (Espey and Dec, 1993). This was quickly adopted and enhanced by developing a hydraulic system allowing a quick release of the cylinder, i.e. a rapid and repeated disassembly and cleaning

(Sunnarborg, 2000). The entire combustion chamber was now accessible optically and mechanically which motivated the attempts to access the three-dimensional nature of the engine's flow. One of the first attempts to do so was conducted by (Brücker, 1997) who used a drum scanner to record different planes at high repetition rates and observed the splitting and shearing of in-cylinder vortices. More recently, the three-dimensional in-cylinder flow was investigated using the latest advancements in PIV (Bücker et al., 2012) (Peterson et al., 2016).

The advancement of optical diagnostic techniques and their increasing availability coupled with the rich history of optically accessible engines and their importance as a tool to obtain the detailed analysis of the in-cylinder phenomena allowed recovering a very diverse database of information (Witze, 1996) (Richter, 2008). A non-exhaustive list can be found in the following table.

Type of database	Optical diagnostic techniques and types of measurements
Species distributions / concentrations	- Laser induced fluorescence (LIF) - Absorption - Raman / Rayleigh - Chemiluminescence
Flow	- Particle image velocimetry (PIV) - Laser Doppler Anemometry (LDA/LDV/PDA) - Tagging techniques
Temperature	- LIF - CARS (Raman) - Rayleigh - Absorption spectroscopy
Mixture preparation	- Shadowgraphs - Spray penetration - Spray angles - LIF (Evaporation) - LIF tracer (Fuel/air mixing)
Combustion characteristics	- Ignition events - Flame propagation - Flame quenching - Knock centres - Low / high temperature regions - Causes of misfires
Pollutant formation	- LIF NOx - LII Soot - Unburnt HC

Table 1-1 Available information via the increasing availability of optical diagnostic techniques

Particularly, when interested in the in-cylinder flow evolution, a wide range of velocity measurements and measured components is covered today going from one point measurements, to planar measurements, to obtaining the full three-dimensional flow field along to its temporal evolution (Figure 1-6). Amongst the techniques emerging as indispensable for fluid flow visualisation is particle image velocimetry that has become a primary diagnostics tool for both industrial needs and fundamental research (Boutier, 2012) (Tropea, 2007). In its different forms, PIV allows obtaining instantaneous velocity fields and describing the local, temporal or three-dimensional evolution of the flow (Schröder and Willert, 2007). Its application in IC engines has led to numerous observations enhancing our comprehension of the different engine strokes and resulting in better engine modelling. Some of the approaches of PIV applications in IC engines found in literature and relative to the scope of this study are relayed in the following.

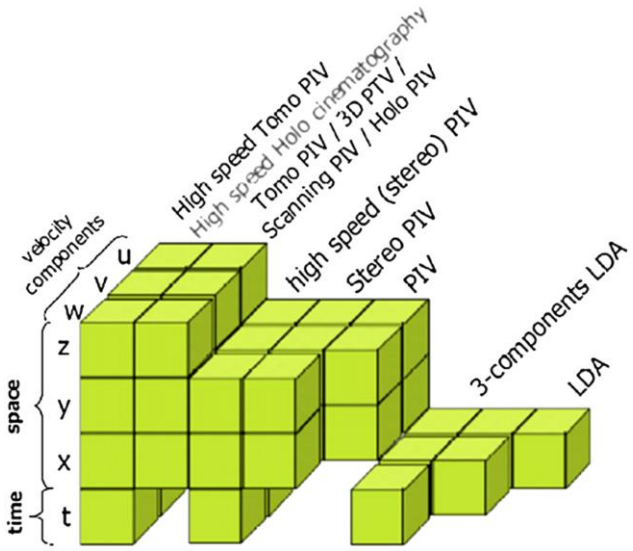

Figure 1-6 Measurement domain and measured components of laser velocimetry techniques (reproduced from (Scarano, 2012)**)**

1.2 Particle image velocimetry and applications in IC engines

Despite the advancements in accessing the internal combustion engines configuration, transient processes still need to be visualized in an optically challenging environment of a confined thick cylinder. Moreover, obtaining instantaneous measurements of the local flow and mixture conditions is important to characterize their influence on ignition and consequently on combustion performance. For the last few decades, these measurements have been particularly possible via the particle image velocimetry technique based on a relatively simple principle allowing a non-intrusive visualisation of a cross-section of the flow (Figure 1-7). The fluid is seeded with particles

which are generally assumed to faithfully follow the flow's dynamics. Then it is the motion of these tracer particles from which the velocity information is calculated. This is done by taking two images shortly after one another and calculating the distance particles travelled within this time between the two images. Both images are divided into a number of sub-images called interrogation windows and a correlation coefficient is computed to find the two corresponding windows. The maximal correlation signal detected refers to the most probable displacement of particles. The velocity field is then obtained by dividing the displacement field by the known separation time between images and the translation of the image plane to the object plane is obtained using a calibration target engraved with previously defined coordinates.

In recent years, the number of PIV applications on engines witnessed a great increase tackling the evolution of the in-cylinder processes with respect to the change in engine parameters such as piston shapes, inlet ports, intake valve lift, spark timing and others. Hereafter, previous studies are presented and separated into 2D and 3D measurements in order to highlight the advancements that PIV allowed for in-cylinder flow analysis.

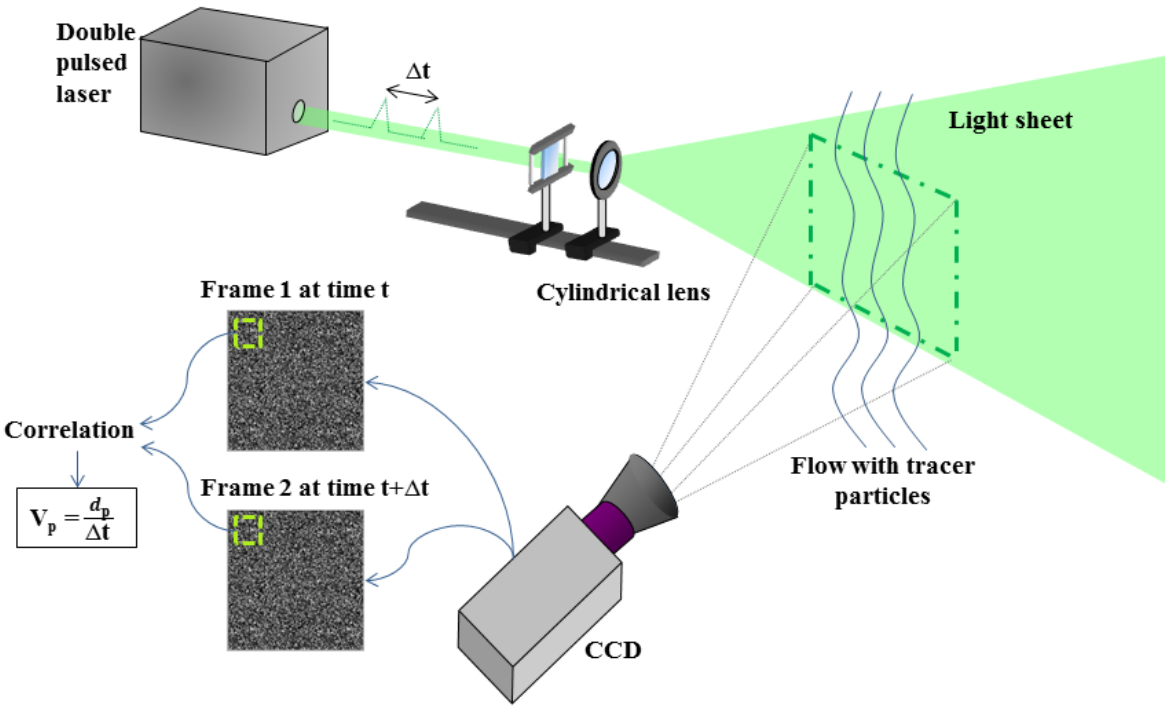

Figure 1-7 Working principle of particle image velocimetry

1.2.1 2D in-cylinder measurements

One of the first applications of PIV to an internal combustion engine was carried out by Reuss et al. who performed planar velocity measurements under motored operation at 600 RPM (Reuss et al, 1989). In a relatively more recent period, Justham et al. simultaneously used two PIV systems to study the intake flow and the in-cylinder flow of an IC engine at the same time (Figure 1-8). This provided an insight to the relationship between cyclic variations of flow structures within the runner and those during the engine's cycle. The lack of time history was however highlighted indicating its importance to correlate the two measured flows (Justham et al., 2006). This was also highlighted by Towers and Towers who pointed out that single snapshots of the velocity vector fields as obtained from a typical double-frame PIV camera are not sufficient to separate the cyclic variability from the turbulence. Thus the importance of time-resolved measurements is revealed, particularly when a range of operating conditions needs to be compared (Towers and Towers, 2008).

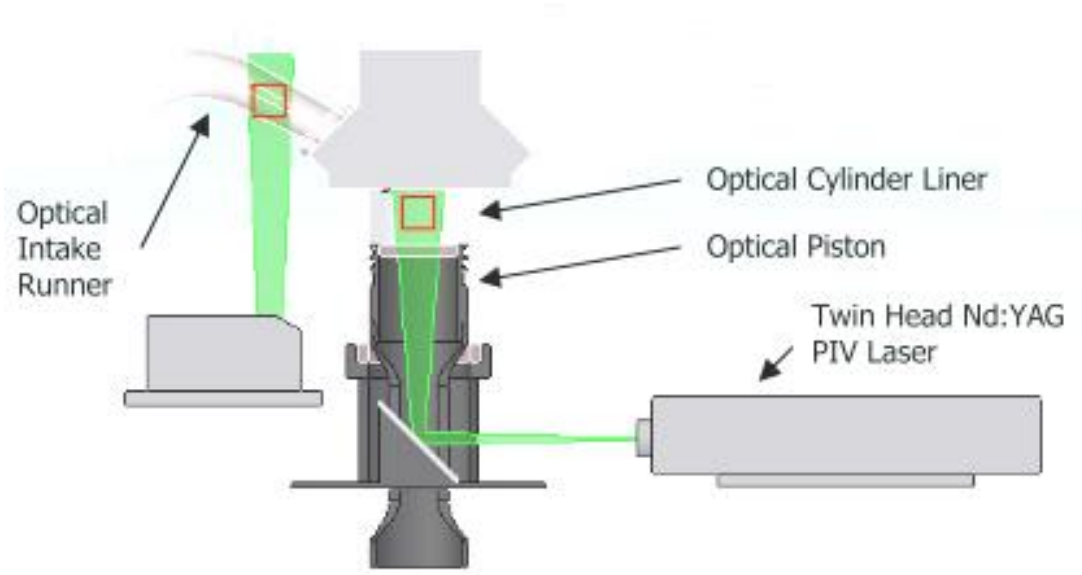

Figure 1-8 Schematic of the simultaneous intake and in-cylinder PIV setup (Justham et al., 2006)

With the advances in technology giving way to cameras with high frame rate and high resolutions, time-resolved measurements became achievable (Willert, 2015). Moreover, the time-resolved data was then compared to the standard PIV process to make sure that no small-scale related information is lost or altered in the process and a correct evaluation of the turbulent kinetic energy dissipation, frequently used in flow modelling, was found (Falchi and Romano, 2009). A wider range of statistical and analytical studies was now possible with the availability of time-resolved data, giving the researcher access to a greater amount of information (Semeraro et al, 2012). Sick et al. particularly describe

the progress that high speed imaging witnessed in the last decades with focus on applications to spark-ignition direct-injection gasoline engines and how time resolved PIV fits in the study of every phase of the engine cycle and its corresponding physical phenomena (Sick et al, 2010).

In one of the early studies using a time-resolved PIV system, Jarvis et al. measured the in-cylinder flow under motored conditions and thus described the evolution of the flow during the engine cycle as well as during a series of consecutive cycles (Jarvis et al., 2006). By calculating the difference between cycle averaged and ensemble average velocity fields, the authors provided a time resolved indication of cyclic variations yet the possibility of finding more descriptive parameters of CCV was argued (Figure 1-9). This was then addressed by (Cosadia et al, 2007) who replaced the standard statistical approach by coupling time-resolved measurements with the proper orthogonal decomposition technique (POD) allowing to extract coherent structures and presenting an optimal technique as far as the kinetic energy contained in consecutive modes is concerned (§3.1).

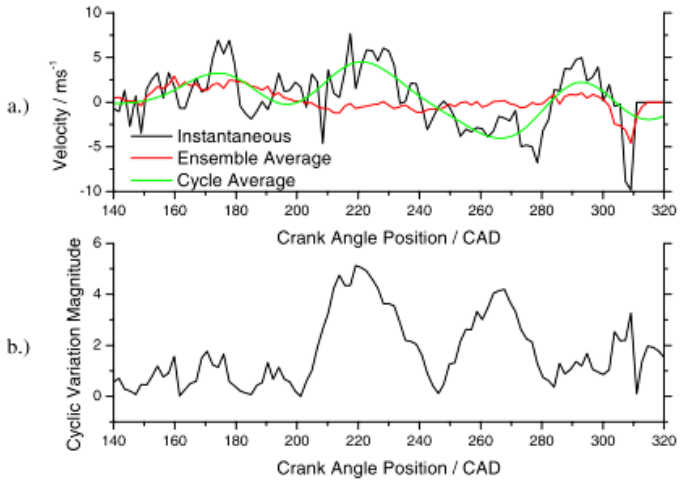

Figure 1-9 Example plot of a) Instantaneous u velocity, Ensemble averaged u velocity, and Cycle averaged u velocity, b.) Calculated Cyclic variation at a given (x,y) location within velocity field (Jarvis et al., 2006)

In another study, the change in the fundamental structure of the in-cylinder flow was evaluated with respect to the change in engine speed (Stansfield et al, 2007). Classical PIV measurements were conducted in the symmetry plane of the engine's cylinder at different crankshaft angles and for three rotational speeds, 750, 2000 and 3500 RPM. The average velocity field was then obtained and the influence of the engine's speed on its internal aerodynamics was described via the evolution of tumble rate. In the same context, time resolved measurements were conducted in the engine's combustion chamber at 6 kHz for

different charge motions and different engine speeds (Müller et al, 2010). In addition to cycle average and ensemble average velocity fields, cycle to cycle variations were quantified using the fluctuations in kinetic energy of the time resolved data at 500, 1000 and 2000 RPM. This showed a larger gradient for decreasing kinetic energy at higher speeds as well as an earlier decline of the turbulent kinetic energy during the compression stroke at higher speeds (Figure 1-10).

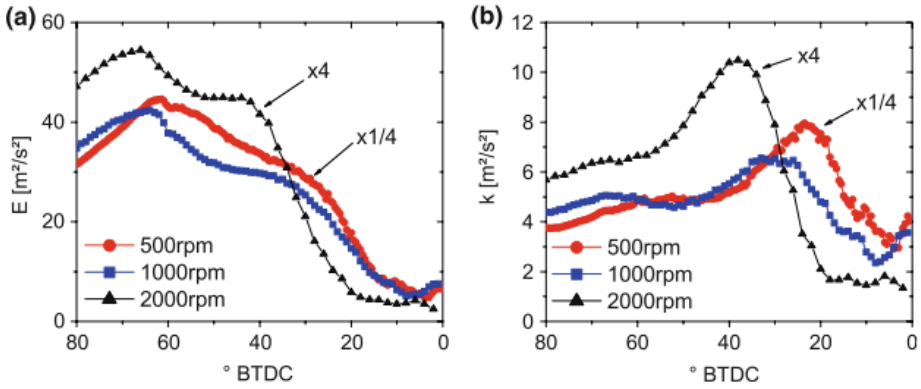

Figure 1-10 Ensemble average of the spatial averaged kinetic energy E (a) and turbulent kinetic energy k (b) for 500, 1,000 and 2,000 rpm. Values are normalized by the square of the engine speed relative to the standard case of 1,000 rpm (Müller et al., 2010)

In addition to the intake flow and engine speeds, in-cylinder flow analyses were conducted with respect to the change in the inlet duct. Towers and Towers for example used a butterfly valve placed in one of the inlet ducts to vary the in-cylinder axial swirl level and showed that the cyclic variability peaked at different points in the engine cycle for the different configurations (Towers & Towers, 2008). It is interesting to note that at the time, available laser power was average and that the price of high speed acquisition rate (up to 12 KHz) was the reduction of the field dimensions and image resolution.

However, with the continuous improvement in lasers and sensor technologies, Kapitza et al. were able to obtain a larger field of view using high-speed PIV, also aiming to identify the relationship between the instantaneous velocity fields in the cylinder and the change in the intake flow (Kapitza et al, 2010). These measurements were carried out by fixing a set of different inlet valve lift (3 or 9 mm), different flow rates (50 or 100 kg/h) and an open or closed tumble flap introduced to the inlet duct. Three frequencies could be determined by describing the transient behaviour of the flow: the vortex detachment frequency induced by the valve geometry, the limiting frequency leading to instabilities of the boundary layer through the valve slot, and the frequency corresponding to the flow fluctuations associated with the shear layer downstream of the edge of the tumble flap.

Many other parameters such as the effect on the in-cylinder flow of piston head shape, the intake valve lift, the mass flow rate and the engine stroke solicited great interest of researchers who employed PIV measurements to quantify them (Murali Krishna and Mallikarjuna, 2010) (Liu et al, 2012) (Cao et al, 2014). Similar studies were conducted using high speed PIV that showed additional valuable information otherwise missed using classical PIV (Buschbeck et al., 2012) (Bode et al., 2016) .

1.2.2 3D in-cylinder measurements

In a complementary effort to reach the three-dimensional description of the in-cylinder flow, Danneman et al. carried out planar time-resolved PIV measurements in 8 planes at several crankshaft angles in an internal combustion engine operating without ignition (Danneman et al, 2011). The flow fields were reconstructed from two-dimensional velocity fields of different crank angles leading to what were referred to as quasi-three-dimensional fields. The authors showed that the flow inside the motored engine has a strong three-dimensional character and presented a 3D description of the large vortex structures and their corresponding temporal behaviour. Despite the ability to describe the ensemble averaged 3D flow field, these findings were unable to capture 3D flow structures for instantaneous cycles nor resolve 3D gradient based flow properties.

Another approach to obtain the 3 velocity components is employing stereoscopic PIV. This PIV approach depicts that by using two distinct axes of views to simultaneously record one region of interest, sufficient information can be obtained to extract the out of plane motion of particles (Willert, 1997). This technique introduces however a distortion of image fields with a varying magnification factor associated with the corresponding imaging configuration. This is usually accounted for by using an accurate calibration procedure based on solving the projection equations for each of the two cameras (Prasad, 2000). While dealing with optical engines, stereoscopic PIV faces additional distortions and experimental constraints caused by the combustion chamber’s geometry (Figure 1-11). Although the technique has proven advantageous in obtaining the 3D description of fluid flows, its application in IC engines is hardly discussed in literature (Calendini et al., 2000) (Bücker et al., 2012) (Karhoff et al., 2013). The main ensuing findings describe a dominant tumble vortex that varies significantly regarding shape, strength and position throughout intake and compression strokes. Moreover, time-resolved stereoscopic PIV measurements showed a high rate of turbulence production during instantaneous intake cycles due to the shear layers between the inlet jets and the in-cylinder flow. Despite providing a thorough description of mean quantities, an extended 3D description of

instantaneous flow features is still limited by the planar nature of stereoscopic measurements.

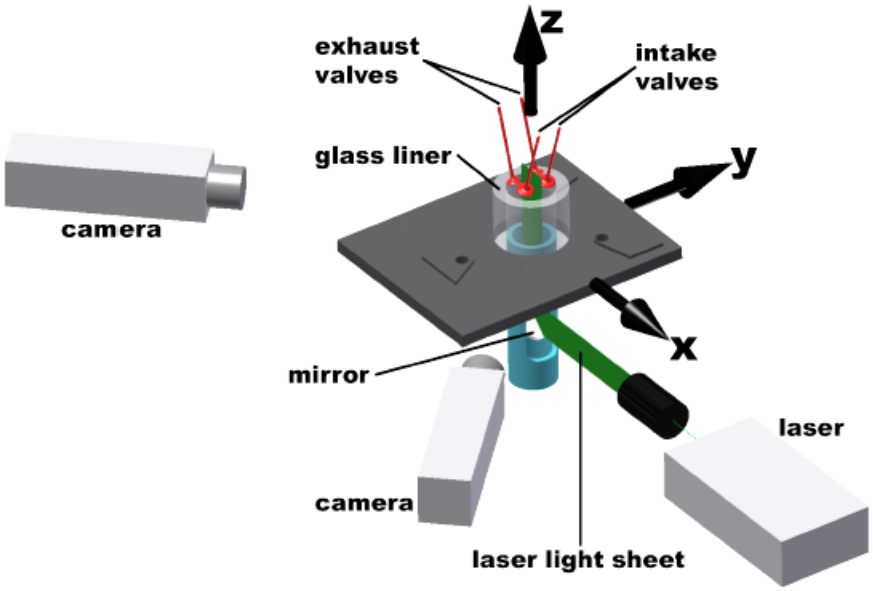

Figure 1-11 Experimental setup for stereoscopic PIV measurements (Karhoff et al., 2013)

Most recently, the tomographic PIV technique has proven to be an extremely useful tool for quantifying the 3D flow structures within a light sheet extended to a continuous volumetric domain instead of a single plane or a series of multi-planar measurements (Elsinga, 2005) (Scarano, 2012). Based on the PIV principle, tomographic PIV allows the instantaneous measurement of the 3 velocity components of the flow in a controllable measurement volume that could be adapted to very small volumes of the order of mm^3 as well as very large volumes (Figure 1-12). However, this technique necessitates on the one hand a large degree of freedom for optical access, since it involves multiple cameras viewing the volume (commonly 4), and on the other hand an accurate calibration process across the investigation volume, which limits its application in confined environments with difficult optical access, such as optical engines.

In fact, like for stereoscopic PIV studies, very few papers can so far be found in the literature about tomographic PIV measurements in IC engines. One is Baum et al. who argues the feasibility of the technique in a motored engine regarding the limited optical access that requires small camera angles, as well as imaging of particles through a thick curved glass cylinder (Baum et al, 2013). They used a camera setup in a Scheimpflug arrangement around the centre axis of the cylinder that ensured a similar distortion for all four cameras. The employed circular ‘X-shaped’ configuration is shown in Figure 1-13.

Two investigation volumes were considered, of 4 mm and 8 mm thickness respectively. A precision within 10% for the velocity gradient tensor was found, i.e. the same order of magnitude as volumetric flow measurements conducted in generic configurations, leading to the indication that tomographic PIV measurements are applicable within a motored optical engine. Furthermore, ensemble-averaged flow fields shown in the central plane were compared for the two measurement volumes, which revealed distinctly different velocity behaviour outside the 4 mm thickness demonstrating the strong three-dimensionality of the flow field. Also, the 2D turbulent kinetic energy (TKE) field showed a region of large velocity fluctuations in the centre of the image plane where the flow from the intake jet interacts with the reversing flow from the piston. In comparison, the 3D TKE field showed that high values of TKE are further extended toward the intake valves, revealing a zone of high turbulence that is influenced by the out-of-plane velocity fluctuation. Finally instantaneous 3D velocity fields were used to reveal cyclic flow variations in the volumetric flow by revealing differences in local velocity magnitude, velocity direction, and regions of strong vortical structures embedded within the flow field during compression.

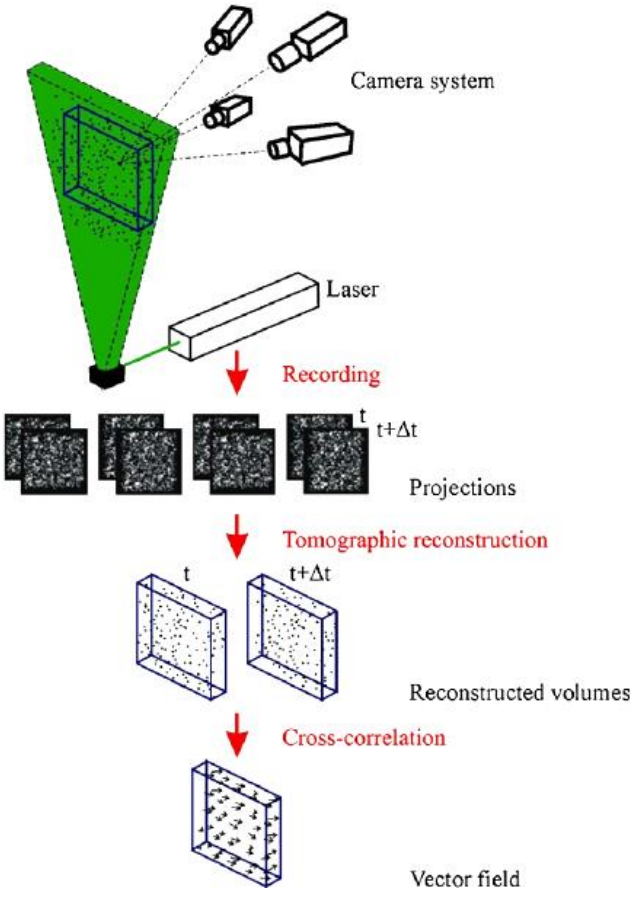

Figure 1-12 Working principle of tomographic PIV reproduced from (Elsinga et al., 2005)

In another tomographic PIV configuration, the 4 cameras were plane from one side of the measurement domain in a circular horizontal area around the centre axis of the cylinder, also ensuring similar distortion for all cameras (Overbrügge et al, 2013) (Figure 1-14). In their set up, 17 calibration planes were used to calibrate and match the viewing planes for each camera and the effect of the distortion caused by the liner was assumed as a systematic error for all measurements. The ensemble averaged velocity fields, the TKE and the vortex centre were analysed at 3 cycle phases, i.e. 3 crank angle degrees during intake and compression strokes. Results provided a 3D description of inlet vortices propagation and tumble formation.

A more recent study by Peterson et al. also addressed the reliability of applying tomographic PIV in an IC engine by applying mass conservation principle and found it as reliable as their high-speed PIV measurements done for engine-spray environment (Peterson et al, 2016). The setup consisted of 4 cameras placed like in the Baum study from both sides of the central plane, on a circular perimeter configuration displaying wider angles from one side where an additional high speed camera was inserted for time resolved recordings. Measurements, done for 5 cranks angle degrees at 800 RPM, spatially quantified the increase in TKE, shear and vorticity from injection and distributions in comparison to non-injection operation, otherwise not available with planar PIV.

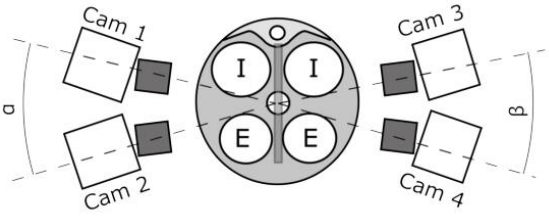

Figure 1-13 Circular X shaped Tomo-PIV configuration (Baum et al., 2013)

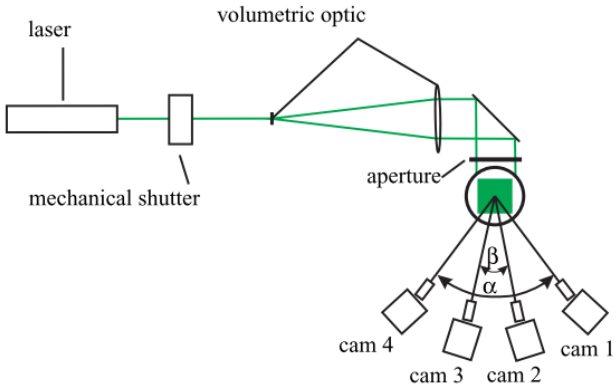

Figure 1-14 Circular arc shaped Tomo-PIV configuration (Overbrüggen et al., 2013)

1.3 Thesis objectives and frame of work

The development of clean and efficient internal combustion engines is constantly faced with the complexity of the in-cylinder phenomena. Today, optical engine configurations allow reaching realistic engine speeds with a complete visualisation of the engine's combustion chamber, as well as performing multiple measurements at the same time. Provided a compromise is achieved between engine operation ranges and maximum

visibility of the in-cylinder processes, measurements of realistic engine operation are feasible and reliable. Additionally, the advancements in optical diagnostic techniques allow the extraction of further information about the in-cylinder flow dynamics, otherwise inaccessible via conventionally embedded sensors. Particle image velocimetry in particular has proven to be a trustworthy technique in capturing the instantaneous and transient nature of the in-cylinder aerodynamics and high speed and volumetric recordings are now giving way to further spatial and temporal analysis of the cyclic nature of the engine flow.

As seen so far, many parameters influence the nature of the in-cylinder flow. The effect of intake flow, engine speed, valve lift, combustion chamber's geometry and many others have been investigated by means of PIV and time resolved PIV that allowed obtaining a spatiotemporal description of correspondingly occurring changes in the flow. Recent efforts seek to gain better understanding of the flow field by obtaining fully three-dimensional quantitative measurements. For that purpose, tomographic PIV have been assessed and found consistent for measurements in IC engines with measurement errors reaching 12% in motored conditions. The few existing 3D studies consist on describing the three-dimensional in-cylinder aerodynamics and spray-induced turbulent flow at relatively low rotational speeds (below 1000 RPM). The considered operation conditions are limited by experimental constraints caused on the one hand by severe optical deformations due to the thick curved cylinder visualised from different angles and on the other hand by the confinement of the combustion chamber limiting the 3D calibration process.

Hence, the characterisation of in-cylinder phenomena in their three-dimensional nature requires further investigations, and the constraints imposed by the engine's environment necessitate an adequately adapted experimental process. For this reason, we aim in our work to investigate the changes in the three-dimensional flow field during intake and compression strokes with respect to the changes in the intake flow at different realistic engine speeds, thus compiling a unique database for in-cylinder flow analysis. For that purpose, 3 inlet duct cross sections are considered by adding different flaps perpendicularly to the inlet flow while running the engine at 2000 and 3000 RPM respectively. Moreover, the experimental process is optimised to respond to the difficulties facing the application of tomographic PIV in an engine-like configuration, i.e. to ease measurements in a complex geometry with confinement, restricted optical access and severe optical deformations. This is done by developing a novel ex-situ calibration procedure combining both mathematical and experimental approaches.

Furthermore, two-dimensional time resolved PIV is first implemented on the engine test bench in order to obtain a spatiotemporal description of the in-cylinder flow on the one hand and validate 3D data on the other hand. We aim thus to identify the variabilities of the in-cylinder aerodynamics and quantify the amplitude of cyclic fluctuations in the mid-cylinder plane under the 6 described operation conditions.

Experiments are lead on the optical engine test bench of CORIA laboratory. It is a transparent 4-valve direct-injection spark-ignition (DISI) single-cylinder engine developed by *AVL*. It can operate at rotational speeds up to 3000 RPM, in both driven or combustion conditions and at an injection pressure reaching 200 bar. It is installed on a vibration-absorbing base in order to avoid disturbing optical measurements (Figure 1-15). One of the main characteristics of this test bench is the interchangeability of the cylinder liner allowing the passage from an opaque configuration (i.e. metallic cylinder) to an optical configuration (i.e. quartz cylinder). The conversion between configurations is done via a high pressure hydraulic system that also ensures a rigorous sealing at the cylinder head during engine operation. The simple handling of the hydraulic system facilitates removing the glass cylinder for cleaning during the experimental runtime and repositioning it with great ease. The transparent cylinder of 25 mm thickness has an internal bore of 82 mm and a stroke of 86 mm; the engine's capacity is 450 cm^3. Further characteristics of the engine are given in Table 1-2.

Additionally, it is possible to change the intake manifolds to include a blocking flap perpendicularly to the axis of the inlet duct (Figure 1-16). Two different flap sizes are available such as 50% or 25% of the inlet duct cross section is admissible therefore bringing alterations to the intake flow. Consequently, three engine inlet conditions can be tested. Hereafter, V100 indicates the original intake flow in the absence of any flap; V50 and V25 correspond to the flaps reducing the intake flow to 50% or 25% of its initial state respectively.

Throughout the study, we'll be addressing the aerodynamics inside the combustion chamber during intake and compression strokes in motored condition, i.e. without injection nor firing. The engine therefore aspires only air, via a sonic throat branched to the output of a compressed air supply allowing to control the intake flow and maintain similar working conditions during all measurements, i.e. environmental conditions at 1 atm and 300 K.

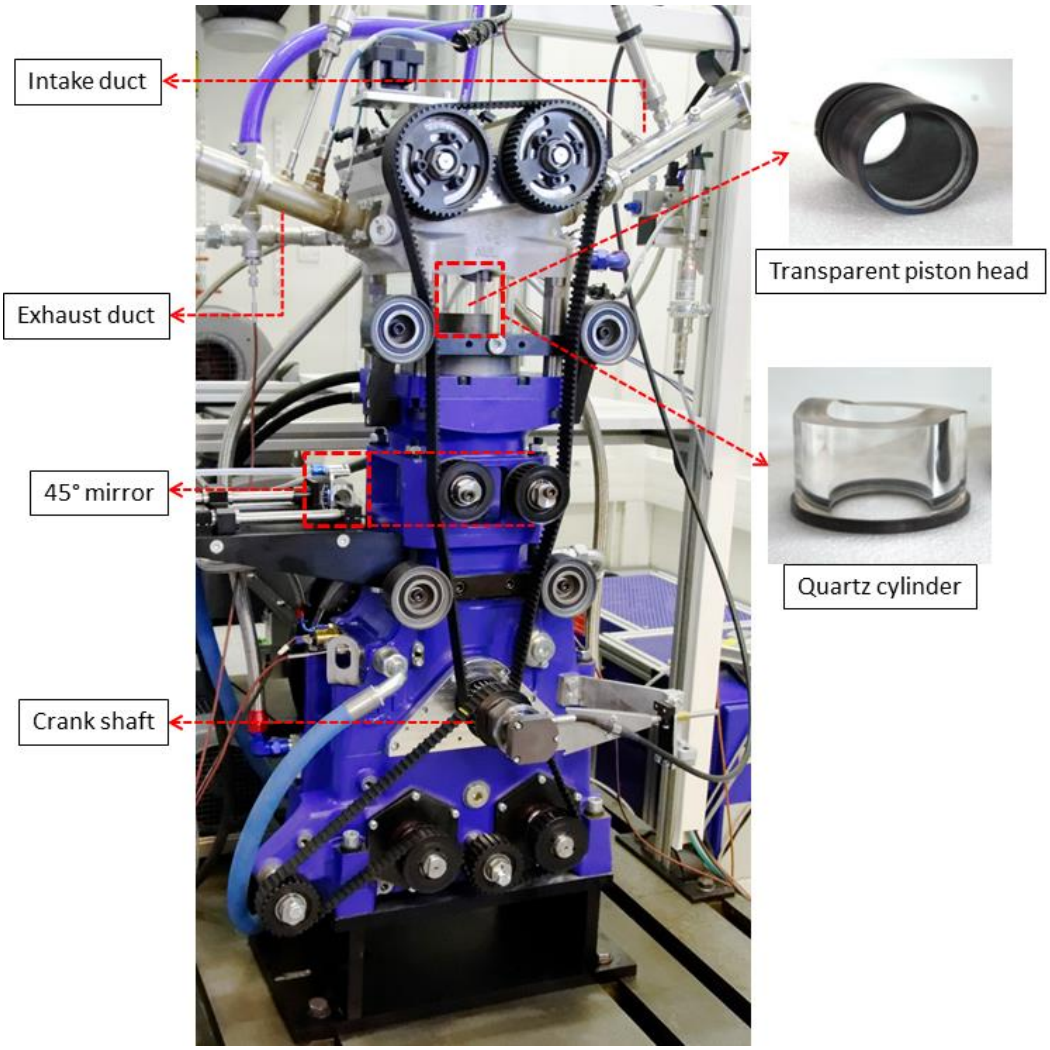

Figure 1-15 AVL optical engine test bench

Figure 1-16 Interchangeable intake flaps

Characteristics	Description	Characteristics	Description
Type	DISI	**Bore**	82 mm
Strokes/cycle	4	**Capacity**	450 cm^3
Number of cylinder	1	**Compression rate**	8.5
Stroke	86 mm	**Polytropic coefficient**	1.35
Lever	144 mm	**Maximal pressure**	40 bar

Table 1-2 AVL Optical engine characteristics

2 Experimental procedures

The purpose of this chapter is to introduce the experimental set-ups used and developed in the scope of our study of in-cylinder aerodynamics. It is thus divided in two main parts. The first describes the established procedures for two-dimensional measurements performed using high speed PIV (TR-PIV), the constraints faced are addressed and the data quality is evaluated. The second part describes the adjustments made for 3D measurements using tomographic PIV (Tomo-PIV). The choice of volume thickness for valid in-cylinder measurements is then demonstrated. Furthermore, we particularly address the 3D calibration procedures facing the confinement of the engine's combustion chamber and its severe optical deformations caused by the thick optical cylinder.

2.1 Time resolved PIV and 2D flow measurements

In order to perform 2D TR-PIV measurements in the engine's combustion chamber, a number of constraints dealing with establishing the measurement field and adequately installing measurements equipment need to be addressed. This mainly involves the camera setup, the optical arrangement, the laser and the timing unit, as well as the quality of seeding particles, all of which are detailed hereafter.

2.1.1 Geometrical considerations and optical arrangement

The laser used is a linearly polarized Dual-Darwin-80, i.e. a dual pulsed PIV laser with 2 cavities combined before the laser's output. At 1 KHz and 532 nm wave length, it provides 25 mJ per pulse. While the engine runs, vibrations and thermal fluctuations are induced. This could cause an unstable operating of the laser which is therefore placed in a room adjacent to the engine's test-bench. A black tunnel through the wall links both rooms and ensures the passage of the laser beam. The optical assembly is then carried out to ensure expediency for adjustments - if needed during operation. The desired field of view is obtained via an optical alignment carefully evaluated along four independent parts: the laser, the engine, the lens assembly and the recording system.

The optical access in the combustion chamber was first achieved by the 45° mirror placed under the transparent piston head. The obtained laser sheet in the combustion chamber goes through a combination of one spherical lens and one cylindrical lens fixed prior to the mirror on a separate bench from the engine in order to avoid any vibrations of

the lenses. Then, optical alignment is achieved so that the field of view corresponds to the cylinder's symmetry plane (Figure 2-1).

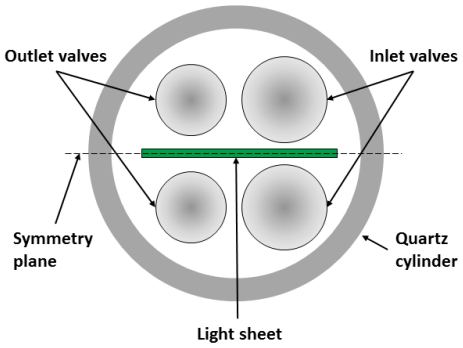

Figure 2-1 Mid-cylinder measurement plane

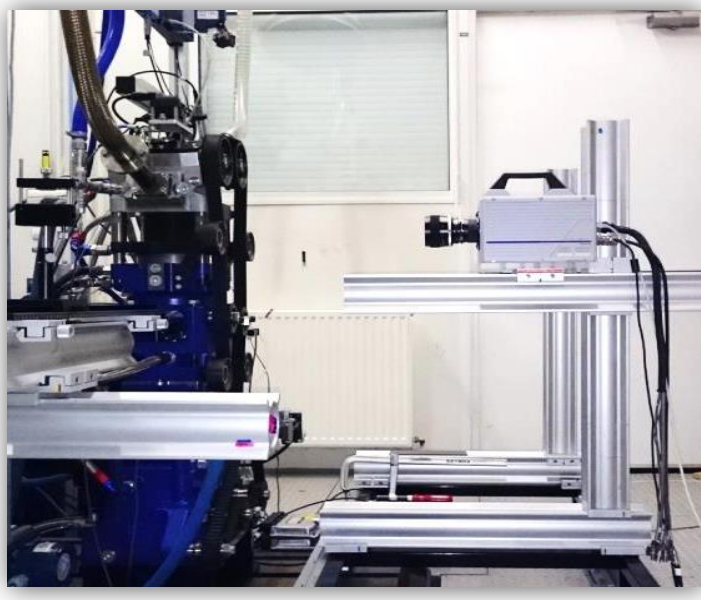

Figure 2-2 TRPIV experimental setup

The laser is coupled with a high speed camera Photron equipped with an 85mm - f1/4 lens, placed parallel to the light sheet plane (Figure 2-2). It was observed that the obtained field of view is limited by the mirror's diameter, i.e. the light sheet's width is considerably smaller than the cylinder's bore (Figure 2-3 (a)). This fact, combined with the fact of dealing with a thin light sheet configuration, motivated the testing of an optical access directly through the transparent cylinder, along its symmetry plane. The obtained field of view is wider than the previous one, i.e. more information is accessible, and therefore this configuration was retained for the 2D TR-PIV measurements (Figure 2-3 (b)).

Despite the thorough alignment process, the curved geometry and the thickness of the quartz cylinder produce strong reflexions that are likely to increase noise level in the background and therefore reduce the signal to noise ratio on particle images. For this reason, the inner background of the cylinder was painted in black. In addition, reflexions occur between the internal and external surfaces of the cylinder caused by the direct optical access and augmented by the surrounding metal columns of the hydraulic system. Black stripes are therefore fixed on the front external surface of the cylinder, at the borders of the field of view.

As a result, the achieved field of view has a resolution of 768×768 pixels corresponding to 91×91 mm². However, eliminating reflexions and optimising calculations led to obtaining velocity fields of 74×84 mm². Moreover, one distinctive trait of experimentally investigating engine flows is the dynamic change of the visualized field during every engine cycle. This is caused by the piston's movement from BDC to TDC and vice-versa. This trait is addressed with a dynamic masking step for each recorded crank angle degree, further described in §2.1.4.

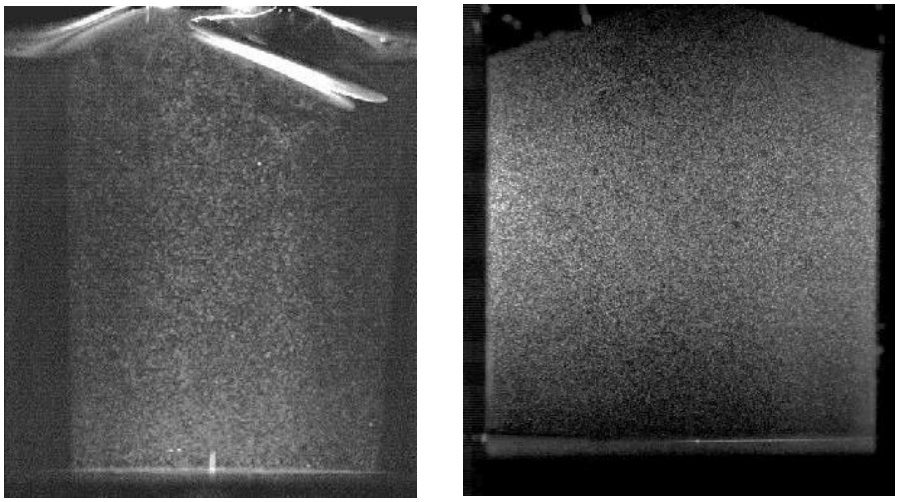

(a) **(b)**

Figure 2-3 Particle images in the mid-cylinder plane obtained (a) via the 45° mirror and (b) via direct access through the liner

2.1.2 Seeding

The quality of PIV measurements and the validity of data sets are highly dependent on the choice of seeding particles. An excess in particle density and/or particle response time can mask the initial flow, as an insufficient number of particles can cause a loss of information.

An in-house aerosol generator is used to provide seeding particles for our measurements and is shown in Figure 2-4. It is subject to alignment sensitivity of the air/liquid nozzles that mainly affects the particles density. This generator allows producing tracer particles having a diameter of 1 to 5 µm that are small enough to faithfully follow the flow. In a first stage, the substance used was Di-Ethyl-Hexyl-Sebacat (DEHS) which is a colourless and odourless liquid suitable for producing steady aerosols. DEHS ensures having spherical particles with well-known optical properties as well as having an easy cleaning/maintenance process. However, it was observed that when reaching the end of the compression stroke, the droplets signal reduced. This was primarily linked to the reduction in droplets diameters as flow temperature rises during compression. Therefore,

DEHS was substituted in a second stage with olive oil that is able to sustain higher temperatures. On the one hand, signal to noise ratio (SNR) increased during measurements since particles size and number were maintained along the engine cycle. On the other hand, it was now necessary to reduce engine operation time in order to clean more often the cylinder's walls that were rapidly smeared by the new substance. Hence, measurement campaigns consisted of recording series of 50 consecutive cycles separated by the time of cleaning the quartz cylinder. During experiments, the desired quantity of seeding particles is specified by a Bronkhorst flow-meter operated via LabVIEW. Finally, the seeder's output flow is introduced far upstream of the engine valves in order not to disturb the in-cylinder aerodynamics.

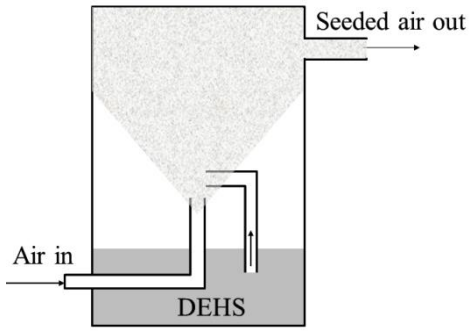

Figure 2-4 PIV seeding particles generator

2.1.3 Synchronisation

In an engine configuration, the synchronization of the PIV chain is one of the main challenges that encounter the experimenter. In order to capture particle images at a certain crank angle degree, pulse timings of all components - i.e. laser, camera and engine - have to be centralised and controlled. Only then, the same phase of the engine cycle is recorded each time an acquisition of particle images is desired.

While performing high speed measurements in particular, a series of multiple crank angle degrees are recorded during each engine cycle. This is not the case for classical PIV recordings, where the same crank angle degree is recorded every few engine cycles. Therefore, it was essential to first determine the crank angle resolution for recordings corresponding to each of the considered engine speeds, i.e. 2000 and 3000 RPM. The angular position of the engine is provided by an AVL timing unit connected to the test bench. It allows extracting a reference pulse at the beginning of every engine cycle with a precision of 0.1 CAD. This reference is used to trigger a sequence of pulses via an external programming unit *Acquitek* such as detailed in Schematic 2-1 where the shown signals correspond to:

1. Cyclic trigger that starts the recording sequence with the beginning of every engine cycle, i.e. the beginning of intake at -360 CAD,
2. Reset of external *Acquitek* unit,
3. Trigger of external *Acquitek* unit,
4. Camera trigger (f = 3 KHz),
5. Camera frame 1 ($t_{exposure}$ = 330 µs),
6. Laser 1 (f = 1.5 KHz),
7. Camera frame 2 ($t_{exposure}$ = 330 µs),
8. Laser 2 (f = 1.5 KHz).

The maximal permissible frequency for recordings is imposed by the camera to 3 KHz at the chosen image resolution. Hence the laser frequency is set at 1.5 KHz for each laser head. By dividing the laser's period over the time needed to achieve 1 CAD rotation at a given engine speed we obtain the recording frequency during one engine cycle. As a result, at 2000 RPM, one image pair is recorded every 8 CAD of the cycle. Similarly, at 3000 RPM, one image pair is recorded every 12 CAD (table 2-1). In total, 300 engine cycles are recorded for each engine operation condition.

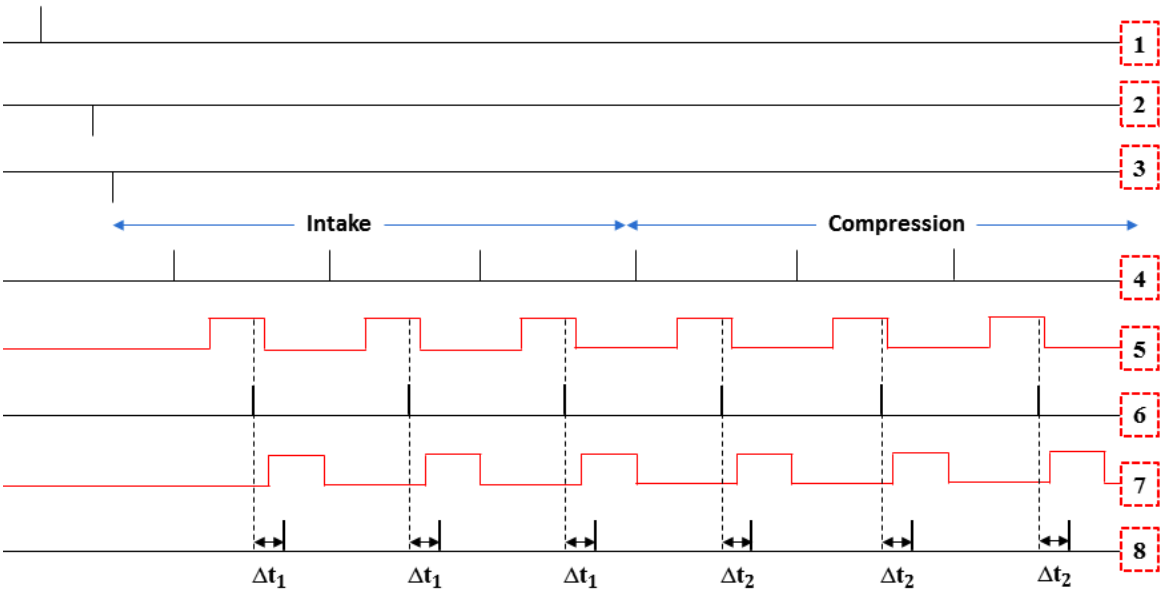

Schematic 2-1 TRPIV Synchronisation, where Δt is the PIV frame separation time, Δt_1 is the frame separation time during intake stroke and Δt_2 is that during the compression stroke.

In the course of this study, we are mainly interested in the intake and compression strokes, i.e. 360 over 720 CAD of the engine cycle (Figure 1-2). Therefore, recordings are ceased during expansion and exhaust strokes which results in 45 recorded phases per cycle at 2000 RPM, and 30 phases per cycle at 3000 RPM.

Finally, the use of a single frame separation time is insufficient to resolve the wide range of in-cylinder velocities and spatial scales encountered throughout the engine cycle (Abraham et al, 2013). Therefore a variable Δt is imposed as a function of crank angle degree via the *Acquitek* programmable unit. According to the in-cylinder dynamics, smaller Δt values are imposed when greater velocity magnitudes are expected, i.e. during intake stroke, and larger Δt are set during the compression stroke.

Engine speed (RPM)	**2000**	**3000**
Engine cycle duration (s)	0.06	0.04
1 CAD duration (µs)	83.33	55.55
Image recording resolution	1 pair every 8 CAD	1 image pair 12 CAD
Δt_{piv} during intake (µs)	10	10
Δt_{piv} during compression (µs)	20	15

Table 2-1 Engine operation point considered for TR-PIV recordings

The recording conditions detailed in Table 2-1 are used for all 2D measurements of the 6 engine operation conditions in order to provide comparable datasets of the flow.

2.1.4 Data processing of TR-PIV measurements

In order to obtain accurate and reliable velocity fields, PIV measurements rely on the quality of particle images on the one hand and on the precision of the calibration process and adaptation of PIV algorithms with respect to flow characteristics on the other hand.

2.1.4.1 2D calibration and image pre-processing

It is essential to establish the correspondence between image plane and object plane in order to describe spatial resolution and to correct optical deformations. This is done by using a black metallic calibration target engraved with a white dotted regular grid, i.e. $\Delta x = \Delta y = 1$ mm. Special symbols allow fixing the origin ($x = 0$, $y = 0$) of the grid. The target is fixed at the centre of a cylindrical base having a diameter equal to the engine piston's diameter to ensure that the calibration plane collides with the measurement plane (Figure 2-5). The coordinates of each grid point are extracted using a pattern recognition algorithm with subpixel precision (Figure 2-6) and two main results are then deduced:

1) A 5^{th} degree polynomial function describing the deformations caused by the cylinder's curvature and thickness,
2) The magnification factor, i.e. 0.125 mm/px.

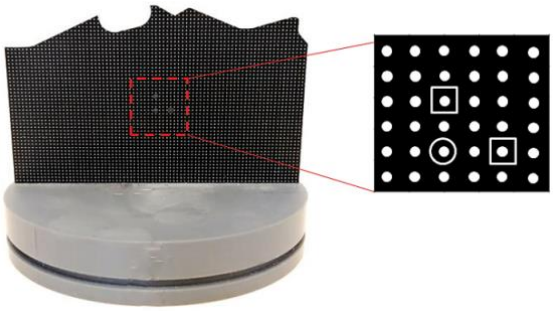

Figure 2-5 Calibration target engraved with regular grid

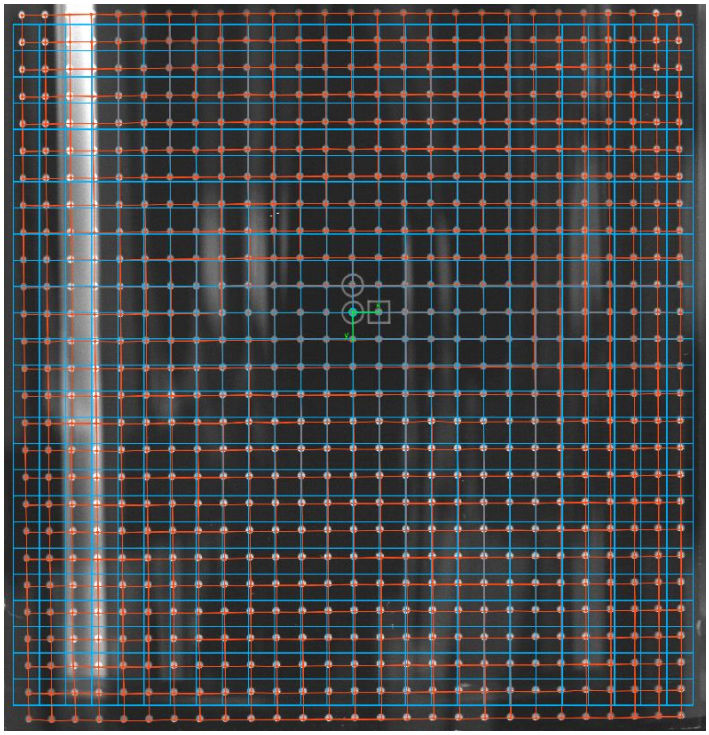

Figure 2-6 Extraction of grid coordinates by pattern recognition algorithm. The raw target grid is shown in red. The grid corrected via the deformation function is shown in blue. Distortions are minimal at the centre of the image and maximal at borders of the image.

The deformation function is obtained using the least square method to find the correspondence between pixel coordinates (X,Y) and real coordinates (x_r,y_r) of target points in order to transform them onto a regular coordinates system:

$$x_r = \sum_{i=0}^{5}\sum_{j=0}^{5} a_{ij}X^iY^j \quad \textbf{(2-1)}$$

$$y_r = \sum_{i=0}^{5}\sum_{j=0}^{5} b_{ij}X^iY^j \quad \textbf{(2-2)}$$

These functions are then used to correct all recorded particle images prior to PIV calculations and eliminate optical deformations of the mid-cylinder plane (Figure 2-6) Clearly the cylinder's geometry doesn't cause only distortions but other optical aberrations such as astigmatism that modifies particles shape. However, in the course of this study, astigmatism has no significant effect since the camera is place parallel to the mid-cylinder plane and only optical distortions are corrected.

Moreover, particle image dimensions vary as a function of crank angle degree with respect to the piston's position between BDC and TDC. Each phase is thus treated with a corresponding filtering technique and a dynamic mask algorithm is applied during calculations. For this purpose, a mean particle image is calculated at every phase and represents a constant background image. On the one hand, by dividing all images at that phase by the obtained background, SNR is increased. On the other hand, each background image serves as a base for creating a mask that renders a zero value to regions surpassing the frame of particles field therefore eliminating all residual reflexions (Figure 2-7). As a result, particle image pre-processing allowed increasing the signal to noise ratio, facilitating the identification of particles during the correlation step and thus obtaining a high validation rate of velocity vectors after PIV calculations.

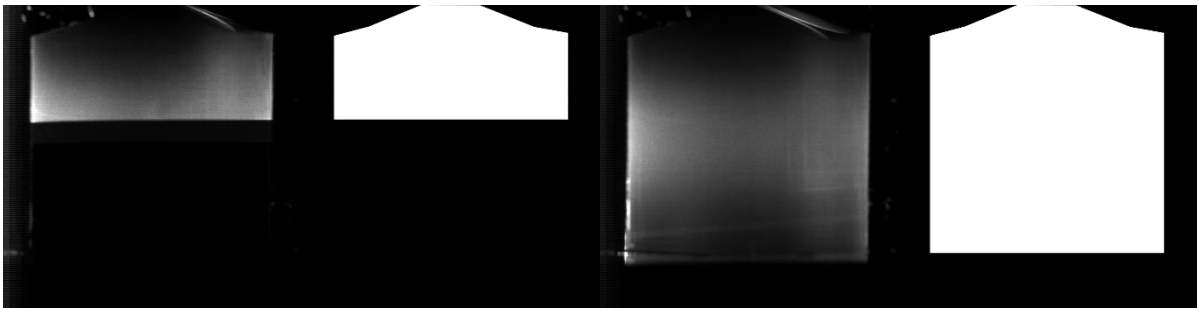

(a) -274 CAD (b) -274 CAD (a) -178 CAD (b) -178 CAD

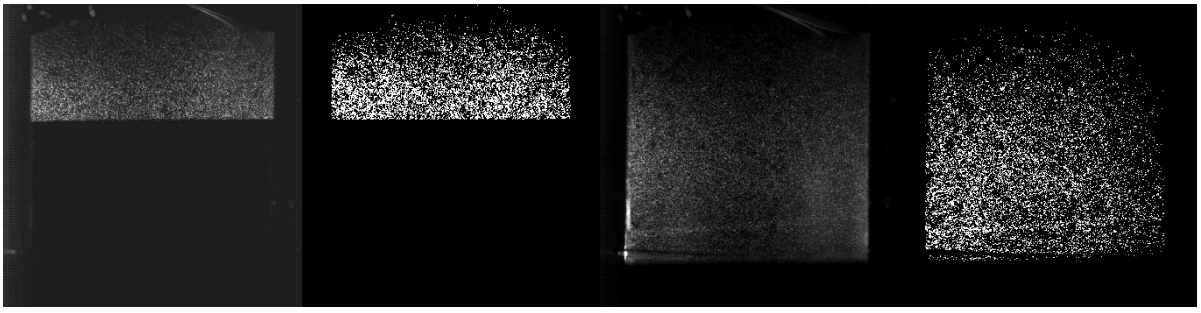

(c) -274 CAD (d) -274 CAD (c) -178 CAD (d) -178 CAD

Figure 2-7 (a) Mean particle image, (b) variable mask image, (c) particle image before pre-processing, (d) particle image after pre-processing.

2.1.4.2 PIV algorithm

Instantaneous velocity fields were obtained using an in-house PIV algorithm based on pattern correlation in particle images (Lecordier, 1997). A multi-pass correlation with sub-pixel iterative shift is realised over interrogation windows going from 32×32 to 20×20 pixels corresponding to 2.4×2.4 mm² with 50% overlap. The final interrogation window size is well adapted to the velocity gradients of the flow so that velocity fields are not excessively smoothed. Moreover, the 50% overlap makes it possible to better follow the speed evolution in the gradient zones with more vectors. The number of iterations for the calculations is dynamically obtained from the local field's residual characteristics. A maximal displacement filter, a minimal signal to noise ratio and a median filter are applied over a squared interrogation area. Finally, the number of iterations normally ranged between 3 and 6 and the dynamic masking was integrated in the velocity field calculation therefore reducing error propagation during the iterative process. These measures added to the image pre-processing step and the dynamic frame separation time described in §2.1.3 ensured having a high rate of validated vectors exceeding 95% in all resulting fields (Figure 2-8).

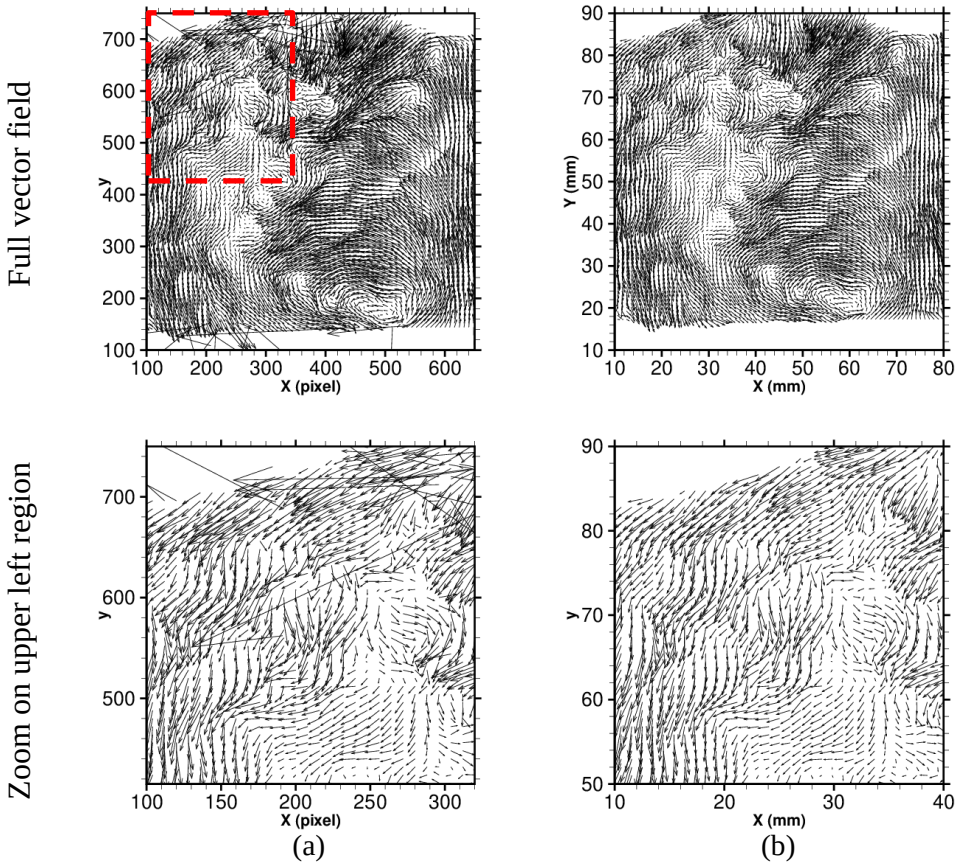

Figure 2-8 (a) Velocity vector field before validation step and (b) after validation step showing less than 5% erroneous vectors

2.1.5 TR-PIV data validation

It is essential to evaluate data validity under the employed measurement conditions prior to any flow analysis. Therefore, convergence of velocity measurements is evaluated at 3 crank angles degrees representing a range of variable in-cylinder dynamics. Moreover, measurements recorded at BDC where the field of view is at its largest dimensions are isolated and treated for the detection of peak-locking bias. Finally, a statistical analysis is performed comparing mean velocity fields and fluctuations obtained from time-resolved PIV measurements to those obtained from classical PIV measurements previously performed on CORIA's engine test bench.

2.1.5.1 Convergence of velocity measurements

The turbulent nature of the engine's in-cylinder flow dynamics results in many variations of the instantaneous velocity fields. It is therefore necessary to record a certain minimal number of images in order to ensure the convergence of average quantities. This is more critical for classical PIV (CPIV) measurements dealing with low frequency recordings but nevertheless verified for the present high speed PIV recordings. Particle images recorded at 2000 RPM and V100 intake condition are considered for the convergence study at 3 crank angle degrees, i.e. during intake at -274 CA°, near BDC at -178 CA° and during compression at -82 CA°. Ensemble average velocity offering a general description of the in-cylinder flow is then calculated for an increasing N number of cycles such as:

$$\overline{u_N}(x,y) = \frac{1}{N}\sum_{i=1}^{N} u_i(x,y) \qquad \textbf{(2-3)}$$

where u_i is the velocity component at a fixed point (x,y) in the instantaneous velocity field i and $\bar{u}_N$ is the ensemble average velocity component at that point computed over N velocity field. Then, by varying N between 25 and 300 with a step of 25 fields, 12 mean velocity fields are obtained and interpreted for convergence analysis. For this purpose, an example of velocity profiles is extracted at the middle of the field of view. This example is representative of the convergence across the field.

Similarly for velocity fluctuations, equations (2-4) represent the ensemble averaged velocity fluctuations computed over N velocity fields.

$$\overline{u'_N}(x,y) = \frac{1}{N}\sum_{i=1}^{N} u'_i\,(x,y) \qquad \textbf{(2-4)}$$

As a result, mean velocity magnitudes converge rapidly with only 50 pairs of particle images needed to ensure convergence. This is shown in the first row of Figure 2-9 showing mean velocity profiles extracted from the largest field of view at -178 CAD. The same tendency of mean velocity magnitudes to converge starting 50 velocity fields is verified across the whole engine cycle. The second row of Figure 2-9 meanwhile shows a later convergence of velocity fluctuations with a minimum of 200 pairs of particle images needed to ensure convergence. Moreover, the three considered CAD reveal very different flow dynamics going from larger magnitudes at the beginning of intake stroke (-274 CAD) to smaller magnitudes towards the end of compression stroke (-82 CAD). This is represented in the different scales of Figure 2-10 where velocity fluctuation profiles are shown at -274 CAD and -82 CAD confirming the conclusion that a minimum number of 200 particle image pairs should be recorded for each engine phase. Finally, in our measurements, 300 engine cycles were recorded for each considered case and convergence is attained.

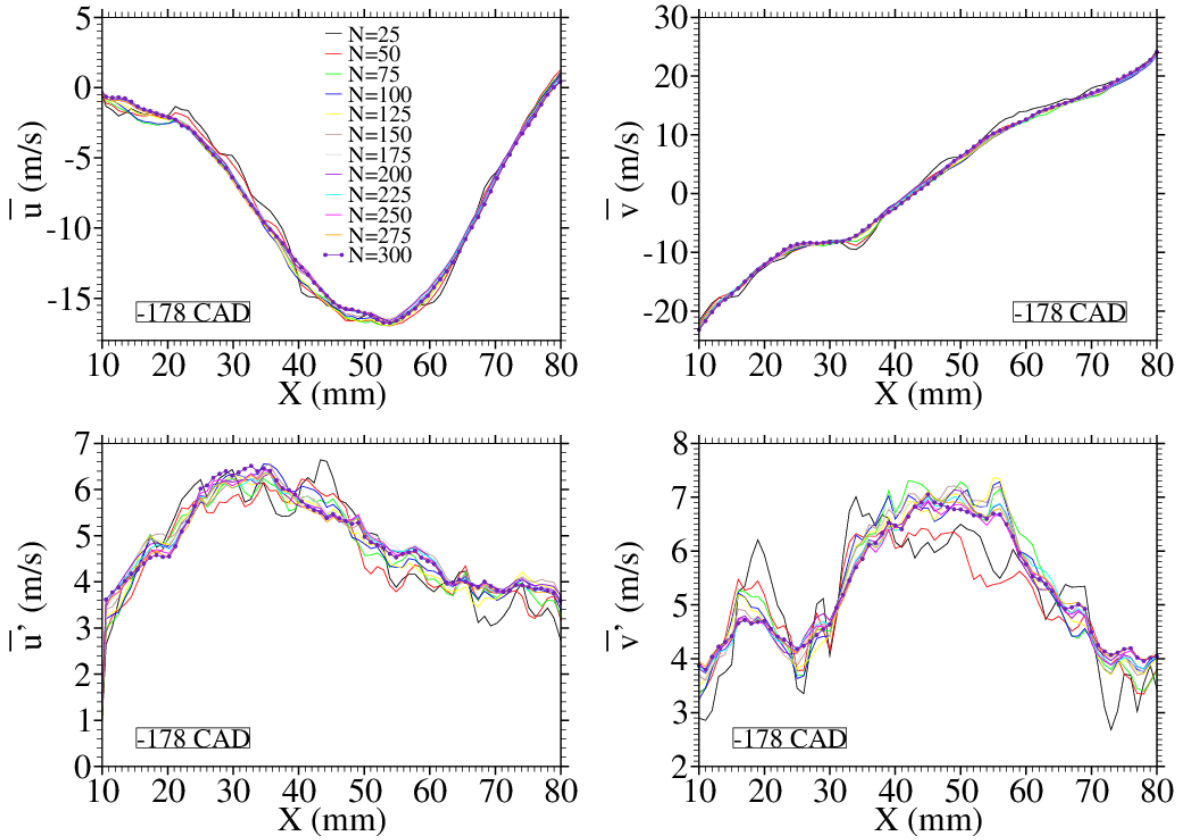

Figure 2-9 Convergence of mean velocity profiles and velocity fluctuations at -178 CAD (Y=46 mm) from TR-PIV measurements

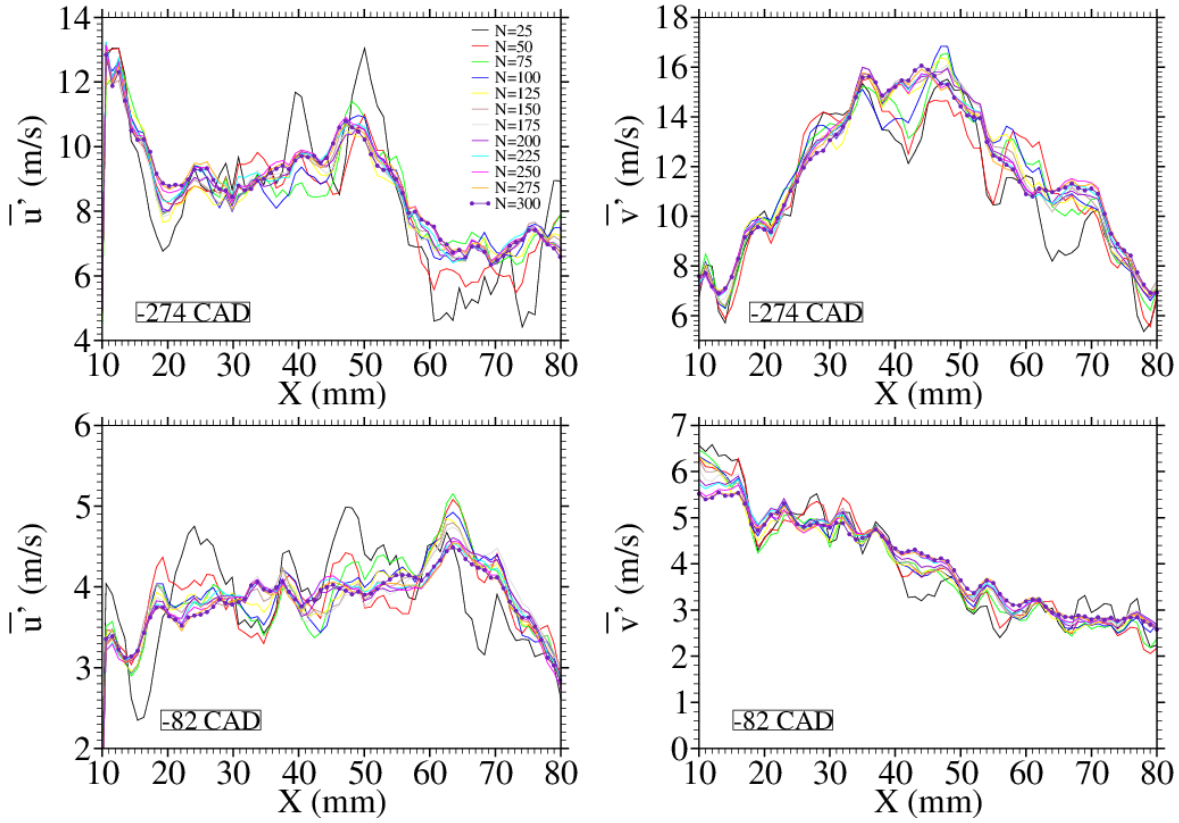

Figure 2-10 Convergence of velocity fluctuation profiles during intake (-274 CAD) and compression

2.1.5.2 Peak-locking bias

Particle images whose dimensions are much smaller than those of the CCD sensors can generate critical cases of signal sampling where the Nyquist criterion is no longer respected. As seen in §2.1.2, tracer particles used for PIV recordings have a very small diameter of 1 to 5 µm. Hence, in order to collect a satisfactory signal from a particle diffusion, the laser power is set to maximum output and the lens aperture is relatively large. Consequently, the image of a small particle is much smaller than the pixel (Lecordier and Trinité, 2006).

This translates in reality into the peak-locking bias that directly affects the measurements quality as a consequence of a decrease in the linear response to particle displacement and an increase in particle dispersion. Peak-locking appears when certain integer velocity categories are privileged in the measured field. Therefore, a common way to demonstrate the presence or absence of peak-locking consists of plotting the distributions of velocity components and making sure it does not manifest any periodic feature of integer nature or any discontinuity for half-pixeled values. (Lecordier et al., 2001).

The histograms of both u and v components in Figure 2-11 are plotted from cumulating 300 instantaneous velocity fields obtained from recordings at BDC, i.e. the largest field of view available, and show that our measurements do not induce any peak-locking bias. This result is a combination of the recording parameters and the PIV algorithm that employs sub-pixel shift ((Lecordier and Trinite, 2004).

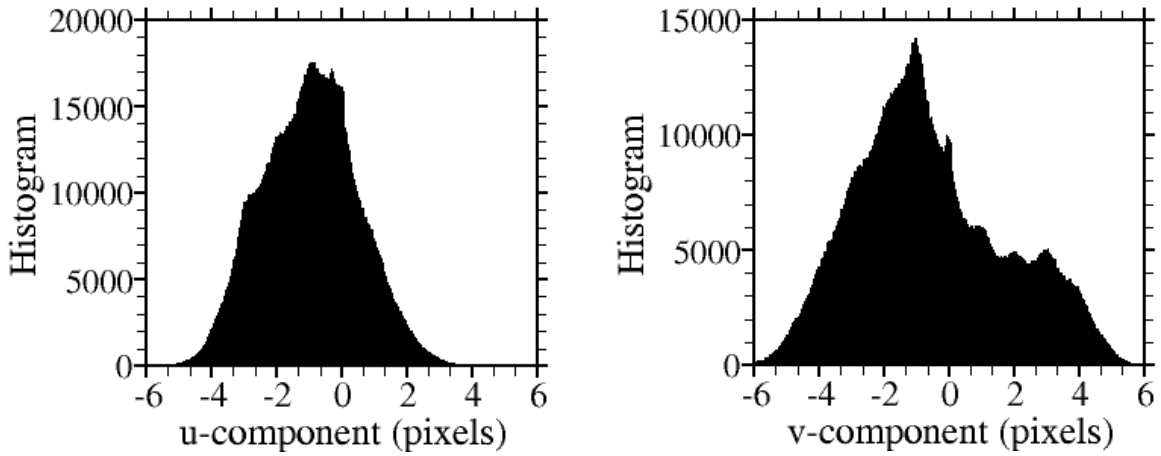

Figure 2-11 Histograms of velocity components distribution

2.1.5.3 Statistical analysis and comparison to Classical PIV measurements

Previous phase-locked 2D PIV measurements were performed on the optical engine test bench likewise used in this study (Lemetayer, 2016). For their measurements, referred to as classical PIV measurements (CPIV), cameras of higher resolution (2048×2048 pixels) and lower recording rate than those presently used for TR-PIV were employed at a double frame recording frequency of 2 Hz. In this section, we aim to demonstrate the validity of our 2D time-resolved data (3 KHz, 768×768 pixels) by comparing the mean engine cycle obtained at 2000 RPM to the reference case in the previous study also treating measurements at 2000 RPM without firing or injection. In fact, although the engine's internal aerodynamics are a complex three-dimensional flow, it presents meanwhile some characteristic structures specific to the engine's geometry. Since both measurements are done in the same symmetry plane and under same intake conditions of pressure and temperature, it is possible to compare the global vortex structures during intake and compression strokes in non-firing conditions for both campaigns. Therefore, keeping in mind that the instability of engine test-bench operations and the great amount of time separating the two campaigns can induce some differences, phase-locked data are extracted from the time-resolved measurements and are compared to the previous classical PIV measurements.

Intake stroke

Figure 2-12 shows the in-cylinder flow of a series of crank angle degrees during the intake stroke. Different flow regions can be identified for each phase and are found to be similar for both measurements. In the left hand column, mean velocity fields obtained from classical PIV measurements are shown. On the right hand side, mean velocity fields obtained from time resolved PIV measurements are shown. It is important to note that the spatial resolution of classical PIV measurements is 2 times greater than the present time resolved PIV measurements. An assessment of the measurement errors relevant to the spatial resolution can be found in literature, revealing that the high spatial resolution data captures the lower velocity magnitudes with greater resolution and better capture velocity vectors of higher magnitude (Abraham et al., 2013). This explains the finer contours of velocity regions of classical PIV images.

Moreover, the in-cylinder flow can be described by identifying 3 main regions during the intake stroke for both measurements:

1. The front valve jet in the upper left part of the combustion chamber,
2. The rear valve jet in the right part of the combustion chamber, and
3. The flow region in the lower part of the combustion chamber, i.e. nearest to the piston head.

Region 1 consists of the largest velocity gradient during the engine cycle reaching values around 50 m/s. The air flow entering the chamber heads in a downward direction toward the left side wall and meets the piston head. This drives the formation of a vortical structure with zero velocity regions under the exhaust valve. Region 2 consists of the air flow entering the chamber through the rear valve jet, rebounding on the right side wall of the chamber on the one hand and meeting the piston head on the other hand. A second vortex structure thus starts to form in region 3 near the piston's head and develops towards the right half of the measurement plane as the piston starts moving towards BDC. In this region, surrounding the vortex, velocity magnitudes reach values over 20 m/s. Moreover, Figure 2-12 reveal for both campaigns the high velocity fluctuations in region 1 exceeding 20 m/s and decreasing as they go towards region 2 and 3 and towards the end of intake.

Compression stroke

In addition to the similarities observed during the intake stroke, Figure 2-13 show the mean and fluctuating in-cylinder flow during the compression stroke for both classical PIV and time-resolved PIV measurements. As previously observed for the intake, similar behaviour and orders of magnitudes are observed with both types of

measurements during the compression stroke: the air in a downward direction is strongly slowed by the piston's upward movement and is deflected to the right while the speed of the air in an upward direction is maintained along several crank angle degrees during the compression. Towards the end of compression, near the piston head, the flow accelerates and reaches again velocities of around 20 m/s. The tumble structure is observed to be compressed with the rise of the piston. Additionally, velocity fluctuations reveal similar distributions across the field of view in both cases. Orders of magnitude are maintained at the beginning of compression and a slight increase is revealed at the end of compression as the piston moves closer to the TDC.

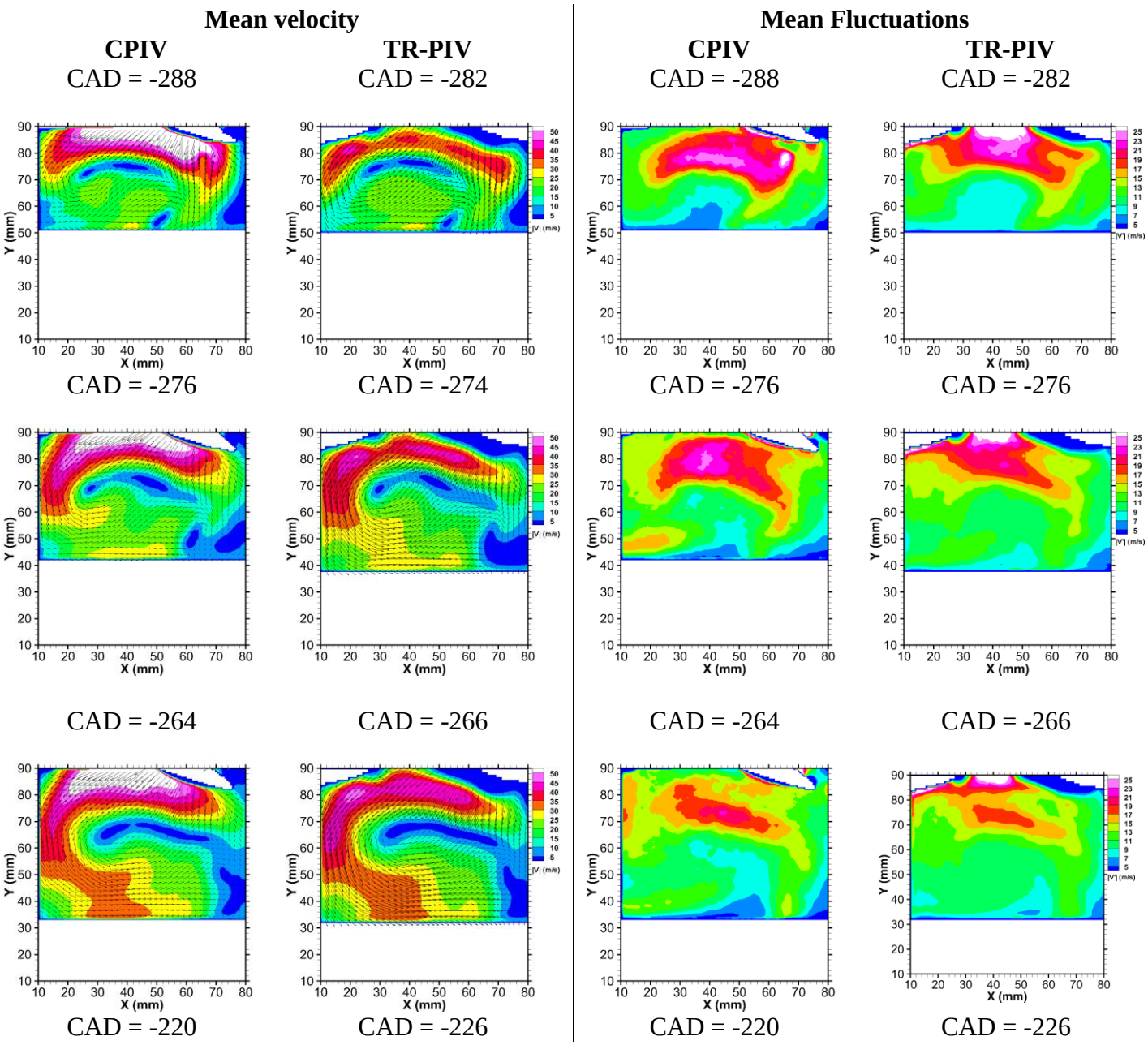

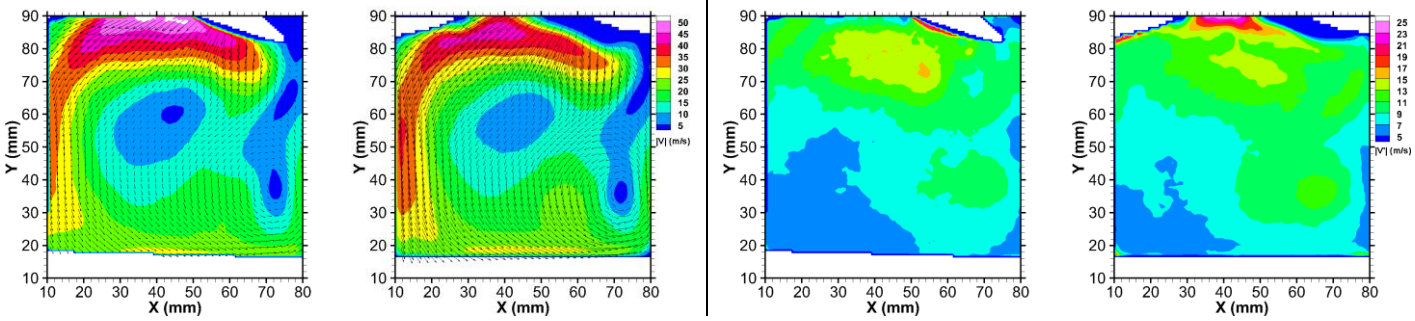

Figure 2-12 Ensemble averaged velocity and fluctuations fields during intake stroke obtained from classical and time-resolved PIV

Mean velocity | **Mean fluctuations**

CPIV	**TR-PIV**	**CPIV**	**TR-PIV**
CAD = -180	CAD = -178	CAD = -180	CAD = -178
CAD = -140	CAD = -146	CAD = -140	CAD = -146
CAD = -100	CAD = -98	CAD = -100	CAD = -98
CAD = -80	CAD = -82	CAD = -80	CAD = -82

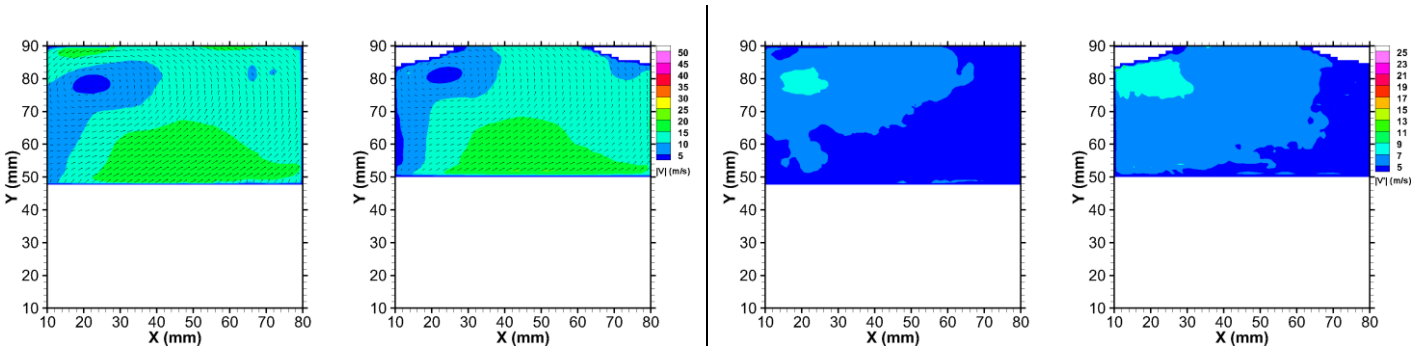

Figure 2-13 Ensemble averaged velocity and fluctuations fields during compression stroke obtained from classical and time-resolved PIV

2.1.6 Summary of time-resolved measurements

Time resolved PIV measurements were performed on a single cylinder optical engine test bench in order to capture the spatiotemporal evolution of the in-cylinder aerodynamics during intake and compression strokes. All experiments were carried out with air at environmental conditions (1 atm and 300 K) and without firing. A number of settings were implemented in order to adapt the application of time-resolved PIV to the engine setup taking into account the optical access, optical deformation, light reflexions, the seeding and the synchronisation process.

The considered data validation approach addressed the convergence of mean magnitudes, the absence of peak locking bias and the comparison of flow features that are characteristics to the engine operation cycle with respect to measurements done using classical PIV under same experimental conditions. As a result, the 2D time-resolved measurements fulfilled all validation criteria and are considered as reliable data sets to study the in-cylinder aerodynamics.

For the test campaigns, 300 engine cycles were recorded for each of the six engine operation conditions: two realistic rotational speeds, i.e. 2000 and 3000 RPM, and three inlet flow conditions provided by adding different ports to the inlet duct, yielding an intake of 100%, 50% or 25% of the initial inlet flow. Recording resolutions per cycle were set to 1 image pair recorded every 12 and 8 CAD for 2000 and 3000 RPM respectively (Table 2-2). During each campaign, the engine was stopped in order to clean the cylinder walls smeared by the tracer particles and avoid blurry images. Therefore, each of the 6 campaigns was performed by recording series of 50 engine cycles at a time, i.e. approximately 2000 particle image pairs. In total, 71 250 particle image pairs are obtained for PIV computations resulting in 71250 velocity fields. The in-cylinder flow characterisation during the different cases is discussed in chapter 3.

Intake duct opening	N = 2000 RPM			N = 3000 RPM		
	Number of cycles	**Recording resolution**	**Image pair per cycle**	**Number of cycles**	**Recording resolution**	**Image pair per cycle**
V100	350	12 CAD	45	350	8 CAD	30
V50	300	12 CAD	45	300	8 CAD	30
V25	300	12 CAD	45	300	8 CAD	30

Table 2-2 Summary of TR-PIV measurement campaigns during intake and compression strokes, [-360, 0] CAD.

Although alterations in engine operation regarding parameters of speed and inlet flow have been previously treated in literature, their expansion to 3D experimental investigation, essential to further understanding the flow and to better validate numerical models, is still very limited. Therefore, in order to access the three-dimensional nature of the flow experimentally, tomographic PIV offers an extension of 2D2C PIV measurements into volumetric 3D3C measurements (§1). It allows investigating 3D flow dynamics experimentally and obtaining more reliable data for the validation of numerical simulations. However, implementing this technique faces many constraints due to the complex engine geometry in terms of confinement, of optical access and of optical deformations and thus the challenge of obtaining accurate 3D measurements. In this context, the application and development of Tomo-PIV to the optical engine are addressed in the following.

2.2 Tomographic PIV and 3D flow measurements

In this section, first the procedures implemented in order to perform Tomo-PIV measurements in the engine, i.e. a confined geometry with restricted optical access, are described in §2.2.1 and consequent in-cylinder measurements are described in §2.2.2. Then, the data processing techniques used to obtain the three-dimensional description of the in-cylinder flow are detailed in §2.2.3. All tomographic PIV codes used for volumetric reconstruction are those developed by PPRIME institute of the University of Poitiers. Results are then validated in §2.2.4 and the choice of the optimal investigation volume used during the course of this study is demonstrated. Finally, a novel *ex-situ* calibration technique aiming to optimize the experimental process and overcome the confinement of the chamber is developed and validated in §2.2.5.

2.2.1 The experimental setup

Our objective here is to adjust and calibrate multiple angles of view to a relatively small and highly confined space with severe optical deformations and reflexions. High speed laser and camera set-up used for time-resolved measurements are substituted with lower frequency equipment for phase-locked measurements which yields to a different synchronisation approach. In addition, the calibration process is extended from the plane to a volumetric domain.

2.2.1.1 Geometrical considerations and optical arrangement

In contrast to TR-PIV, Tomo-PIV deals with a thick laser sheet, instead of a thin one, as well as high laser energy, over 10 times greater than TR-PIV, and greater sensibility of the CCD sensors, which aggravates the problem of reflexions and light deviations caused by the curved surfaces of the thick cylinder. Therefore, the optical access in the combustion chamber is no longer possible directly through the cylinder wall as described in §2.1.1. It is now achieved via the 45° mirror placed under the piston head (Figure 2-15 (a)). In addition, the light sheet configuration is achieved using one cylindrical lens of focal length f_{cm} = -100; the spherical lens used during 2D measurements is no longer needed to bring the laser beam to focus and is hence eliminated in order to exploit the beam's diameter for reaching the largest investigation volume thickness.

A thorough alignment is ensured between the laser, the periscope, the cylindrical lens and the 45° mirror in order to establish the desired investigation volume at the middle of the combustion chamber, i.e. vertically centred at the mid-cylinder plane previously considered for TR-PIV measurements. Knife edged cutters are then used to control the laser sheet thickness and are placed between the cylindrical lens and the mirror, parallel to

the laser sheet. By installing them on micrometric translations and defining the mid-cylinder plane as the reference plane Z_0=0, different investigation volume thicknesses ranging between 1 and 8 mm could be tested by widening the inter-cutters distance around Z_0 position (Figure 2-15(b)). This was verified by imaging the laser sheet profile reaching the in-cylinder investigation volume with respect to the inter-cutters distance and results are shown in Figure 2-14. The laser sheet crosses an optical path passing by the lenses, the mirror and the piston head. This path as well as the divergence of the laser sheet explain the differences between the measured thickness and the cutters positions. Beyond 8 mm thickness, the laser sheet loses its top-hat profile thus degrading the quality expected for particle image reconstruction.

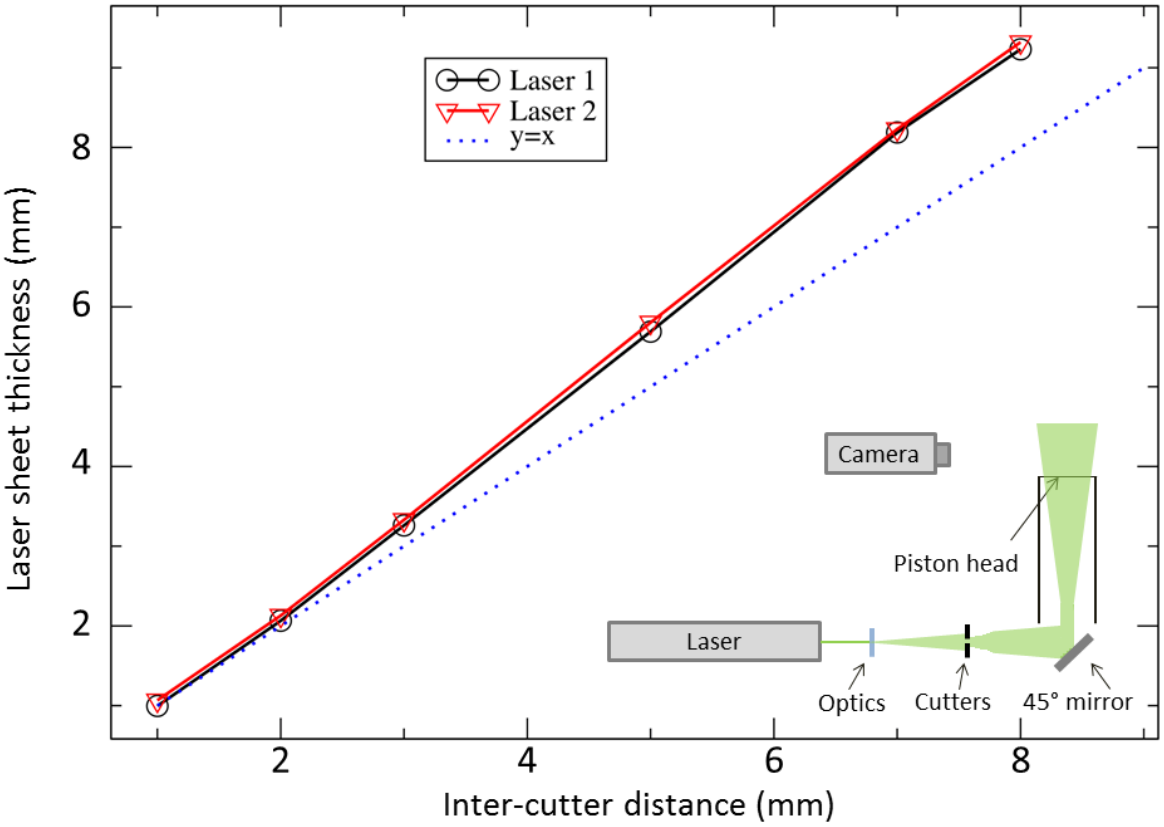

Figure 2-14 Laser sheet thickness measured in the investigation volume with respect to fixed inter-cutter distance and accompagnied schematic of the laser sheet's optical path

It was then observed that residual reflexions prompted from illuminating a closed combustion chamber surrounded by various metallic components were inevitable. Therefore, the quartz piston head was partially painted in black in order to minimize them. This allowed only the light sheet to go through the piston head and eliminated thus any reflexions caused by the inner piston background. Moreover, dealing with multiple angles of view resulted in reflections manifesting differently with respect to the considered angle

of view on the one hand and to the considered crank angle degree on the other hand. For this reason, an adjustable knife edged system is designed and installed in front of each lens which allows correcting reflexions for each angle of view in an independent manner (Figure 2-16). Finally, remaining reflexions are eliminated in an image pre-processing step detailed in §2.2.3.

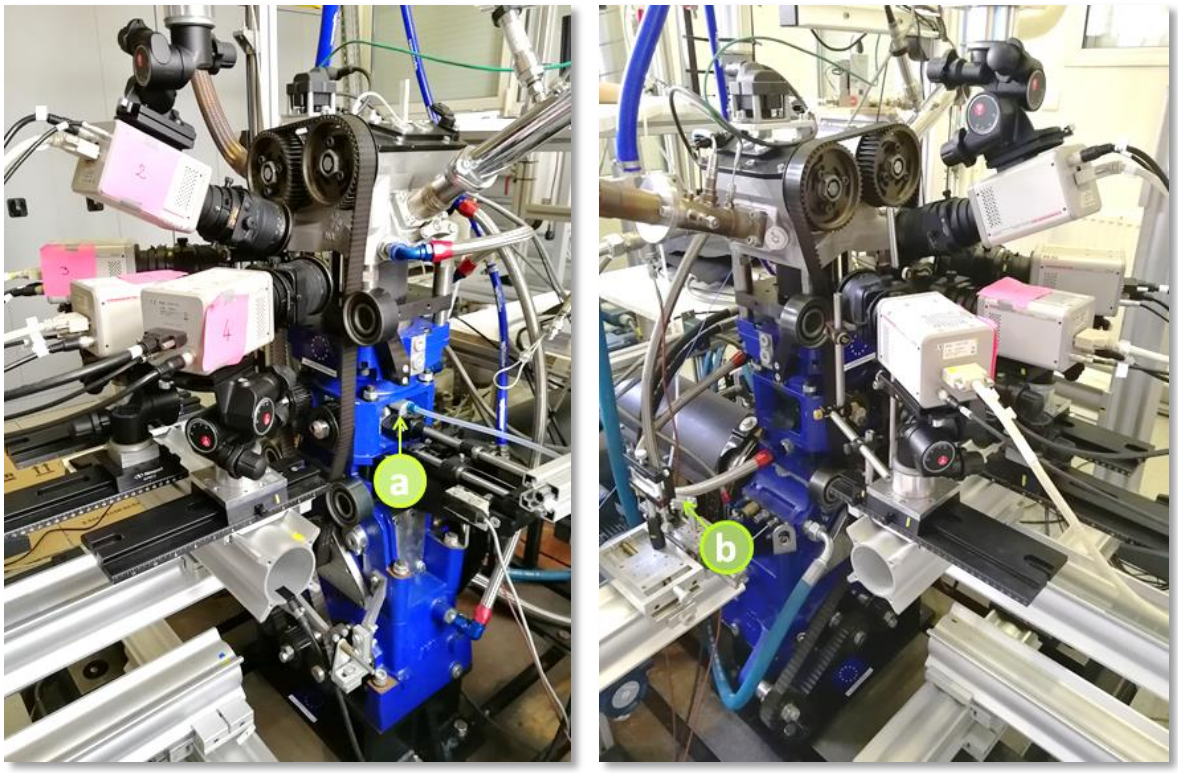

Figure 2-15 Tomographic PIV pyramidal configuration: (a) 45° mirror (b) knife edge cutters

The Tomo-PIV recording system used consists of four 4K×4K pixels Hamamatsu CCD cameras and a PIV Spectra Physics laser delivering 350 mJ per pulse while at 532 nm and 10 Hz. The cameras are equipped with PC-E Micro NIKKOR lenses (45mm f/2.8D) with Scheimpflug adapters for perspective control allowing both tilt and shift corrections. Unlike what is found so far in the literature (Baum et al., 2013) (Peterson et al., 2016), a compact pyramidal disposition of the cameras is chosen to ensure 4 independent angles of view (Figure 2-15). However, the restricted optical access into the chamber depicts placing the cameras as close as possible to the engine's combustion chamber as well as considering small angles of views with respect to the cylinder's axis. Therefore the considered angles range between 20° and 30° and a minimal distance of 25 cm is set between the cameras and the investigation volume. Finally, the achieved field of view has a resolution of 2048×2048 pixels corresponding to 81×81 mm². However,

matching the field of view for the 4 cameras, eliminating reflexions and optimising calculations led to obtaining velocity fields of $51 \times 51 \times \Delta Z$ mm^3.

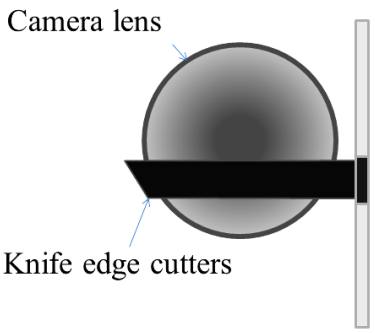

Figure 2-16 Knife edge cutter for reflexions control

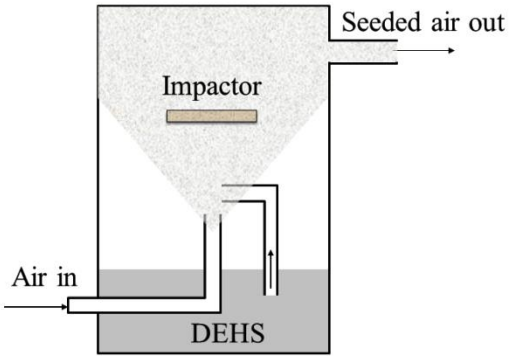

Figure 2-17 Atomiser particle generator with impactor for seeding refinement

2.2.1.2 Seeding

As previously seen, the quality of tracer particles and seeding density is crucial for PIV measurements. For the Tomo-PIV setup, the same particle generator seen in §2.1.2 giving tracers of 1 to 5 µm diameter is used. However, the particular sensitivity of Tomo-PIV to triangulation errors, i.e. errors in identifying a particle in the 3D investigation volume, necessitates further refinement of the seeding flow and particles concentration (Atkinson et al., 2011) (Thomas, Tremblais, & David, 2014).

Therefore, seeding density is adjusted with respect to volume thickness in order to maintain adequate particle distribution for each case and always obtain around 0.005 ppp. A series of test recordings were performed in order to determine this density by fixing different input to the Bronkhorst flow-meter whose output is always introduced far upstream of the engine valves in order not to disturb the in-cylinder aerodynamics. The ppp value was then given via the Tomo-PIV algorithm computing the number of particles in the volume divided by the number of active pixels in the considered image, which in turn are defined as the pixels whose line of sight (LOS) is crossing the volume.

Finally, particle production is refined by adding an impactor in the generator that prevents by aerodynamic selection the larger particles from crossing to the output flow (Figure 2-17). Eliminating the largest drops limits the aerodynamic response times and thus allows avoiding bulky spotlights on the particle images which improves the homogeneity of particle images.

2.2.1.3 Synchronisation

In order to obtain phase-locked data, it is essential to make sure of retrieving the same crank angle reference at every recording. Unlike time-resolved measurements where high speed laser and cameras allow recording several crank angle degrees per engine cycle, it is not possible in Tomo-PIV measurements to impose one cyclic reference pulse and one a crank angle resolution per cycle since recordings are performed at the same crank angle degree for a series of engine cycles. Phase-locked measurements necessitate identifying the considered engine phase in each cycle, then synchronising this pulse with laser frequency. The latter meanwhile oscillates at 10 HZ ± 1Hz and the recording frequency is imposed by the camera's capacity at 2 Hz in double frame mode. Therefore, 1 every 5 laser pulses is retained and synchronised with the engine. Depending on the engine's speed, every few cycles, the desired phase reference pulse will coincide with the retained laser flash light pulse. When this condition if fulfilled, an authorisation pulse is sent to the cameras and the laser heads switch-on in order to start particle image acquisition and record the phase-locked data.

In order to implement this process, the programmable *Acquitek* synchronization board is again used to collect and command the different pulses of image recording sequences. As shown in Schematic 2-2**,** the authorisation pulse is deduced from the accordance between the engine phase and the retained laser pulse. If no accordance is met, the *Acquitek* board retains a loop of recurring cycles without any particle image acquisition. This schematic can therefore be divided into 2 main parts for the sake of clarity, the recurrent cycles sequence and the recording sequence that are further detailed in Schematic 2-3 and Schematic 2-4 respectively.

DF indicates the laser's flash lamp time delay with respect to the authorisation pulse and depends on the engine rotational speed and hence on the corresponding period of one crank angle degree at that speed.

DQ is the laser beam switch delay with respect to the flash lamp; it is a specific characteristic of the laser that is imposed in order to operate in optimal conditions, i.e. deliver maximal laser energy at the considered recording frequency. Throughout our measurements, the cameras impose a frequency of 2 Hz. As a consequence DQ is fixed at 215 µs allowing us to obtain a maximum of 300 mJ per pulse.

Finally, Δt is the PIV frame separation time changed with respect to the engine phase in order to follow at best the flows dynamic range. Therefore, during the intake

stroke where velocity magnitudes are larger than during the compression stroke, a shorter Δt is set.

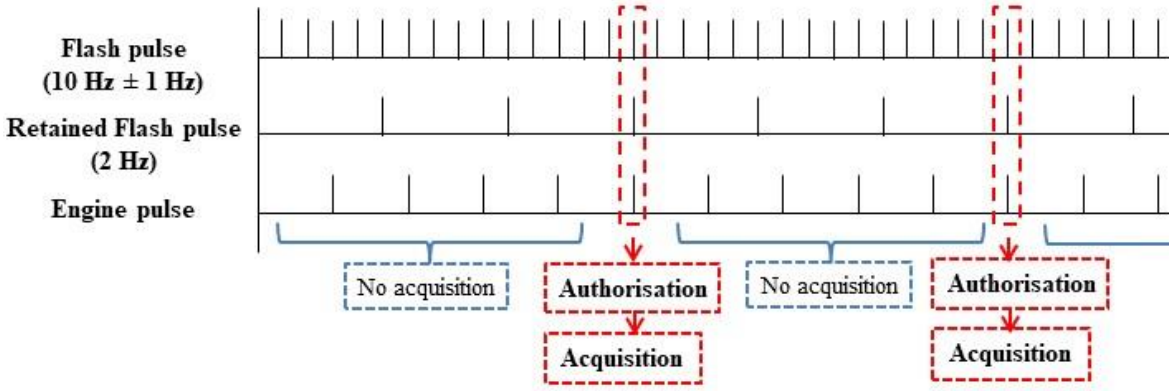

Schematic 2-2 Synchronisation principle for TPIV measurements. The engine pulse depends on the engine speed

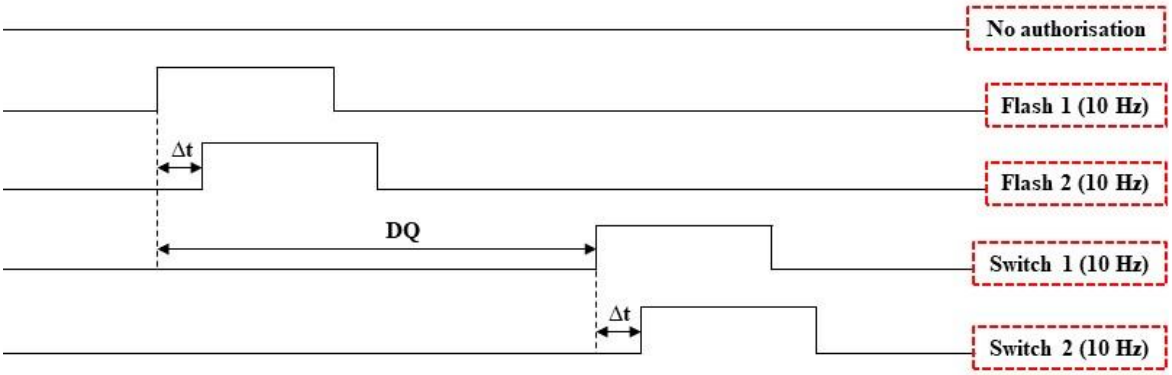

Schematic 2-3 Recurrent cycle loop

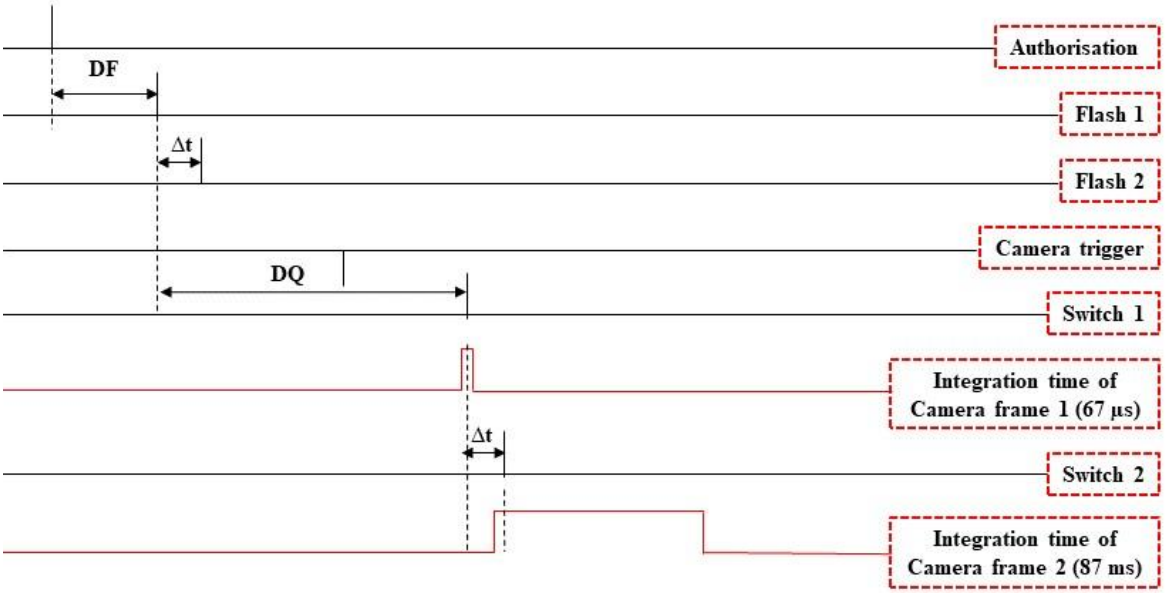

Schematic 2-4 Acquisition sequence

In conclusion, the recurrent cycle allows a stable functioning of the lasers which will run at a frequency of 10 Hz as long as the reference and authorisation pulses do not coincide. Cameras are not triggered and no images are recorded. Once the authorization is given, the recurrent cycle loop is stopped and the recording sequence is executed. By implementing this synchronisation procedure, phase-locked measurements can be performed for different engine speeds while maintaining an optimal operation of the laser as well as ensuring the parallel recording of the 4 cameras without any loss of images.

2.2.2 In-cylinder recordings and 3D calibration

In addition to geometrical considerations, optical arrangement, seeding homogeneity and synchronisation accuracy, obtaining a precise calibration of the investigation volume is vital to the quality of 3D data. It consists on establishing the link between the image space and the object space, the latter being a volumetric domain in this case. As a consequence, Tomo-PIV requires multiple calibration planes to be recorded across the volume so that each camera model could faithfully back-project the investigation domain.

However, the complexity of the engines geometry introduces important calibration restraints caused by:

- the confinement of the combustion chamber that makes it rather impossible to move a calibration target with precision along z-direction,
- the limited angles of view for optical access due to the columns and surrounding belts,
- the variable optical distortions as a function of the depth of field caused by the cylinder's thickness and curvature.

These factors cause calibration errors to accumulate and measurements precision to decrease. So far in literature, this was considered as systematic errors, i.e. unavoidable, resulting in Tomo-PIV measurement errors up to 12% (Zentgraf et al., 2016) (Peterson et al., 2016) (Baum et al., 2012) . Commonly, when indicated, a double-level target is used to calibrate images and match viewing planes from multiple cameras. This is still however limited in the number of planes available for the calibration as well as in the number of dots per plane available for the model computation (Prasad, 2000).

Motivated hence to obtain a precise description of the investigation volume and enhance measurements accuracy, we introduce in the following a calibration procedure allowing us to obtain a complete in-cylinder calibration accounting for volume thickness and the occurring optical distortions. Throughout the rest of this manuscript, this will be referred to as the *in-situ* calibration procedure.

- **In-situ calibration**

In order to access the entire investigation volume, a new set up eliminating the chamber's confinement obstacle is mounted next to the engine's test bench (Figure 2-18). It consists on first installing the cameras assembly on a translation rail in front of the engine which allows moving it without compromising the cameras adjustments. Moreover, a metallic arrangement replicating the base of the engine's quartz cylinder is installed coaxially to the combustion chamber so that the position of the mid-cylinder plane Z_0 is preserved with respect to the cameras. For this purpose, the base is mounted on several translation plates allowing its displacement in X, Y and Z directions. Using these translations along to a laser level indicator (Figure 2-18 (6)) allows obtaining a micrometric precision of the cylinder's new positioning.

The first adjustments of the 4 cameras are made using a regular grid calibration target placed at the mid-cylinder plane Z_0 inside of the original combustion chamber, similarly to what is usually done for classical PIV measurements. Once the in-cylinder Z_0 plane is recorded, the recording assembly is translated and the investigation volume's position with respect to the CCD sensors is verified by removing the calibration target and the quartz cylinder from the engine and placing them on the new set up where the in-cylinder domain is easily accessible. By comparing the grid coordinated of the new in-cylinder Z_0 plane to the previously recorded one, the repositioning of the cylinder can be obtained with a pixel precision.

In this new configuration, it is now possible to freely move the calibration target across the whole investigation volume in the presence of the cylinder which in turn is easy to place or to remove. In order to do so, the target plate is fixed on a translation stage that ensures a displacement precision up to 5µm. Using this stage, 21 calibration planes are recorded over a 10 mm range, i.e. covering the desired investigation volume range, centred at Z_0 and separated by $\Delta Z = 0.5$ mm:

$$Z = -5 \text{ mm} < Z_0 < Z = 5 \text{ mm}.$$

Using the in-house pattern recognition algorithm (§2.1.4), grid coordinates can be extracted with sub-pixel precision from the 21 in-cylinder target planes with respect to each of the 4 cameras in order to compute their corresponding camera model referred to as the *in-situ* models hereafter. After obtaining the target images at the known span wise positions, the cameras are translated back to their initial position in order to record phase-locked particle images for the self-calibration step of camera models (Wieneke, 2008). For this purpose, particle images of very low density (0.005 ppp) are recorded at BDC, i.e. -

180 CAD, where the piston is at its lowest position in the combustion chamber and hence the field of view is the largest. This calibration procedure allows obtaining valid camera models described in the following paragraph, resulting in a high quality volumetric reconstruction of the in-cylinder flow.

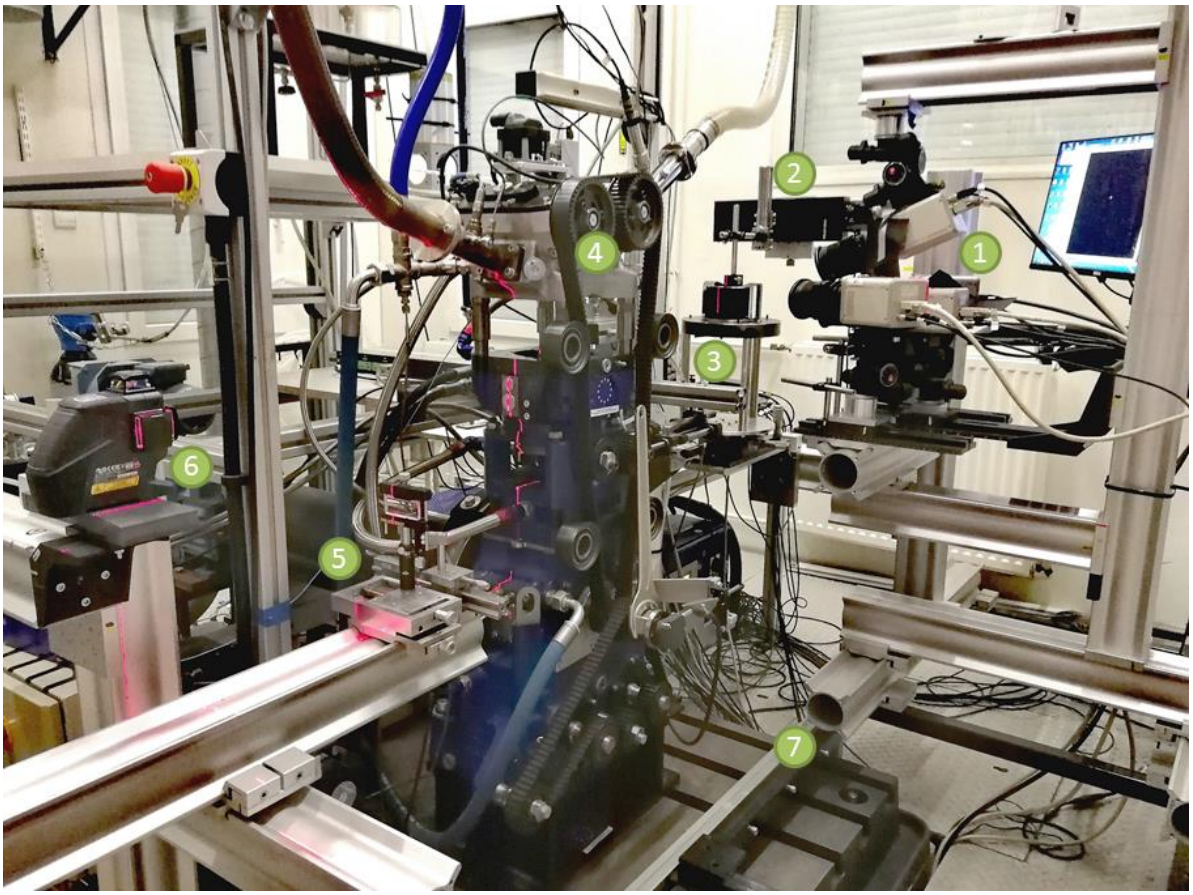

Figure 2-18 *In-situ* calibration setup: 1. Recording assembly 2. Micrometric translation and calibration target 3. Cylinder base 4. Combustion chamber 5. Cylindrical lens 6. Level indicator 7.Translation rails

- **In-cylinder measurements**

Knowing that the in-cylinder aerodynamics consist of a highly three-dimensional flow, it is beneficial to extend the investigation volume's dimensions to the largest admissible ones in order to reach more information and enhance our understanding of the in-cylinder flow. However, the thickness of the illuminated investigation volume is one of the main parameters influencing the quality of 3D velocity measurements. It particularly limits particle concentration to less than 0.1 particles per pixel (ppp) in all cases. Additionally in IC engines, optical distortions and astigmatism effect on particles caused by the cylinder's multi-curved glass interface introduce further limits to the size of the investigation volume due to their alterations in areas surrounding the focus plane.

For this reason, multiple sets of in-cylinder recordings are performed in order to validate data with respect to the increase in volume thickness, i.e. z-dimension, and select the largest admissible investigation domain. The seeding density is then simultaneously adjusted in order to optimize Tomo-PIV computations. Three volume thicknesses ΔZ = {3, 5, 8} mm are first investigated at BDC, i.e. -180 CAD, by varying the space between the knife edge cutters placed prior to the 45° mirror and verifying the laser sheet thickness by sheet profile measuring (§2.1.1). Hereafter, data corresponding to ΔZ = 3, 5 and 8 mm are referred to as L3, L5 and L8 respectively. Low density recordings at 0.005 ppp served for the self-calibration of camera models. Higher density recordings at 0.05 ppp served for the volumetric reconstruction of velocity fields.

After ensuring the good quality of Tomo-PIV measurements and computations for the largest volume and validating the choice of investigation domain, 7 phase-locked recording campaigns were performed in order to describe the in-cylinder flow during intake and compression strokes. Similar campaigns were done for the six considered engine operation conditions, i.e. for the 3 intake flows at 2000 and 3000 RPM (§1.3). The considered engine phases are chosen to correspond with those recorded during TR-PIV measurements in order to show the contribution brought by 3D measurements with respect to planar measurements. Hence, 500 particle images are recorded at CAD = {-274, -250, -226, -178, -130, -106, -82} by correspondingly adjusting particles density and frame separation time for each case.

2.2.3 Data processing of Tomo-PIV measurements

As seen in §2.1, it is essential to optimize the quality of recorded particle images for PIV calculations and adjust the PIV algorithm accordingly.

2.2.3.1 Image pre-processing

Particularly while performing Tomo-PIV measurements, different sets of particle images are obtained with respect to each angle of view and therefore need to be assessed separately before 3D reconstruction. This is a critical step since it reflects directly on the weighting matrix that represents the contribution of the intensity in each pixel of each camera in the intensity of each voxel.

In order to make sure image pre-processing is optimized and eliminate any residual reflections, a mean background image is obtained for each laser head with respect to each of the 4 cameras and is then subtracted from all corresponding particle images. Then a division by a mean particle image is performed and a 3×3 Gaussian filter is applied. This significantly reduces the noise for image reconstruction (Figure 2-19 and Figure 2-20). It

is particularly worth noting that these image pre-processing steps allowed particles in the bottom of the field of view otherwise confused with the cylinder base background to stand out and be easily identified.

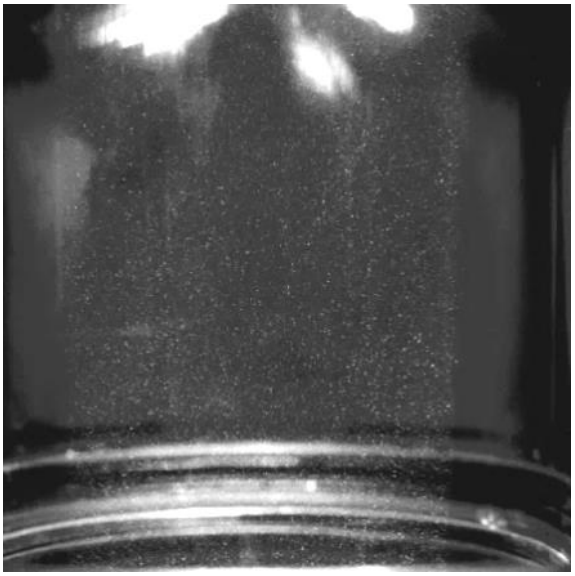

Figure 2-19 Raw particle image

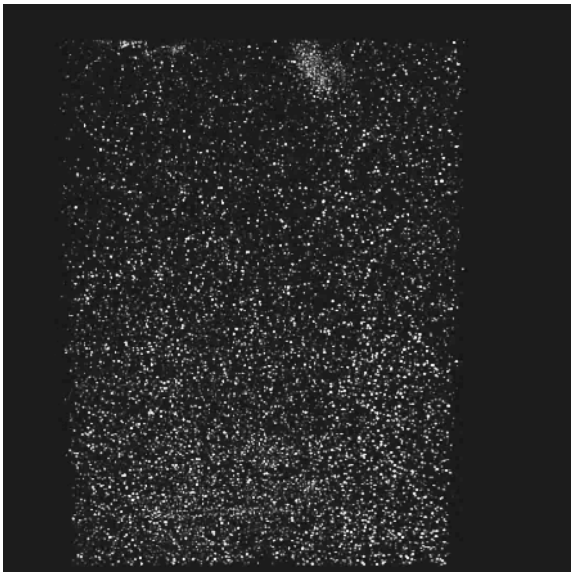

Figure 2-20 Particle image after pre-processing

2.2.3.2 Camera models and self-calibration

After extracting grid coordinates of the 21 *in-situ* target planes, a Soloff model is calculated for each of the four cameras. Projection errors of approximately 1 to 1.5 pixels are noted for each. Volumetric self-calibration step (Wieneke, 2008) is then performed using the 500 pre-processed particle images in order to refine the cameras' mapping functions and minimise triangulation errors. Images of low particle densities were used for the self-calibration procedure that was iterated, starting with a search radius of 6 pixels gradually reduced to a final radius of 2 pixels. After the final iteration of self-calibration, projection errors decrease from 1 to 1.5 pixels to about 0.02 pixel, and triangulation errors are lower than 0.12 pixels in the entire domain.

Using the reconstructed particles in self-calibration, the laser intensity profile is calculated. Figure 2-21 displays the laser profile in z-direction for $\Delta Z = 8$ mm and show approximately 10% of ghost particle level indicated by the remaining normalized intensity at the tails of the light sheet, keeping in mind that ghost particles occurring also inside the investigation volume cannot be easily accounted for. Further tests to enlarge the light sheet width resulted in ghost particle level at the edges exceeding 25% for $\Delta Z \geq 9$ mm. Consequently, volumetric investigations were fixed to 8 mm or smaller, thus the choice to test 3, 5 and 8 mm volume thicknesses.

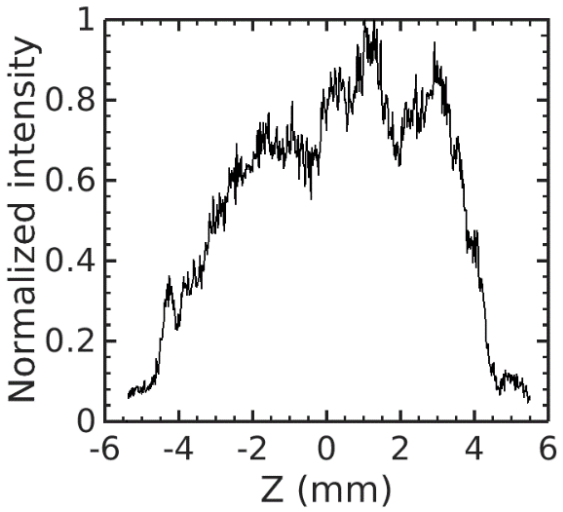

Figure 2-21 Normalized intensity profile calculated by the reconstructed particle intensity for ΔZ = 8 mm

2.2.3.3 Tomo-PIV algorithm

By means of the codes developed by PPRIME institute, pre-processed images are reconstructed using a multi-pass Smart Multiplicative Algebraic Technique (SMART) with SMART_FAST initialization method that encompasses a minLOS first step, i.e. a minimum line of sight intensity initialisation, and n iterations of SMART_FAST, i.e. a fast version of the SMART algorithm (Thomas et al., 2014). Two iterations with raytracing interaction method and a variable relaxation parameter are employed. Finally, a 10% enlargement of volume dimensions was imposed in order to ensure that the laser sheet profile intensity is correctly reconstructed.

Moreover, the combination of a volume Gaussian filter with a volume threshold has been shown to increase reconstruction quality. Therefore, different threshold levels were tested during the volumetric reconstruction step where intensities are normalized between 0 and 1 and a value of 0.001 volume threshold was found to provide an optimal reconstruction quality. The volume threshold level is a linear function of the image signal ratio N_s defined as the percentage of non-black pixels in the active pixel's set (Scarano, 2013) (Thomas et al., 2014).

The three investigation volumes had similar spatial resolution and similar volume steps of 0.18×0.18×0.054 mm^3, hence 295×301×k volume grid dimensions where k = {55, 90, 170} for L3, L5 and L8 respectively. As a result, high quality reconstructed particle volumes of 53×53×ΔZ mm^3 are obtained, i.e. back-projection qualities exceeding 80% in all cases.

Velocity fields are then computed from pairs of volumes by means of normalized 3D cross-correlation with Gaussian sub-pixel peak interpolation method and a Spline image interpolation method. The spatial resolution is similar between the different light sheet thicknesses. In the iterative calculation process, the final pass is done over 20×20×20 pixel^3 interrogation window size corresponding to 0.8×0.8×0.8 mm^3 with a 75% overlap factor. A grid of 50×50×k vectors is obtained.

Finally, 250 instantaneous velocity fields are calculated for each of L3, L5 and L8 and the 3 datasets are compared and analysed in order to validate in-cylinder engine measurements and the choice of investigation volume.

2.2.4 Tomo-PIV data validation and choice of investigation volume

2.2.4.1 Convergence of mean quantities

The statistical convergence of the three velocity components and their corresponding fluctuations is evaluated across the 250 velocity fields in order to determine the sufficient number of recorded cycles for data analysis.

This is obtained for the three volume thicknesses by calculating the ensemble averaged velocity field $\mathbf{F_{mean}(x,y,z)}$ of N number of fields $\mathbf{f(x,y,z)}$ such as $25 \leq N \leq 250$, increasing N by a step of 25 fields:

$$\boldsymbol{F_{mean_N}(x,y,z)} = \frac{1}{N}\sum_{i=1}^{N} \boldsymbol{f_i}\,\boldsymbol{(x,y,z)} \qquad \textbf{(2-5)}$$

where **f** is the velocity vector (**u**,**v**,**w**).

Figure 2-22 describes the u-component of the L8 ensemble average velocity fields and fluctuations obtained from N = 50, 200 and 250 fields showing greater differences between N = 50 and N = 200 than between N = 200 and N = 250. Hence, 250 pairs of recorded images seem to be sufficient to ensure the convergence of mean quantities.

This is shown furthermore in Figure 2-23 showing profiles of $\bar{u}$, $\bar{v}$ and $\bar{w}$-components as well as $\overline{u'}$, $\overline{v'}$ and $\overline{w'}$. All profiles are extracted along X-direction at Y = -5 mm and Z = 0. This illustrates on the one hand a more rapid convergence of u and v components than w components, although in all cases, 250 velocity fields ensure statistical convergence. On the other hand a more rapid convergence of the mean velocity fields can be observed with respect to the convergence of velocity fluctuations.

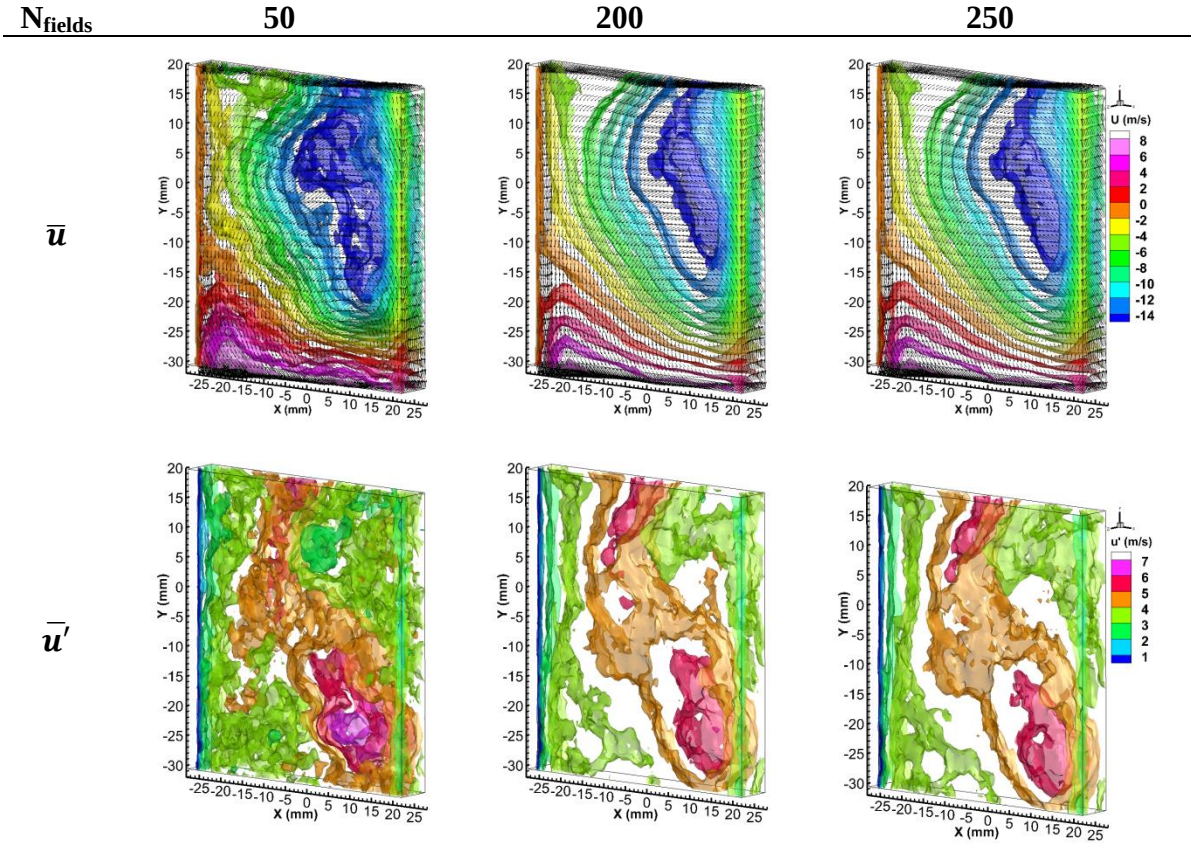

Figure 2-22 Convergence of mean velocity component u and mean velocity fluctuation u'

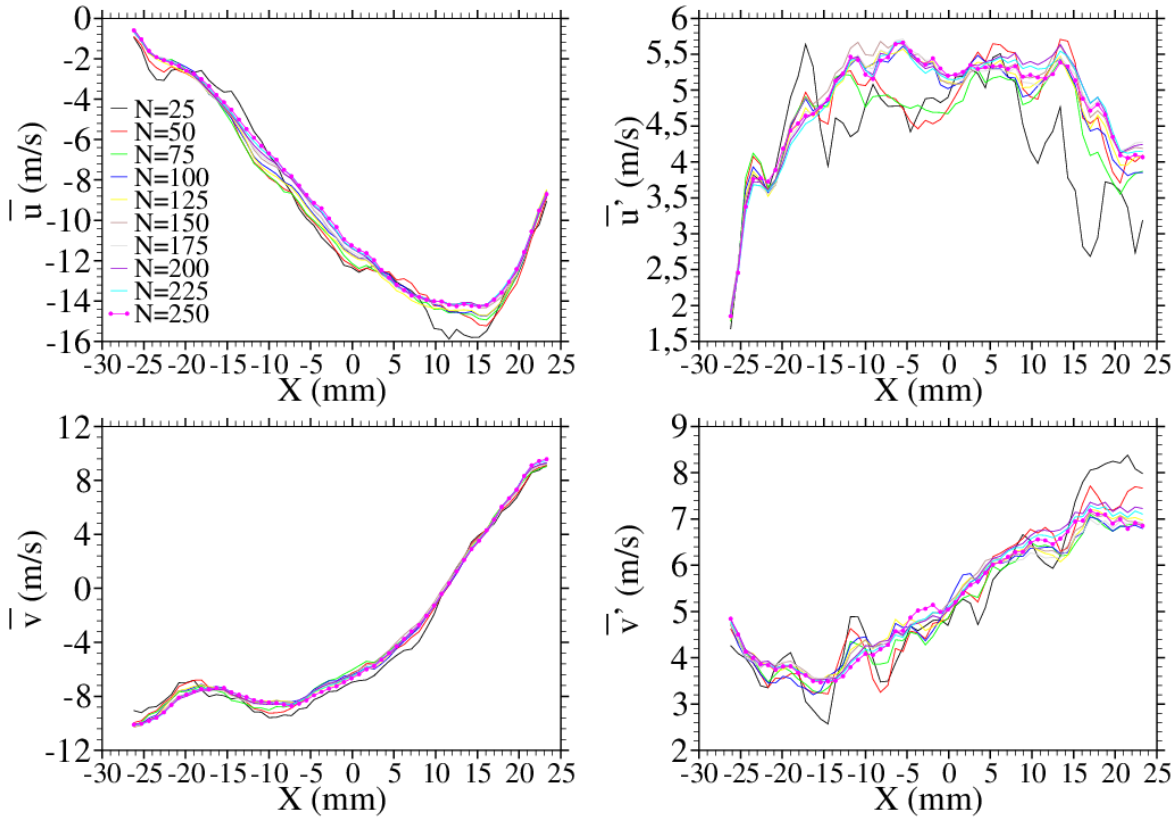

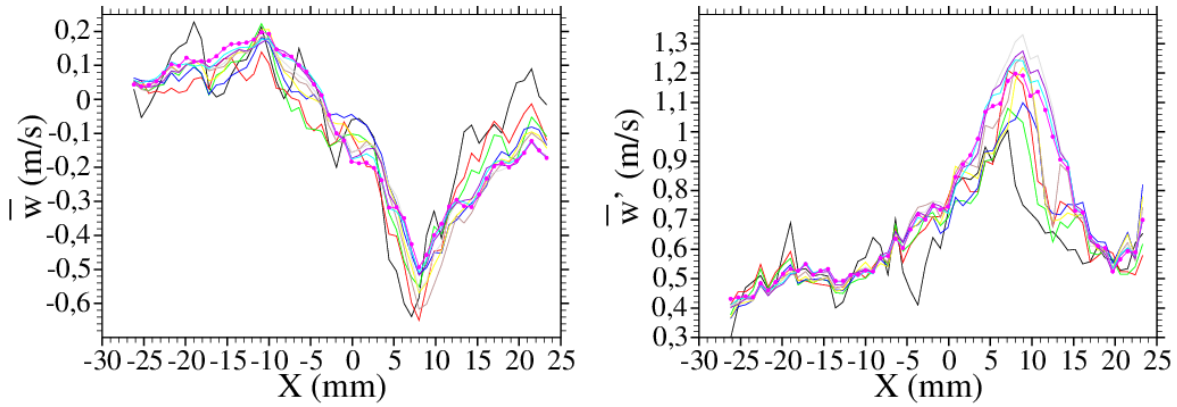

Figure 2-23 Convergence of velocity profiles and velocity fluctuations along u, v and w components

2.2.4.2 Statistical analysis

In order to validate data for the largest investigation volume ΔZ = 8mm, the global mean in-cylinder flow at BDC is described for L3, L5 and L8 then statistical quantities are compared at the mid-cylinder plane Z_0 as well as at common border planes, i.e. at Z = ±1.5 mm.

2.2.4.2.1 Mean velocity fields

Mean velocity fields are shown in Figure 2-24 for an engine operation condition of 2000 RPM and 100% intake flow. Velocity vectors represent the 3D velocity (**u,v,w**) and discrete levels of velocity magnitudes are displayed by 3D iso-surfaces for each measurement volume. Four flow regions can thus be identified for all cases.

The first is the upper right of the field, where the largest velocities appear. It represents the tail of the intake jet, the intake valves being on the upper right hand side. Similar velocity magnitudes can be noted for L3, L5 and L8 while comparing the same spatial domain reaching values over 15 m/s. Particularly in this region, flow field captured for L8 show distinctly different velocity behaviour outside the L3 and L5 measurements boundaries, revealing the strong three-dimensionality of the in-cylinder flow.

The second region is the upper left side of the field where several U-shaped iso-surfaces manifest velocity magnitudes lower than 7 m/s in the 3 cases. The third region is the lower right of the field where a strong vortex structure forms, i.e. the tumble motion, and velocities tend to zero magnitude at approximately the same position for the 3 volume thicknesses.

Finally, the forth region at the centre and lower left of the field of view show parallel C-shaped iso-surfaces with velocity magnitudes decreasing as the flow is met on the one hand by the left side cylinder wall and on the other hand by the tumble motion.

In order to further visualise these global similarities, Figure 2-25 shows the mid-cylinder plane Z_0 extracted from each volume. It confirms again that 4 regions can be identified and are described similarly for L3, L5 and L8. Figure 2-25 also shows the ensemble averaged velocity fluctuations for L3, L5 and L8 in Z_0 plane. In the 3 cases, the vortex and intake regions show the greater fluctuations in the field, decreasing as they meet in the middle and as we move towards the borders of the field of view.

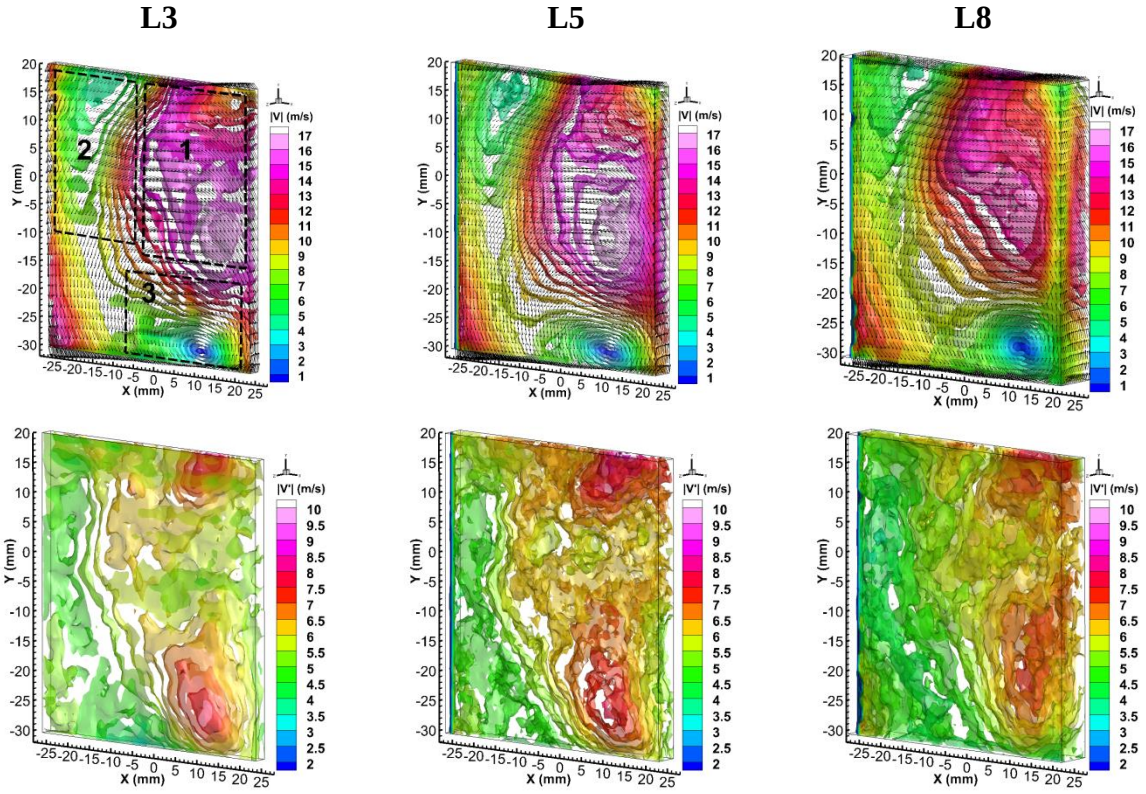

Figure 2-24 Mean (up) and fluctuating (down) velocity fields of L3, L5 and L8

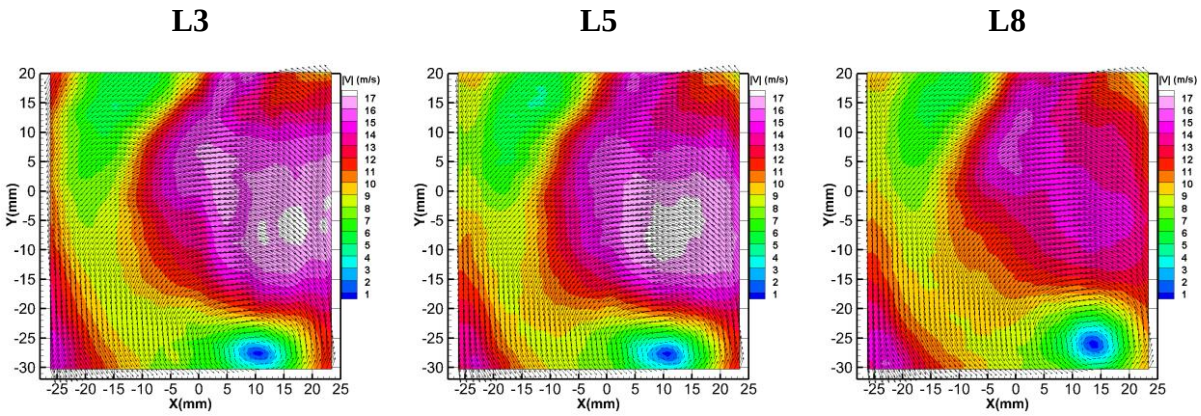

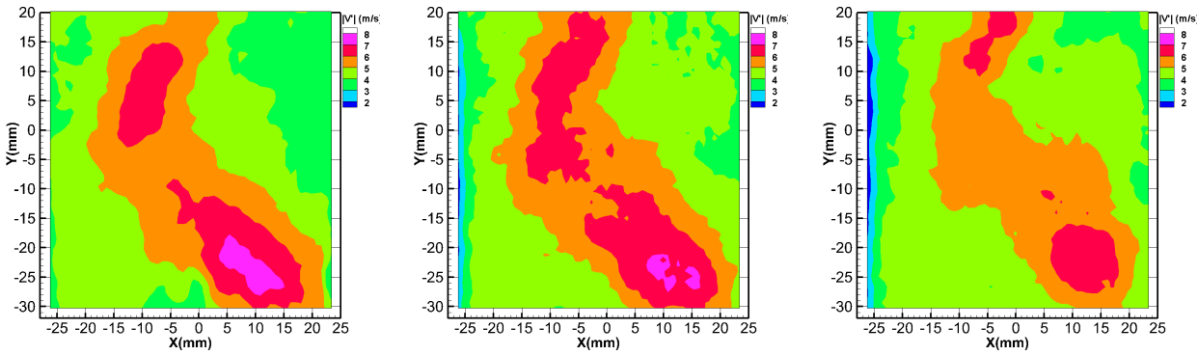

Figure 2-25 Mean (up) and fluctuating (down) velocity fields extracted at mid-cylinder plane Z_0 of L3, L5 and L8

2.2.4.2.2 Instantaneous velocity fields

Having found similar global behaviour of mean flow dynamics, it is essential to evaluate instantaneous velocity fields' evolution during a series of engine cycles in order to refine the comparison between the three volumetric measurements at BDC, particularly in the common area, and validate the obtained data. Due to the unsteady nature of the in-cylinder flow, individual instantaneous velocity fields obtained from L3n L5 and L8 at separate times cannot be compared for the three thicknesses. Rather a statistical approach is considered to describe the flow's evolution along the recorded series of engine cycles.

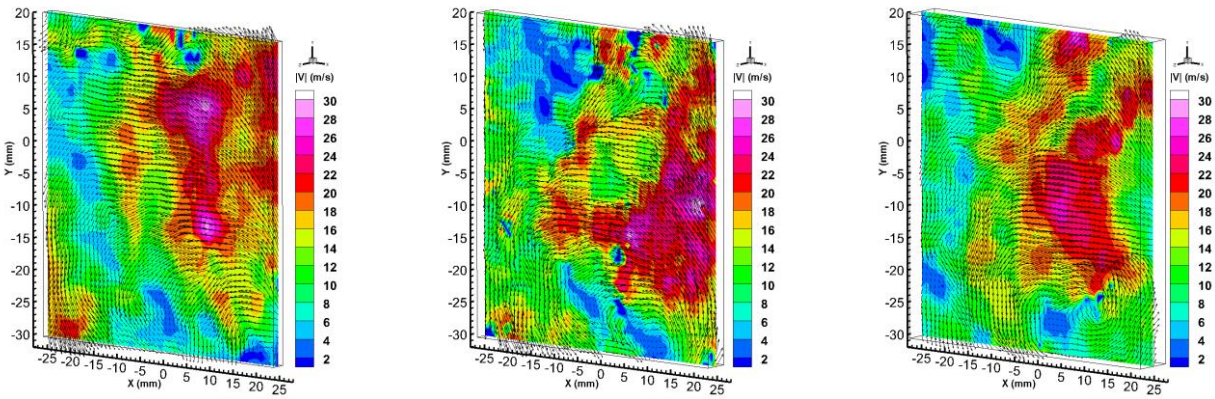

(a) **(b)** **(c)**

Figure 2-26 Example of instantaneous velocity fields of (a) L3 (b) L5 and (c) L8

The example of velocity fields in Figure 2-26 show the very different velocity magnitudes that can be observed in the same instantaneous field as well as the different vector directions and vortical positions revealing the wide range of unsteady flow dynamics in the engine. Although individual fields cannot be compared, it is possible to statistically analyse the flow's behaviour along a series of engine cycles. For this purpose, spatial mean velocity components and their corresponding standard deviation are

computed according within different planar positions of the 250 instantaneous velocity fields at BDC according to:

$$< u >_i = \frac{1}{n_x n_y} \sum_{1}^{n_x} \sum_{1}^{n_y} u_i\,(x,y) \qquad \textbf{(2-6)}$$

$$< u' >_i = \frac{1}{n_x n_y} \sum_{1}^{n_x} \sum_{1}^{n_y} u'_i\,(x,y) \qquad \textbf{(2-7)}$$

where i is the velocity field i and (n_x,n_y) is the number of points (x,y) in the considered plane of the field i.

Three planes in the common region of L3, L5 and L8 are particularly described hereafter: the mid-cylinder plane $Z_0 = 0$ and the border planes of the common volume, Z = ±1.5 mm. Figure 2-27 first shows the evolution of mean u-component in Z_0-plane as well as its fluctuation $< \overline{u'} >$ for L3, L5 and L8. It can clearly be observed that the turbulent nature of internal engine aerodynamic induces many variations from one instantaneous velocity field to another. However, the amplitude of variation seems to be similar for the 3 cases. This is then summarized in the first graph of Figure 2-28 where error bars correspond to velocity fluctuation range. Figure 2-28 also illustrates the behaviour of the 3 velocity components in each of Z_0, Z = +1.5 and Z = -1.5 mm for L3, L5 and L8. Consequently, similar range of variations of u and v components is observed for the 3 volume thicknesses with a slight shift of the mean components of L8 velocity fields. When considering the w-component in particular, the comparison appears more subtle because of the near zero mean values and 3 different magnitudes are revealed for the 3 volume thicknesses. In addition to the 3 data sets being recorded at different time periods, the shift in magnitudes values can be caused by the fact that as the volume thickness increases, and while maintaining a constant particles density in all cases, the number of particles describing the flow decreases. Moreover, the integrated number of ghost particles in the investigation volume increases. These factors simultaneously decrease the quality of volumetric reconstruction. Although, as noted in 2.2.3.3, back-projection quality exceeds 80% in all cases, it is still greater for L3 case than for L5 which in turn is greater than L8.

In conclusion, the flow's evolution across for the three volume thicknesses reveals a similar global behaviour of results in the common region. This fact, added to the main interest of obtaining a 3D characterisation of the flow, promotes the use of an 8 mm light sheet for in-cylinder measurements.

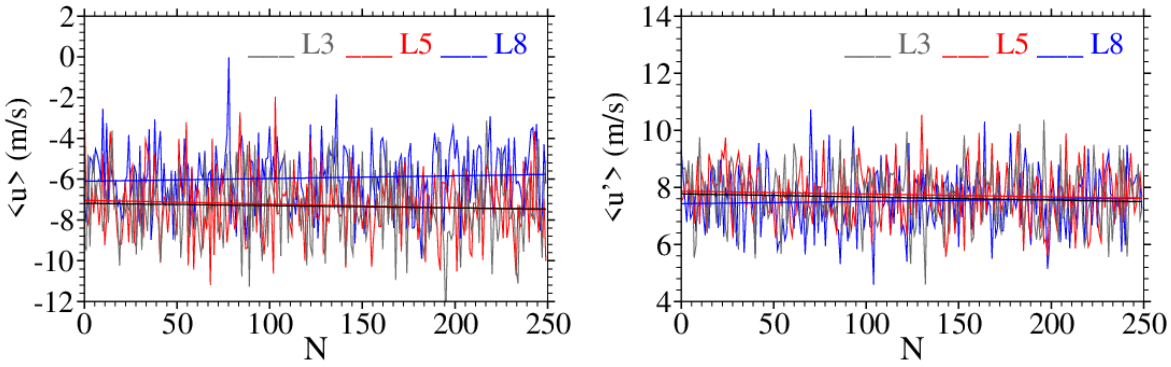

Figure 2-27 Spatial averaged u component and standard variation of instantaneous velocity fields at Z_0 for L3, L5 and L8

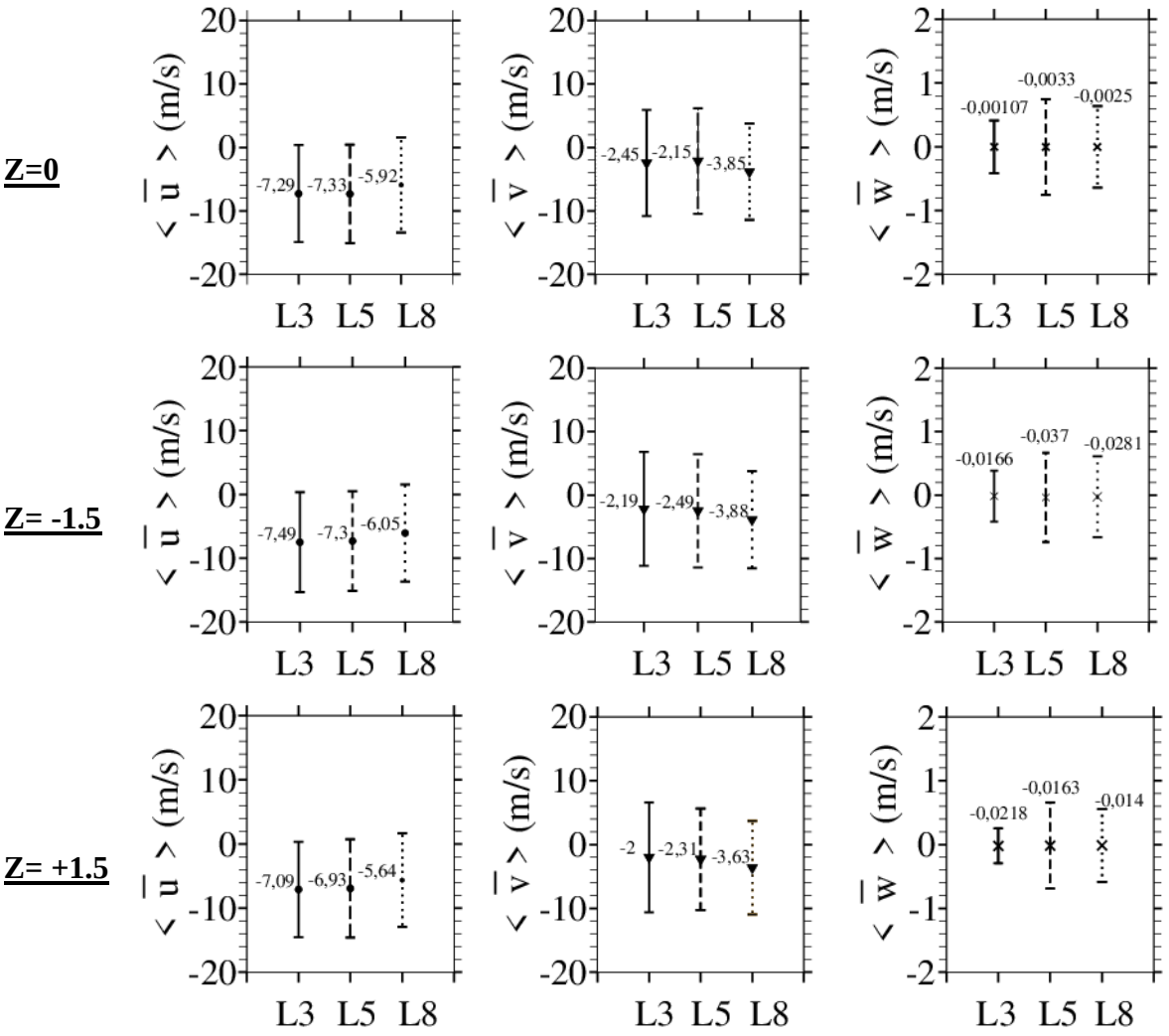

Figure 2-28 Mean velocity components (annotations) and standard variation (error bars) of instantaneous velocity fields for L3, L5 and L8

2.2.4.3 Conservation of mass

In order to validate furthermore the quality of our 3D measurements, the uncertainty of the 3D velocity data is quantified for the three volume thickness cases at BDC, i.e. the largest field of view (Zhang et al., 1997) (Baum et al., 2013). For this purpose, the mass conservation principle is applied:

$$\rho^{-1}\left(\frac{\partial \rho}{\partial t}\right) + \frac{\partial u_i}{\partial x_i} = 0 \qquad \textbf{(2-8)}$$

Moreover, at BDC, the term $\rho^{-1}\left(\frac{\partial \rho}{\partial t}\right)$ is neglected because density ρ is assumed to be uniform with time since $\frac{\partial \rho}{\partial t}$ is commonly found to be two orders of magnitudes below the divergence of the velocity field. As a result, continuity at BDC can be approximated by:

$$\frac{\partial u_i}{\partial x_i} = 0 \qquad \textbf{(2-9)}$$

Considering control volumes of 4×4×4 grid region corresponding to 3×3×3 vectors, the velocity flux $\Delta V = \Delta u + \Delta v + \Delta w$ can then be calculated in order to quantify its relative deviation from mass conservation. For this, the used velocity vectors are the averaged vector normal to the surfaces of the control volume. The pdf of velocity flux are shown for L3, L5 and L8 in Figure 2-29.

By normalizing the velocity flux with respect to the averaged velocity entering each control volume, its deviation from the true value is found by equation 2-11 (Overbrüggen et al., 2013) for each investigation volume thickness.

$$\sigma = \sqrt{\frac{\mathbf{1}}{\boldsymbol{N-1}}\sum_{\boldsymbol{cv}}\left(\frac{\boldsymbol{\Delta V(cv)}}{\boldsymbol{V_{av}(cv)}} - \sum_{\boldsymbol{cv}}\frac{\boldsymbol{\Delta V(cv)}}{\boldsymbol{V_{av}(cv)}}\right)^2} \qquad \textbf{(2-10)}$$

According to literature, this deviation is on the one hand associated with the discretization errors of the velocity measurements (Zhang et al., 1997), like inhomogeneous particle distribution within an interrogation volume and limited spatial resolution, and on the other hand it may be attributed to vibrations of the engine's environment as well as residual distortions from the curvature of the thick cylinder (Baum et al., 2013).

The obtained values of σ remain meanwhile within 10% or less and are therefore in good agreement with other tomographic measurements in turbulent configurations which demonstrates the validity of our 3D velocity measurements (Fulvio Scarano & Poelma, 2009) (Zhang et al., 1997) (Overbrüggen et al., 2013).

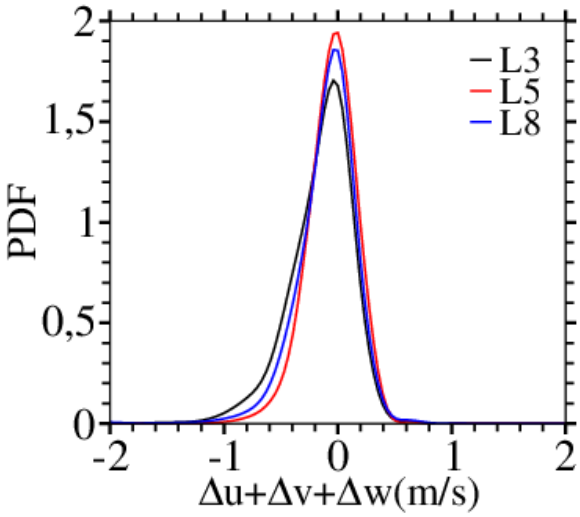

Figure 2-29 PDF of velocity flux for L3, L5 and L8

Volume thickness	Deviation of mass conservation
ΔZ = 3 mm	$\sigma = 3.92\ \%$
ΔZ = 5 mm	$\sigma = 7.33\ \%$
ΔZ = 8 mm	$\sigma = 8.14\ \%$

Table 2-3 Deviation of velocity flux

2.2.4.4 Comparison to 2D measurements

The last step for validating the tomographic PIV measurements is to compare the resulting velocity fields, particularly mid-cylinder plane of the investigation volume, to time-resolved measurements previously performed. In X and Y-directions, the dimensions of Tomo-PIV field of view are reduced with respect to TR-PIV field of view as is shown in the black dashed square of Figure 2-30(a). The presented velocity fields have different origins of coordinate system due to the use of different calibration targets for the two types of 2D and 3D measurements. Properly rescaling the two coordinates systems onto the same origins revealed to be inaccurate thus current origins are retained and the common zone is isolated from TR-PIV measurements and exploited for comparison with the Tomo-PIV velocity fields (Figure 2-30 (b) and (c)).

It is then clear that global mean characteristics of in-cylinder flow fields are similarly observed in the mid-cylinder plane of the 3D data. The main structures at each CAD are found and velocity magnitudes are generally of the same order. Few differences and additional observations are however worth noting.

One observation is the reduced Y-dimension of Z_0 fields of view near the piston head for certain engine phases, such as -250 CAD or -106 CAD, with respect to 2D

measurements. This is caused by the positioning of the knife-edge cutters needed to eliminate the saturation of CCD sensors by light reflexions caused the thick laser sheet crossing the piston head (Figure 2-16) and hence reducing the field of view. In addition to the cutters, the automatically generated image masking mainly influenced by image noise level refines the field's dimension and can furthermore reduce it.

Similarly, the common regions of TR-PIV velocity fluctuations fields are compared to the mid-cylinder plane in Figure 2-31. A globally inferior order of magnitudes is noted for the different CAD with respect to 2D measurements. This can be produced by a number of factors. One is the greater measurement errors implied by 3D techniques such as the unavoidable presence of residual ghost particles inside the investigation volume despite the advanced image pre-processing. Recalling that a ghost particle is present in both images of a recorded Tomo-PIV image pair since it is linked to the presence of true particles in those images. Hence, the displacement of ghost particles is derived from the displacements of the true particles as their mean value and it therefore leads to an underestimation of velocity gradients (Atkinson et al., 2011). Another factor is the lower spatial resolution of Tomo-PIV measurements with respect to planar PIV: albeit their capacity to provide accurate flow description, spatial resolution is limited. Finally, the separated periods of 2D and 3D experiment time can also influence the results because of possibly different engine operations.

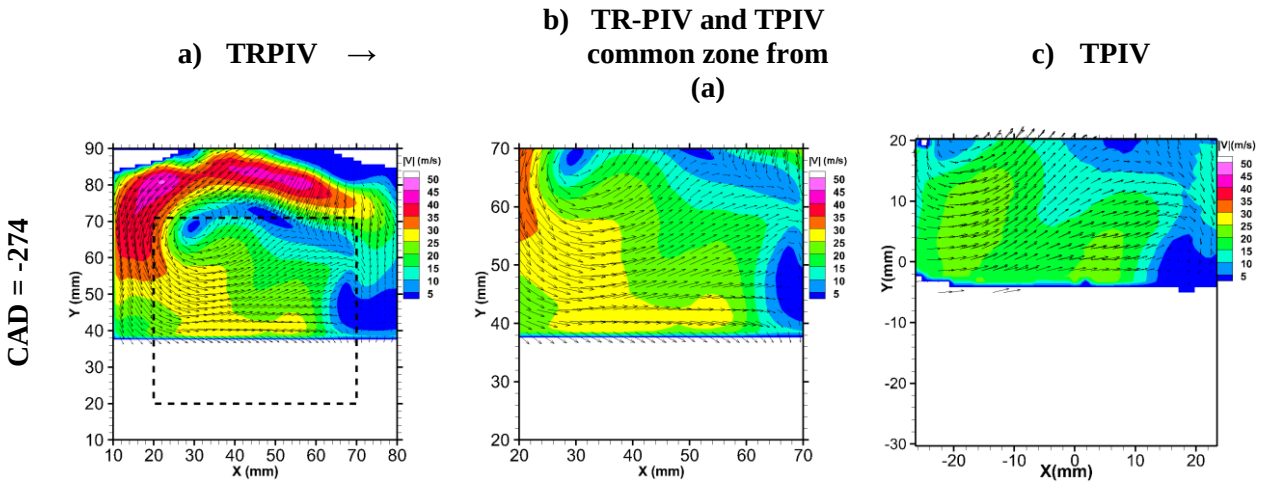

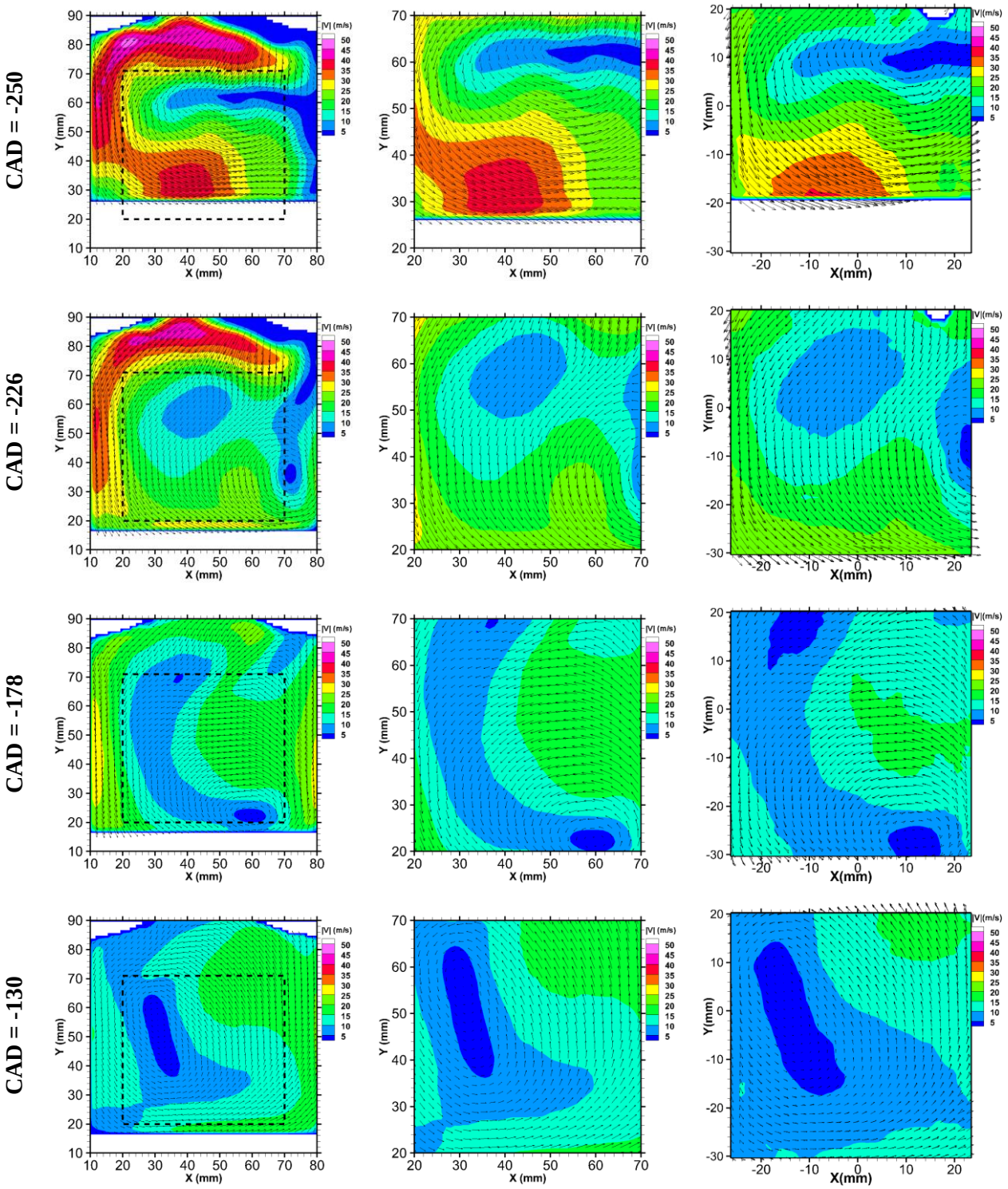
CAD = -250
CAD = -226
CAD = -178
CAD = -130
X (mm)
Y (mm)
X(mm)
Y(mm)
|V| (m/s)

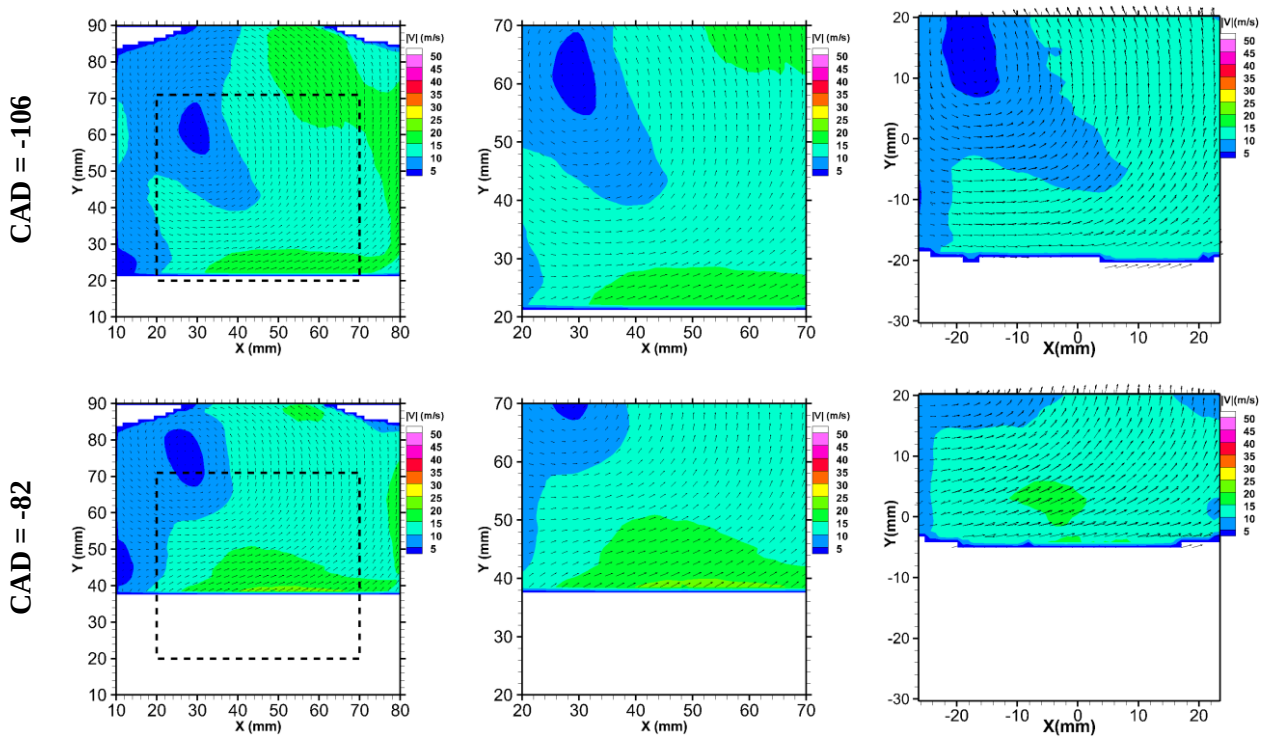

Figure 2-30 (a) Ensemble average velocity field from TR-PIV measurements. The black square represent the common region with Tomo-PIV measurements. (b) Isolated common region of ensemble average velocity field from TR-PIV measurements (c) Mid-cylinder plane of ensemble average velocity field of Tomo-PIV (L8)

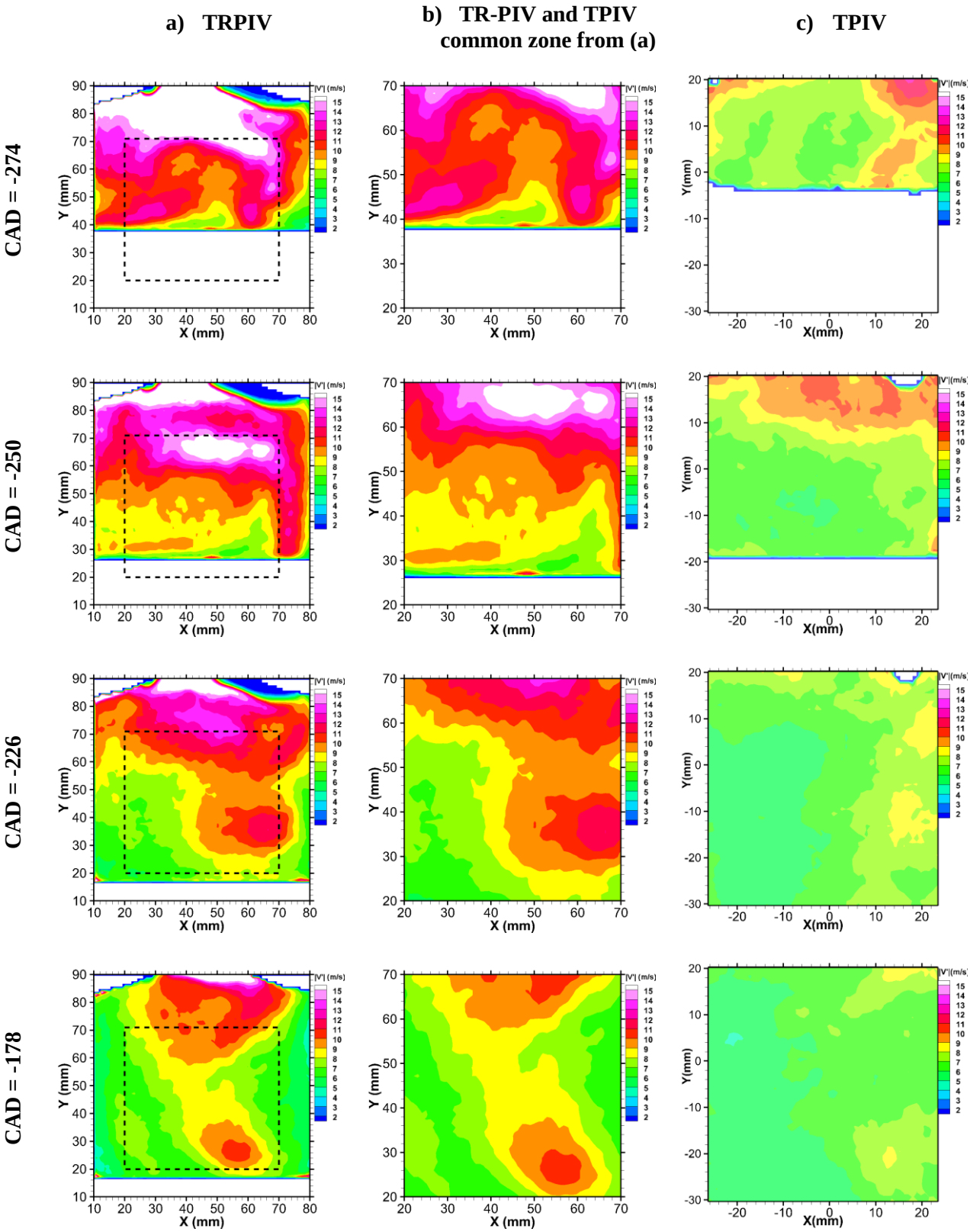
a) TRPIV
b) TR-PIV and TPIV common zone from (a)
c) TPIV
CAD = -274
CAD = -250
CAD = -226
CAD = -178
X (mm)
Y (mm)
X(mm)
Y(mm)
|V'| (m/s)

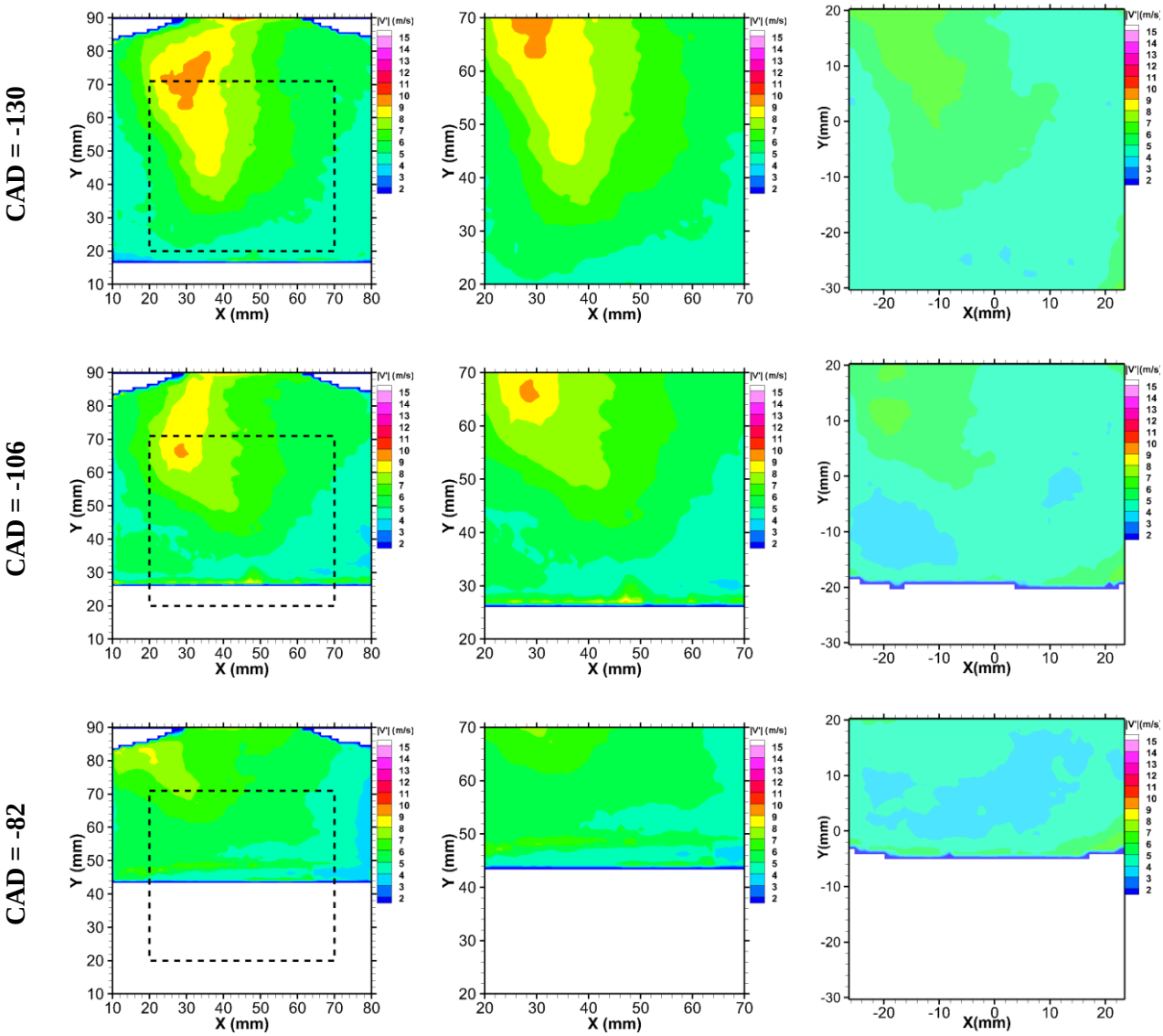

Figure 2-31 (a) Ensemble average velocity fluctuations from TR-PIV measurements. The black square represent the common region with Tomo-PIV measurements. (b) Isolated common region of ensemble average velocity fluctuation from TR-PIV measurements (c) Z_0-plane of ensemble average velocity fluctuations of Tomo-PIV (L8)

2.2.5 Ex-situ calibration process

2.2.5.1 Objectives

As seen so far, the complexity of the engine's geometry introduces experimental constraints like the confinement of the chamber due to its nature and the limited angles of view for optical access due to the columns and surrounding belts. These constraints limit the applicability of Tomo-PIV and particularly limit the possibility to perform a full volumetric calibration inside the combustion chamber and obtain accurate camera modelling. This fact motivated the search for an alternative calibration process that is able to overcome confinement and optical distortions yet accurately describe the investigation volume while avoiding the need to install additional set ups to the test bench or move the tomographic recording system. For this reason, a novel *ex-situ* process is developed and evaluated for the in-cylinder flow and is found to be a suitable solution to the problem.

To be able to make this assessment, volumetric reconstructions resulting from the e*x-situ* process are compared to those resulting from the classical *in-situ* calibration described in §2.2.2. To perform the latter, the confinement of the engine's combustion chamber had to be eliminated in order to gain free access necessary to move the calibration plate through the entire investigation volume.

We aim with this procedure to overcome the need for full *in-situ* calibration for confined geometries by using the *ex-situ* process that includes a polynomial deformation function to be applied on particles images allowing thus to cross to a no-window configuration. Having reduced optical deformation, lower order camera models can be used reducing thus computation time.

2.2.5.2 Ex-situ Procedure

Placing the calibration target at the measurement region and moving it with precision inside the combustion chamber is a rather impossible task to achieve. It requires accessing a highly confined chamber and fixing the target plate parallel to the mid cylinder plane (i.e. controlling the axial and rotational orientations) then scrolling it for multiple positions scanning the 3D investigation volume.

In the absence of these constraints, a calibration target is usually placed on a translation stage and recorded across the whole investigation volume at previously fixed locations. A mapping function is then computed, based on a linear or a non-linear approach (Basanta J. et al, 2013), to describe how each element of the three-dimensional

physical domain relates to the two-dimensional image domain. This cannot be achieved however without a certain level of accessibility into the investigation volume.

Therefore, the approach proposed here establishes the correspondence between an originally confined investigation volume and its mapping function computed in the absence of confinement. A full 3D calibration process is done in the absence of the optical window and is then associated to a single fixed calibration plane recorded at the central position of the confined investigation volume, i.e. in the presence of the optical window. The optical distortion introduced by the window is compensated by the ex-situ calibration model obtained by performing four main steps:

(1) The first step is recording the calibration target in multiple planes across the investigation volume in the absence of the optical window, i.e. confinement. A reference plane Z_0 is used to identify the central plane of the investigation volume. The recorded targets are then used to extract grid coordinates at all considered Z-positions and compute the mapping function of each camera using adequate modelling such as pinhole, Soloff, polynomial or other.

(2) The second step is recording the calibration plate at Z_0-plane of the confined chamber, i.e. in the presence of the optical window. Then, a deformation function is computed to describe the transformation between two grids: Z_0 obtained 'in-window' and Z_0 obtained with 'no-window'. Having the same calibration target in the same physical space, the coordinates in that space, referred to as real coordinates, are the same with and without window:

$$\begin{pmatrix} X_{r\_i} \\ Y_{r\_i} \end{pmatrix} = \begin{pmatrix} X_{r\_n} \\ Y_{r\_n} \end{pmatrix} \quad \textbf{(2-11)}$$

where the subscripts r_i and r_n refer to real in-window and real no-window coordinates respectively. However, the corresponding pixels coordinates are different as a result of the change in the optical path after adding the window. This difference is described via a deformation function F_{def} such as:

$$\begin{pmatrix} X_{p\_n} \\ Y_{p\_n} \end{pmatrix} = F_{def} \begin{pmatrix} X_{p\_i} \\ Y_{p\_i} \end{pmatrix} \quad \textbf{(2-12)}$$

where the subscripts p_i and p_n refer to pixels in-window and pixels no-window coordinates respectively.

(3) The deformation function F_{def} is then used to project all particle images recorded *in-window* on the *no-window* domain. Hence, a new spatial domain is obtained where Z_0 grid deformations are taken into consideration and corrected.

(4) In a last step, a volumetric self-calibration step is performed using the projected low density particle images of (3) to refine the ensuing camera models computed in (1) thus resulting in the *ex-situ* camera models which will be used for volumetric reconstruction of the new no-window domain.

As a result, the ex-situ procedure allows overcoming confinement while reducing optical deformations which in turn highly impact computation time since they usually necessitate high order camera models in order to be taken into account in flow reconstruction.

In order to test and validate the ex-situ calibration process, a comparison is made between its resulting volumetric reconstructions and those resulting from classical camera modelling previously obtained via the *in-situ* calibration process. The three datasets L3, L5 and L8 recorded at BDC are considered, i.e. measurements at three volume thicknesses and an engine operation condition of 2000 RPM and 100% intake flow.

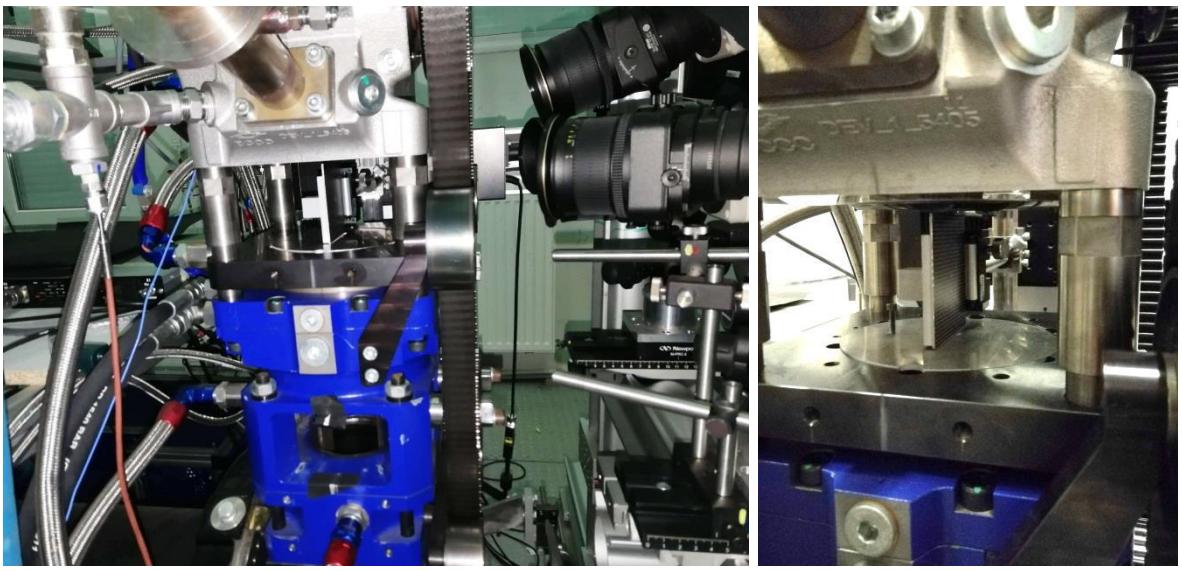

Figure 2-32 *Ex-situ* calibration process in the engine's combustion chamber

2.2.5.3 Validation of ex-situ process

2.2.5.3.1 Qualitative analysis

In order to evaluate the validity of the new ex-situ procedure, identical parameters as described in §2.2.3 were used for volumetric reconstruction of L3, L5 and L8 in the *no-*

cylinder domain, i.e. using the *ex-situ* camera models. All particle images were thus projected beforehand using F_{def} that is now defined as a 5^{th} degree polynomial function given by equations (2-1) and (2-2). *Ex-situ c*amera models are obtained similarly to the *in-situ* procedure using a Soloff approach and the self-calibration step is performed using the low density projected particle images. Similarly to *in-situ* camera models, projections errors prior to self-calibration are of the order of 2 pixels while after self-calibration, projection errors decrease to less than 0.02 pixels in the entire *no-window* investigation volume.

Results obtained from both in-situ and ex-situ processes are then compared. First, the ensuing ensemble averaged velocity fields are shown for the 3 cases in Figure 2-33 where iso-surfaces reveal magnitudes of the velocity and their fluctuations are shown in Figure 2-34. This first result reveals identical mean flow characteristics in consequence of both calibration processes. In both cases, a decrease in mean velocity magnitudes is noted as the flow gets further away from the intake jet and an increase in velocity fluctuations is seen near the vortical regions of the flow. Moreover, Figure 2-35 show velocity profiles extracted at different positions of the Z_0-plane. Velocity profiles ensuing from the *ex-situ* calibration are overlaid to those ensuing from the *in-situ* process and show perfect correlation.

In further analysis of the mean flow fields, mean planar properties $< \overline{|V|} >$ and $< \overline{|V'|} >$ are extracted across Z-dimension in order to evaluate the effect of the deformation function described in §2.2.5.2 over the change in optical deformation across the investigation volume. This is shown in Figure 2-36 and Figure 2-37 for all planes Z_k of L8 dataset with k varying from 1 to 31 in a ±4 mm range. A perfect correlation evidently appears in the mid-cylinder Z_0-plane from which derives the deformation function. Meanwhile, the relative error between the mean values of *in-situ* and *ex-situ* planes slightly increases while moving towards the borders of the investigation volume. However, the maximal deviations noted at Z = ±4 mm are still less than 2.5% of the initial value and therefore are considered acceptable.

Moreover, by closely examining the border planes in the velocity profiles of Figure 2-38, quasi-identical *in-situ* and *ex-situ* deduced velocity magnitudes are revealed in the entire field with slight differences for the region nearer to the cylinder wall. It can hence be deduced that the observed differences in Figure 2-36 reflect the inclusion of regions closer the cylinder wall where optical deformations are most stringent.

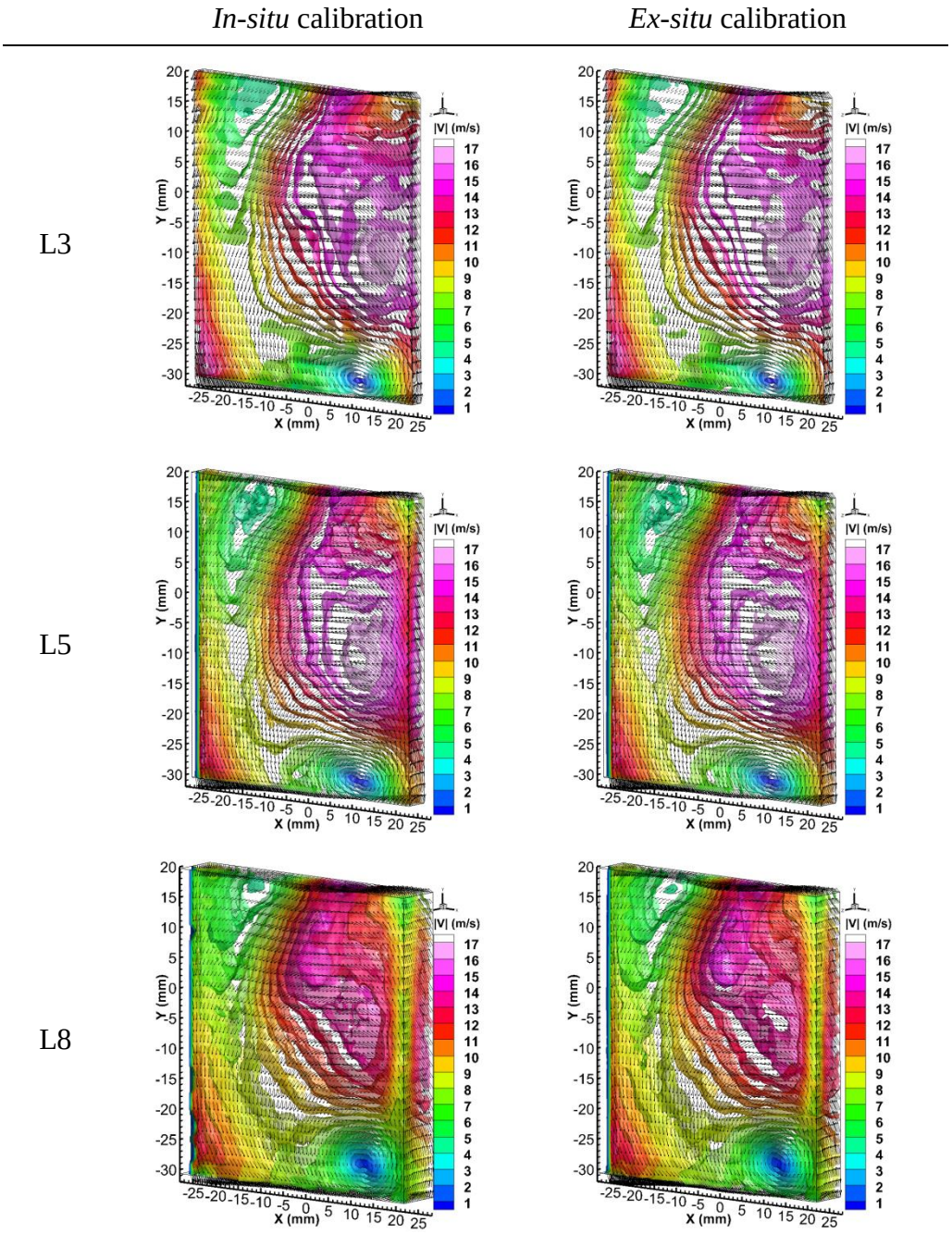

Figure 2-33 Ensemble averaged velocity fields obtained from *in-situ* and *ex-situ* calibration processes

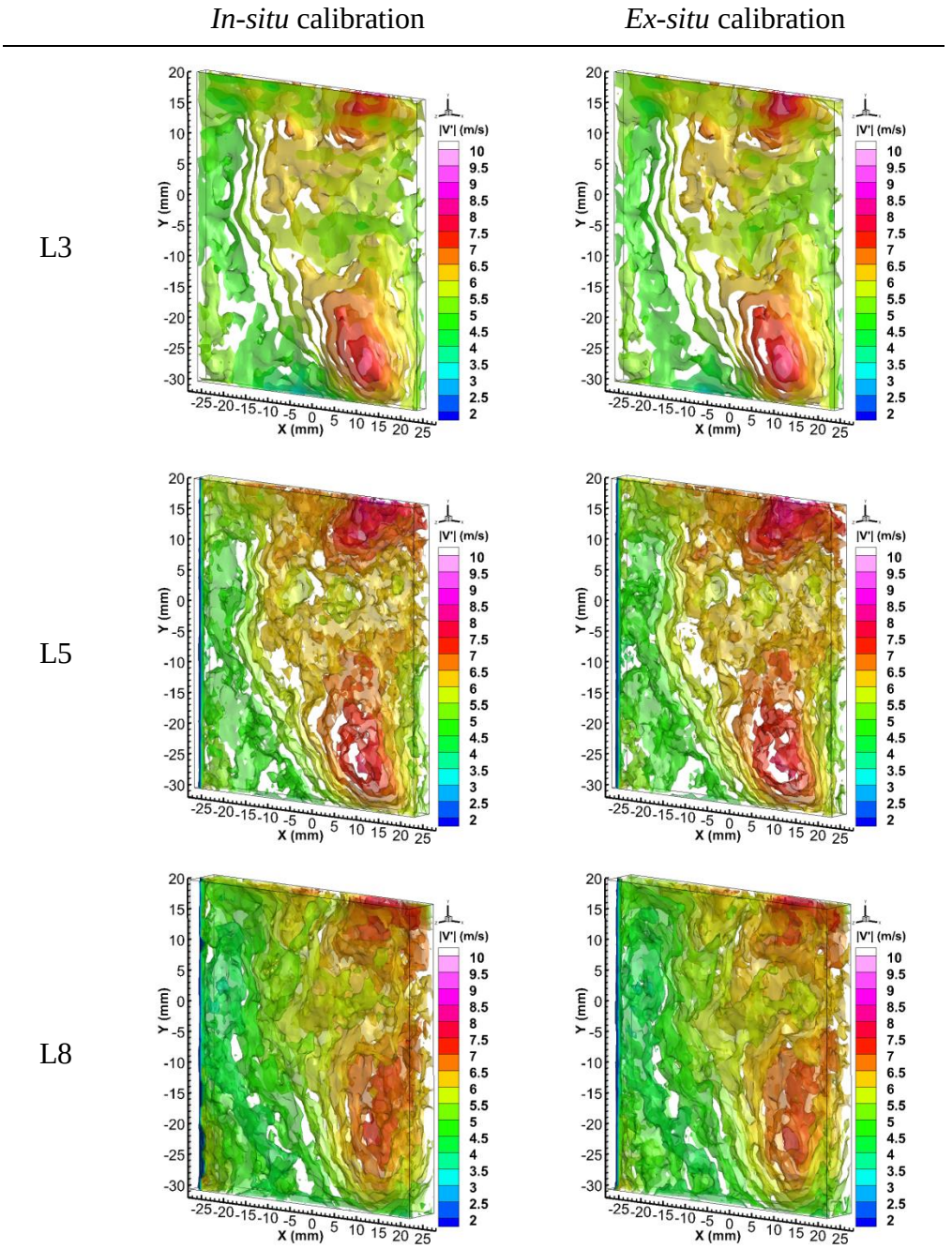

Figure 2-34 Ensemble avergaed velocity fluctuations obtained from *in-situ* and *ex-situ* calibration processes

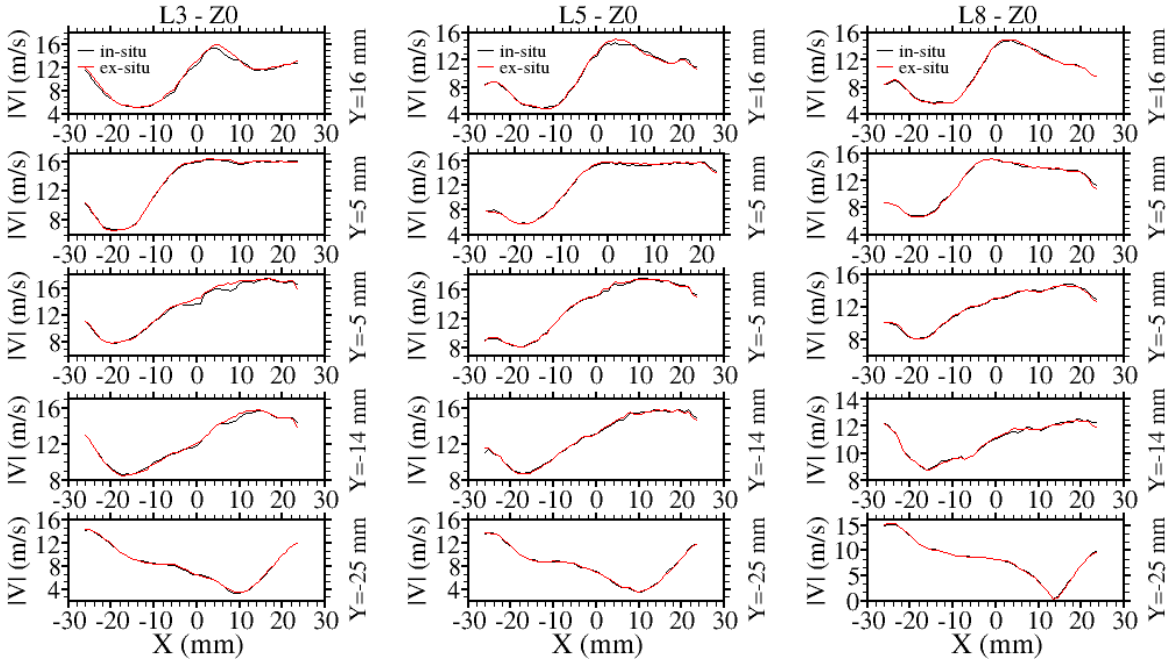

Figure 2-35 Profiles of mean velocity magnitude extracted at mid-cylinder planes

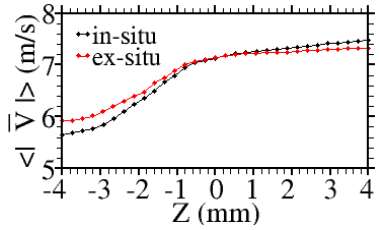

Figure 2-36 Mean velocity magnitude in XY planes across L8 for *in-situ* and *ex-situ* calibrations

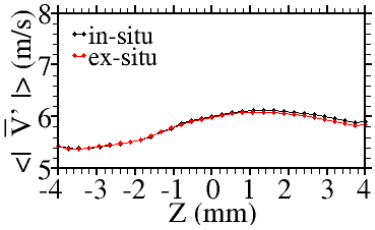

Figure 2-37 Mean velocity fluctuations in XY planes across L8 for *in-situ* and *ex-situ* calibrations

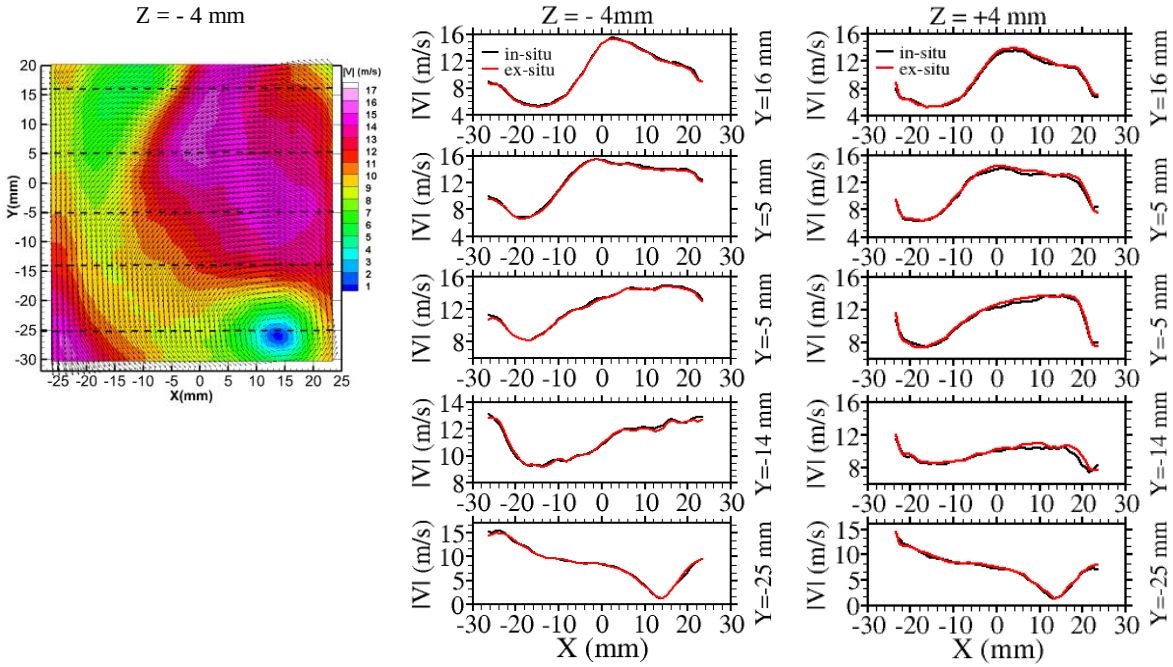

Figure 2-38 Comparison of *in-situ* and *ex-situ* mean velocity profiles of L8 in planes Z = ± 4 mm

2.2.5.3.2 Quantitative analysis

The cyclic and turbulent nature of engine operation makes it essential to characterize the different scale structures of the in-cylinder flow. Therefore, making sure that the *ex-situ* process is capable of faithfully reporting these scales in the reconstructed instantaneous velocity fields is of paramount importance (Figure 2-39).

In a first step to reveal the correlation between the two techniques, the evolution of velocity components is described along the 250 instantaneous velocity fields obtained from the two processes in Figure 2-40. Both $< u >$ and $< v >$ components reveal exact similarity of instantaneous velocity fields. A slight shift appears however in $< \mathrm{v} >$ component. This is believed to reflect the averaging over the whole volume and thus the accumulation of relative errors. Then in order to refine the comparison, instantaneous velocity profiles (u,v,w) are extracted along x-direction at 3 different y-positions in the mid-cylinder plane Z_0 and boundary planes Z = ±4 mm (Figure 2-41). The described similarities are again observed across the entire volume with increasing shift at the regions closer to the cylinder wall, in the border planes.

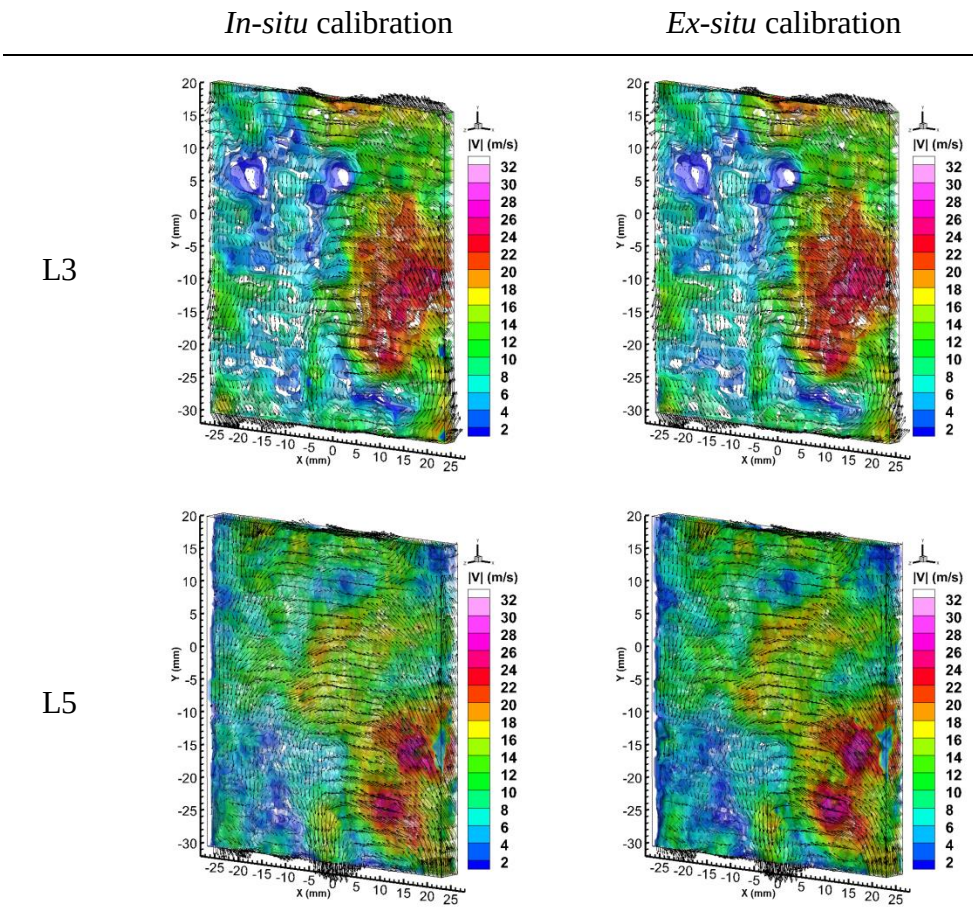

L8

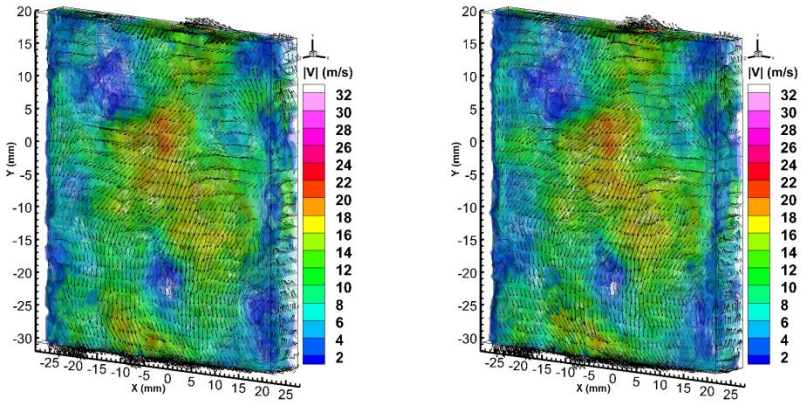

Figure 2-39 Instantaneous velocity fields obtained from *in-situ* and *ex-situ*

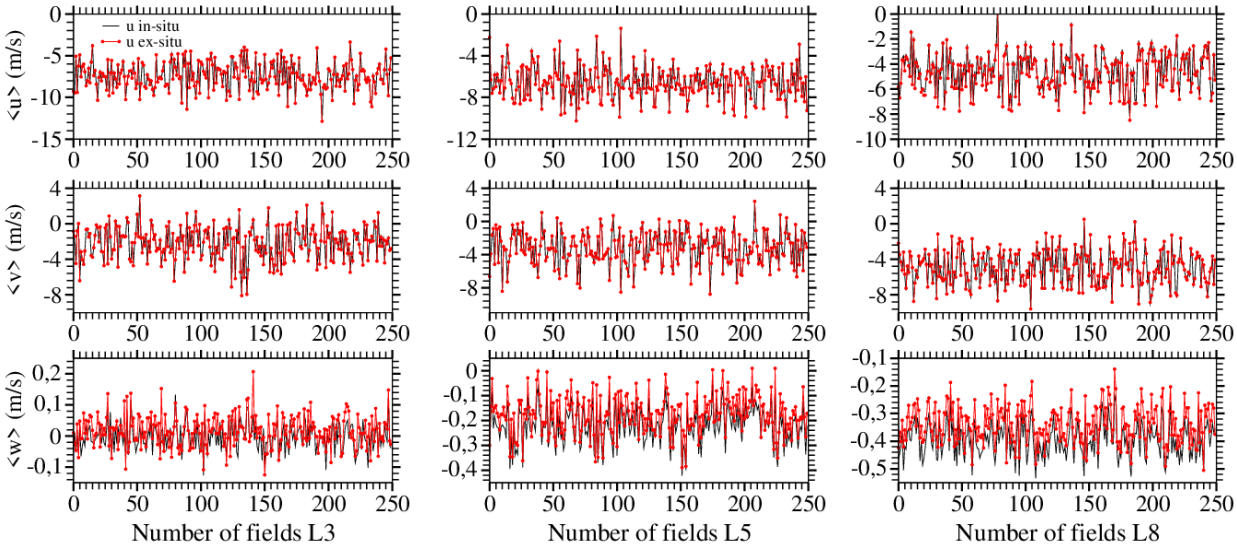

Figure 2-40 Comparison of instantaneous velocity fields obtained from *in-situ* and *ex-situ* calibrations

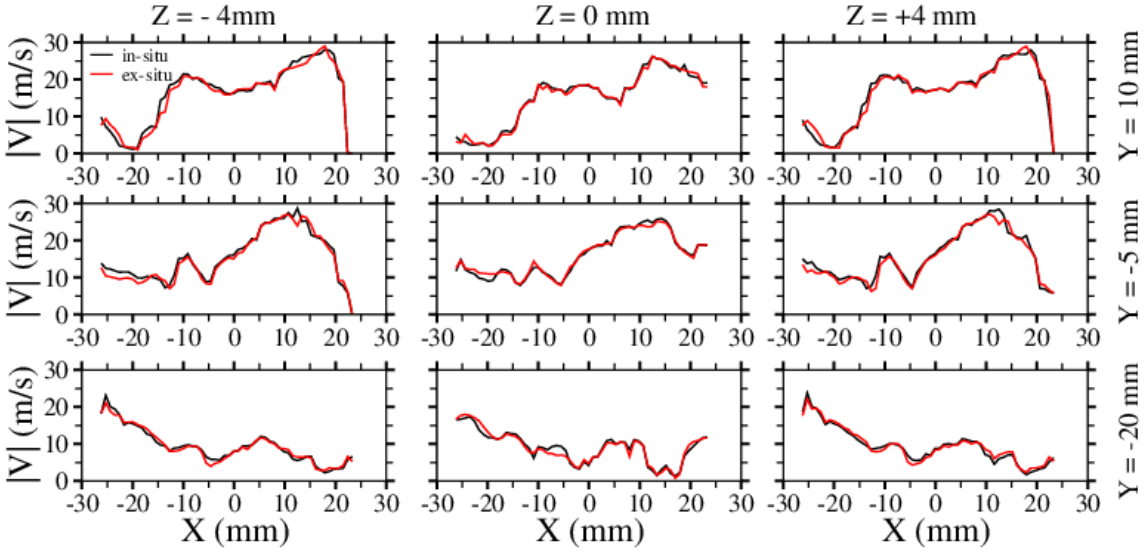

Figure 2-41 Example of instantaneous velocity profiles extracted from L8 mid and border planes

In order to additionally refine the comparison, u, v and w-components are extracted at one random point in space (X,Y,Z), from the 250 velocity fields. Figure 2-42 thus represents the instantaneous (u,v,w) ex-situ components versus (u,v,w) in-situ components at the same spatial location. Strong symmetry of u and v components reveals the high agreement between the two techniques. The comparison is more delicate for w-component considering the small velocity magnitudes in z-direction at the middle of the combustion chamber, i.e. across our investigation volume. Nevertheless, a clear correlation between *in-situ* and *ex-situ* procedure is revealed thus validating the reliability of the latter.

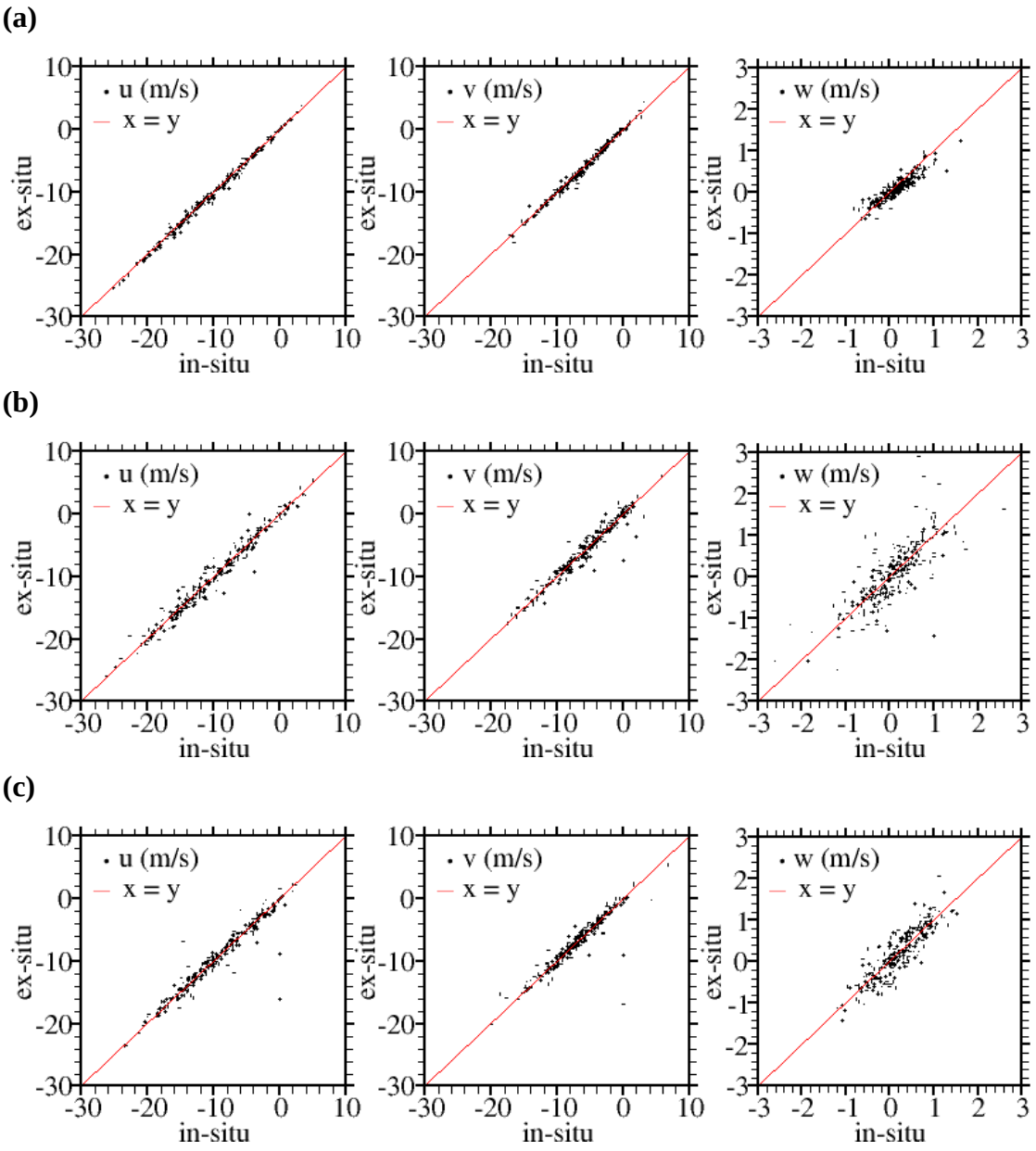

Figure 2-42 *Ex-situ* vs. *in-situ* local components for a) L3, b) L5 and c) L8

2.2.6 Summary of Tomo-PIV measurements

Experimentally describing the three-dimensional in-cylinder flow is fundamental for understanding the real behaviour of internal engine aerodynamics. It is possible nowadays to access such three dimensional flow structures via the tomographic PIV technique. However, its application to environments with complex geometries still faces a great deal of constraints limiting the investigation volume's dimensions and measurements accuracy. This is particularly the case for the present engine configuration whose combustion chamber consists of a highly confined geometry with severe optical deformations since these characteristics prevent the calibration process from properly describing the domain in question.

For that reason, an *in-situ* calibration setup was first developed and applied to the optical engine test bench. It consists on mounting the tomographic PIV recording system on translation rails then on associating it, in an adjacent position to the engine, to an additional assembly replicating with precision the position of the investigation volume with respect to the cameras. In this configuration, the calibration target is free to move in the presence of the cylinder thus allowing us to establish a complete description of the investigation volume.

Moreover, as the volume thickness is a primary concern for the accuracy of 3D measurements, particle images for three volume thicknesses ΔZ = 3, 5 and 8 mm were recorded in order to determine the largest admissible volume for 3D measurements and confirm the validity of the resulting data. The main flow characteristics were compared for a series of 250 velocity fields.

It was found that the different volumetric measurements reveal similar global flow characteristics in the common regions with an extent of information given by L8 in the regions beyond ±2.5 mm. Moreover, instantaneous velocity fields demonstrated similar flow evolution across the recorded engine cycles and showed the extremely turbulent nature and the wide dynamic range of in-cylinder flow. Moreover, by quantifying the deviation of mass conservation for each volumetric domain, values in the range of 10% were found and the validity of data was proven and therefore the validity of measurement campaigns at ΔZ = 8 mm was demonstrated. It is also worth noting that beyond 8 mm, ghost particle levels become unacceptable and exceed 25% which implied 8 mm to be the maximal investigated thickness. As a result of data validation, phase-locked measurements for the 6 considered engine operation conditions were recorded for 7 crank angle degrees during intake and compression strokes yielding 250 velocity fields for each case. In total,

12000 particle images recorded by the 4 cameras allowed obtaining a total of 1 500 three-dimensional velocity fields from Tomo-PIV calculations (Table 2-4).

CAD	**-274, -250, -226, -178, -130, -106, -82**			
Intake duct opening	**N = 2000 RPM**		**N = 3000 RPM**	
	Number of cycles	**Particle images per camera**	**Number of cycles**	**Particle images per camera**
V100	250	500	250	500
V50	250	500	250	500
V25	250	500	250	500

Table 2-4 Summary of Tomo-PIV measurement campaigns during intake and compression strokes

The *in-situ* process provided the means to obtain a complete calibration of the investigation volume otherwise confined and unreachable in its totality. However, it implicated a displacement of the recording system as well as a cost for an additional assembly capable of replicating the engine's combustion chamber's position. Moreover, a great trust in the used equipment is essential to judge the new system as highly accurate.

These facts motivated further optimization of the calibration process so that direct calibration of the investigation volume is possible at its initial location. This was then called the *ex-situ* process since it consisted of obtaining a model from a 3D calibration in the absence of the optical cylinder associated to one in-cylinder plane. Having both mid-cylinder planes recorded with and without cylinder, a deformation function can be calculated and used to obtain *ex-situ* camera models capable of describing the entire confined investigation volume without the need for additional measures. Applying the deformation function to all particle images prior to self-calibration results in volumetric reconstructions faithfully describing the flow.

In order to demonstrate the validity of the *ex-situ* process, mean and instantaneous velocity fields were compared with results obtained from *in-situ* calibration and were found identical in the mid-cylinder plane and less than 2.5% mean error was noted in the border planes, i.e. $z = \pm 4$ mm.

In conclusion, the *ex-situ* technique allows overcoming the obstacle of confinement while eliminating optical deformations and ensuring computations accuracy.

3 In-cylinder flow characterisation: from 2D to 3D

This chapter carries out a detailed analysis of in-cylinder flow dynamics by means of 2D and 3D tools presented so far and developed furthermore hereafter. The evolution of coherent structures during intake and compression strokes as well as their variations with respect to engine operation conditions are reported, extending 2D information to 3D. Throughout the chapter, the six engine operation conditions are treated and compared. At first, engine speed is fixed and the mean in-cylinder flow in the tumble plane as well as the mean velocity fluctuations are described for the different inlet flow conditions from TR- PIV measurements. Then, the influence of engine speed on in-plane aerodynamics is presented for each inlet flow condition during intake and compression strokes. The combined effect of inlet flow and engine speed variations on flow characterisation is quantified with respect to tumble vortex positioning in the field of view as well as the variations of turbulent kinetic energy. The correlation between both engine parameters is deduced. The third part of the chapter describes the changes witnessed by the instantaneous flow field, particularly cyclic fluctuations of in-cylinder coherent structures, obtained via TR-PIV. In order to visualise coherent structures, the large range of existing flow dynamics is filtered using the proper orthogonal decomposition technique. Finally, a three-dimensional flow analysis is reported for 7 CAD measured via Tomo-PIV, showing the essential contribution that tomographic PIV measurements bring to the understanding of flow evolution.

Operation condition	Engine Speed	2000 RPM			3000 RPM		
	Intake	V100	V50	V25	V100	V50	V25
TR-PIV	Number of CAD	45 per cycle	45 per cycle	45 per cycle	30 per cycle	30 per cycle	30 per cycle
	Number of cycles	350	300	300	350	300	300
	Range (CAD)	[-360,0]	[-360,0]	[-360,0]	[-360,0]	[-360,0]	[-360,0]
Tomo-PIV	Number of CAD	7	7	7	7	7	7
	Number of cycles	250	250	250	250	250	250
	Range (CAD)	for each case: -274, -250, -226, -178, -130, -106, -82					

Table 3-1 In-cylinder measurements

3.1 Influence of intake flow on mean in-cylinder aerodynamics from TR-PIV

In order to study the effect of the inlet flow motion on the in-cylinder flow dynamics during intake and compression strokes, the mean flow field and its corresponding fluctuations are first compared for cases V100, V50 and V25 (Figure 1-16) at 2000 RPM. The air intake pressure was maintained at 1 atm during all measurements hence the primary intake flow is preserved for each engine rotational speed. The main factor contributing to the change in the in-cylinder flow characterisation is the intake flap opening, thus the speed of the flow in the intake runner. The results of 2D TR-PIV measurements in the tumble plane are presented to describe the spatiotemporal flow evolution during the engine cycle. Since 45 engine phases per cycle were recorded at 2000 RPM, only a selected number of velocity fields are explicitly shown while other representative quantities, defined along the chapter, describe the resolved intake and compression stokes and the complementary fields can be found in annexe 1.

3.1.1 Ensemble averaged flow in tumble plane

The cyclic nature of internal combustion engine flows implies the use of an ensemble average velocity offering a general description of the in-cylinder flow. This is shown in equation (3-1) revoked hereafter for the u velocity component:

$$\bar{u}(x,y,z) = \frac{1}{N}\sum_{i=1}^{N} u_i(x,y,z) \qquad \textbf{(3-1)}$$

where N is a significant number of cycles and where the subscript i denotes the instantaneous velocity component. Consequently, the mean kinetic energy can be obtained according to:

$$KE(x,y,z) = \frac{1}{2}\left(\bar{u}^2(x,y,z) + \bar{v}^2(x,y,z) + \bar{w}^2(x,y,z)\right) \qquad \textbf{(3-2)}$$

Figure 3-1 shows the ensemble average of the in-cylinder flow computed over the 300 velocity fields obtained from TR-PIV measurements. A first observation can then be made during the intake stroke, i.e. before -180 CAD, that as the inlet duct opening decreases, an increase of velocity magnitudes is observed in the regions nearer to the intake valves. Moreover, with respect to the initial inlet condition of V100, an increase in the regions near the piston head is observed for V50 at -274 CAD while a slight decrease appears in these regions for V25.

Going farther in the intake stroke, i.e. at -250 CAD, the front valve jet travelling towards the left cylinder wall undergoes a considerable increase in velocities that exceed

50 m/s in all three cases, particularly remarkable for V50. The intake flow then rotates to the middle of the field of view. For V100 and V50, the flow's velocity continues to increase exceeding 35 m/s near the piston head while it remains around 20 m/s for V25. Regions of low velocity magnitudes (< 10 m/s) propagate from the right cylinder wall and are most remarkable for V25.

Near the end of the intake stroke, an opposite behaviour appears between the flow near the intake valves and the rest of the combustion chamber. As the intake duct opening decreases, the flow's velocity continues to considerably increase near the valves while it decreases in the middle of the field. With respect to V100, this decrease is more important for V25 than V50 and continues to be so at the beginning of the compression stroke, i.e. -178 CAD, where dominant regions of velocities less than 10 m/s can be observed.

In all cases, a tumble structure can be observed in the lower right of the field of view. And as the compression takes place, the tumble motion goes from a vertically elongated shape to a more compact one. Particularly near the end of compression, shown at -82 CAD, V25 reveals velocity magnitudes approximately two times smaller than V50 and V100 and a mean tumble structure that is closer to the piston head. Meanwhile, the tumble structure in the cases of V50 and V100 is transported nearer to the exhaust valves.

In conclusion, as the inlet flow section decreases, the mean in-cylinder flow exhibits higher velocity magnitudes in the regions of the front intake jet. Particularly at 50% of the original intake flow, large velocities in an upward direction appear near the piston head during the intake stroke and the forming tumble structure is compressed from the bottom right to the top left of the field of view during the compression stroke. At 25% of the original flow, the rear intake jet presents larger velocities under which regions of much smaller velocities take over, propagate and persist until the end of compression where the tumble structure seems closer to the piston head than to the top left under the exhaust valves. These observations reveal a different behaviour of the in-cylinder flow with respect to the inlet condition. Particularly at the end of compression, the initial conditions marking the ignition quality will be affected and consequently the flow's evolution during intake and compression strokes has a direct influence on the development of combustion. Ensemble average velocity descriptions offer a general description of the in-cylinder flow but remains meanwhile of limited capacity for further detailing the flows characteristics. In the following, vortex identification technique and velocity fluctuations are presented in order to complete the mean flow analysis and a detailed description of cyclic flow evolution is presented afterwards in §3.3.

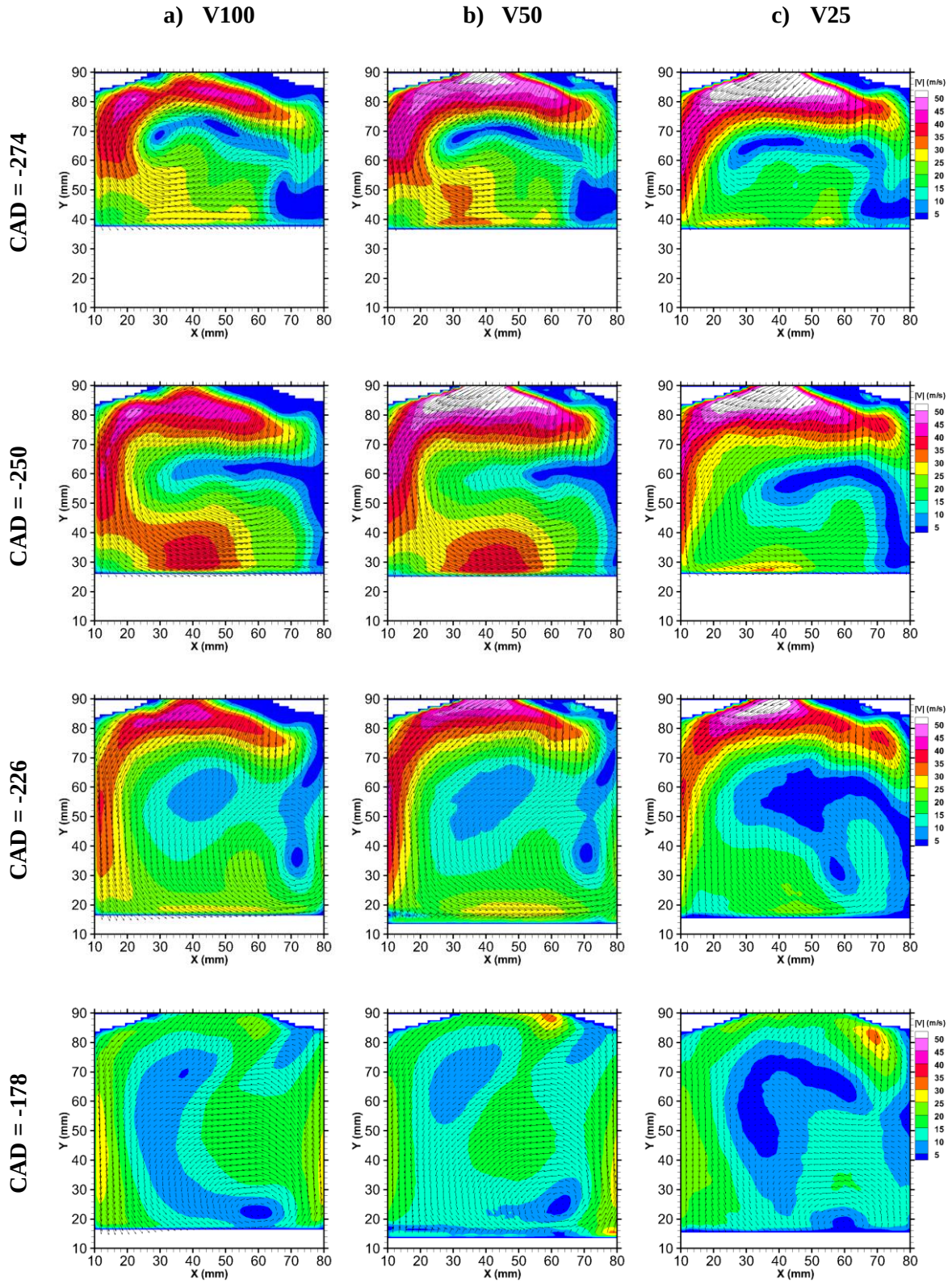
a) V100
b) V50
c) V25
CAD = -274
CAD = -250
CAD = -226
CAD = -178
Y (mm)
X (mm)
|V| (m/s)

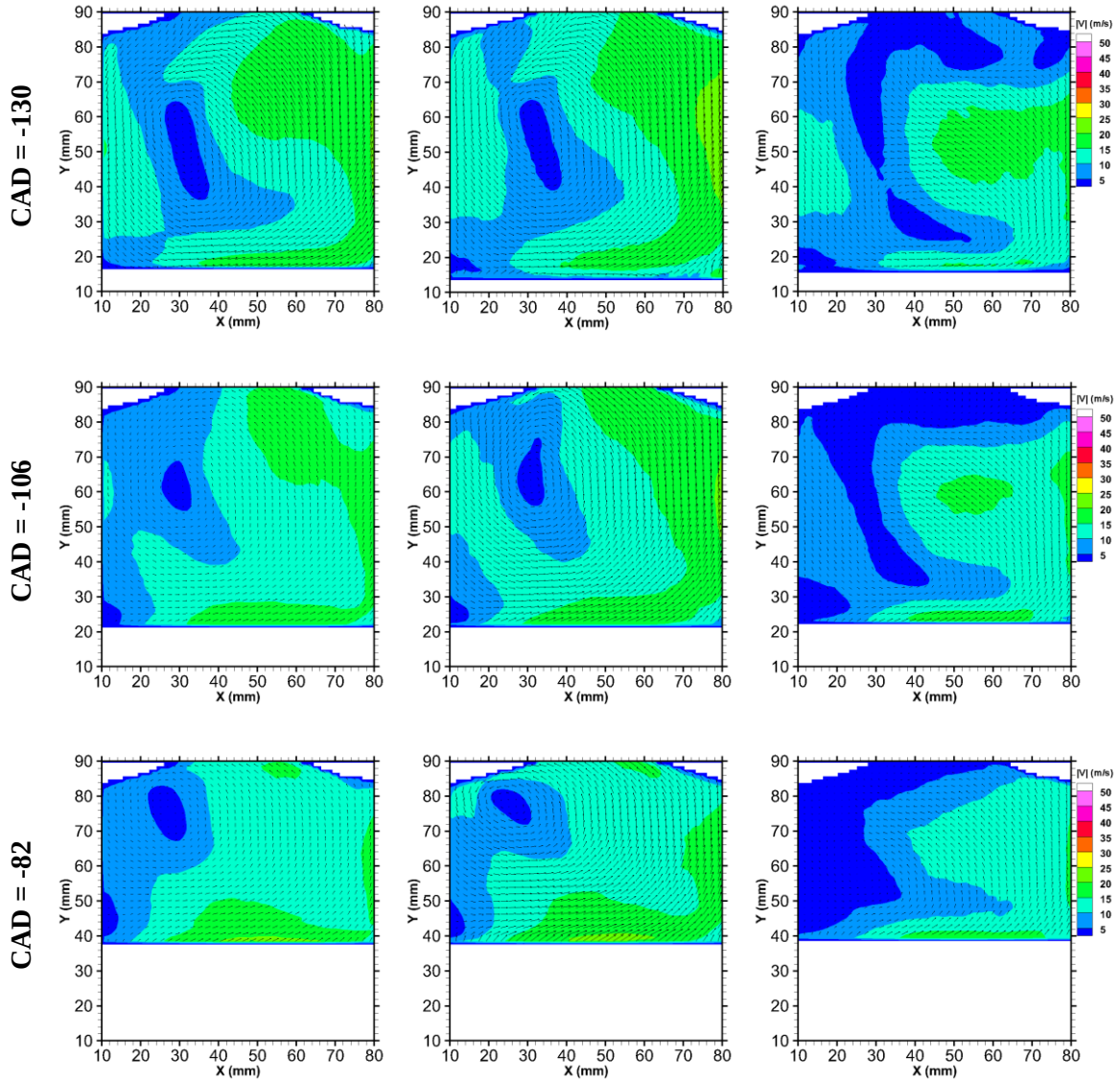

Figure 3-1 Ensemble averaged velocity fields at 2000 RPM from TR-PIV

3.1.2 Vortex centre identification and Temporal tracking of tumble

One mean to quantify the described flow characteristics and further compare the effect of the three inlet flow conditions is identifying the tumble centre location and tracking it across the engine cycle for each case.

A survey on the most popular vortex-identification methods used such as the Q-criterion, the Δ criterion and the λ_2 criterion can be found in (Kolar, 2007). Particularly in our study, the vortex centre in 2D measurements is identified using the Γ criterion (Graftieaux et al, 2001) that is a simple yet robust technique based on the topology of the

velocity field. It is determined as the normalized angular momentum across a predefined grid area:

$$\Gamma = \frac{1}{N}\sum_{S}\frac{\left\|\overrightarrow{OM} \wedge \overrightarrow{V_M}\right\|.\vec{z}}{\left\|\overrightarrow{OM}\right\| \cdot \left\|\overrightarrow{V_M}\right\|} \quad \textbf{(3-3)}$$

where S is the grid surface around O, N is the number of points in S, $\overrightarrow{V_M}$ is the velocity vector at point M and $\vec{z}$ is the unit vector normal to S.

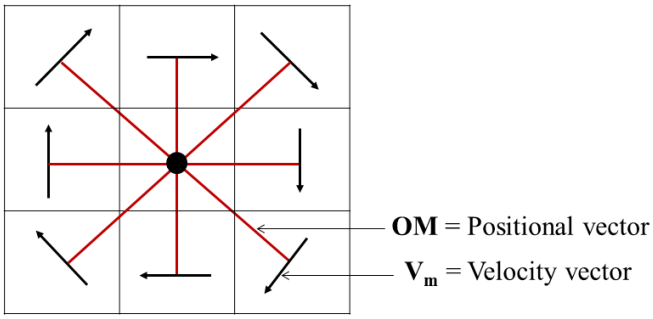

Figure 3-2 Vortex centre identification by Γ criteria

This criterion suggests then to find the zone in which the angle between the velocity vector at a point in space and the segment linking this point to the centre of rotation is maximal. Thus, values of Γ range between -1 and 1, the sign of which depends on the rotation direction. An example of a Γ scalar field obtained from a mean vector field at BDC is shown in Figure 3-3. Surfaces of 10 mm² were considered for calculations. Then it remains to follow the evolution of Γ_{max} in order to follow the tumble across the engine cycle as is shown in Figure 3-4, and evaluate the influence of the inlet flow condition on in-cylinder aerodynamics. The two observed trajectories of V100 and V50 show slight differences at the beginning of intake. Meanwhile, as the in-cylinder flow develops towards the BDC and through the compression stroke, positional differences become more important. These differences are most remarkable between mid-intake and mid-compression strokes. Moreover, the mean tumble trajectory of V25 witnesses very significant variations during the intake than during the compression stroke. By comparing the 3 mean trajectories across the engine phases, V25 also reveals a straighter and narrower path than V50 and V100 that draw more elliptical ones. A general lower tumble location, closer to the piston head and closer to the centre of the field of view, is observed in V25 velocity fields and is verified via the Γ criteria. This can be linked during the intake stroke to the stronger front inlet jet seen in Figure 3-1 with respect to the other two cases. The intense downward motion reaching the left cylinder wall generates an intense recirculation of the in-cylinder flow impacting the piston head and travelling back to the centre of the field of view. Finally, the lower tumble positioning for V25 during the

compression stroke can be related to the lower velocity magnitudes observed at the end of compression thus a slower transport of the vertical structure across the field. As the whole V25 in-cylinder flow decelerates more than V50 and V100 during compression, the tumble travels slower through the field.

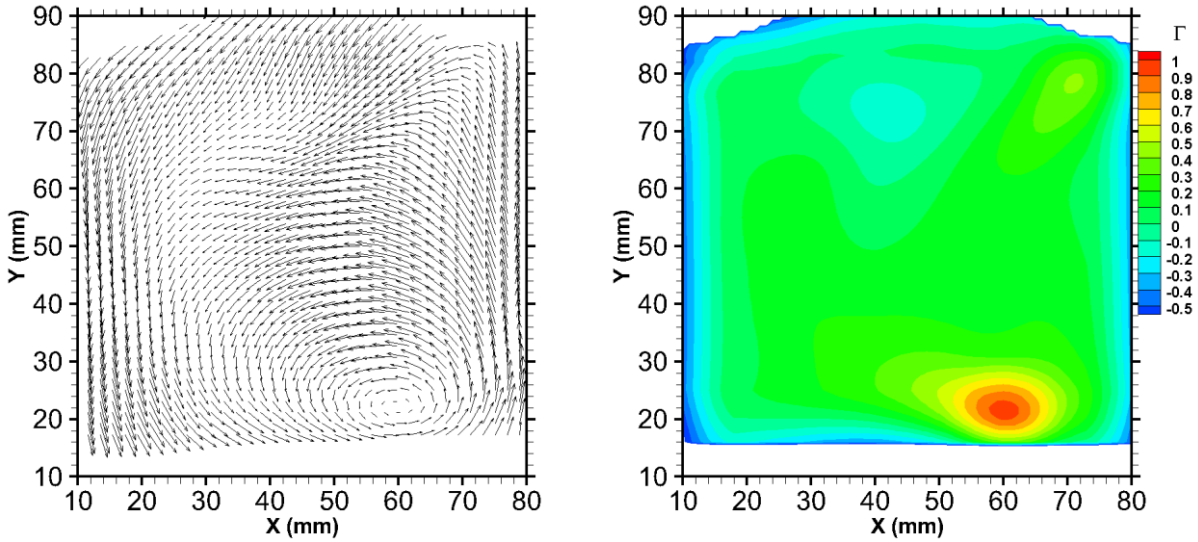

Figure 3-3 Tumble centre identification via *Γ* criterion: (a) vector field (b) *Γ* scalar field

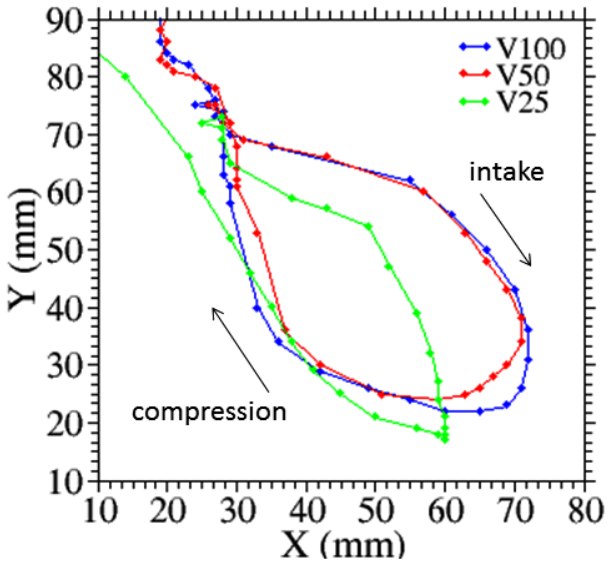

Figure 3-4 Mean tumble trajectory at 2000 RPM with respect to the different inlet conditions

3.1.3 2D ensemble averaged velocity fluctuations in tumble plane

In addition to the mean velocity flow field, ensemble averaged velocity fluctuations are presented in Figure 3-5 and Annexe 1. In this section, velocity fluctuations refer to the

term ensuing from the classical Reynolds decomposition which separates an instantaneous velocity u_i into the sum of a mean component $\bar{u}$ and a fluctuating component u′. With this definition, the magnitude of velocity fluctuations averaged over a series N of *i* engine cycles is obtained according to the following equation (3-4):

$$\overline{u'_N}(x,y,z) = \frac{1}{N}\sum_{i=1}^{N} u'_i\,(x,y,z) \qquad \textbf{(3-4)}$$

Consequently, the turbulent kinetic energy TKE can then be deduced according to:

$$\overline{TKE}\,(x,y,z) = \frac{1}{2}(\overline{u'_N}^2(x,y,z) + \overline{v'_N}^2(x,y,z) + \overline{w'_N}^2(x,y,z)) \qquad \textbf{(3-5)}$$

Moreover, a mean TKE can be computed in order to represent each velocity field fluctuations by a generic value. This value integrates the different scales of fluctuations inside the same field but can be used to compare the same field under different operation conditions. This is given in the following equation (3-6):

$$< \overline{TKE} > = \frac{1}{n_x n_y n_z}\sum_{1}^{n_x}\sum_{1}^{n_y}\sum_{1}^{n_z} TKE_i(x,y,z) \qquad \textbf{(3-6)}$$

By comparing the three engine inlet conditions at 2000 RPM during the intake stroke as shown in Figure 3-5 for -274 CAD, it can be seen that, analogous to the evolution of mean velocity magnitudes, u′ increases near the intake valves as the inlet duct opening decreases and as the intake stroke progresses. Particularly in the case of V50, u′ also increases at the end of intake and the beginning of the compression stroke in the regions near the piston head while it continues to decrease in the middle of the field of view. During the compression stroke, velocity fluctuations reveal an opposite behaviour to velocity magnitudes previously described. While the latter decreases with the decrease of inlet flow, velocity fluctuations increase, particularly for V25. This is further illustrated in Figure 3-6 showing $\overline{TKE}$ at every CAD for the three inlet conditions through the two recorded engine phases recalling that at 2000 RPM, 1 phase was recorded every 8 CAD. The differences in velocity fluctuations of V50 and V25 with respect to V100 are most important between -274 CAD and -106 CAD, i.e. mid-intake and mid-compression strokes, reflecting the differences observed with respect to tumble location previously described. In the same range of CAD, V100 reveals smaller variations of $\overline{TKE}$ than V50 and V25 that demonstrates a steep increase reaching a peak at -226 CAD, i.e. near the end of intake, followed by a steep decrease until -178 CAD is reached. After that, at the beginning of compression, the decrease in $\overline{TKE}$ occurs less intensely with respect to the

end of intake for the three inlet cases, with greater magnitudes for V25 than V50 and V100.

Although $\overline{TKE}$ is representative of the global flow behaviour with respect to the engine's operation condition, one should keep in mind that both turbulence and cyclic variations are taken into consideration in the total velocity fluctuations. Then it remains to separate the contribution and the effect of each on the in-cylinder flow characterisation.

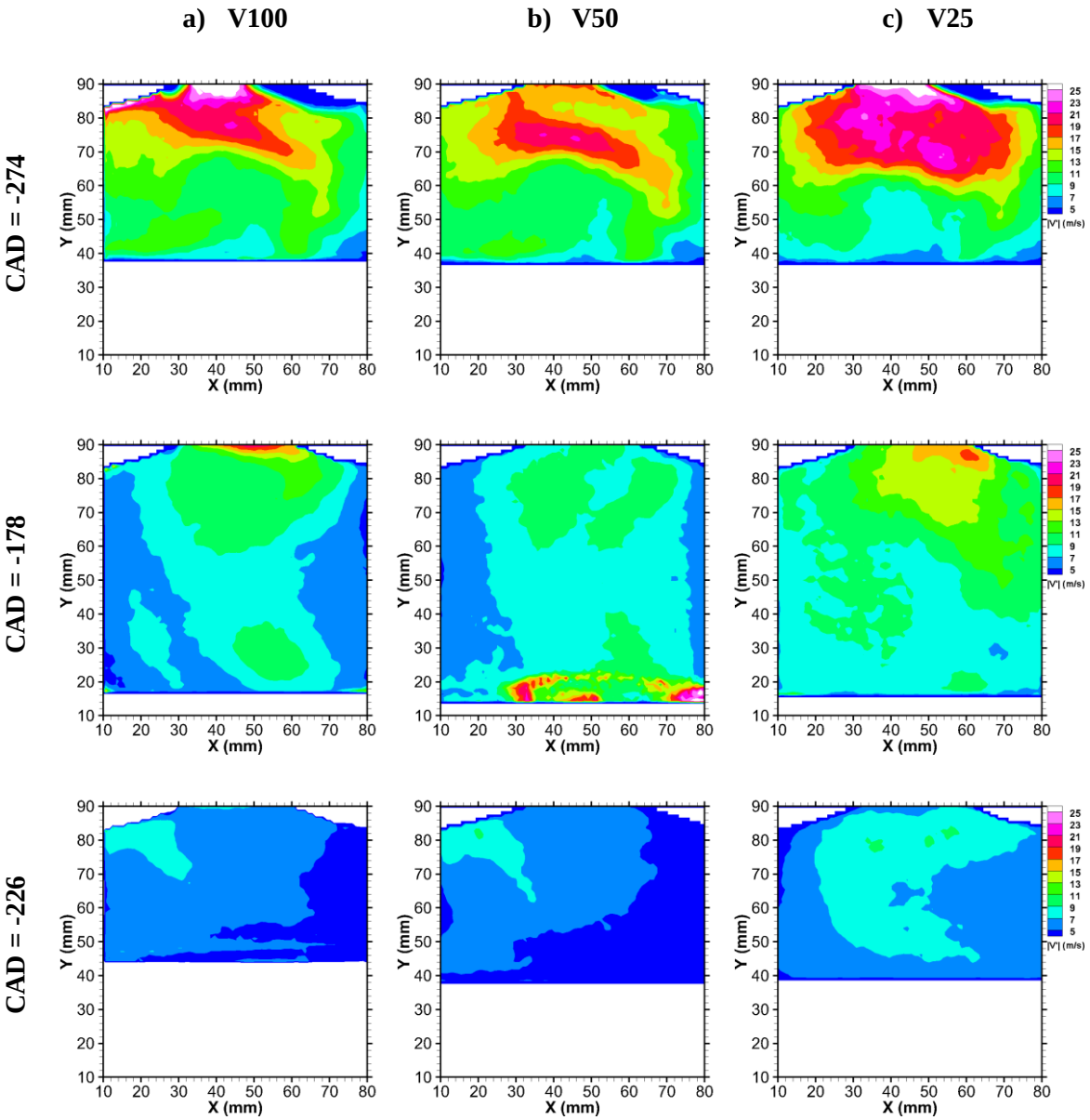

Figure 3-5 Ensemble averaged velocity fluctuations in tumble plane from TR-PIV measurements at 2000 RPM

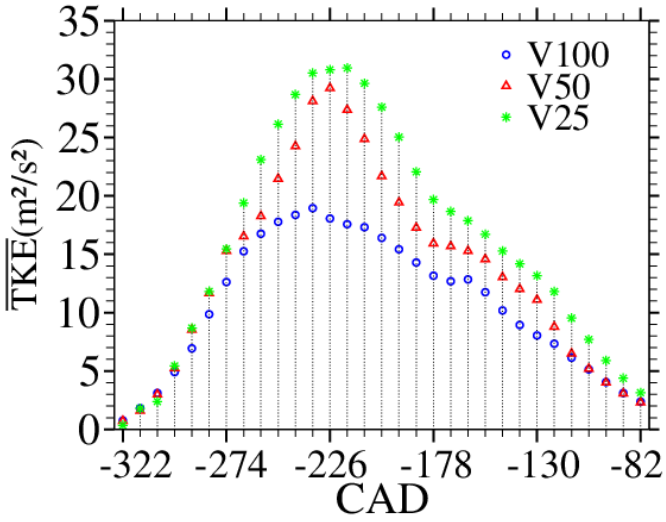

Figure 3-6 Temporal tracking of turbulent kinetic energy TKE of the mean engine cycle at 2000 RPM for V100, V50 and V25 (recording resolution = 8 CAD).

3.2 Influence of engine speed on mean in-cylinder aerodynamics from TR-PIV

Using 2D PIV measurements, it has been shown that the engine's speed significantly influences in-cylinder aerodynamics due to the accompanying variations of inlet air flow motion (Stansfield et al., 2007). In this section we aim to show that the influence of engine speed also depends on the initial inlet flow condition, i.e. the two parameters are strongly correlated. In order to describe this correlation, mean tumble location is again identified using the Γ criterion (Graftieaux et al., 2001) and mean tumble trajectories are compared for the different inlet cases at 2000 and 3000 RPM.

3.2.1 2D ensemble averaged flow in tumble plane

The ensemble average velocity fields computed over 300 engine cycles recorded via TR-PIV measurements at 2000 and 3000 RPM are shown at different CAD for the different inlet cases in figures 3-8 to 3-11. At 3000 RPM, the effect of inlet flow on the in-cylinder aerodynamics can be described similarly to what was observed at 2000 RPM in §3.1, with higher velocity magnitudes involved.

With respect to engine speed, a strong increase in velocity magnitudes is observed in the front intake jet at -274 CAD, going from the intake valves to the left of the field of view (Figure 3-7). The inlet flow meets the left cylinder wall and heads back towards the middle of the combustion chamber forming a tumble structure in the upper left side of the field of view. For V100, velocities are around 30 m/s when at 2000 RPM and exceed 40 m/s near the piston head when at 3000 RPM. For V50 at 3000 RPM, velocity magnitudes

in the same regions exceed 50 m/s as well as in extended regions toward the middle of the field and farther at the rear inlet jet. For V25, the increase in velocity magnitudes with respect to engine speed is the most important in the regions of the front intake jet and the bottom left of the field of view.

Approaching towards the end of intake, at -226 CAD shown in Figure 3-8, the tumble structure is located in the lower right of the field of view in all inlet cases. Regions of low velocity magnitudes (less than 10 m/s) accompanying the tumble structure at 2000 RPM are greatly lessened at 3000 RPM where velocities surrounding the tumble exceed 20 m/s. For V100 and V50, a similar global behaviour is observed with velocity magnitudes increasing near the left cylinder wall and the piston head, exceeding 50 m/s for V50. For V25, this increase seems to be more significant in the rear jet regions and the middle of the piston head with magnitudes exceeding 25 m/s. It is also worth noting that, with respect to engine speed, the increase in velocity magnitudes while going from 2000 to 3000 RPM is more important for V50 than for V100 and V25.

Then near BDC at -178 CAD (Figure 3-9) marking the beginning of the compression stroke velocity magnitudes continue to increase predominantly near the cylinder walls and most significantly for V50. Meanwhile for V25, the rear intake flow witnesses a more significant increase in the upper right regions of the field of view as a consequence of the high velocity magnitudes observed during the intake stroke. One can then deduce that the effect of engine speed on the in-cylinder flow during the intake stroke highly depends on the investigated region and the corresponding inlet flow condition.

Furthermore, during the compression stroke, velocity magnitudes seem to be maintained across several CAD (Figure 3-10). However, they are greater for an engine speed at 3000 RPM than at 2000 RPM. Particularly at the end of compression, the velocity distribution surrounding the tumble structure reaching under the exhaust valve reveals greater magnitudes for 3000 RPM than 2000 RPM where regions of velocity magnitudes lower than 10 m/s are rather dominant.

In order to further characterise the described flow with respect to the variation of engine speed, the mean tumble trajectory is identified and compared for each inlet case at 2000 and 3000 RPM in Figure 3-11 via the Γ criteria. It first shows for V100 very slight differences at the beginning of intake. These differences increase from mid-intake to mid-compression stroke, particularly in x-direction. Furthermore, the mean tumble trajectories of V50 (Figure 3-11 (b)) reveal greater alterations of tumble centre location during the compression stroke between 2000 and 3000 RPM, in both x and y-directions. Finally, the

influence of engine speed on the mean tumble trajectory of V25 (Figure 3-11 (c)), while is important during the whole engine cycle, is more significant during the intake than during the compression stroke. Moreover, at 3000 RPM as at 2000 RPM, the mean tumble trajectory of V25 draws a straighter and narrower path than V50 and V100.

In conclusion, the influence of engine speed on mean in-cylinder aerodynamics is not occurring in a regular direction, with respect to inlet flow, and can be summarized as follows:

- During the intake stroke: differences in velocity magnitudes between 3000 and 2000 RPM are more pronounced with respect to V50 and V25 than they are for V100,
- At BDC, an increase in engine speed influence the in-cylinder flow in case of V25 and V50 more considerably than in case of V100, and
- During the compression stroke: V100 reveals a greater velocity increase accompanying the increase in engine speed compared to V50 and V25.

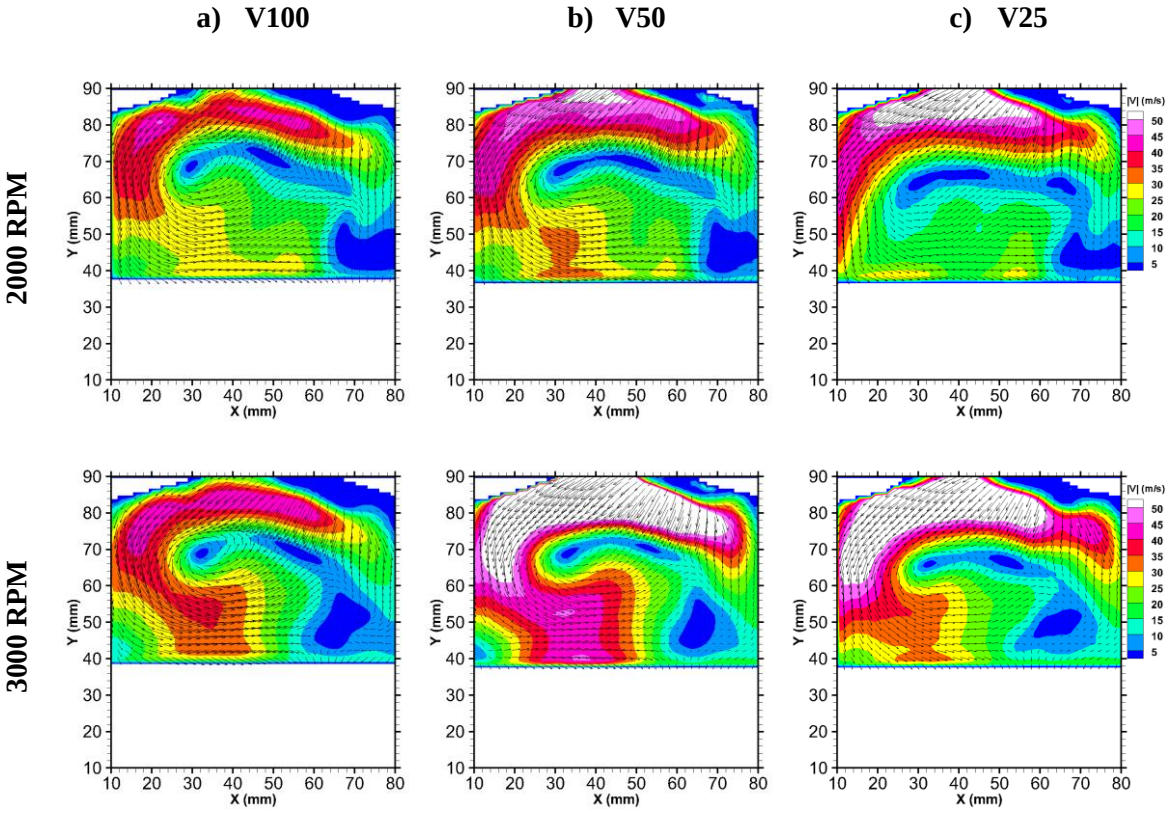

Figure 3-7 The effect of engine speed on in-cylinder flow at -274 CAD with respect to inlet flow condition

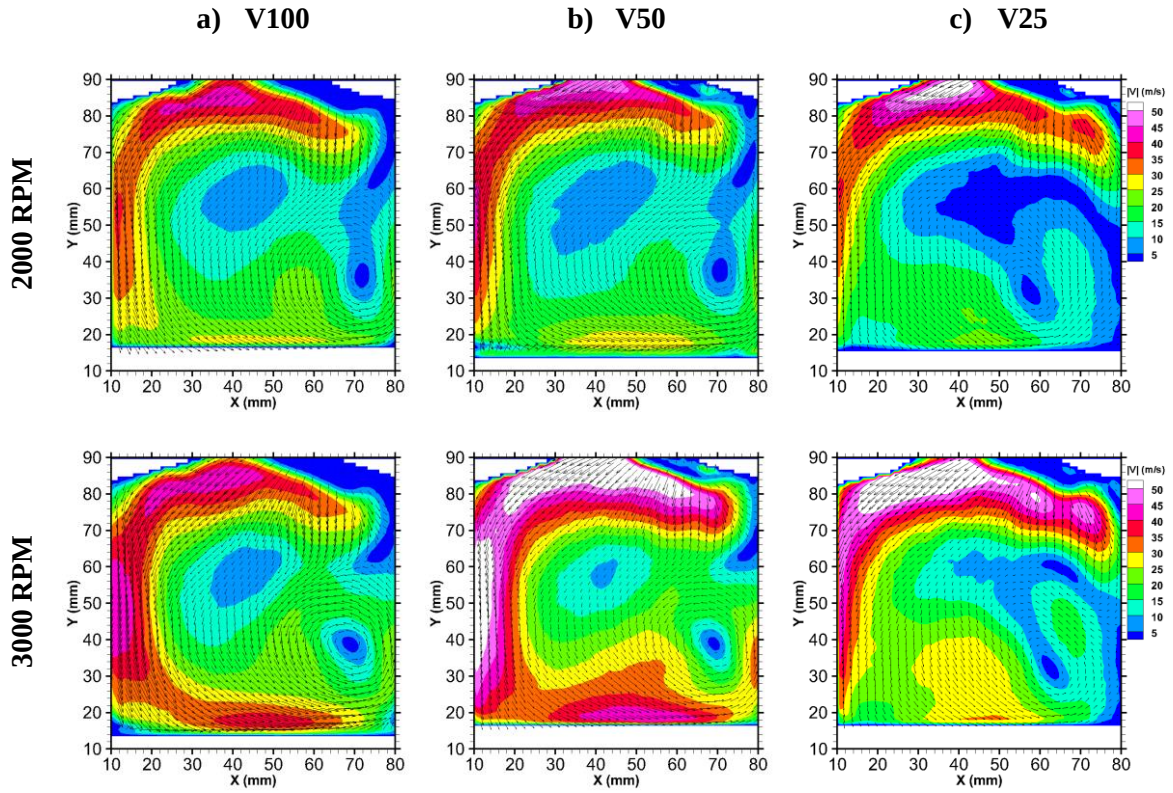

Figure 3-8 The effect of engine speed on in-cylinder flow at -226 CAD with respect to inlet flow condition

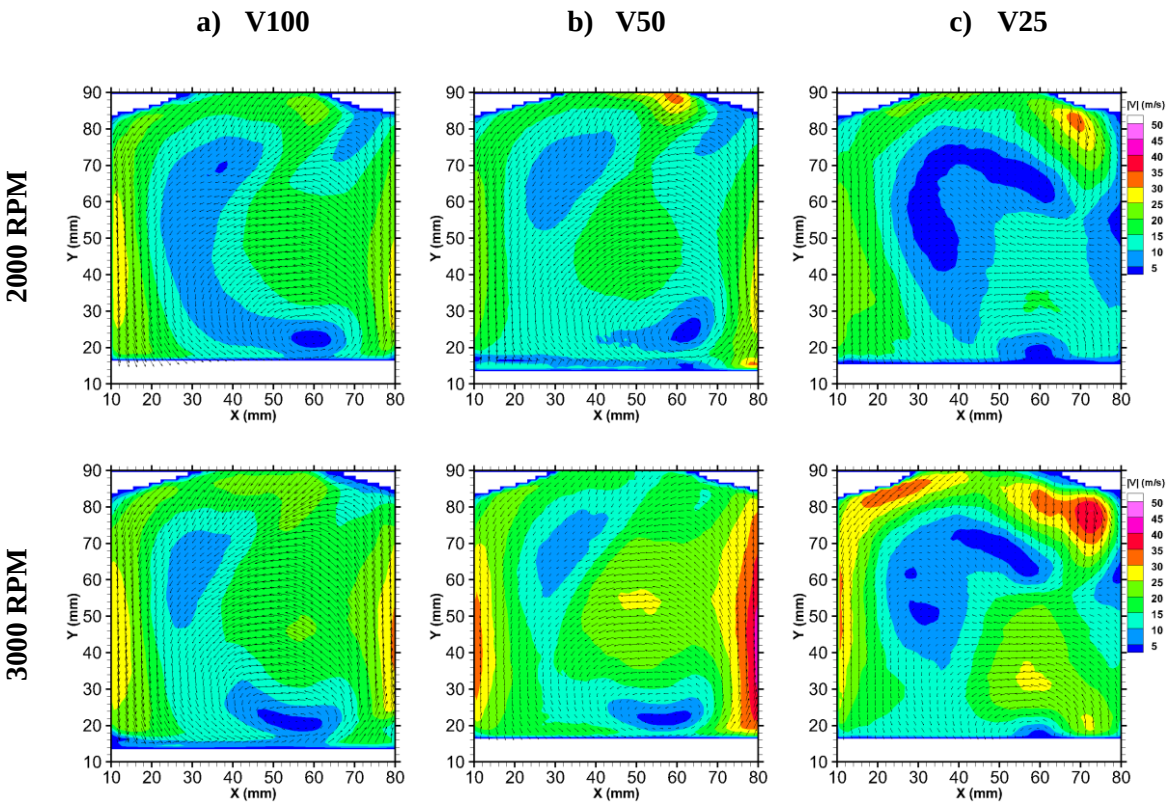

Figure 3-9 The effect of engine speed on in-cylinder flow at -178 CAD with respect to inlet flow condition

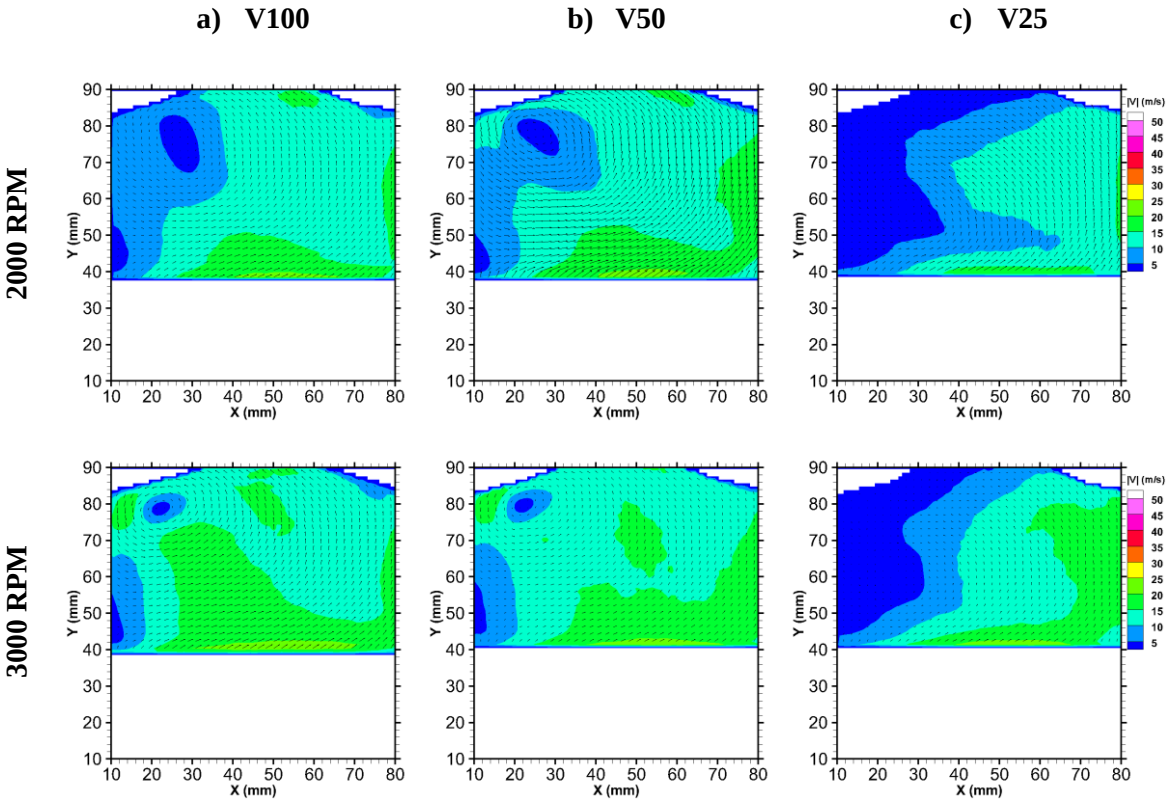

Figure 3-10 The effect of engine speed on in-cylinder flow at -82 CAD with respect to inlet flow condition

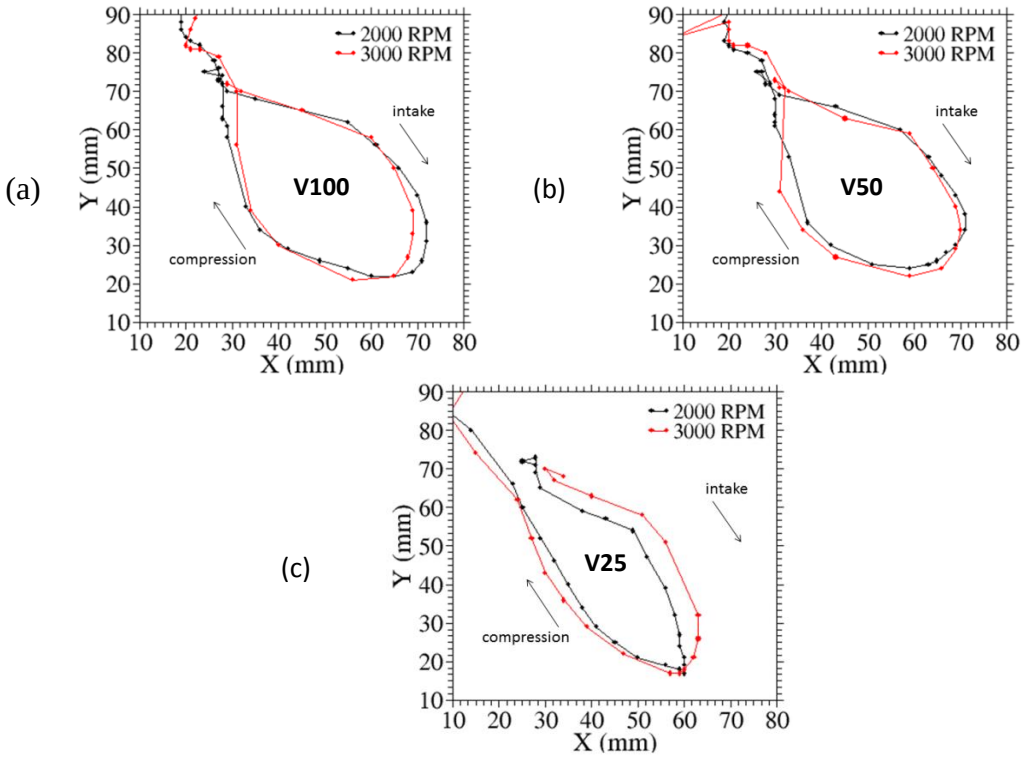

Figure 3-11 Mean tumble trajectory defined via Γ_{max} at 2000 and 3000 RPM for (a) V100, (b) V50 and (c) V25

3.2.2 2D ensemble averaged velocity fluctuations in tumble plane

Using the Reynold definition (3-4), velocity fluctuations of the mean flow at 3000 RPM are compared for the different CAD to fluctuations at 2000 RPM for V100, V50 and V25. Figure 3-12 then shows the increase during the intake stroke in velocity fluctuations, particularly in the upper part of the field of view, with respect to the decrease in inlet duct opening. Moreover, the inverse behaviour observed at 2000 RPM of velocity fluctuation with respect to the velocity magnitudes evolution Figure 3-5 is again observed at 3000 RPM where higher velocity fluctuations are observed during the compression stroke for V25 than V50 and V100.

Additionally, TKE is calculated to represent the global behaviour of velocity fluctuations fields, then an influence ratio IR is computed to quantify the level of influence of the engine operation speed in order to draw its correlation to engine intake such as:

$$IR_V = \frac{< \overline{TKE} >_{3000\,rpm}}{< \overline{TKE} >_{2000\,rpm}} \quad \textbf{(3-7)}$$

where V is the inlet flow condition V100, V50 and V25. The resulting ratios are compared with respect to inlet flow condition. Consequently, Figure 3-13 shows a more important increase in TKE, and therefore of velocity fluctuations, across the intake and compression strokes at 3000 RPM than at 2000 RPM. Additionally, at 3000 RPM, V50 reveals higher amplitudes than V25 between the beginning and the mid-intake stroke, i.e. before -226 CAD. A rapid decrease in TKE of V50 then follows starting at -226 CAD, remaining greater than TKE of V100 but considerably less than V25 during the compression stroke. This is better illustrated with the IR in Figure 3-14 showing that V50 and V25 undergo greater variations than V100 with the change in engine speed. Moreover, these variations are more important for V50 during intake while for V25 during the compression stroke.

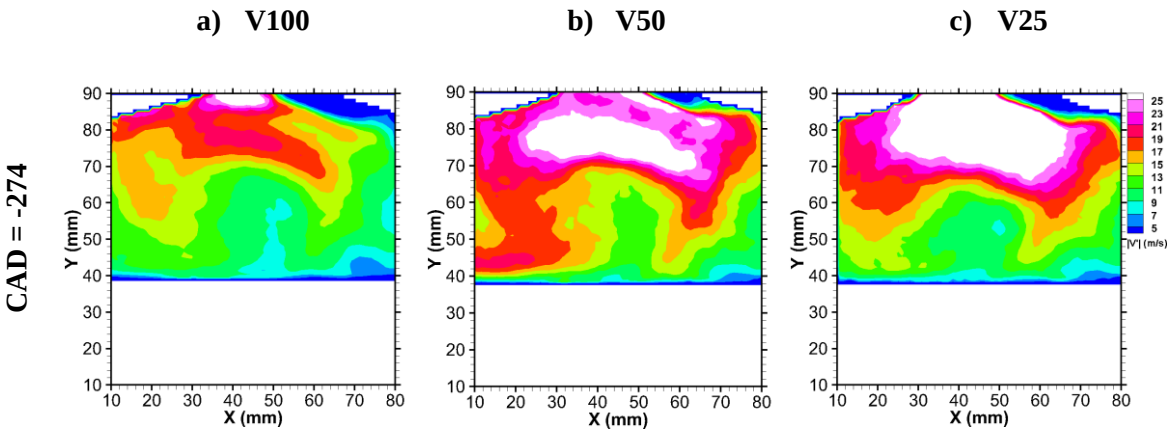

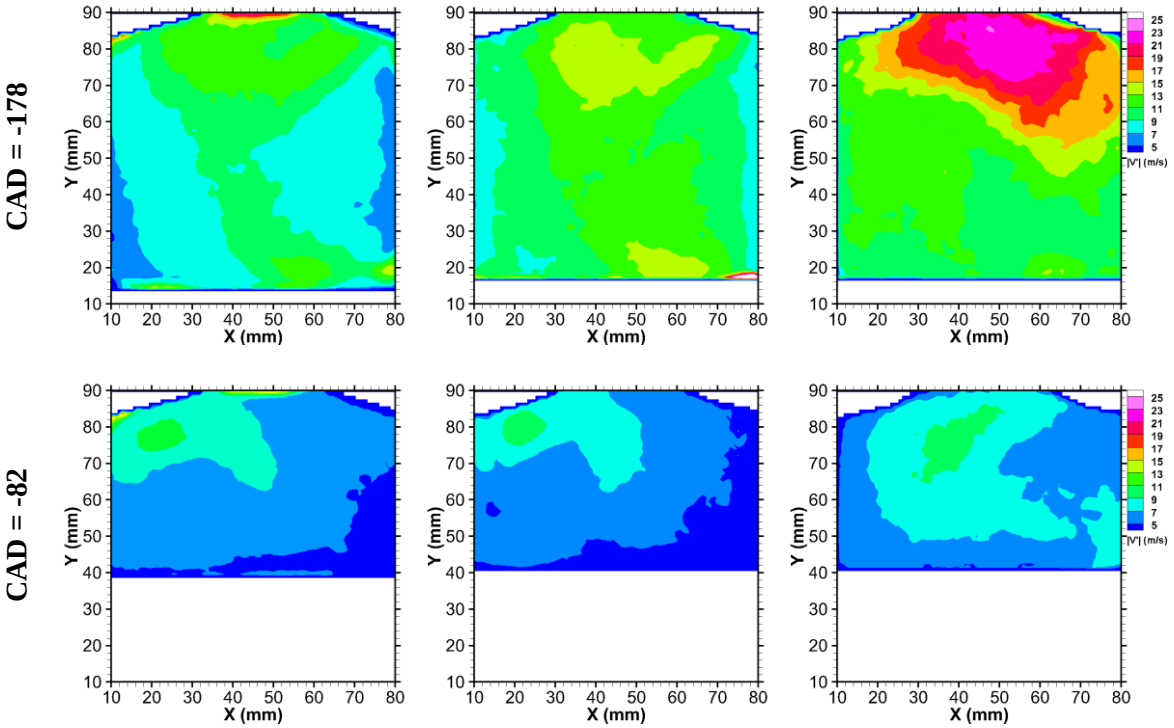

Figure 3-12 Velocity fluctuations at 3000 RPM for different CAD at (a) V100, (b) V50 and (c) V25

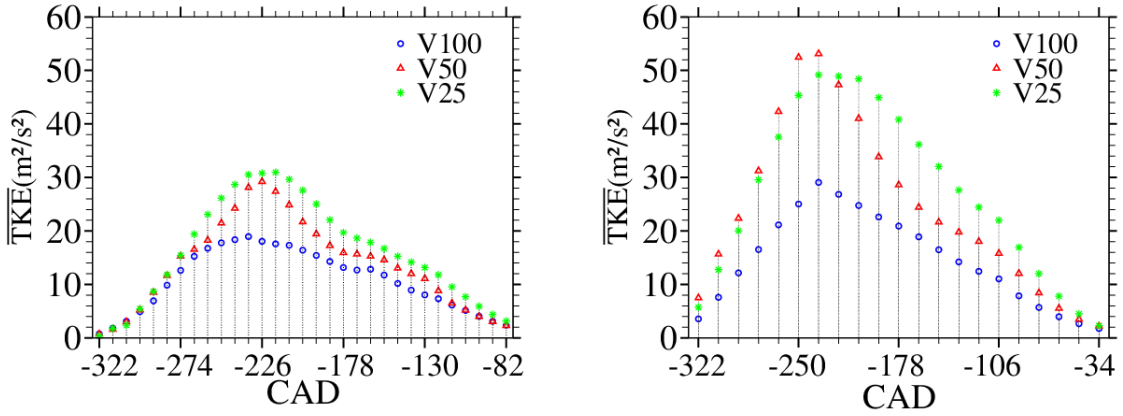

Figure 3-13 Temporal tracking of TKE of the mean engine cycle at (a) 2000 RPM (recording resolution = 8 CAD) and (b) 3000 RPM (recording resolution = 12 CAD) for V100, V50 and V25

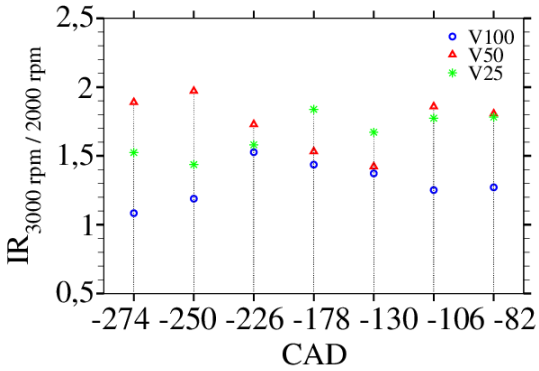

Figure 3-14 Influence ratio of engine speed with respect to inlet flow condition

3.3 Influence of engine parameters on instantaneous in-cylinder flow from TR-PIV

3.3.1 Cycle-to-cycle variations

In addition to a mean flow analysis, the strongly unsteady and turbulent nature of engine flows depicts as essential the study of the instantaneous engine flow. In fact, two consecutive engine cycles never reveal an identical in-cylinder flow. This motivates, for decades now, the search for the underlying chain of cause and effects of this non-repeatability (§1.1).

Traditionally, turbulence has been defined using the Reynolds decomposition as shown in equation (3-4) as the sum of a mean component $\bar{u}$ (time independent) and a fluctuating component u_i'. However, velocity fluctuations are not necessarily linked only to the random variations in space and time of the velocity fields during the engine cycle but can also include cycle-to-cycle fluctuations of the mean flow. Therefore, u_i' can be separated into two components of turbulence (u'_{cy}) and cycle-to-cycle variations (u'_{ccv}) so that the velocity decomposition is described in equation (3-8) as:

$$u_i = \bar{u} + u'_{ccv} + u'_{cy} \quad \textbf{(3-8)}$$

The identification of CCV can then be done with respect to the coherent structures cyclic positioning. The behaviour of coherent structures is hence of paramount importance for the fuel/air mixture and the combustion that will follow since they can contribute to up to 30% of the total turbulent kinetic energy inside the combustion chamber (Voisine et al, 2010).

In many flow configurations, the fluctuations in position of large scale coherent structures remains difficult to characterize. These instabilities influence the magnitude of the fluctuating velocity field obtained by a classical Reynolds decomposition. It is thus difficult and essential to dissociate their fluctuations from those associated with the chaotic character of a turbulent flow. One of the techniques regularly adopted is the filtering of temporal signals, which consists of stopping the spectrum of the velocity field at a certain cut-off frequency so as to leave, when returning to the real space, only the structures corresponding to a desired frequency range. However, the problem in this method lies in the choice of the cut-off frequency (Nobach, 2007) (Towers & Towers, 2008) (Jarvis et al., 2006) (Falchi & Romano, 2009) (Ölçmen, 2012). This ambiguity arises from the fact that in order to visualize the structures intended to explain a poorly known phenomenon, one should already know the characteristic frequency of this

phenomenon. This contradiction, often avoided by an empirical approach of filtering, weakens the reliability of the conclusions.

One of the means concerning the structural study of turbulence is the Proper Orthogonal Decomposition, POD (Lumley, 1967) (Holmes, 1997) (Sirovich, 1987). This method proved in a variety of flows to be adapted to the understanding of energy transfer phenomena between the different structures present. This has been particularly discussed for the engine's in-cylinder flow where POD proved to be advantageous for analysing CCV since it is designed to extract the most energetic structures from the turbulent flow making it ideal for the study of tumble breakdown (Fogleman, 2005) (Ölçmen, 2012) (Cosadia et al., 2007) (Cordier & Bergmann, 2006) (Chen, Reuss, & Sick, 2012) (Liu & Haworth, 2011) (Voisine et al., 2010). Hence in this chapter we suggest to use the POD with our experimental results for the extraction of coherent structures and the analysis of corresponding kinetic energy.

In the following, the working principle of POD is first presented. Then, results of a phase-dependant decomposition of the engine flow are discussed. This POD approach corresponds to the decomposition of a set of instantaneous fields belonging to the same engine phase. Even though this method has its limitations with respect to a phase-independent decomposition that takes into account all engine phases at once, it is retained in our study in order to compare results with the phase-locked 3D data.

3.3.2 Proper Orthogonal Decomposition

POD is essentially a linear procedure which consists in determining a basis of orthonormal modes representative by definition of the most likely occurrences. The key idea of POD is to reduce a great number of interdependent variables to a much smaller one of uncorrelated variables while keeping as much as possible of the fluctuations of the original variables. Compared to other techniques, the POD does not require an a priori knowledge of the flow and offers an optimised process from an energetic point of view detailed farther in this section.

Having a set of velocity fields $u_{i = 1 \text{ to } N}$, an orthonormal basis functions $\varphi_{i = 1 \text{ to } N}$ is determined such as:

$$u_i = \sum_{j=1}^{N} C_{ij}\varphi_j \qquad \textbf{(3-9)}$$

The basis functions, or modes, are determined by minimizing the expression:

$$\sum_{i=1}^{N} || u_i - \sum_{j=1}^{N} C_{ij}\varphi_j || \rightarrow min \quad \textbf{(3-10)}$$

while imposing orthogonality and thus maximizing the 'resemblance' on an energetic scale between the basis and the ensemble of velocity fields u. Each of the spatiotemporal coefficients C_{ij} is obtained by projecting u_i onto φ_j. Each velocity field u_i is referred to as a snapshot.

In fact, whereas the classical POD carries out a spatial cross-correlation of the data, the snapshot method performs a correlation of timely shifted data at the same spatial location (autocorrelation). This approach was proposed for the first time by (Sirovich, 1987) and has distinctive advantages in comparison to the classical POD in cases where the number of points in space (here velocity vectors) is significantly larger than the number of points in time (number of snapshots, here velocity fields).

The velocity field from the i^{th} engine cycle can be reconstructed by summing all the modes multiplied by their respective coefficient for that cycle using equation (3-8). Since φ_j is normalized and C_{ij} is the amplitude, the kinetic energy that the j^{th} mode contributes to the i^{th} velocity field is given by:

$$KE_j = \frac{1}{2} {C_{ij}}^2 \quad \textbf{(3-11)}$$

Then the total kinetic energy is the sum of KE_j over all the modes:

$$KE_{total} = \sum_{j=1}^{N} KE_j \quad \textbf{(3-12)}$$

Finally, for phase-dependent POD, u_i is a set of velocity fields obtained at a single crank angle from multiple cycles. The intent is to extract dominant structures at a particular engine phase. However, this method has its limitations. This decomposition gives rise to defined modes for each engine phase as if the flow at a given phase is independent from the others. Thus, evaluating the evolution of a mode's energy during the different phases of the flow amounts to comparing the energy of modes which do not come from the same decomposition.

It would be more relevant to trace the evolution of a mode coming from the same decomposition. This is known by phase-invariant POD. In this case, snapshots sampled at multiple crank angles and from multiple cycles are analysed (Di Mare et al, 2014). They provide a single set of modes that is representative of the flow dynamics over the full engine cycle (Semeraro et al, 2012). Although phase-invariant POD is advantageous, it

requires time-resolved measurements to properly converge. Since our 3D data are phase-locked and offer 250 velocity fields per phase, the present analysis will restrict in a first time to the use of phase-dependant POD for both 2D and 3D data in order to suit the comparison process. Coherent structures are identified at each considered CAD and their cycle-to-cycle variations are described with respect to instantaneous tumble centre location.

3.3.3 Identification of cycle-to-cycle variations from TR-PIV measurements

Snapshot POD is performed on the 300 instantaneous velocity fields obtained from TR-PIV measurements. The first POD modes, i.e. most energetic, are used to reconstruct velocity fields and separate coherent structures of the flow to quantify their cyclic variations. The number of retained POD modes is identified via a kinetic energy analysis. At each phase, POD is performed over 50 modes whose corresponding kinetic energy is presented in Figure 3-15.

As seen, the first POD mode referred to as mode-0 contains the greatest fraction of the kinetic energy exceeding 85% of KE_{total} in all cases. The topology of this mode-0 is very similar to the ensemble average velocity field (Figure 3-16) although not identical, and thus it constitutes an excellent estimate of the mean flow. Mode-0 also shows the dominant presence of the mean flow structures in all engine cycles.

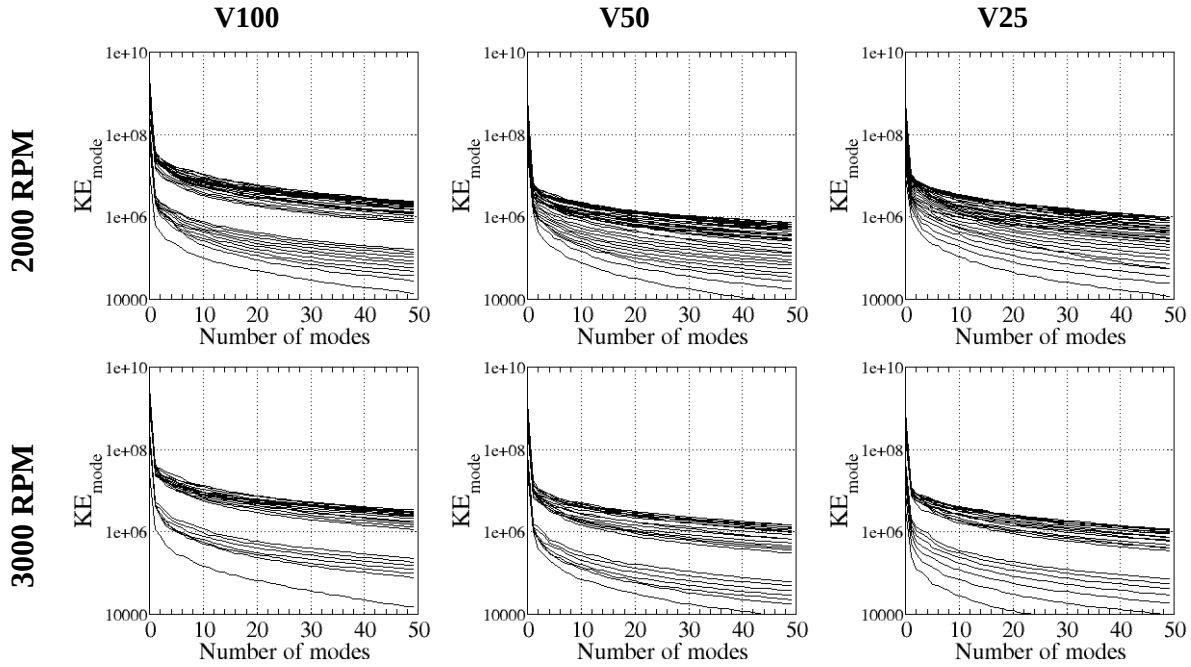

Figure 3-15 Kinetic energy per POD mode. In each plot, each curve corresponds to a CAD

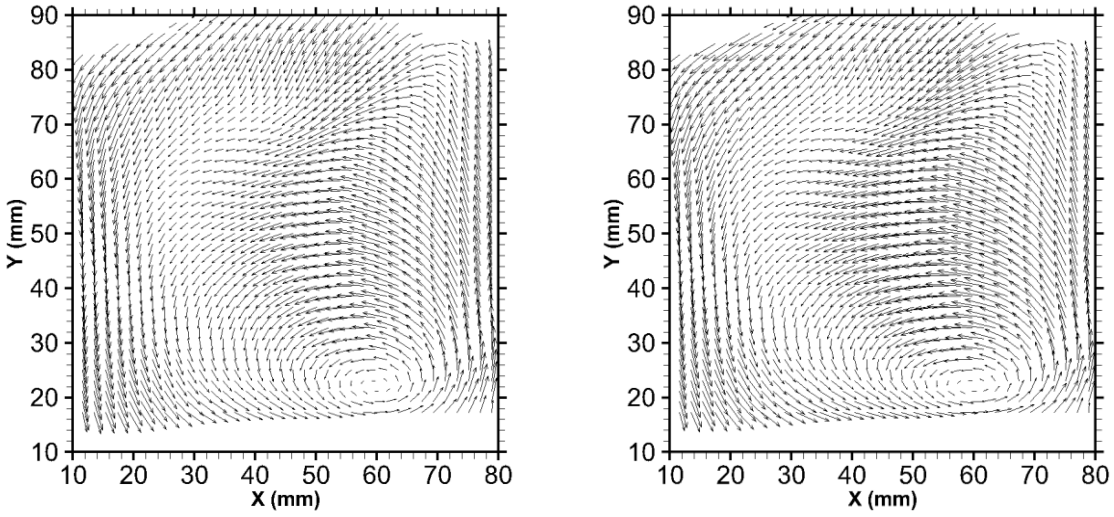

Figure 3-16 Example of (a) Mean velocity field at BDC (V100, 2000 RPM) and (b) POD mode-0 obtained at the corresponding CAD

Then in order to determine the number of POD modes needed to reconstruct the instantaneous coherent structures, the cumulative energy fraction of POD modes is plotted in Figure 3-17, where energy fraction if given by:

$$\frac{KE_j}{KE_{total}} \tag{3-13}$$

This shows again that mode-0 contains over 85% of the energy and that modes 0 to 4 contain over 95% of the energy. Therefore using the first 5 POD modes for the reconstruction of velocity fields appear to be suitable for the separation of coherent structures from the flow and the identification of their cyclic variabilities while conserving the greater part of the field's energy. An example of the obtained velocity field after reconstruction is shown in Figure 3-18.

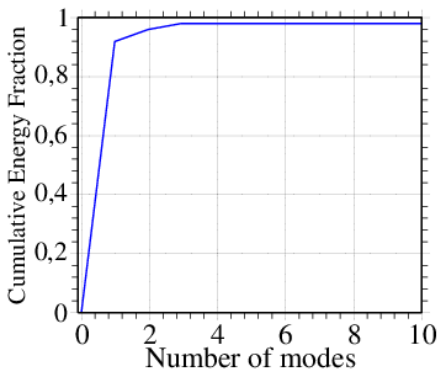

Figure 3-17 Cumulative energy of POD modes (example shown corresponds to POD at BDC)

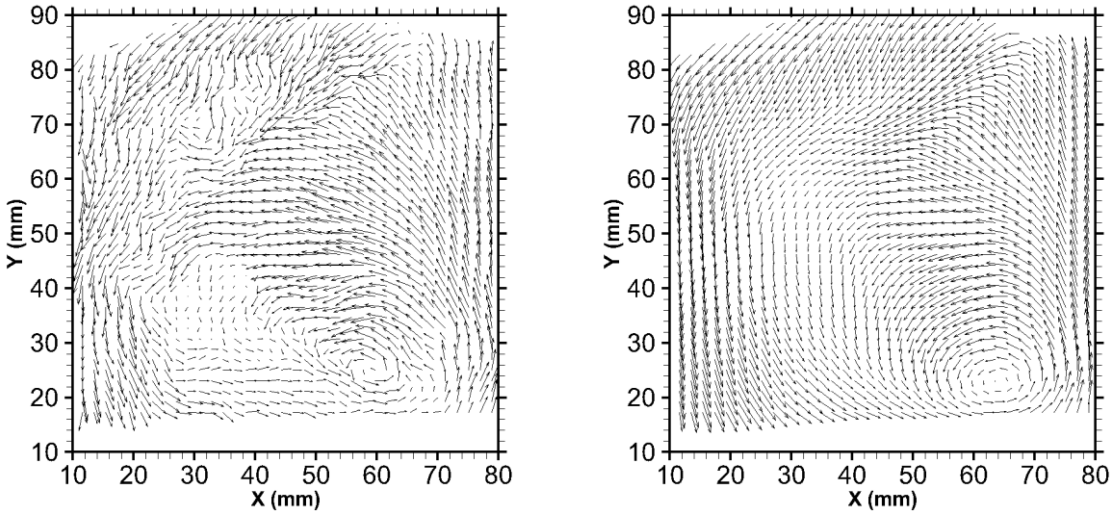

(a) (b)

Figure 3-18 (a) Instantaneous velocity field (snapshot) (b) Velocity field reconstructed via the 5 first POD modes

- **Flow configurations and CCV with respect to tumble position**

Having all filtered velocity fields at each CAD via the 5 POD modes, the location of instantaneous tumble centre is identified using the previously presented Γ criterion. Hence, the variations of tumble centre from cycle to cycle can be observed for each engine operation condition. Figure 3-19 then illustrates CCV of the studied engine operation conditions as well as their corresponding mean tumble trajectories. It is clear that in all cases, the greatest dispersions of tumble centre locations, particularly in y-direction, are observed during the compression stroke (Voisine et al., 2010) as is shown here particularly for -162, -138 and -122 CAD at 2000 RPM and for -178, -154 and -130 CAD for 3000 RPM. Moreover, the global differences between V50 CCV and V100 CCV as seen in Figure 3-19 are less significant than those observed between V50 and V25. The RMS of X and Y coordinates are then computed in order to better compare CCV of tumble centre location for the different operation conditions and are shown for the three inlet flow cases at 2000 and 3000 RPM in Figure 3-20 and Figure 3-21 respectively. In all cases, V25 seems to globally exhibit the largest fluctuations particularly during early intake and late compression strokes. This leads to a first conclusion that a reduced inlet flow is a source of excessive cycle to cycle fluctuations across the engine phases. Meanwhile, V50 reveals the lowest fluctuations at 2000 RPM in both x and y-directions during intake. Moreover, the evolution of V50 fluctuations presents a similar behaviour to V100 in X and Y-directions at both 2000 and 3000 RPM with slightly higher fluctuations observed at the beginning of compression. Overall, the alterations of tumble centre location are the greatest during intake in X-direction and during compression in Y-direction. This can be

explained by the inlet jets driving the flow sideways during intake and the piston pushing the flow upwards during compression. The differences in magnitudes are mainly related to the present TKE of the fields as previously seen.

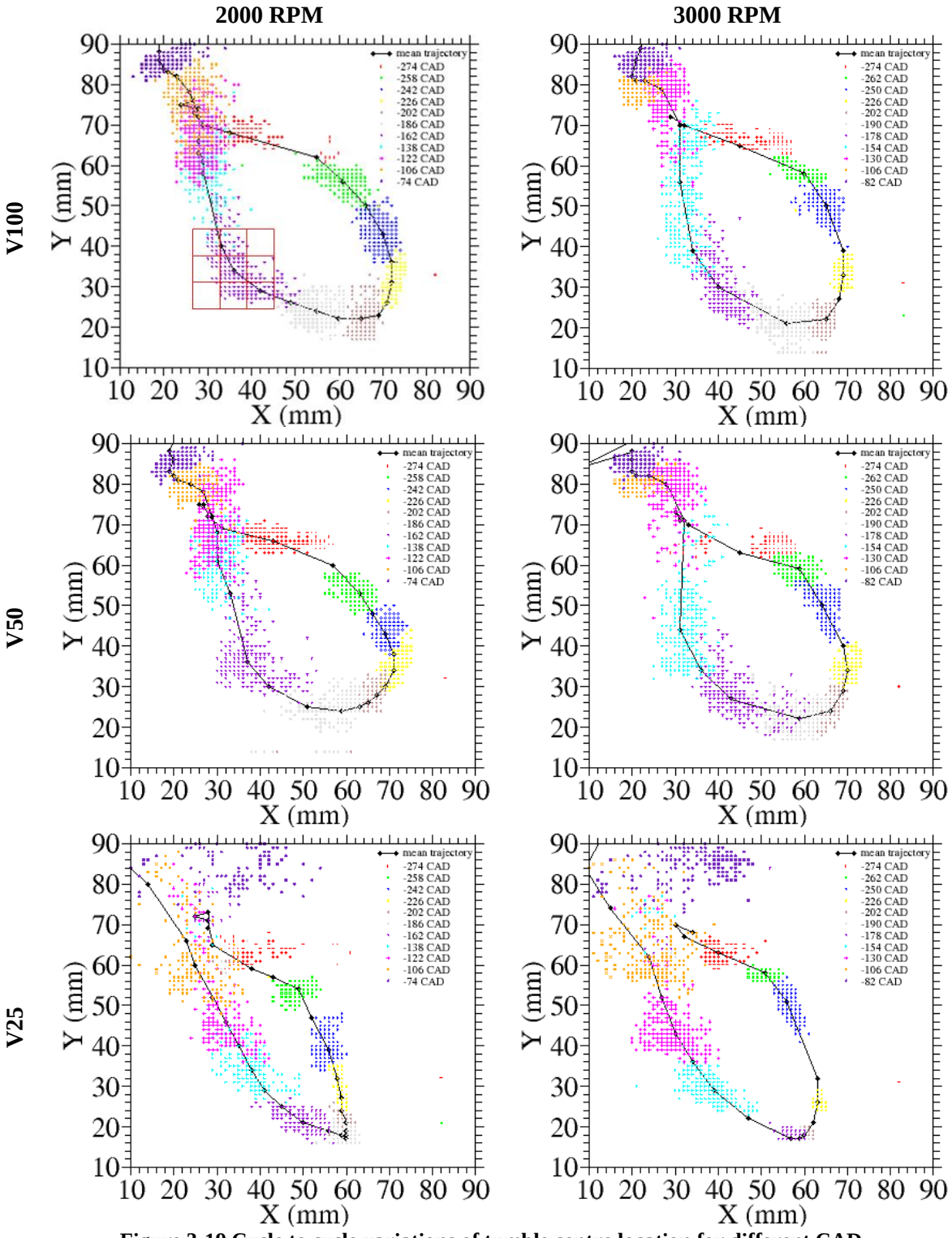

Figure 3-19 Cycle to cycle variations of tumble centre location for different CAD

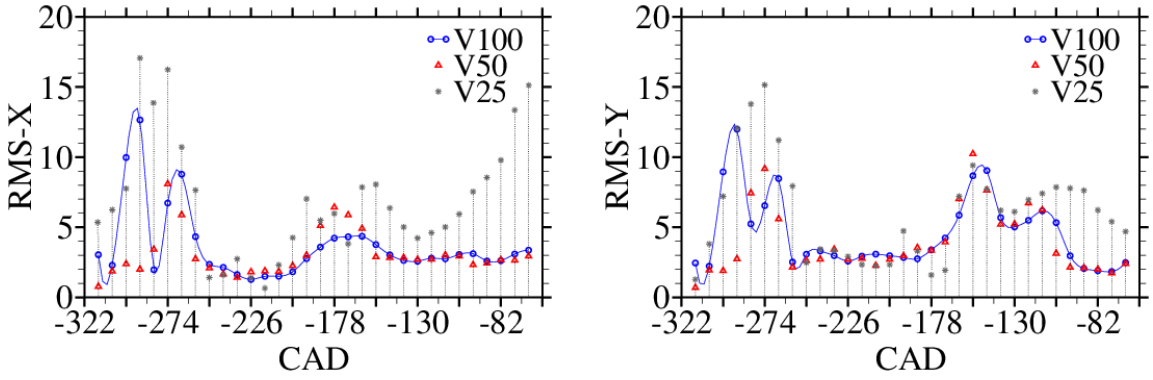

Figure 3-20 RMS of X and Y positions of tumble centre at 2000 RPM

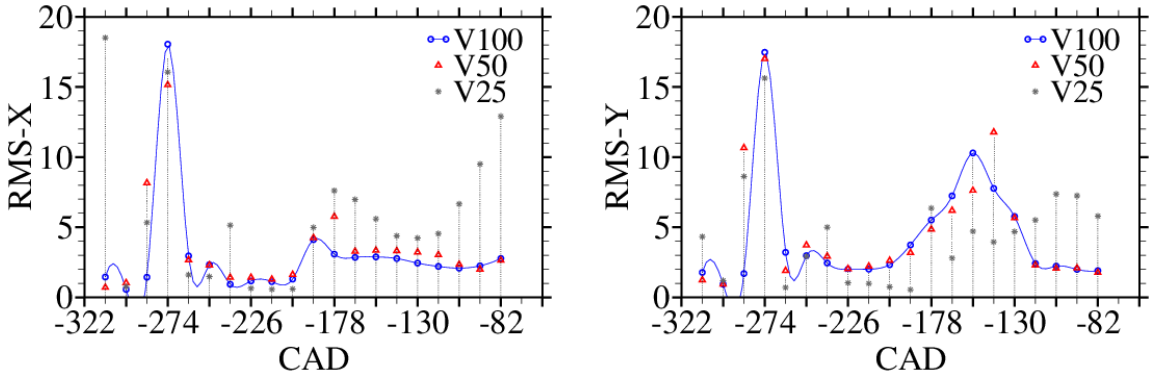

Figure 3-21 RMS of X and Y positions of tumble centre at 3000 RPM

Finally, in order to study the influence of the spatial cyclic variations of tumble centre on the instantaneous velocity fluctuations (u',v'), a classification of velocity fields was done with respect to the tumble position. For this purpose, 9 areas of 4×4 mm² centred around the mean tumble position were defined as is shown on the first plot in Figure 3-19. Corresponding instantaneous velocity fields were then sorted in each zone with respect to the tumble centre position (x,y). Hereafter, this approach is shown and interpreted for an engine operation at V100 and 2000 RPM considering the flow at -250 CAD where larger fluctuations of tumble position are commonly found.

Figure 3-22(a) first shows the mean velocity field **u** of a category of fields referred to as group 5 whose mean tumble centre is marked with a red x. The mean tumble position of the 8 remaining categories are represented with a black x, noting that the 9 mean fields reveal similar global structures. Then the fluctuation between the 9 mean fields of the different groups is computed and shown in Figure 3-22(b) revealing the main zone of variations between the categories which is in the region of the tumble centre positions correspondingly to our classification criterion. Moreover, ensemble average velocity fluctuations of each category of fields is computed and the example of group 5 is shown in Figure 3-23. Then a mean fluctuating field is computed from the 9 obtained fluctuations

fields and is shown in Figure 3-24(a). The aim of this illustration is then to insulate the contribution of spatial variations of tumble position to the global velocity fluctuations. Therefore, the ensemble average fluctuations computed over the 300 instantaneous velocity fields are shown in Figure 3-24(b).

As a result, the fluctuations observed in the tumble region of the ensemble averaged field significantly decrease of approximately 30% in magnitude. This shows that the main cause of higher fluctuations in these regions is the positional variations of the tumble that were now removed in Figure 3-24(a). Additionally, since the cyclic variations of tumble can be linked to a variation in position as well as to a variation in intensity or size of the structure, it can be deduced that the effect of tumble position outweighs the effect of its intensity that seems to undergo less significant cyclic variations at a considered engine phase. By applying this type of classification approach, or other more elaborated techniques (Voisine et al., 2010), to the ensemble of engine phases, a cyclic evolution of the tumble positions' contribution to the total kinetic energy can thus be obtained offering a more realistic estimation of the RMS (or TKE) of each individual engine cycle. This contribution is then expected to be more significant during the compression stroke where the greatest RMS of tumble positions were observed.

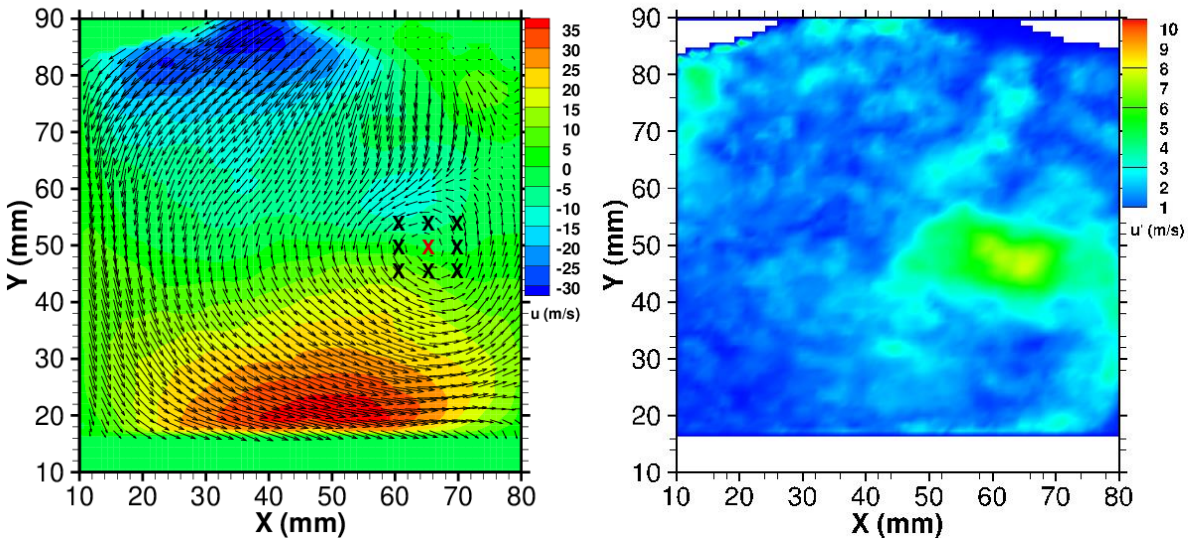

(a) (b)

Figure 3-22 (a) Example of ensemble average velocity u from group 5. The 9 marks show the mean tumble position for each of the 9 categories (b) Velocity fluctuations obtained from mean categories

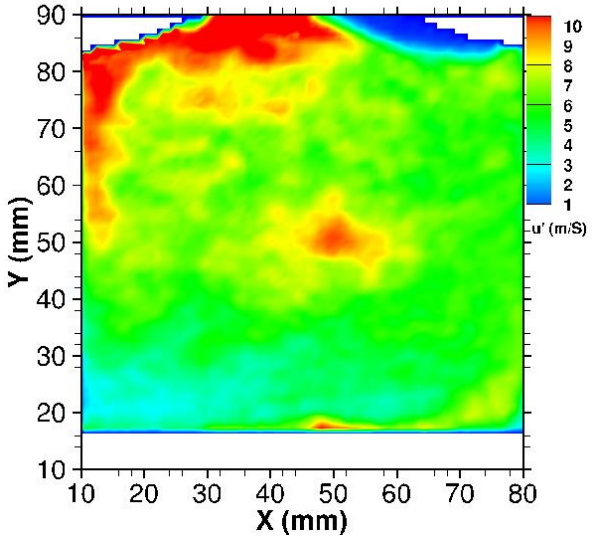

Figure 3-23 Example of ensemble average velocity fluctuations u' from group 5.

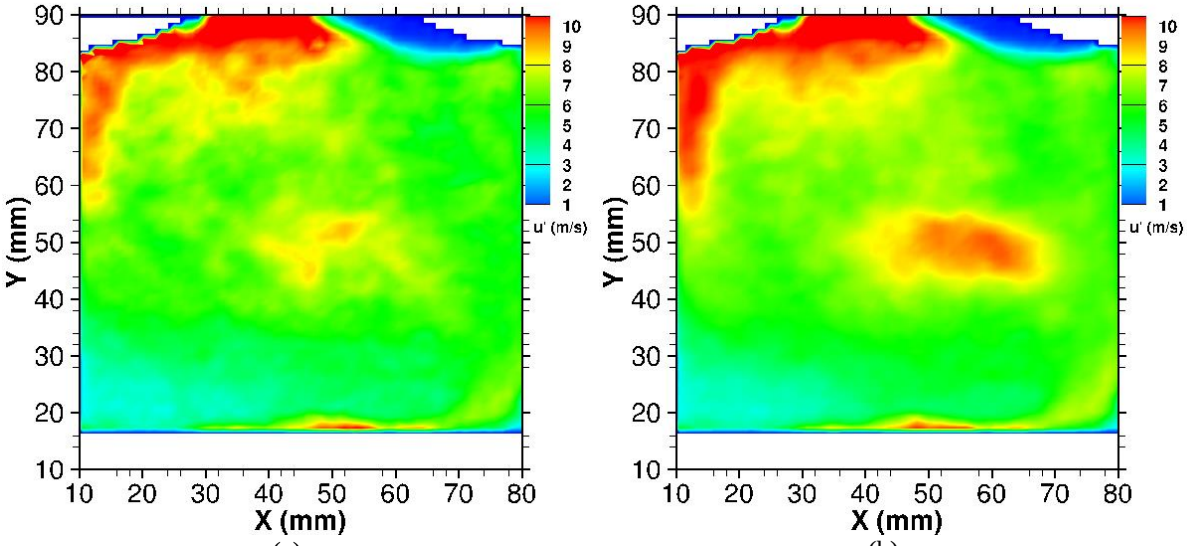

(a) (b)

Figure 3-24 (a) Ensemble average velocity fluctuation u' at -250 CAD (b) Velocity fluctuations obtained from the average fluctuations of categories

In conclusion, it was seen in a first step that identifying the positional variations of coherent structures of the in-cylinder flow is essential to quantify their contribution to the total of velocity fluctuations obtained by a classical Reynolds decomposition. This information has been previously reported in literature but is still however limited to the mid-cylinder plane and does not allow an extended analysis of the three-dimensional nature of the flow. Therefore, in a second step, the three-dimensional analysis that Tomo-PIV measurements allowed is presented in the following paragraph and an extended description of the volumetric velocity field is discussed.

3.4 3D analysis of in-cylinder aerodynamics from Tomo-PIV measurements

As seen so far, a temporal tracking of the flow in the mid-cylinder plane and a conditional analysis of flow fluctuations allowed quantifying the contribution of cyclic variations to global fluctuations for different engine operation conditions. In order to further visualise the flow in its three-dimensional nature, our experimental study was pursued by 3D tomographic measurements as described in §2.2. Recording campaigns for the 3 intake flows at 2000 and 3000 RPM were performed at 7 engine phases, CAD = {-274, -250, -226, -178, -130, -106, -82}, corresponding to TR-PIV measurements in order to show the contribution brought by 3D measurements with respect to planar measurements. Results observed in the mid-cylinder plane are found equivalent to 2D measurements and are relayed in Annexe 3. Hereafter, volumetric velocity fields are described and analysed to further characterize the in-cylinder aerodynamics.

3.4.1 Ensemble averaged 3D flow fields

Considering the three inlet flow conditions, 3D ensemble average velocity fields are shown during intake, near BDC and during compression in Figure 3-25, Figure 3-26 and Figure 3-27 respectively, for an engine speed of 2000 RPM and 3000 RPM. Velocity vectors represent the 3D velocity (**u, v, w**) and discrete levels of velocity magnitudes are displayed for each CAD by 3D iso-surfaces. For all operation conditions, the flow can be globally characterised by high velocity magnitudes in the lower regions of the field of view during the intake stroke, i.e. in the regions near the piston head as it travels towards the BDC. As the inlet charge motion stops with the closing of intake valves, the in-cylinder flow meets the abrupt motion of the piston in an upward direction thus slowing the flow field across the compression stroke and pushing the tumble structure and lower velocity regions towards the exhaust valves. Although these characteristics apply to the general in-cylinder engine flow, the order of velocity magnitudes and velocity distribution within the fields at a fixed CAD highly depends on the intake flow condition as well as the engine speed, as was also described for the 2D measurements (see Annexe 2 for an illustration of all phase-averaged Tomo-PIV measurements).

During the intake stroke in particular, shown at -250 CAD in Figure 3-25, iso-surfaces parallel to the flow direction show the precipitation of the front intake jet towards the left cylinder wall and its recirculation in an upward direction above the piston head at high speed. The upper right corners of images reveal the tumble motion complemented by the 3D iso-surfaces showing its three-dimensional shape and how it varies in position and magnitude with respect to engine speed and inlet conditions.

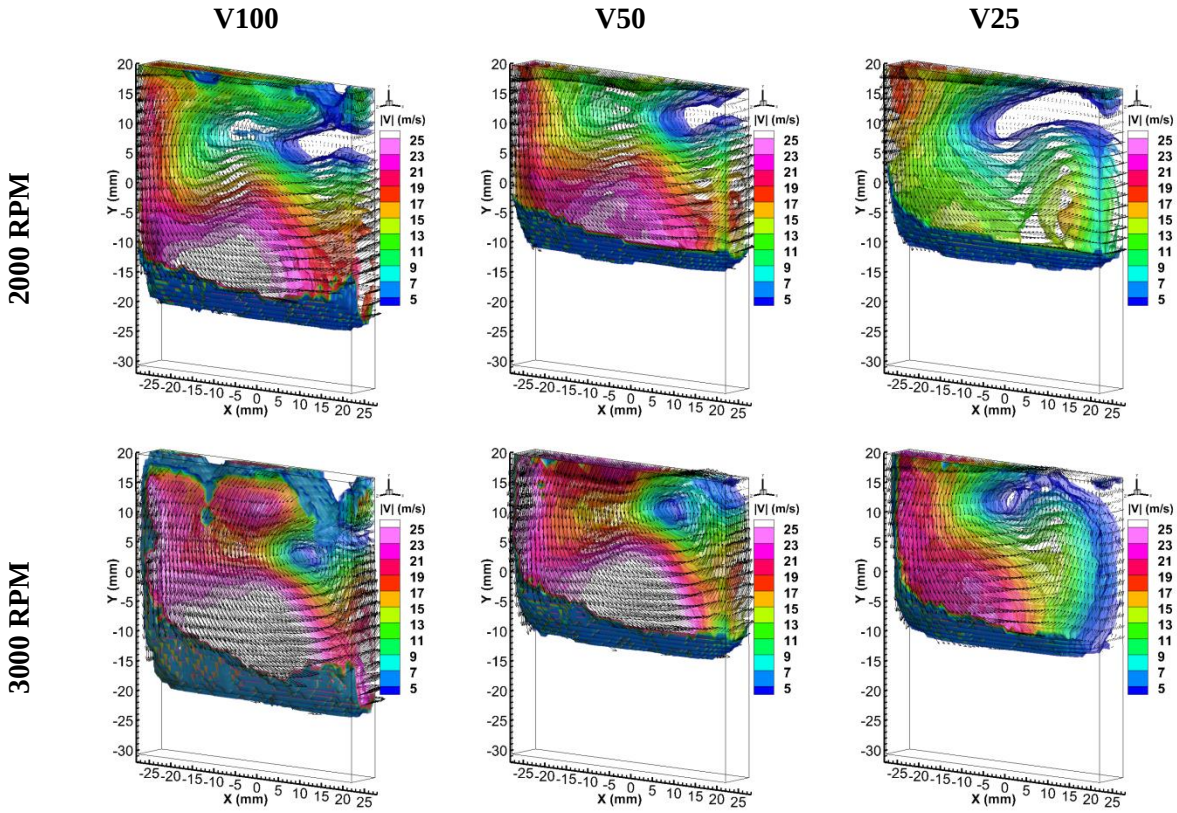

Figure 3-25 Volumetric Ensemble average velocity fields at -250 CAD at 2000 and 3000 RPM from Tomo-PIV

Just after BDC, at -178 CAD, shown in Figure 3-26, the phase averaged flow field is no longer characterized by large velocities of an inlet jet, but exhibits smaller velocities due to the braked piston movement and near closing of the intake valves. Moreover, with respect to the intake duct opening, V25 reveals the smallest velocity magnitudes in the field of view while during intake it revealed the largest magnitudes. The tumble centre at this CAD is located at the bottom right of the imaged volume. The direction of tumble core can be observed differently across the volume's Z-dimension. However, a portion of the tumble structure is not visible within the field of view for V25. This is the case for several CAD (Annexe 2).

As the compression stroke progresses, 3D velocity iso-surfaces and velocity magnitudes, at 2000 RPM or 3000 RPM, remain at a similar magnitudes level throughout the stroke. Figure 3-27 shows in particular the phase average velocity field at mid compression stroke revealing velocity magnitudes close to what was observed at the beginning of compression. Moreover, the three-dimensional fields during compression reveal less significant 3D structure alterations compared to what is observed for the ensemble average flow fields during intake.

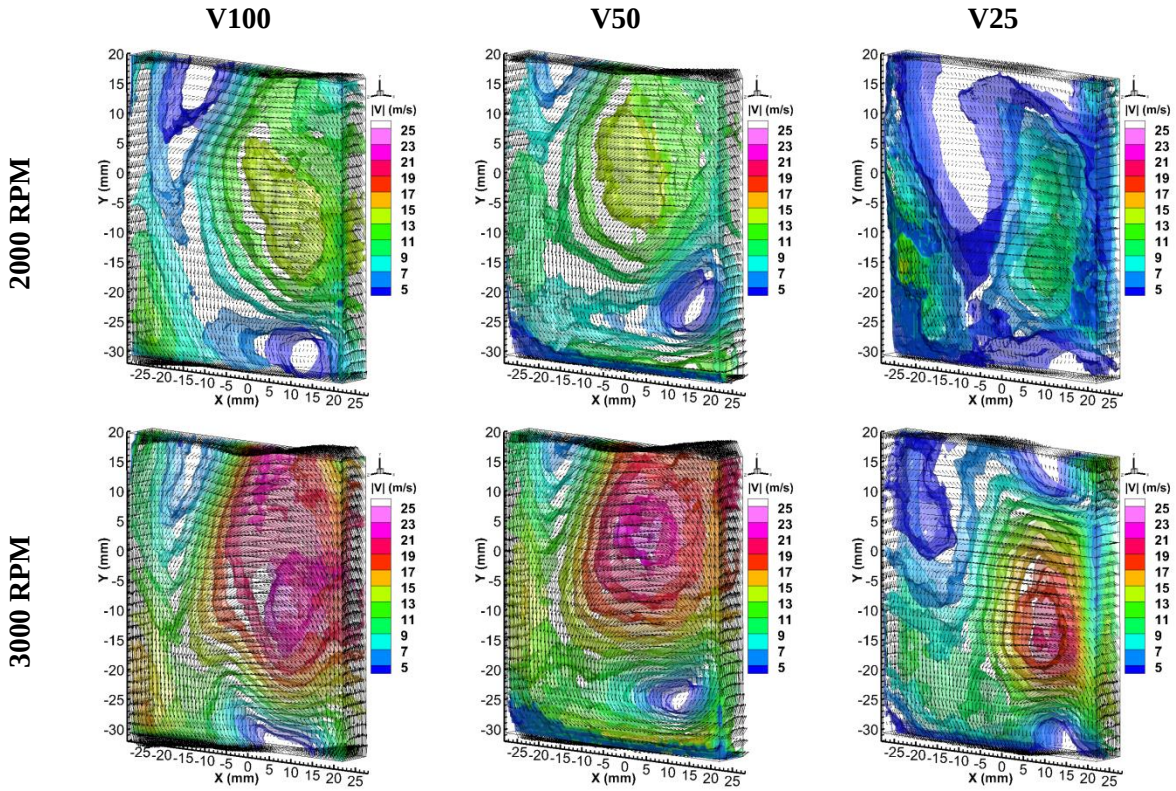

Figure 3-26 Volumetric Ensemble average velocity fields at -178 CAD at 2000 and 3000 RPM from Tomo-PIV

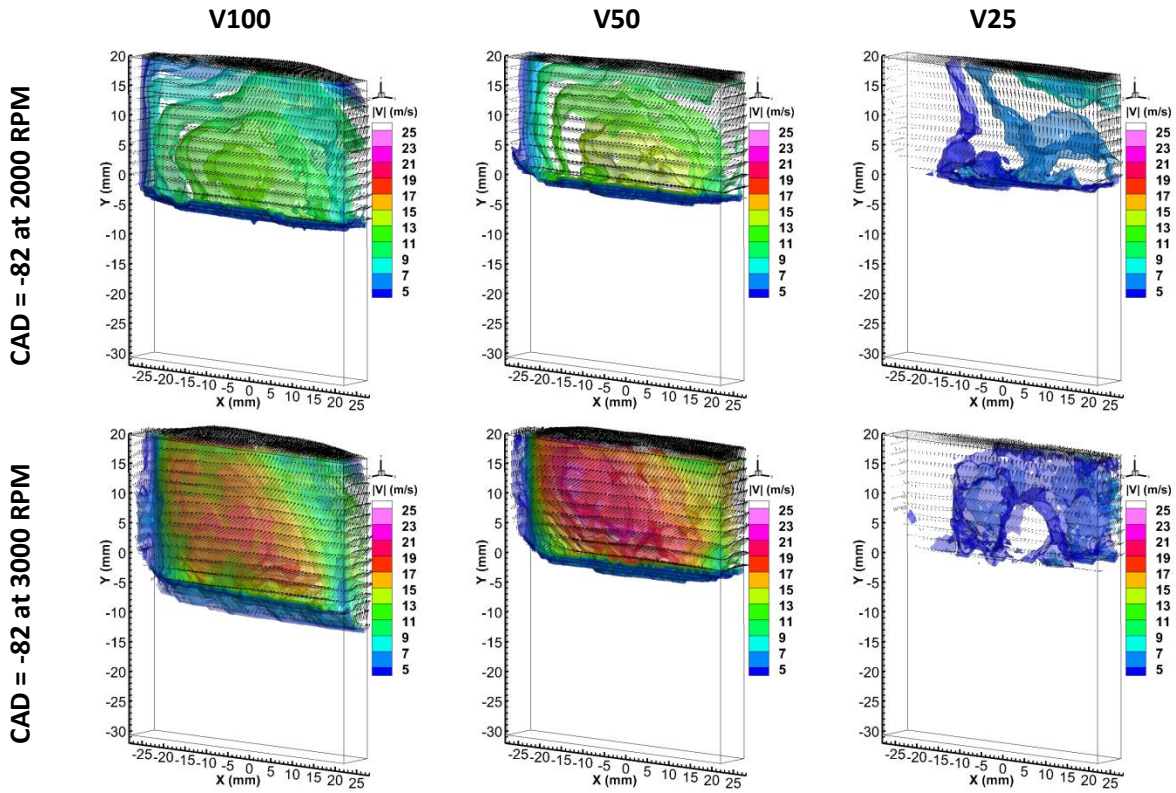

Figure 3-27 Volumetric Ensemble average velocity fields at -82 CAD at 2000 and 3000 RPM from Tomo-PIV

3.4.2 Ensemble average velocity fluctuations and turbulent kinetic energy

From the Reynolds decomposition, defined in equation (3-4), ensemble average velocity fluctuation fields are computed for the different engine operation conditions. In the following, velocity fluctuation fields are shown for the reference case of V100 intake condition at 2000 RPM. During the intake stroke, shown at -250 CAD in Figure 3-28 (a), fluctuations across the measurement field reveal the highest magnitudes compared to the rest of the other phases of the engine cycle, particularly in the upper regions that are nearer to the engine valves. At -178, shown in Figure 3-28 (b), fluctuation magnitudes are the largest at the right side of the field, particularly in the tumble zone at the bottom. They decrease gradually while moving to the left of the field. At that phase, the inlet valves are still open and the intake flow meeting the piston head and the cylinder walls is recirculated in an upward motion. Until this phase, iso-surfaces of velocity fluctuations reveal clear 3D alterations of magnitudes. During the compression stroke, shown at -82 CAD in Figure 3-28 (c), velocity fluctuations remain under 5 m/s and reveal less significant alterations in Z-direction compared to the preceding engine phases.

Moreover, profiles of velocity fluctuations u', v' and w', at -250 CAD, are first extracted across Z-dimension at the middle of the field of view (X=0 mm) for different positions along Y-direction and are shown in Figure 3-29. In the top region of the field (profile extracted at Y=15 mm), v' component reveals the largest magnitudes compared to u' and w' in that region. This is explained by the intake flow's dominant downward motion in the area under the intake valves as well as the occurring inter-jet interactions. Additionally, the alterations of v' magnitudes are more important in the front of the investigation volume (Z>0) where v' decreases approximately 25% with respect to its value in the mid-cylinder plane, while it deceases around 15% in the rear investigation volume (Z<0). With respect to w' component, the fluctuation profiles distinctively shows a steep decrease in magnitudes at the borders' planes corresponding to the borders of the laser sheet. This decrease can be attributed to the propagation of computational errors and lower measurement precision in these planes. Finally, considerable differences in flow dynamics can be noted within the same field during intake with greater 3D alterations as well as greater magnitudes seen in the top region of the field than in the lower regions (profile extracted at Y = -5 mm). This in-field difference is however less considerable farther in the engine cycle.

Figure 3-30 then shows u', v', w' profiles during different engine phases revealing the decrease in magnitudes of velocity fluctuations as we move from the intake stroke towards BDC and the compression stroke as well as smaller alterations of the profiles.

This is also illustrated by the corresponding TKE profiles across the investigation volume. Particularly during intake, the combined effect of greater magnitudes of v' in the top of the field and its dissymmetric variations with respect to the mid-cylinder plane is reflected in the TKE profile (Figure 3-30 (a)) revealing a clear dominance of the contribution of v' to the TKE in the region near the intake valves.

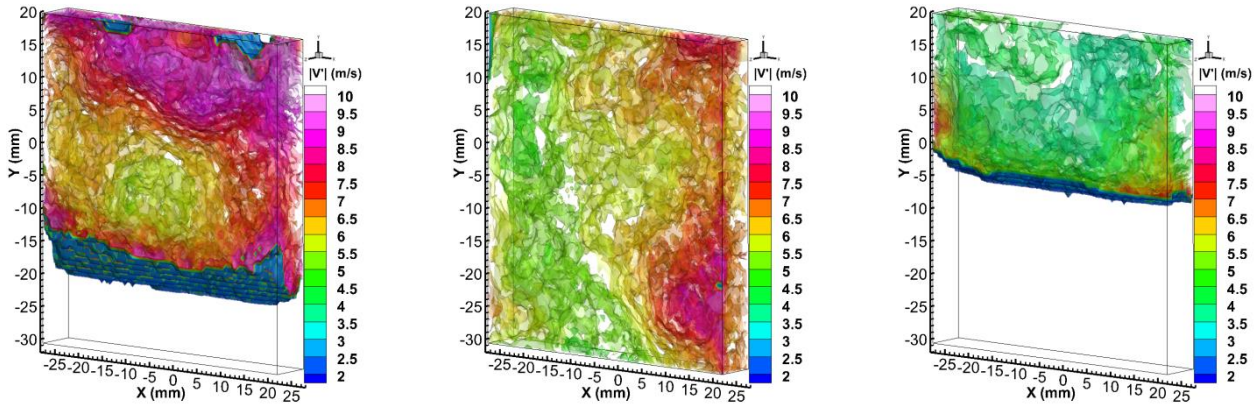

(a) (b) (c)

Figure 3-28 Ensemble average velocity fluctuations from tomo-PIV at V100 and 2000 RPM at (a) -250 CAD (b) -178 CAD (c) -82 CAD

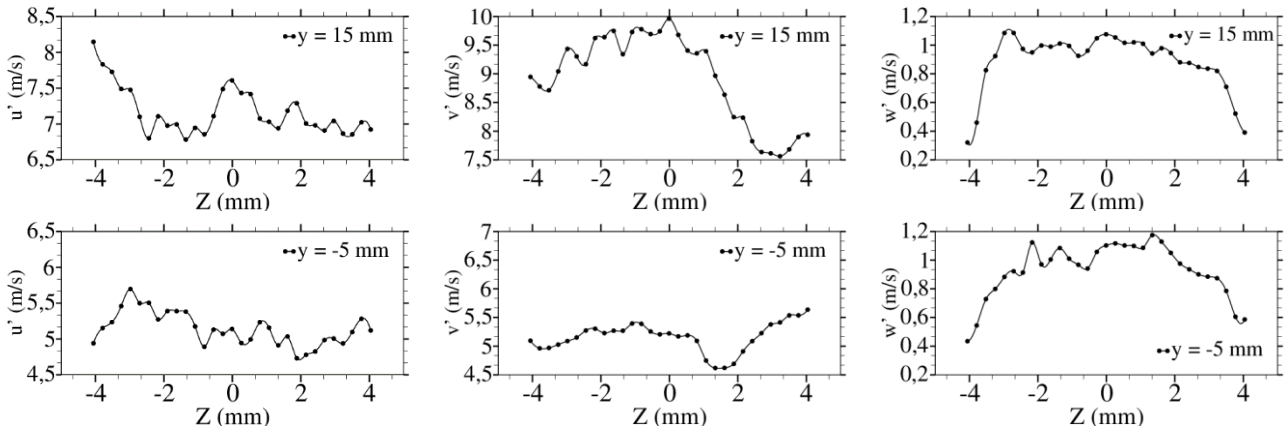

(a) (b) (c)

Figure 3-29 Velocity fluctuation profiles at 250 CAD near the top of the field of view (Y=15 mm) and near the bottom of the field (Y = -5 mm) at X = 0 mm

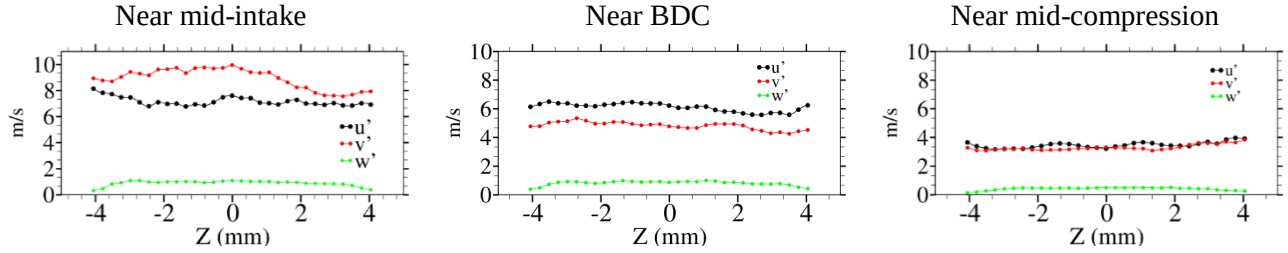

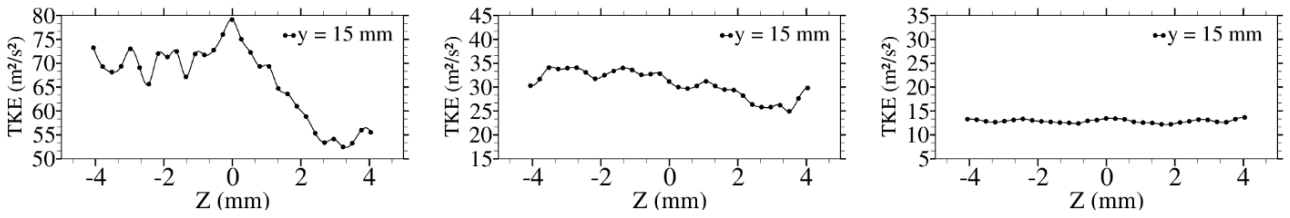

Figure 3-30 Velocity fluctuation profiles along Z-direction at X=0 mm, Y=15 mm and corresponding TKE profiles for (a) -250 CAD (b) -178 CAD (c) -82 CAD

3.4.3 Characterisation of the three-dimensional instantaneous flow by POD

In this section, an analysis of the large scale tumble structure and its positional fluctuations revealed by 3D Tomo-PIV results is proposed. Based on the POD of the volumetric fields and the determination of 3D Γ criterion, cyclic variations of the tumble structure are described regarding the 3D location of tumble cores. Moreover, a conditional approach of in-cylinder flow characteristics is suggested based on the energetic contribution of POD modes coefficients.

In the literature, POD has been applied to reconstruct the 3D mean velocity field. This approach relied on fields obtained in parallel PIV planes or orthogonal planes of the in-cylinder engine flow to calculate mean coefficients of the first POD modes and eventually interpolate and extrapolate these coefficients (Druault & Chaillou, 2007). However, the discontinuity of the planar PIV domains brings uncertainties that can propagate along the reconstruction procedure. With the possibility to obtain the third velocity component from Tomo-PIV measurements, POD can now be directly applied for the characterisation of the in-cylinder flow by separating the different scales of structures and classifying the flow motions with respect to the coefficients of POD modes (§3.3.2).

3.4.3.1 Cycle-to-cycle variations of 3D tumble structure

In a first step a volumetric description of cycle-to-cycle variations of the in-cylinder flow is presented. Instantaneous velocity fields are reconstructed via POD (§3.3.2). The number of POD modes chosen for the volumetric reconstruction is fixed, similarly to 2D measurements, after an analysis of the POD modes cumulative kinetic energy revealing again over 90% of the total kinetic energy in the first 5 POD modes. An example of a 3D vector field at -178 CAD is represented in Figure 3-31 (a) before and (b) after reconstruction via 5 POD modes. One every three vectors is shown.

Having isolated the tumble structures, the tumble core can then be determined in the volumetric domain. For this purpose, the Γ criterion (§3.1.2) is adapted for three-dimensional computations by defining a 7×7×3 investigation volumes and extracting the

location of tumble centre with respect to in-volume depth ($X_c(z)$, $Y_c(z)$). The regions of Γ_{max} allow thus identifying a vortex core describing the tumble's 3D shape and therefore adding information to what could have been identified in 2D.

In order to illustrate results of the Γ criterion, the tumble core is first shown for the mean velocity fields at 2000 RPM for V100 and V50 and at 3000 RPM for V50, in Figure 3-32, Figure 3-33 and Figure 3-34 respectively. Both volumetric and in-plane (XZ) and (YZ) representations are shown for each case. In the volumetric domains, iso-contours represent the regions of Γ_{max} that seem to have a similar extent in diameter for the 3 considered fields implying a close size of tumble core for the different engine operation conditions. With respect to position along Y-direction, the tumble core is the highest in the field of view for the case V50 at 2000 RPM and is the lowest for V100 at 2000 RPM which is in agreement with observations made at -178 CAD in the mid-cylinder plane via 2D measurements (Figure 3-4). For V50 at 3000 RPM, the tumble core is close in position to V50 at 2000 RPM which is in agreement with observations made in Figure 3-11 from 2D measurements. Additionally, the comparison of tumble core in the XZ-plane shows a common shape of the structure which is a straight core along Z-direction at the corresponding X-range. The main difference observed between the fields appears in YZ-plane where an upward curved shape is revealed only for V100 at 2000 RPM in the front regions of the volume (Z > 0) and a slight curvature appears in the lower regions for the two other cases. These mean curvatures from one side or another of the volume could be related to a small dissymmetry effect of the intake flows in the mid-cylinder domain.

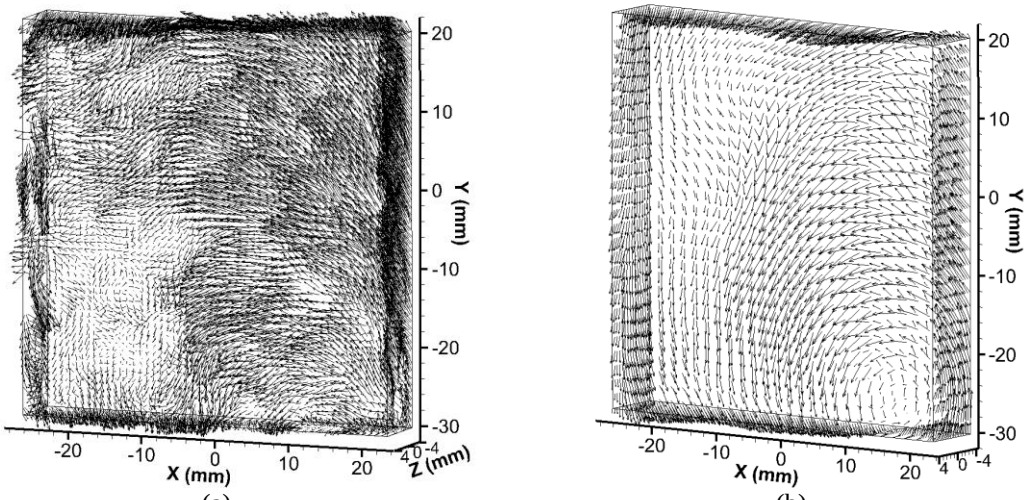

Figure 3-31 3D-POD : (a) instantaneous velocity field at -178 CAD, 2000 RPM, V100 (b) filtered velocity field reconstructed via 5 POD modes

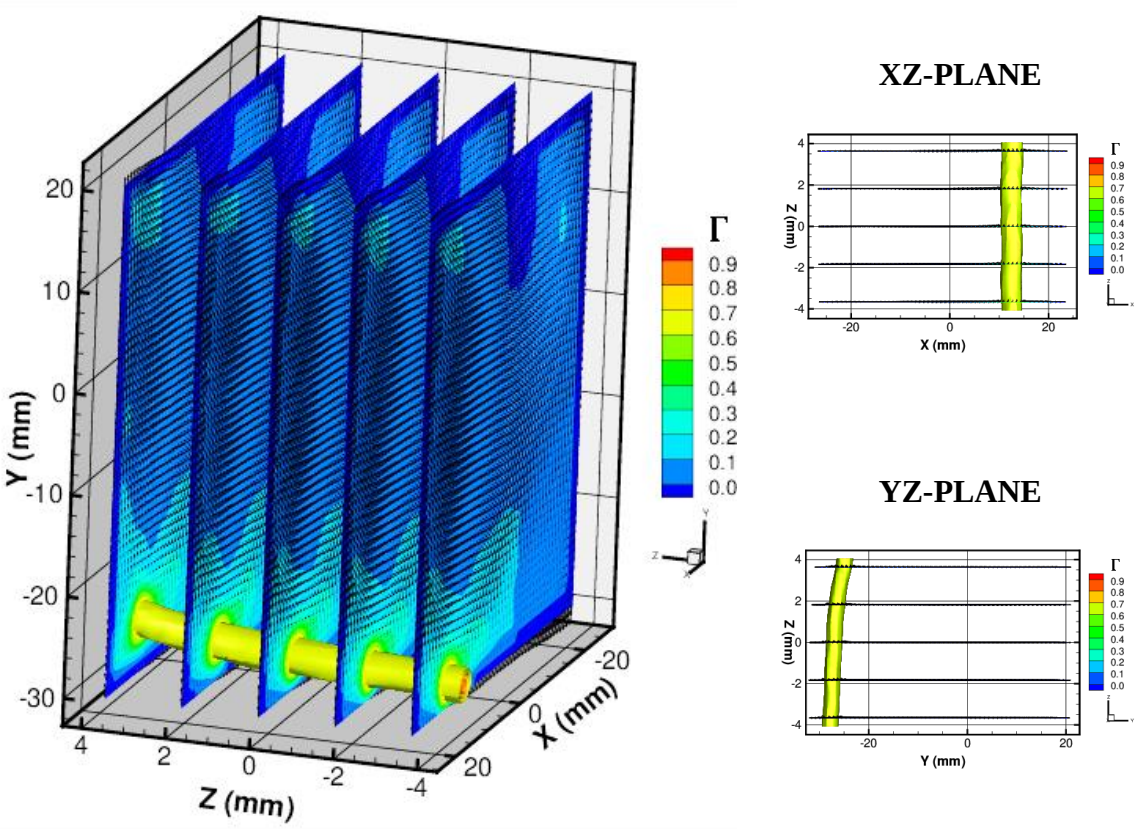

Figure 3-32 Γ criterion and tumble core for 2000 V100 at -178 CAD (near BDC)

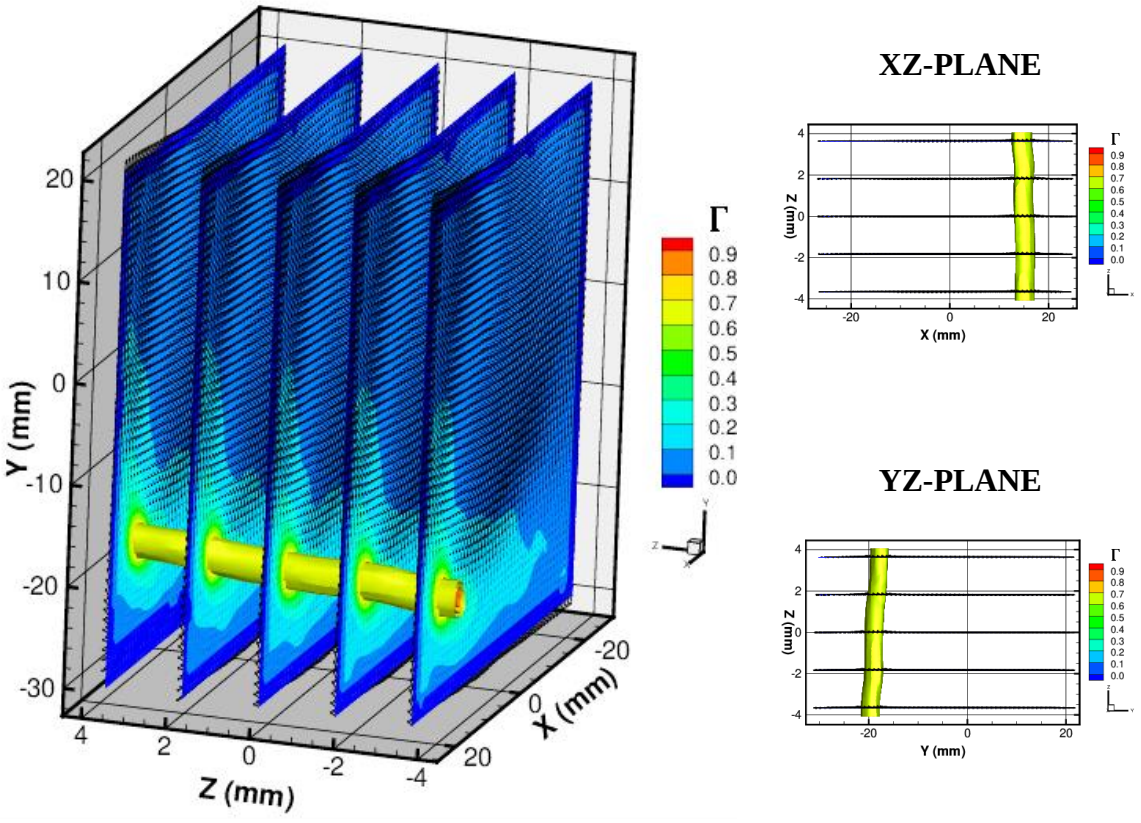

Figure 3-33 Γ criterion and tumble core 2000 V50 -178 CAD (near BDC)

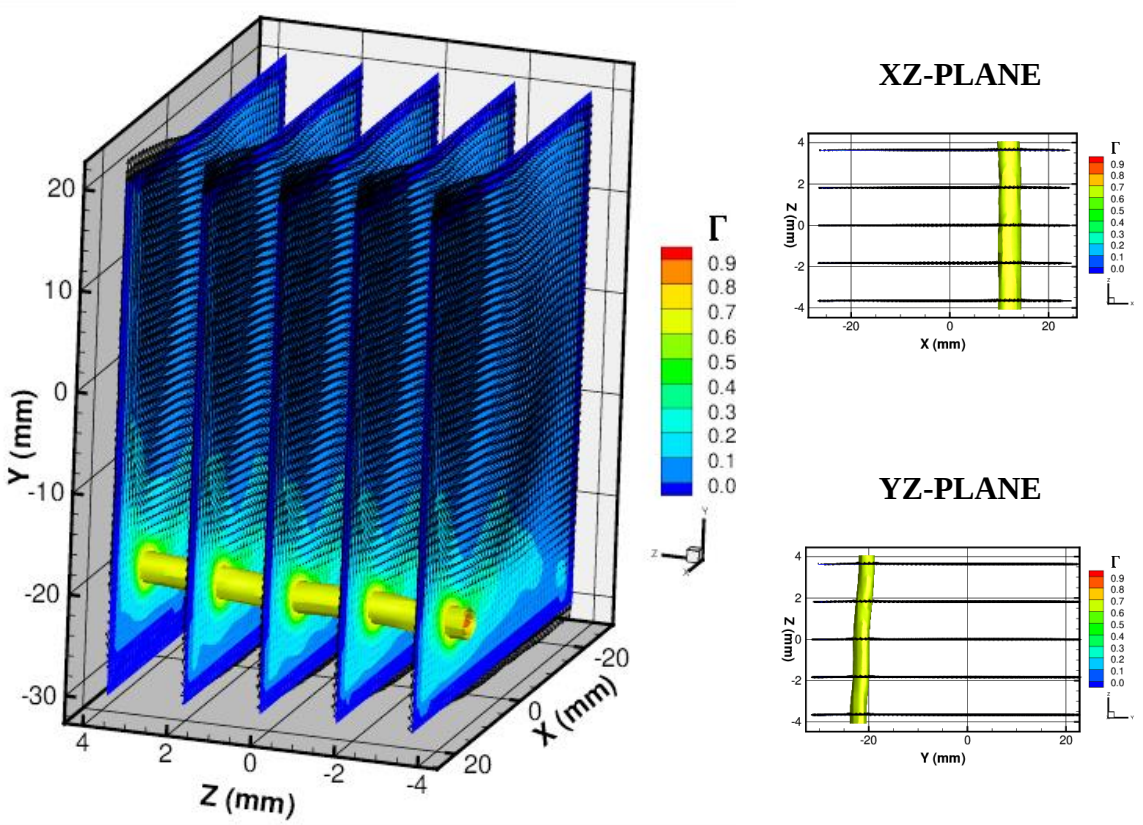

Figure 3-34 Γ criterion and tumble core 3000 V50 -178 CAD (near BDC)

Using a similar extraction approach of vortex cores and applying it to reconstructed velocity fields at consecutive engine cycles, it is now possible to describe and quantify the 3D CCV with respect to 3D tumble positioning and shape. Figure 3-35 illustrates a series of instantaneous tumble cores revealing the 3D fluctuating character of the structure along engine cycles. The variations of tumble core diameter are observed between the different cycles as well as its variation with respect to in-volume depth Z. Moreover, unlike the straight mean tumble core, a multi-curved behaviour of the instantaneous core is revealed across the volume. This clearly shows the need for a 3D description of the in-cylinder flow structures in order to provide a more realistic analysis of the accompanying phenomena.

In some cases, the tumble travels farther in the combustion chamber than what is captured in the field of view (Figure 3-35(h)). However, a main structure is found and can be the subject of further analysis by correlating the experimental data to a numerical vortex modelling and finding the best fit. This can thus provide additional information concerning the position, size and shape of out-of-volume tumbles. Moreover, this out-of-plane tendency occurs for several crank angle degrees during our measurements as is shown in annexes 2 and 3. Particularly in the case of V25, a complete tumble position

often escapes the field of view since the tumble reaches lower locations along the vertical axis Y, as also seen via the 2D measurements. Finally, the three operating conditions chosen for illustrations hereafter are at -178 CAD for (V100, 2000 RPM), (V50, 2000 RPM) and (V50, 3000 RPM) since they best capture the entire tumble structure in the investigated volume for the majority of recordings. Two parametric comparisons are then allowed; one with respect to engine rotational speed and another with respect to inlet flow blockage section.

For each one of the three studied cases, analysis of the distribution of the instantaneous tumble location are performed in the mid cylinder plane at Z = 0 and at the border planes at Z = -3.79 and Z = 3.77. Figure 3-36 below illustrates the captured results and initial findings indicate similar distribution of the instantaneous tumble location between the different planes. However, the distributions differ for each case.

For the case V100 at 2000 RPM, tumble centre locations draw a circular envelope centred at the mean tumble location in that plane (red dot). Particularly at the bottom of the envelope, we can note a number of tumble locations limited by the lower border of the field of view in planes Z = -3.79 and Z = 0. These tumble locations reflect however values of Γ criterion that are greater than 0.9 and therefore they are not necessarily erroneous but can rather be further investigated via an adapted vortex modelling technique. Finally, tumble locations are generally higher in plane Z = 3.77 which reflects the mean upward curvature of tumble core observed in Figure 3-32. This is also shown by the mean tumble location in plane Z = 3.77 (red dot) that has a higher location compared to the mean centres in the other two planes.

For the case V50 at 2000 RPM, instantaneous tumble centre locations draw an elliptical inclined envelope in the different planes with the mean location in plane Z = -3.79 positioned slightly lower in Y-direction, correspondingly to the slight curvature observed in the mean field of Figure 3-33. In both X and Y direction, tumble centres seem to be more dispersed than in the reference case V100. Finally, for the case V50 at 3000 RPM, tumble centre locations draw a horizontal elliptical envelope in the different planes showing a greater distribution of tumble centres along X-direction.

In conclusion, 3D velocity fields obtained by Tomo-PIV and filtered by POD allow the identification of instantaneous 3D tumble structures that in turn provide the means to analyse the in-cylinder flow variations with respect to different engine conditions.

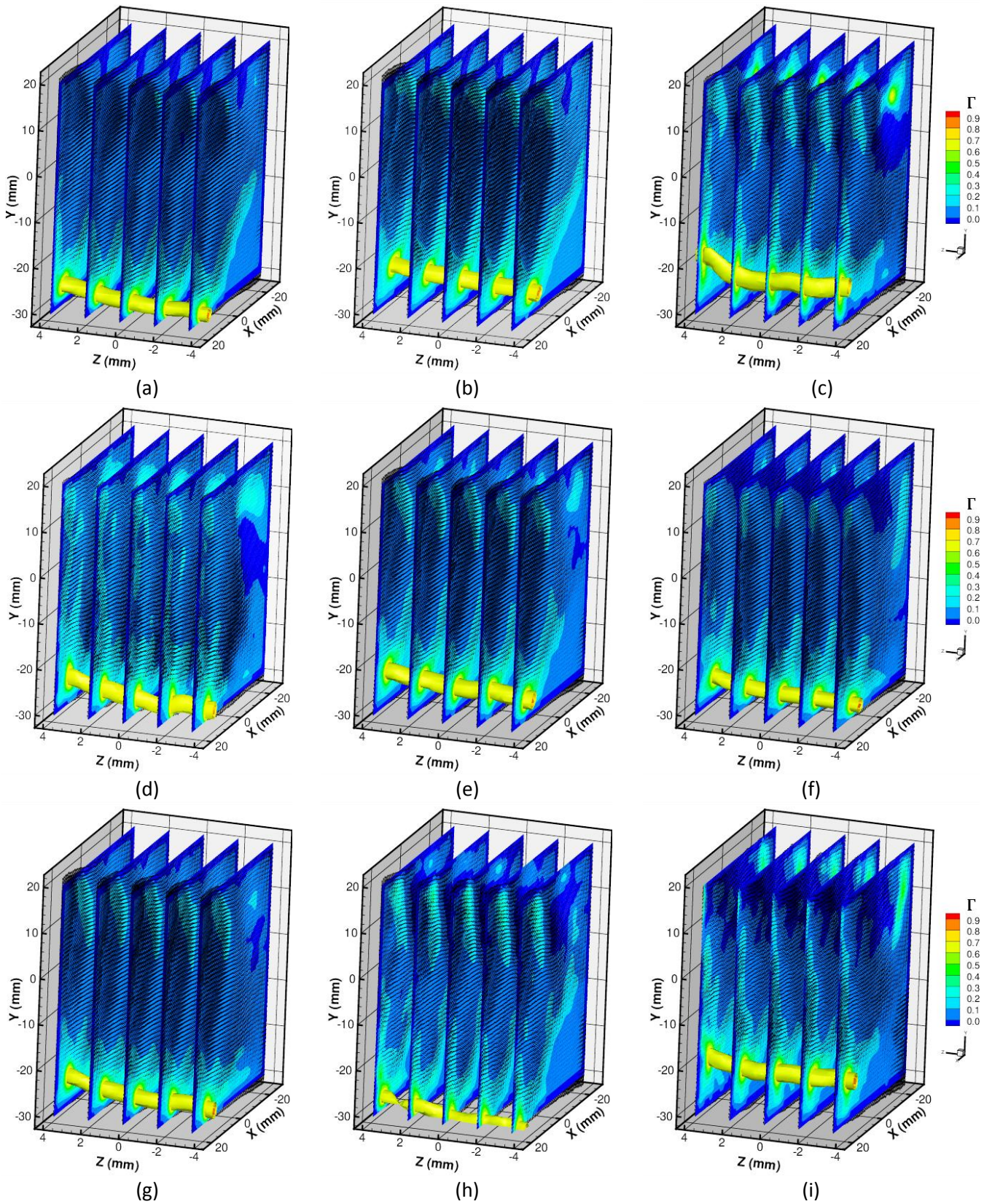

Figure 3-35 Instantaneous Γ criterion and tumble core from reference case 2000 RPM at V100

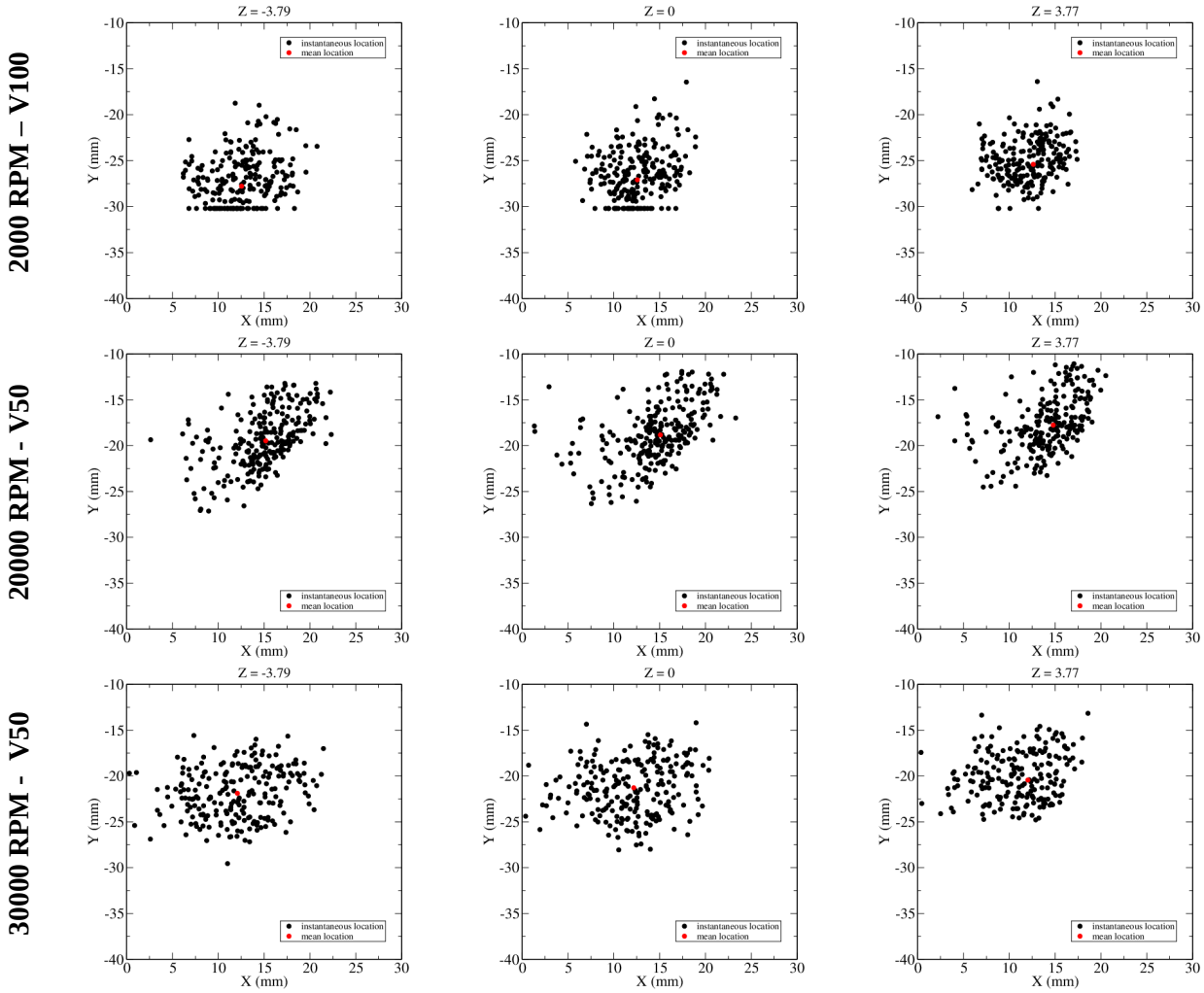

Figure 3-36 Instantaneous and mean tumble centre location in mid-cylinder planes and border planes for three engine operation conditions

3.4.3.2 Classification of in-cylinder flow patterns

In a second step, a conditional approach for the characterisation of in-cylinder large scale structures is suggested based on the energetic contribution of POD modes' coefficients. In fact, one of the main challenges for the analysis of the engine's in-cylinder flow is identifying a number of characteristic flow patterns enabling the classification of engine cycles under well-defined categories. The aim of this classification is to provide for a group of cycles sharing common characteristics, a shell allowing to distinguish their particular flow structures, quantify the velocity fluctuations within the shell and finally estimate the contribution of this defined group of flow structures to cyclic variations. Consequently, engine cycles can be individually evaluated within the shell with respect to their contribution to the flow's global turbulent kinetic energy with higher precision since CCV are mined out of the evaluation. Furthermore, this classification aims to find correlations between the different categories of flow structures in order to extract

information linking the consequent behaviour of one category to another such as the positioning of the tumble structure in the combustion chamber and the valves' jets interactions.

In order to perform such a conditional classifications of velocity fields, a multitude of methods can be considered such as:

1. Using an analytical modelling technique to find flow parameters enabling a minimisation between flow structures defined beforehand and those experimentally obtained. However, this method necessitates a prior knowledge of recurrent flow structures such as the type of vortices or the intensity of a flow structure in order to apply the minimisation approach and classify fields.
2. Defining flow categories based on prefixed flow characteristics such as tumble ratio, tumble geometry or tumble position like what was previously presented in paragraphs 3.3.3 and 3.4.3.1. This method allows quantifying the kinetic energy associated to specific flow characteristics and describes their influence on the global flow. However, it is still limited when a large number of global flow characteristics needs to be assessed simultaneously.
3. Classifying flow patterns without prior knowledge of the flow field characteristics using conditional statistics to distinguish categories of flow configurations. One example is the resemblance coefficient computed by (Cao et al., 2014) enabling them to build a cluster of categories and observe the exchange of energy between these categories (particularly the transfer of energy from large scale structures to smaller structures near TDC at the end of compression). Another example is (Voisine et al., 2010) using phase-invariant POD and multi-time statistics to distinguish flow structures into groups that are then used for conditional statistics.
4. Applying deep-learning techniques could in future works offer a particular approach for the identification of recurrent patterns and for finding correlations between categories of structures.

In our study, the third classification method is addressed, i.e. no prior knowledge of the flow characteristics is required. A similar approach to what was proposed by (Voisine et al., 2010) is carried out. In their sturdy, each group of engine cycles was obtained by evaluating the projection of each field onto the first global POD mode (mode-0) that was found to be a good indicator of the level of tumble breakdown, after observing that its decrease in kinetic energy during compression was accompanied with an increase in kinetic energy of the other modes. Their use of mode-0 allowed identifying categories of flow behaviours with respect to their resemblance to the mean flow filed.

Our correlation coefficients meanwhile are computed, for a given engine phase, between each instantaneous cycle and a mean flow (F_m) obtained from velocity fields reconstructed via the 4 POD modes following mode-0 at that phase and not including mode-0 in the reconstruction. In other words, the dominant structure of the mean flow field is excluded from F_m and only the most recurrent large scales are retained. Then, instantaneous velocity fields (f_i) are reconstructed via the first 14 POD modes that contain approximately 99% of the flow's energy (Figure 3-17). Finally, a normalised projection coefficient C_i is computed between F_m and the instantaneous velocity field f_i reconstructed such as:

$$C_{ui} = \frac{< \boldsymbol{u}_i(x,y,z).\boldsymbol{u}_m(x,y,z) >_{volume}}{\sqrt{< u_i(x,y,z)u_i(x,y,z).u_m(x,y,z)u_m(x,y,z) >_{volume}}} \quad \textbf{(3-14)}$$

where the subscript *u* denotes the u velocity component, *i* denotes the instantaneous velocity field and *m* denotes the mean component of F_m. Using a similar equation to 3-14, C_v and C_w are also computed. A null projection coefficient translates a minimum of correlation to F_m, translating into a maximum of correlation to the mean flow field, which increases as the values of C_i approaches 1 or -1, the sign of which depends of the directions of velocity component. A classification of instantaneous cycles can then be performed by distinguishing their level of correlation to the velocity components of F_m which mainly describes the large scales cyclic fluctuations. Finally, this analysis is illustrated in the following for few engine phases of the reference case V100 at 2000 RPM.

Figure 3-37 first shows for the 250 velocity fields at -178 CAD, the correlation coefficients C_u, C_v and C_w, ranging between -1 and 1. Five groups spanning the distribution of the correlation coefficient in intervals of equal width of 0.4 are defined in order to perform a conditional analysis based on the resemblance of F_m and f_i flow structures, with respect to each velocity component. The velocity fields in each group are then averaged and a mean flow field as well as a flow fluctuations field are obtained for each of the five groups. Moreover, a statistical probability is computed for each group of fields as shown in Figure 3-38 for C_u. Then, for each group, the corresponding Γ criterion of the group's mean flow field is computed and represented in the Z_0-plane of the investigation volume in Figure 3-38. Iso-contours represent the magnitude of Γ and vectors represent the in-plane velocity. The main observation drawn from the mean Γ fields of the different groups obtained from C_u distribution is a clear displacement of the mean tumble centre location towards the right of the field in an upward direction. This reveals a direct correlation between our classification approach with respect to the first

POD modes and a recurrent cyclic positioning of the tumble structure influenced by the u velocity component. Indeed, the mean tumble centre positon of group 3 (C_u=0) compared to the tumble position in the mean flow field at -178 CAD is found to be similar thus confirming that the level of C_u is representative of the disparity of instantaneous velocity fields from the mean flow.

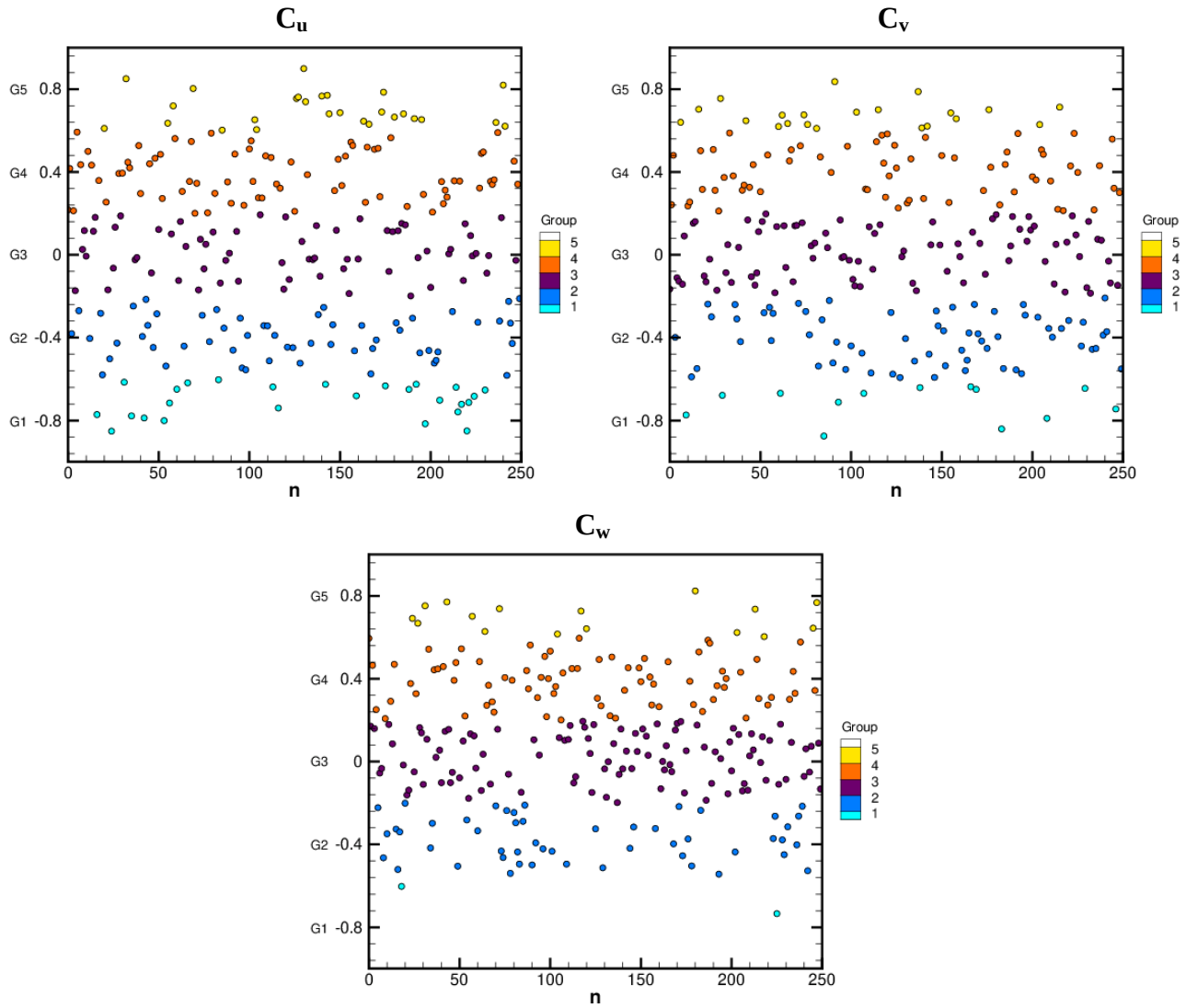

Figure 3-37 Distribution of correlation coefficients C_u, C_v, C_w obtained from velocity fields at -178 CAD (near BDC) for V100 at 2000 RPM

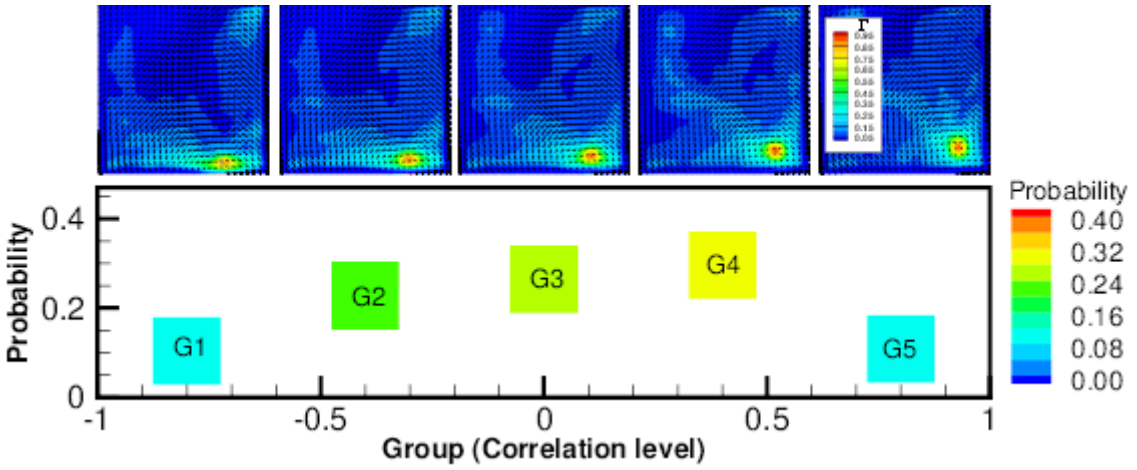

Figure 3-38 Classification of velocity fields at -178 CAD (V100, 2000 RPM) regarding C_u coefficient

C_v and C_w are then presented in a similar manner in Figure 3-39 and Figure 3-40 respectively. Both distributions show a maximum probability of velocity fields to be in group 3. The two figures also show very light variations of the mean tumble location in X-direction with respect to the different groups of C_v and C_w at -178 CAD. One exception is group 1 of C_w where the mean tumble location is seen displaced upward to the left. This mean field is however computed from a very small number of velocity fields corresponding to the very low probability of fields to be in group 1. It is hence considered erroneous and this variation of tumble location is assumed inaccurate. In conclusion, the correlation along u-component seems to offer the most demonstrative way for the classification of large scale tumble structures at -178 CAD.

This is further illustrated in Figure 3-41 where the groups' mean 3D tumble cores obtained via the 3D Γ criterion are illustrated in the volumetric domain. Group 1 reveals an incomplete tumble structure that exceeds the lower borders of the field of view. As noted in the mid-cylinder plane, the groups' mean tumble is then observed moving upward to the right of the field of view to finally reach the highest position in Y-direction for group 5. A quasi constant tumble core diameter is observed for the 5 groups with a cylindrical shape along Z-direction. Particularly for group 5, curves along the core are observed.

Finally, the five fluctuating velocity fields u' corresponding to the five groups obtained from C_u distribution are presented in Figure 3-42 in order to show the flow's variations within one group and compare these variations to the global velocity fluctuation field obtained from the ensemble of 250 engine cycles. As a result, fluctuations of the five groups are very alike and show low magnitudes within the same group thus revealing the resemblance of flow dynamics in that group. The likeness of the five velocity fluctuations

fields also shows the reliability of the presented approach for the classification of velocity fields sharing common recurrent flow characteristics. Compared to the global velocity fluctuation field, over 50% of reduction in magnitudes is observed. This considerable decrease in magnitude between global and groups' fluctuations is similarly observed along v'-component in Figure 3-43 that also shows the resemblance between the groups' mean fluctuation fields. Groups along w' component show similar behaviour but are not presented here since the contribution to TKE of the very small magnitudes of w' at -178 CAD is minor.

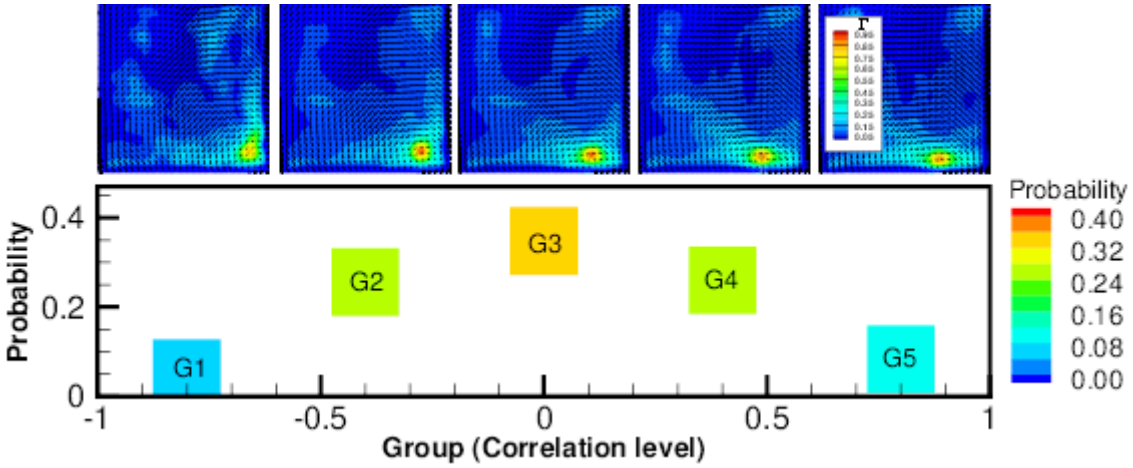

Figure 3-39 Classification of velocity fields at -178 CAD (V100, 2000 RPM) regarding C_v coefficient

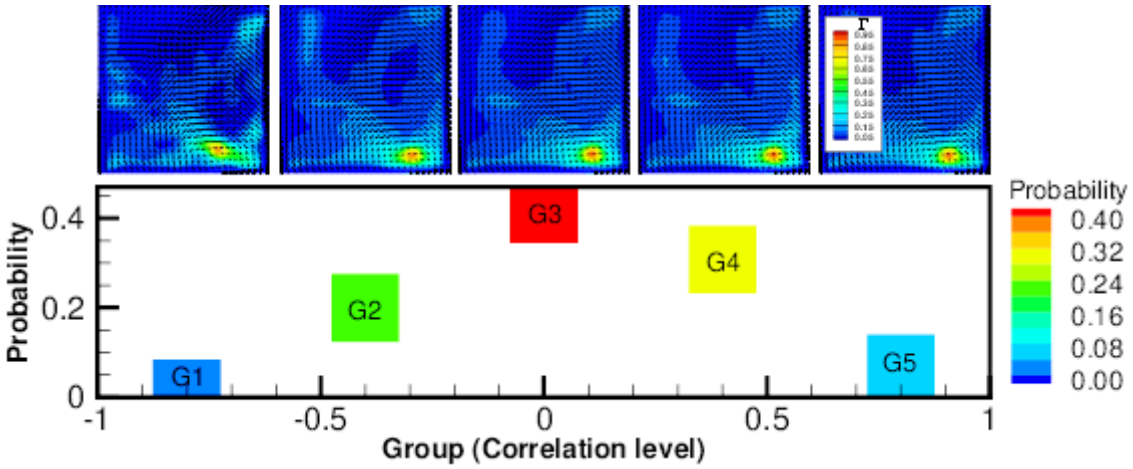

Figure 3-40 Classification of velocity fields at -178 CAD (V100, 2000 RPM) regarding Cw coefficient

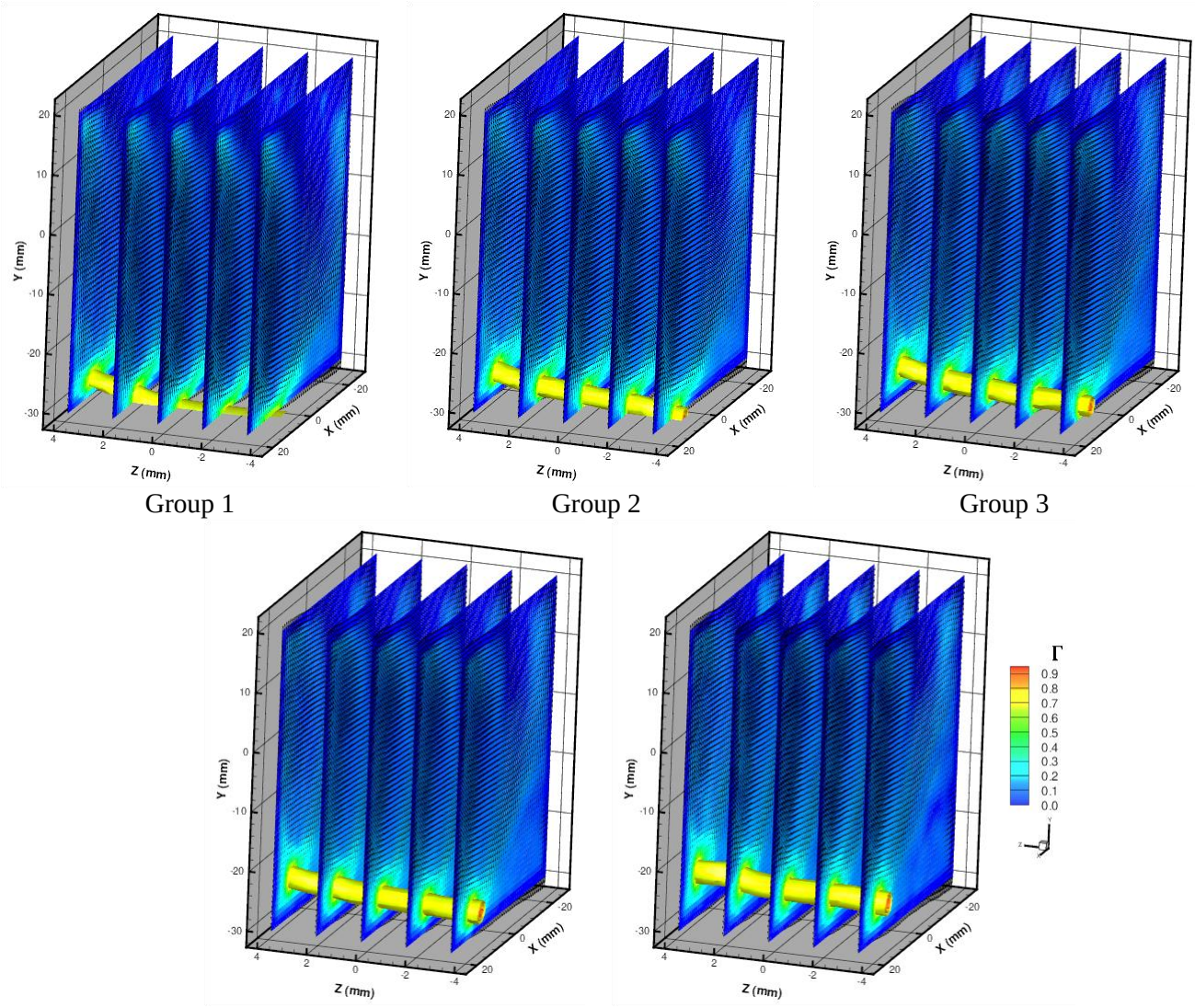

Group 1 Group 2 Group 3

Group 4 Group 5

Figure 3-41 3D tumble core of the five conditional groups mean flow fields

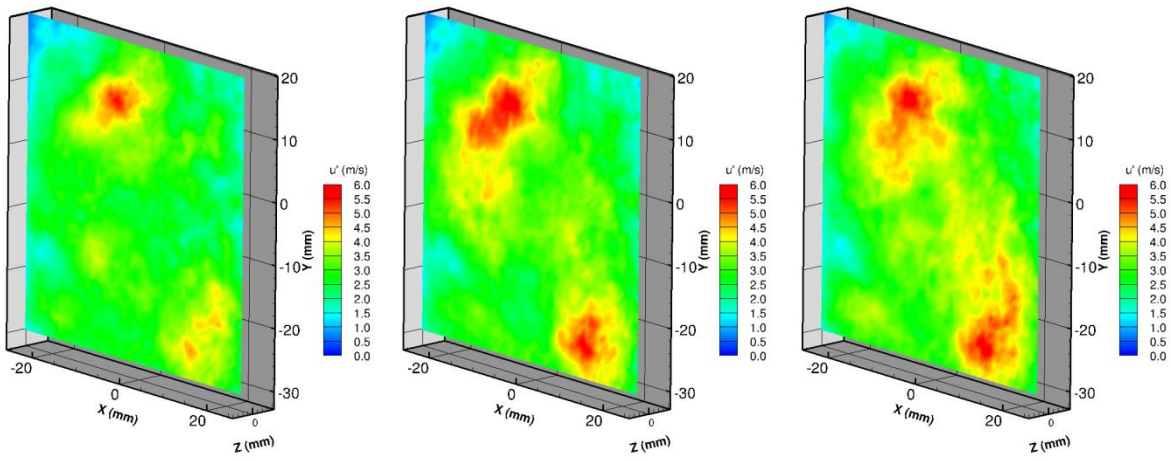

Group 1 Group 2 Group 3

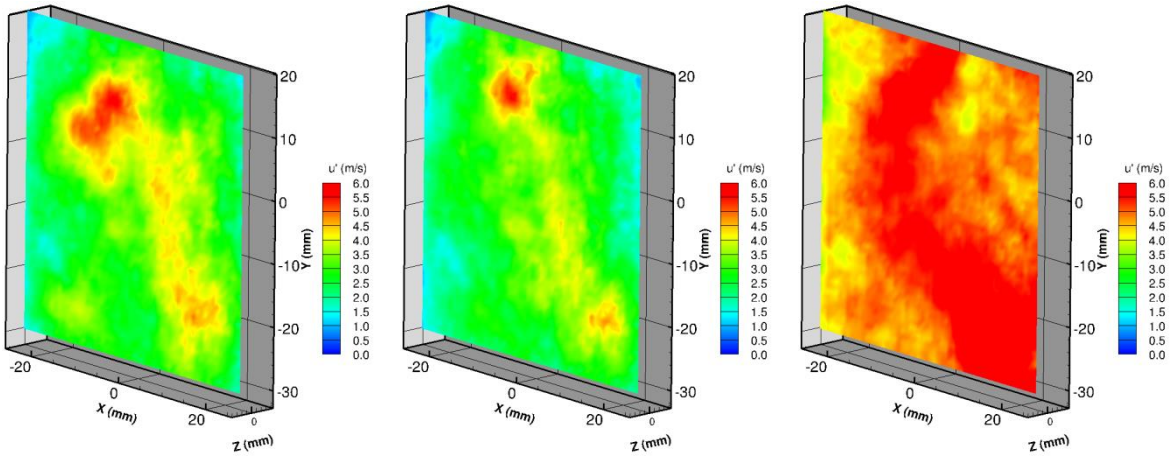

Group 4 Group 5 Global velocity fluctuations

Figure 3-42 u' velocity fluctuation of the five C_u conditional groups and global velocity fluctuations averaged over the ensemble of 250 velocity fields

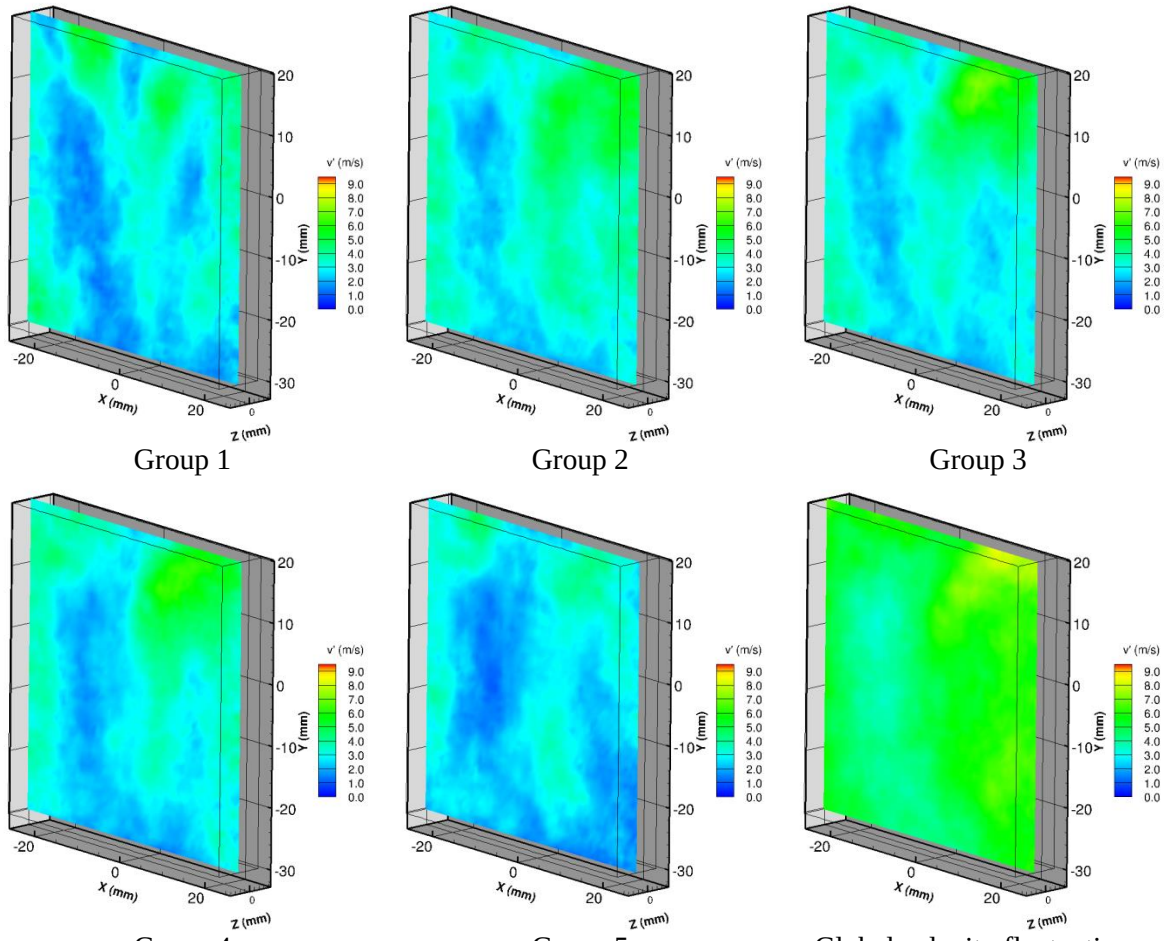

Group 1 Group 2 Group 3

Group 4 Group 5 Global velocity fluctuations

Figure 3-43 v' velocity fluctuation of the five C_v conditional groups and global velocity fluctuations averaged over the ensemble of 250 velocity fields

Using a similar classification approach for velocity fields acquired at -130 CAD (during the compression stroke) where w-component is more considerable than near BDC, groups of flow structures obtained from C_w distribution is presented in Figure 3-44 showing a maximal probability of fields in group 4 and a minimal probability of groups 1 and 5. For each of the five mean group flow fields, the Γ criterion is computed and presented in the Z_0-plane of the volumetric domain. The main tumble structure is observed in the upper left region of each field and small variations of its centre location are observed along Y-direction. Group 1 revealing the least probability of fields is considered inaccurate with respect to mean tumble location since the number of fields that is averaged is small. Furthermore, for each group, the mean flow field is presented. Iso-contours correspond to the mean w-component and vectors represent the in-plane velocities. Groups 3 and 4 then reveal clear similarities in magnitudes and velocity distributions while groups 2 and 5 reveal a reversed effect of velocity distribution. The w-component is negative on the upper left (directed towards the rear of the investigation volume) and positive on the lower right (directed towards the front of the investigation volume) of the mean field of group 2 and this is reversed for group 5. This is illustrated in the volumetric domain in Figure 3-45 leading to the conclusion that each group defined with respect to C_w distribution reveal a very distinctive flow characteristic whose contribution to the total TKE can now be individually addressed.

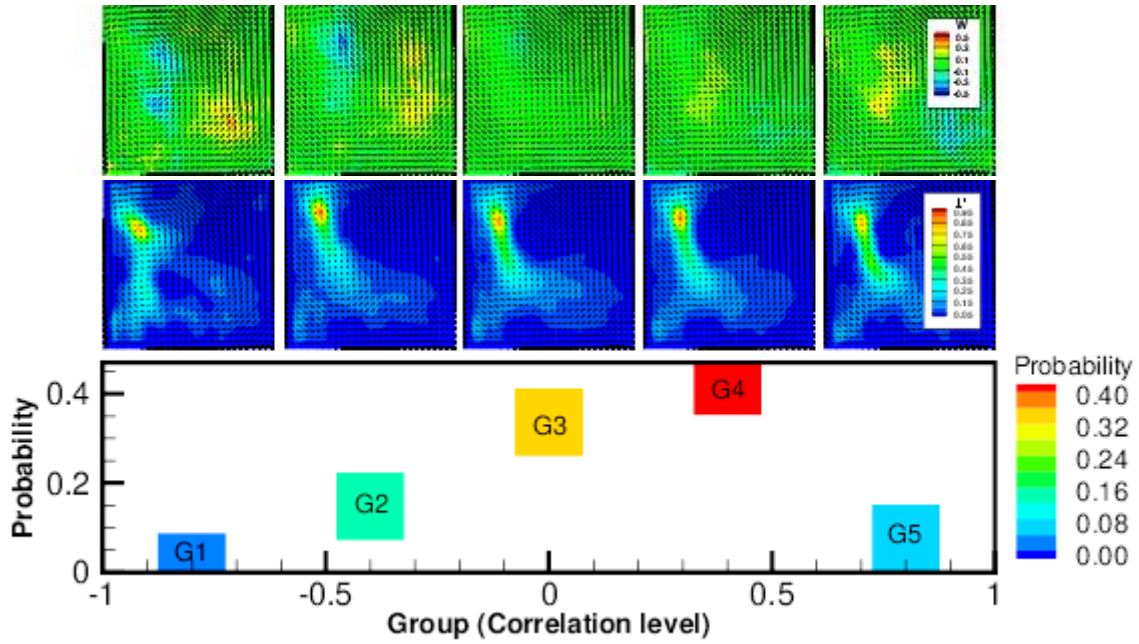

Figure 3-44 Classification of velocity fields at -130 CAD (V100, 2000 RPM) regarding C_w coefficient

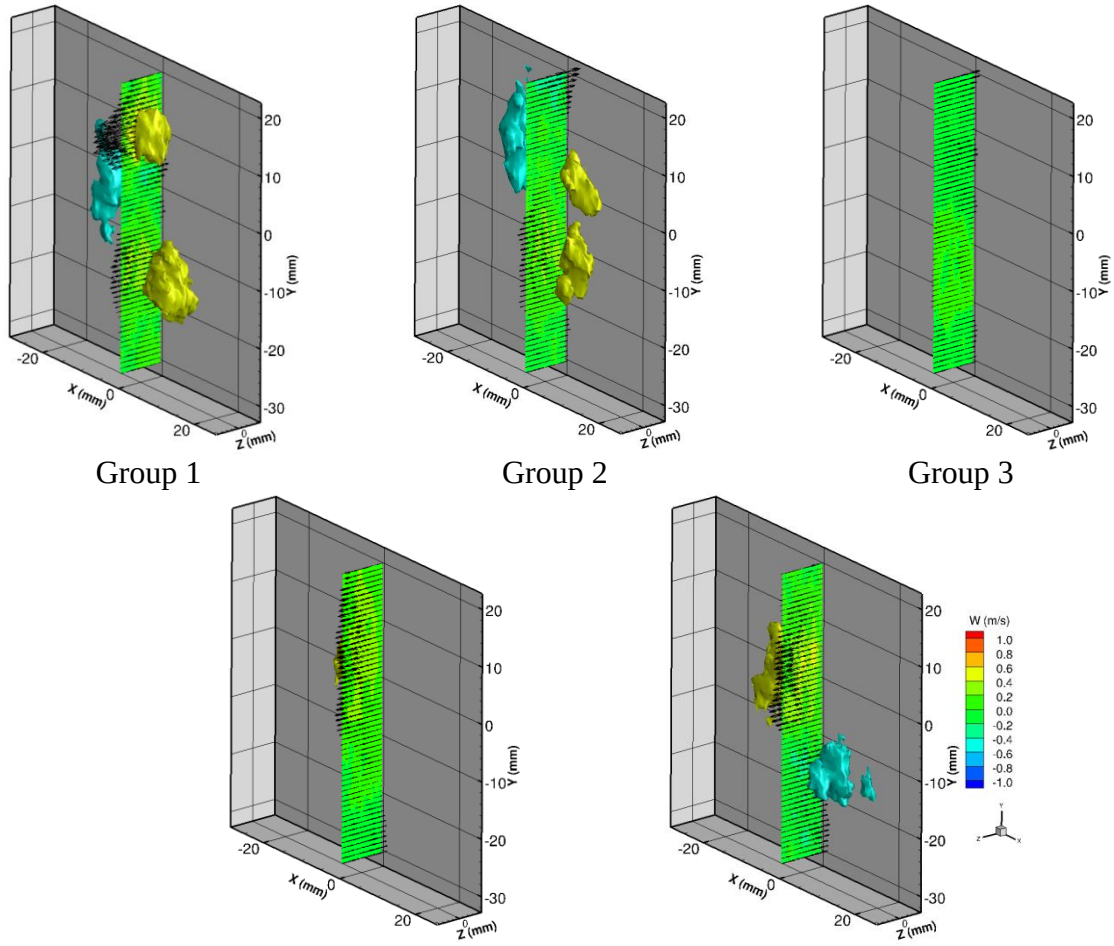

Figure 3-45 w' velocity fluctuation of the five C_w conditional groups at -130 CAD

- **Probability maps of C_u, C_v and C_w correlation coefficients**

In a last step, probability maps of the three correlation coefficients are presented in Figure 3-46 in order to cross-correlate groups of maximal probability of fields. This step aims to identify a correlation between groups of structures and define, if possible, a physical link of cause and effect between the behaviours of these groups. Three types of maps are shown. The first plots the five groups C_v versus those of C_u, the second plots C_w versus C_u and the third plots C_w versus C_v. The three plots are shown for each of the 7 crank angle degrees of the reference case V100 at 2000 RPM. As a result, a peak of cross-correlation is rarely seen between common flow structures identified from C_u and C_v. Meanwhile, cross-correlation peaks are often noted between groups obtained from Cw and C_u on the one hand and those obtained from C_w and C_v on the other hand. Around mid-intake for example, shown at -274 CAD, groups 3 of velocity fields show strong correlations with respect to the 3 velocity components. Therefore, it can be concluded that flow structures in that group are most recurrent and most resembling to F_m and hence contribute the most the TKE of CCV as that engine phase. During mid-compression,

shown at -106 CAD, strong cross-correlations appear between group 4 obtained from C_w and groups and 4 obtained from C_u and C_w. This implies a dominant behaviour of the w-component at mid-compression that corresponds to the flow characteristics of group 4 and that this behaviour is mainly linked to the behaviour of u and v components in groups 3 and 4.

In conclusion, the classifying of flow patterns without prior knowledge of the flow field characteristics using conditional statistics drawn from phase-dependant POD and based on the correlation to a mean flow field F_m describing the CCV at fixed engine phases allowed distinguishing specific categories of flow configurations as well as correlating these configurations to trace back the chain of cause and effect linking them. However, in this first analysis, we did not establish a strong physical correlation between particular groups of flow structures that could explain for example the tumble position with respect to the flapping on intake jet or the dissymmetry of the flow in the mid-cylinder domain. In order to complete this study and further interpret the experimental results, a phase-invariant decomposition is required to be able then to correlate the different engine phases and describe the large scale structures during compression with respect to those during intake for example. Nevertheless, this analysis was made possible by the information brought by Tomo-PIV measurements that allowed a volumetric visualisation of tumble cores in the mid-cylinder domain and revealed the necessity of 3D measurements to further our understanding of the in-cylinder phenomena.

-82 CAD

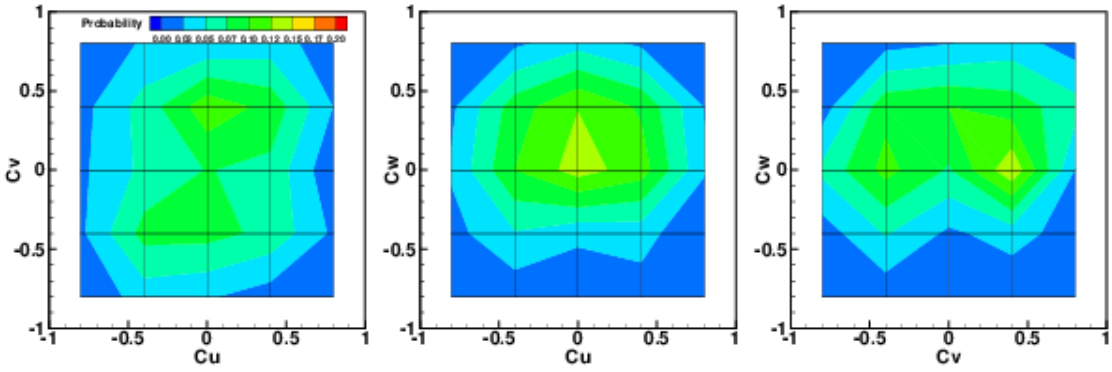

-106 CAD

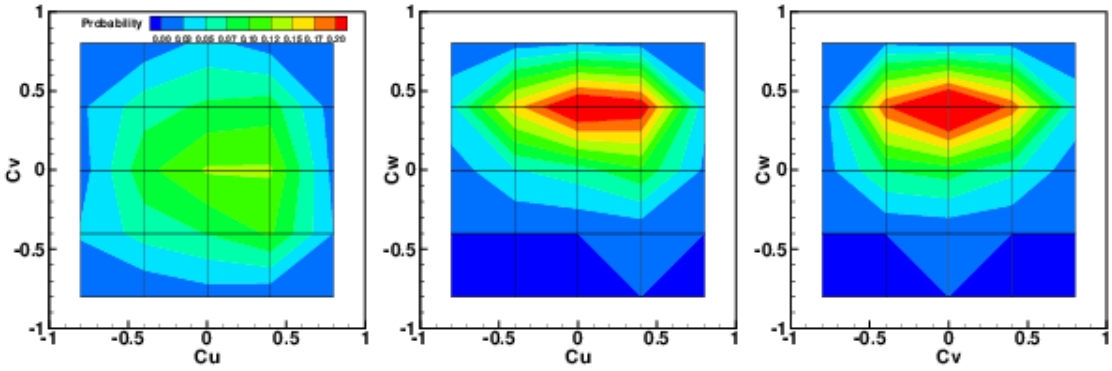

-130 CAD

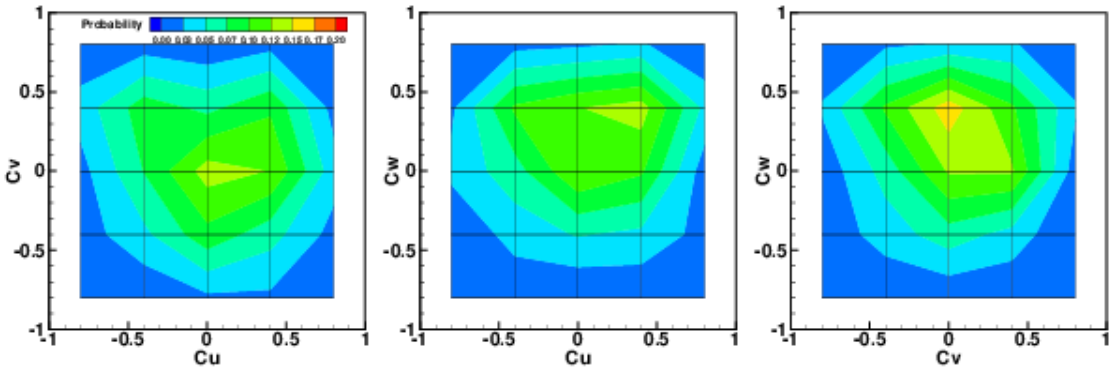

-178 CAD

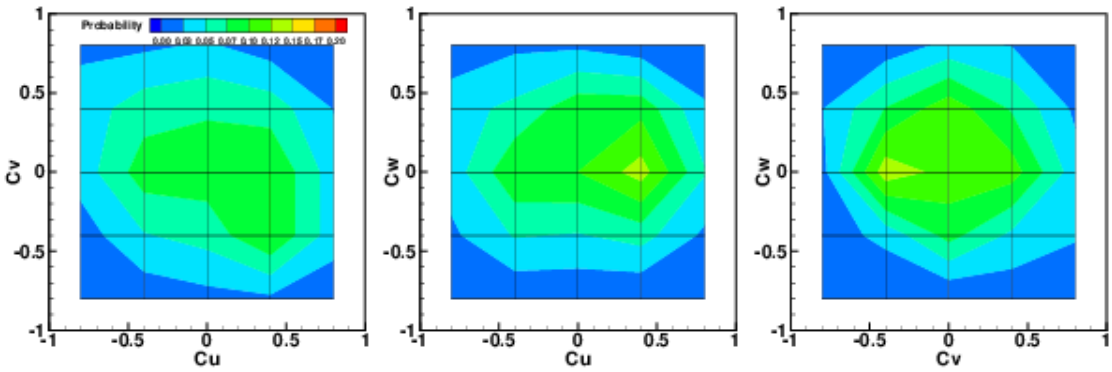

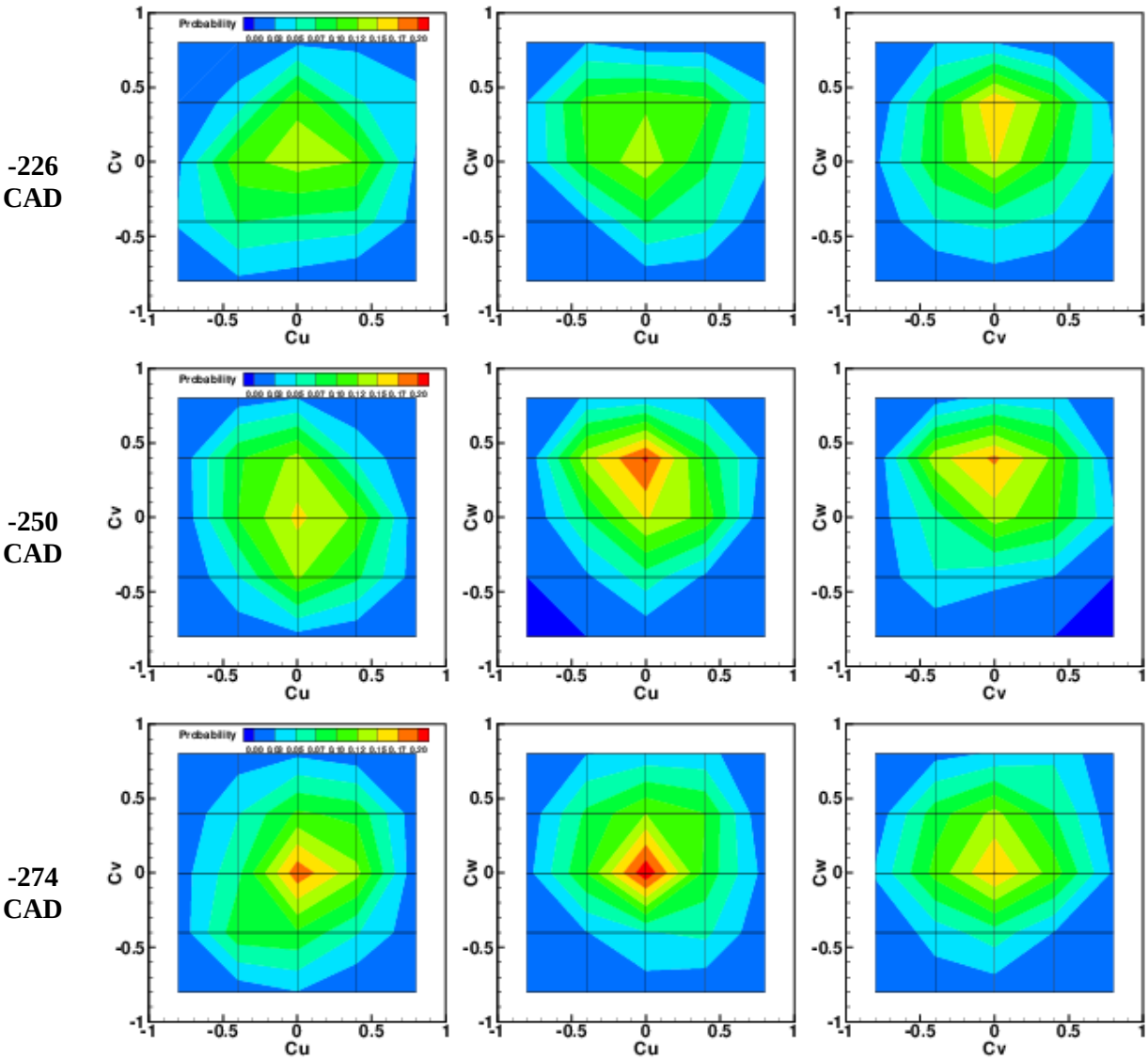

Figure 3-46 Cross-correlation maps got reference case V100, 2000 RPM

4 Summary and Outlook

The characterisation of unsteady confined flows is vital to understand and control their dynamics. Hence, acquiring a temporal tracking as well as a 3D description of the flow paves the way to obtaining the required thorough spatiotemporal analysis. With the technological advancements witnessed in the world today, industrial products can be simplified into experimental benches capable of reproducing the same operation conditions and output. By coupling these advancements to the progress witnessed by diagnostics and measurement techniques, it is possible today to measure a large number of flow parameters. In particular, non-intrusive laser diagnostic techniques allow visualising the flow and measuring its properties without compromising their natural portrayal. One technique that has proven its reliability to report a flow's velocity field and fluctuations is the particle image velocimetry technique, PIV.

In the course of this study, two types of PIV were applied and adapted to an optical spark ignition engine which is an excellent application of complex confined geometries and unsteady flows. The first technique is time-resolved PIV. The goal was to describe the temporal evolution of the in-cylinder unsteady flow and identify its variabilities with respect to different operation conditions. The second technique is tomographic PIV. The goal was to extend the collected data into the real three-dimensional space and investigate the extent of reliability of 3D measurements with respect to experimental constraints.

In addition to developing the application of the PIV techniques under difficult experimental conditions, studying the engine's in-cylinder aerodynamics in particular was mainly motivated by two reasons. The first is the fundamental role of in-cylinder aerodynamics in influencing the quality of the air/fuel mixing process that in turn influences the quality of combustion and cyclic pollutant emissions. The second more global reason, deriving from the first, is the dominant place of internal combustion engine in the transportation sector of the 21st century and its main contribution to global warming that is being urgently addressed with international policies and regulations.

Consequently, the efforts of this thesis consisted on one hand of investigating the internal engine aerodynamics with respect to realistic engine operation conditions by means of the optical engine test bench in CORIA laboratory. On the other hand, it consisted of developing new processes to adapt the application of 3D Tomo-PIV to complex confined geometries, facilitating thus the investigation of flows facing similar experimental constraints.

The bibliographic study presented in chapter one first revealed the need to visualise the engine's in-cylinder's aerodynamics and quantify the occurring phenomena. Advancements witnessed in the optical engine configuration and the additional measurements it allowed via the combination to optical diagnostic techniques were therefore briefly described showing their mutual role in visualising the in-cylinder flow.

The role of particle image velocimetry was particularly emphasised for its importance in providing an accurate description of flow evolution. A survey of the working principle of the main PIV techniques as well as results obtained from PIV experimental studies in IC engines was presented revealing the role of this work in furthering our knowledge of the in-cylinder flow. Although planar PIV measurements are wide-spread today and well adapted to the optical engine configuration, the experimental process of implementing them still faces a number of constraints that needs to be carefully addressed. And as a 3D description is essential for a coherent and realistic understanding of the underlying phenomena, the application of 3D tomographic PIV to the engine test bench proves to be a challenging task since it involves using a thick laser sheet and dealing with a curved and confined optical geometry. However, 2D and 3D measurements remain complementary in the sense where the first ensures higher measurements accuracy and the second provides information otherwise missed.

The objectives of this work were set to measuring via 2D TR-PIV and 3D Tomo-PIV the physical properties of the engine's in-cylinder aerodynamics during intake and compression strokes, particularly the large scale tumble structure. Adequate experimental procedures were needed and six engine operation conditions were considered while varying intake duct opening conditions (100%, 50% and 25% of the total intake duct opening) and testing 2 realistic engine rotation speeds (2000 RPM and 3000 RPM) while preserving environmental inlet conditions of 1 atm and 300 K, without firing.

Chapter two consisted of two main parts. The first treated the 2D time-resolved measurements (2D2C) and the second addressed the 3D tomographic measurements (3D3C).

For the implementation of TR-PIV, a high-frequency Photron camera was associated with a dual pulsed Darwin-80 laser delivering an energy of 25 mJ at 1 KHz per cavity. The measurement light sheet was fixed in the vertical plane between the two intake valves, the tumble plane, with the laser directly crossing through the cylinder. The field of view of the camera was set to 91×91 mm^2 corresponding to an image resolution of 768×768 pixels. The flow was seeded with oil particles of approximately 1 to 5 μm in diameter, faithfully following its dynamics. These particles were introduced far upstream of the inlet valves to not disturb the in-cylinder aerodynamics. A procedure for optimizing the quality

of particle images and eliminate strong reflections was performed, consisting of a variable masking algorithm and a subtraction of a mean background image. This resulted in 74×84 mm² velocity fields' dimensions. An original synchronization unit was developed to adjust the time interval Δt between 2 laser pulses, i.e. 2 particle images, with respect to the engine's phase dynamics. The recording frequency was fixed to 3 KHz which translated into 45 recorded phases per cycle at 2000 RPM, and 30 phases per cycle at 3000 RPM. Velocity fields were then obtained from the pre-processed particle images via an in-house developed PIV algorithm with sub-pixel shifting precision. Data validation relied on investigating the convergence of velocity components, the peak locking bias, and comparing TR-PIV ensemble average velocity fields to those obtained from classical PIV previously performed on CORIA's engine test bench.

For the desired Tomo-PIV measurements, the investigation volume was fixed by establishing a thick light sheet between the intake valves centred at the cylinder's tumble plane (Daher et al., 2016)(Daher et al., 2016). Access into the combustion chamber was done through a 45° mirror fixed under the transparent piston head. The light sheet thickness was controlled via knife-edge cutters fixed on micrometric translation plates placed between the cylindrical lens and the mirror, parallel to the laser sheet. Laser sheet profiles were measured to establish the relation between inter-cutter distance and light sheet thickness. The laser used was a double pulsed PIV Spectra Physics delivering 350 mJ per pulse while at 532 nm and 10 Hz. It was coupled to four Hamamatsu CCD cameras equipped with PC-E Micro NIKKOR lenses (45mm f/2.8D) with Scheimpflug adapters for perspective control. Unlike what has so far been reported in the literature, a compact pyramidal configuration of the recording system installed at the engine test bench was chosen. This configuration ensured 4 independent angles of view ranging between 20 and 30 degrees with respect to the cylinder's axes. The light reflections manifesting differently with respect to each of the 4 cameras were reduced via an adjustable knife edged system independently placed in front of each lens. The in-house synchronisation box was adjusted to ensure phase-locked measurements at 7 CAD going from mid-intake to mid-compression (-274, -250, -226, -178, -130, -106 and -82 CAD). Beyond these limits, the field of view was obstructed. Finally, the achieved field of view had a resolution of 2048×2048 pixels corresponding to $81\times81\times\Delta Z$ mm^3.

The main constraints for Tomo-PIV were defining the investigation volume thickness on the one hand and obtaining an accurate 3D calibration of the cameras on the other hand. Since the investigated volume is highly confined and moving a calibration target across the entire domain in the presence of the cylinder is not possible, a first calibration procedure was introduced using an additional setup that allowed translating the recording system and reproducing the test section positioning with respect to the cameras

thus granting free access into the cylinder. Using this *in-situ* calibration procedure, *in-situ* camera models were computed and corrected via the self-calibration technique using low density particle images. Then 3 campaigns for 3 volume thicknesses (3, 5 and 8 mm) were considered in order to establish the largest admissible domain. 3D velocity fields were obtained from pre-processed particle images using Tomo-PIV codes developed by PPRIME institute after optimisation of the codes input parameters. The in-cylinder measurements were then validated for the thickest domain of 8 mm in z-direction by evaluating the convergence of velocity components, assessing the mean and fluctuating velocities as well as the evolution of instantaneous velocity magnitudes for a series of 250 engine cycles. Moreover, conservation of mass was applied and results in the mid-cylinder plane were compared to 2D measurements and were found equivalent.

In a second step, and to avoid any displacement of the recording system in addition to overcoming confinement, a novel *ex-situ* calibration procedure was introduced associating the displacement of a calibration target in the absence of confinement to a geometrical transformation acquired from the central plane of the confined investigation volume. This translates into a deformation function used to project all in-cylinder particle images onto a no-cylinder domain then use them for the self-calibration of the *ex-situ* camera models. This combination resulted in 3D camera models that take into account optical deformations introduced by the confinement and that are able to ensure high quality of volumetric reconstruction which was performed after projecting all recorded particle images using the computed deformation function. Results of the *ex-situ* process were compared to those of the *in-situ* process and were found quasi-identical with less than 2.5% differences in the planes farthest from Z_0-plane.

In chapter three, results obtained from the high-speed PIV measurements in the combustion chamber were analysed and interpreted for the 6 engine operation conditions. First the ensemble average velocity fields and their fluctuations were described. A global tracking of turbulent kinetic energy showed the higher fluctuations of V25 compared to V50 fluctuations which in turn were higher than V100. Using the Γ criterion for the identification of vortices based on the topology of the velocity, the position of the tumble centre was identified for the different recorded engine phases and mean tumble trajectories were compared. Few similarities were observed between V50 and V100 while V25 revealed a very different trajectory centred in the field of view.

Furthermore, using phase-dependant proper orthogonal decomposition (POD), the coherent structures in instantaneous velocity fields were isolated at the same engine phase and their cyclic variabilities were identified with respect to tumble centre positioning. The first 5 POD modes were used for the reconstruction of velocity fields after a cumulative

kinetic energy analysis showed that they contain over 95% of the total energy. An analysis of tumble centre location variations at a determined crank angle degree was conducted for the 300 recorded snapshots. The RMS of X and Y positions at each crank angle degree were then deduced to show the tumble centre fluctuations with respect to the engine operation condition. This showed greater variations of tumble centre along Y-direction during compression, in all cases. Particularly in the case of V25, high fluctuations are revealed during both intake and compression strokes. Depending on the inlet flow blockage (V100, V50, V25), the behaviour of cycle-to-cycle fluctuations with respect to engine speed varied in a non-uniform manner. This was revealed by computing an influence ratio IR between TKE at an engine speed of 3000 RPM and TKE at 2000 RPM, for each of the three inlet flow conditions. Case V50 exhibited greater IR during the intake stroke compared to the other cases showing a greater sensitivity to the increase in engine rotational speed while V25 revealed the greatest IR values during the compression stroke. Furthermore, a classification approach of velocity fields was performed regarding the instantaneous tumble positions. Hence, the influence of the spatial cyclic variations of tumble centre on the instantaneous velocity fluctuations (u', v') was quantified and found to contribute up to 30% to the local TKE. This approach of classification of engine cycles with respect to a fixed flow characteristic (tumble position) allows a more realistic estimation of the TKE of each individual engine cycle with respect to the global TKE since CCV are removed from the evaluation.

Results obtained from Tomo-PIV measurements showed a greater 3D character of the in-cylinder flow during intake than during compression. In other words, the third velocity component w is more important during intake than during compression. The flows behaviour with respect to the six engine operation conditions was examined, similarly to the 2D measurements, with an extension of information beyond the mid-cylinder plane. With respect to velocity fluctuations, the very small magnitude of the third velocity component w compared to the other velocity components reflected in a very small contribution of w' to the total turbulent kinetic energy in the investigation volume, particularly near BDC. When studying small scales turbulence, it is believed that 2D measurements can provide greater accuracy than volumetric measurements. With respect to studying the cyclic fluctuations of coherent structures, tomographic PIV measurements provided a continuous overview of the complete 3D vortex core otherwise difficult to obtain via 2D measurements. For this purpose, phase-locked 3D-POD was performed over 250 snapshots to separate large scale structures from small turbulence in instantaneous velocity fields. Then, the Γ criterion was adapted to the volumetric domain by defining 7×7×3 investigation windows. This allowed obtaining a description of instantaneous and mean tumbles cores' positioning. Three operating conditions were chosen for illustrating

cyclic variabilities with respect to tumble positioning at -178 CAD for (V100, 2000 RPM), (V50, 2000 RPM) and (V50, 3000 RPM) since they best captured the entire tumble structure in the investigated volume. In the cases of incomplete tumble structure, the application of a vortex modelling technique is suggested arguing that input parameters from the incomplete tumble structure obtained from experimental measurements can be essential to obtain a complete tumble model and provide valuable information. Finally, a conditional approach for the characterisation of in-cylinder large scale structures is suggested based on the energetic contribution of POD modes' coefficients. At a given engine phase, a correlation coefficient was computed for each velocity component between instantaneous engine cycles (reconstructed via the first 14 POD modes containing 99% of the flow's energy) and a mean flow field (obtained from velocity fields reconstructed via the 4 POD modes following mode-0 without including the latter in the reconstruction.) Hence, three correlation coefficients were obtained for each engine phase, C_u, C_v and C_w, describing the resemblance between instantaneous cycles and the most recurrent large scales. Moreover, a classification approach was performed based on the distribution of C_u, C_v and C_w, and was found reliable for the separation of characteristic flow structures into groups. This was reflected in the mean flow field and the fluctuating velocity field of each group which revealed much smaller variations compared to the global ensemble average fluctuating velocity field. This analysis was illustrated for the reference case V100 at 2000 RPM, near BDC and near mid-compression. Finally, cross-correlation maps where presented in order to reveal common peaks of correlations between groups obtained from C_u, C_v and C_w. The possibility of tracing back these groups of velocity fields to find a link between their corresponding behaviours was discussed.

Outlook.

The results obtained in this study open the way for future work using the PIV technique to further investigate unsteady confined flows. Particularly in the perspectives of the 3D in-cylinder flow computation, an evaluation should be made of the *ex-situ* volumetric reconstruction which takes into account a part of optical deformations, using lower order camera models thus reducing computation time. Additionally, the phase-locked measurements presented in this work can be complemented by time-resolved 3D measurements allowing a 3D temporal tracking of coherent structures fluctuations across the engine's cycle, particularly during the compression stroke.

The conditional analysis of in-cylinder flow characteristics can be complemented in two main manners. One is leading an iterative classification process consisting of using the mean fields of groups, obtained from the distribution of correlations coefficient C_u, C_v and C_w, as an input field F_m in equation (3-14) in order to refine each group of fields by minimising the fluctuations between the fields comprised in that group. The second way is to perform a phase-invariant POD establishing one basis function for the entire engine cycle and extracting the cause and effect chain of cyclic variabilities on the one hand and the relation between the flow at the different engine phases on the other hand, using the proposed cross-correlation of coefficients C_u, C_v and C_w.

In the context of spray/flow interactions studies such as the previous work of Julien Lemetayer applying F-PIV on the CORIA's engine test bench, 3D temporal PIV measurements can complement their results and provide an extended description of gas-droplet dynamics in the engines combustion chamber (Lemetayer, 2016). The 3D distribution of drops can thus be obtained providing coupled information of position and velocity of a droplet in the 3D domain. This might remain limited however with respect to light reflexions and optical visualisation since accessing in-cylinder regions nearer to the fuel injector or ignition spark plug by means of multiple cameras is an extremely difficult task. Greater precision can be obtained by performing two-dimensional stereoscopic PIV allowing to obtain the 3 velocity components of the in-cylinder flow (2D3C). While limited instantaneously compared to Tomo-PIV measurements offering a coherent 3D velocity gradient, Stereo-PIV can offer a description of the mean in-cylinder flow in the entire volume of the engine's combustion chamber if a series of multiple planes recordings are performed.

Finally, the results obtained in the course of this work show the possibility of applying equal procedures to different experimental setups facing similar geometrical constraints of confinement, difficult optical access and harsh optical deformation.

Annexe 1

➢ Ensemble average velocity fluctuation from TR-PIV at 2000 RPM

	V100	V50	V25
CAD = -274	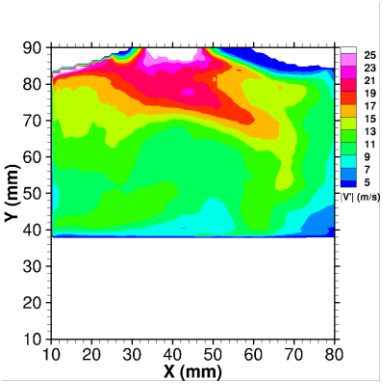	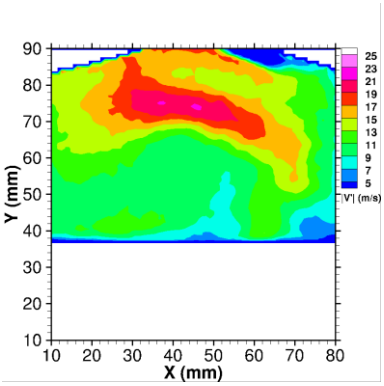	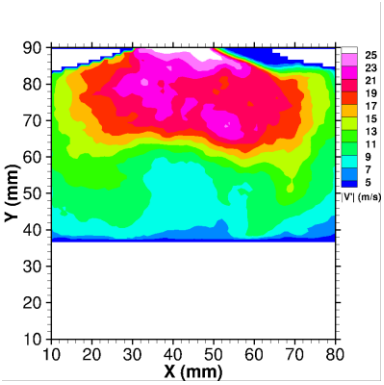
CAD = -250	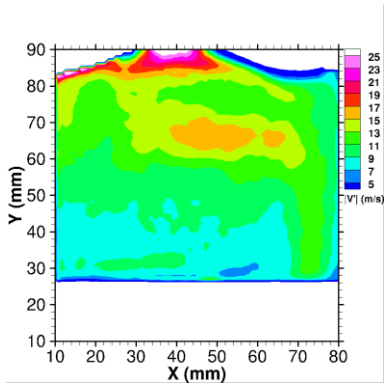	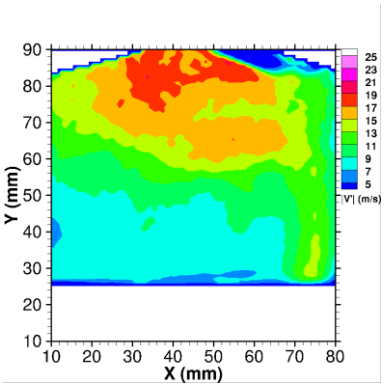	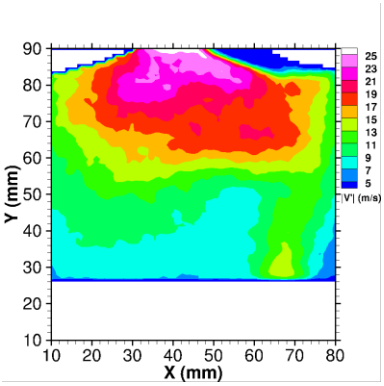
CAD = -226	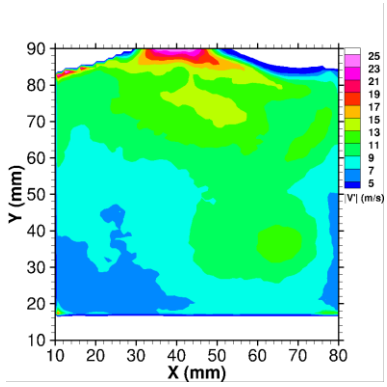	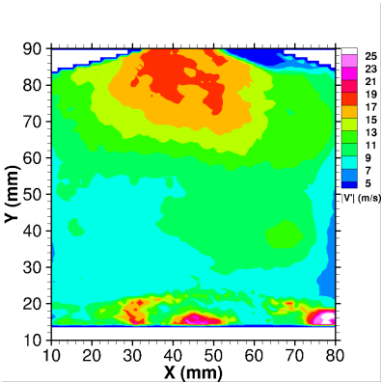	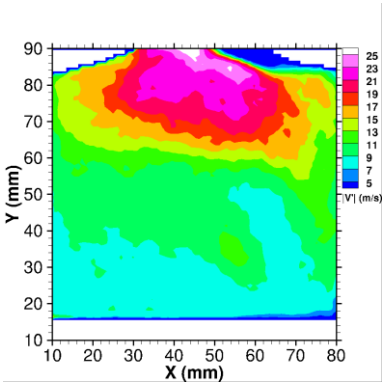
CAD = -178	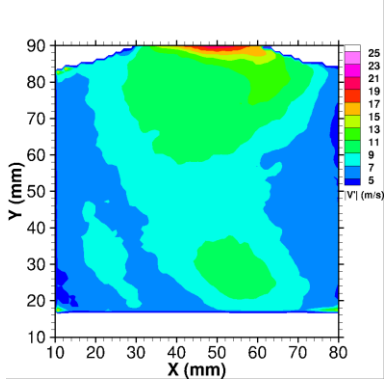	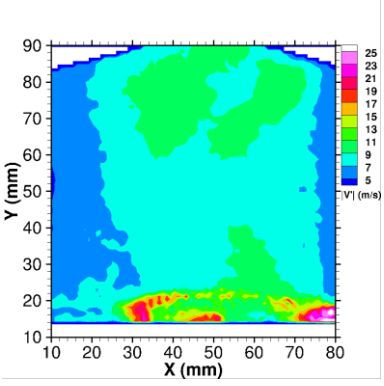	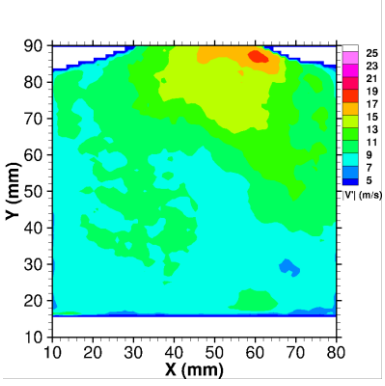

CAD = -130

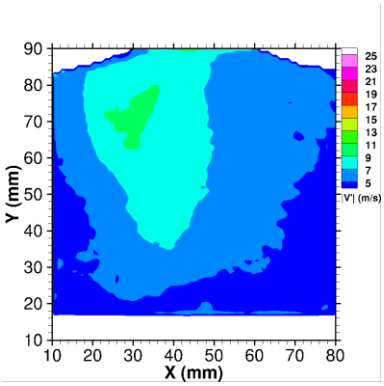

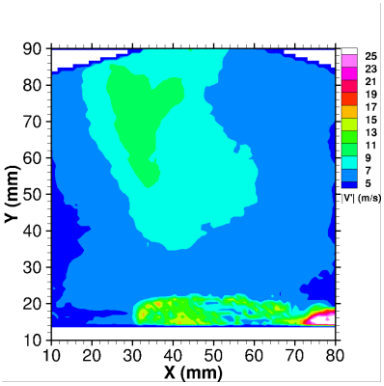

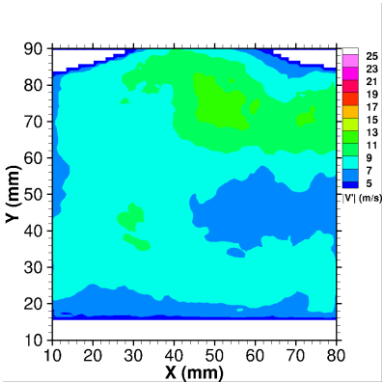

CAD = -106

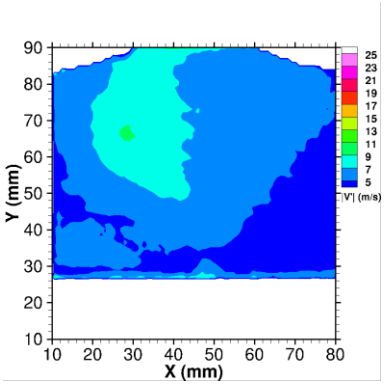

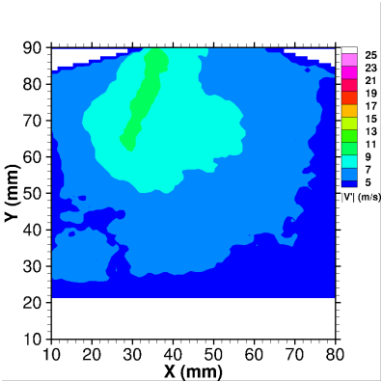

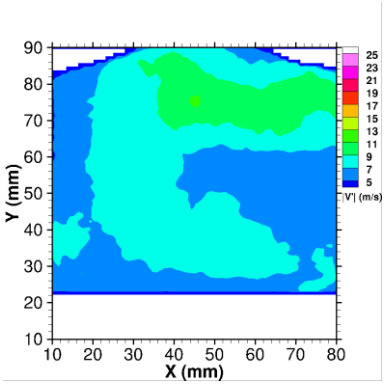

CAD = -82

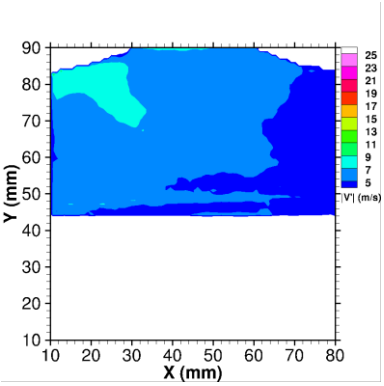

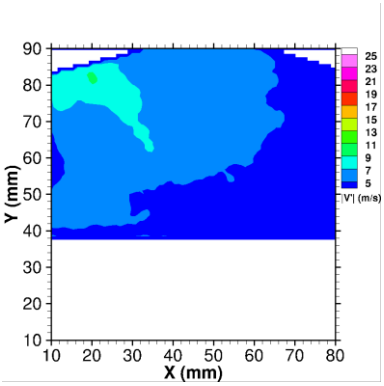

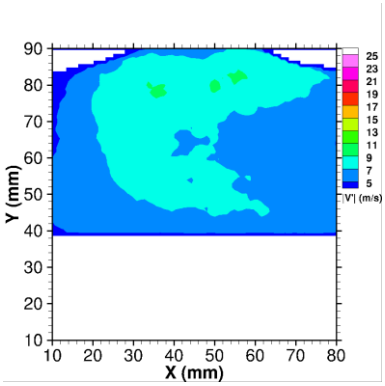

➢ Ensemble average velocity fluctuation from TR-PIV at 3000 RPM

	V100	V50	V25
CAD = -274	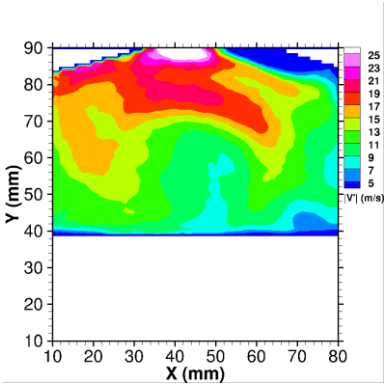	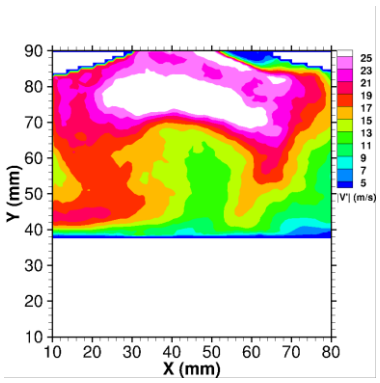	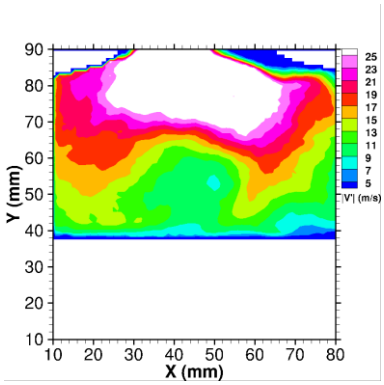
CAD = -250	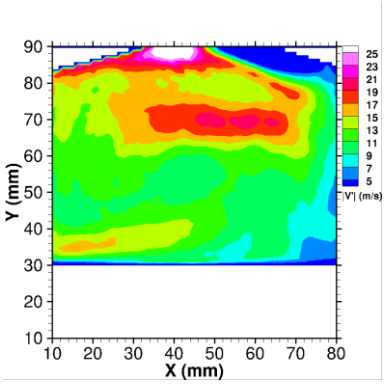	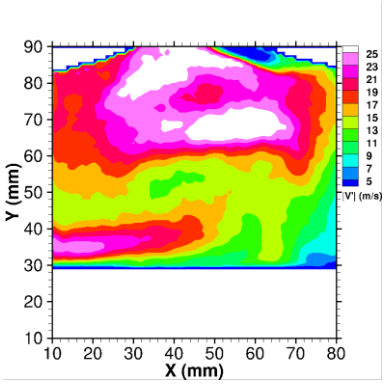	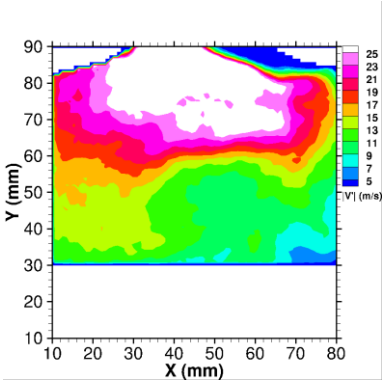
CAD = -226	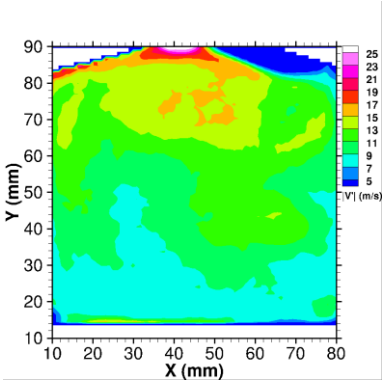	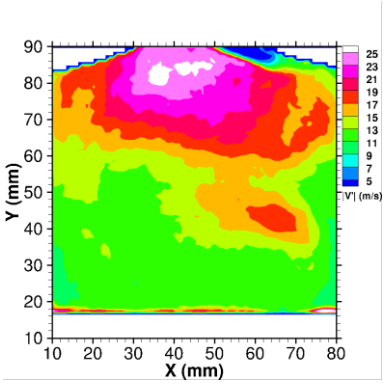	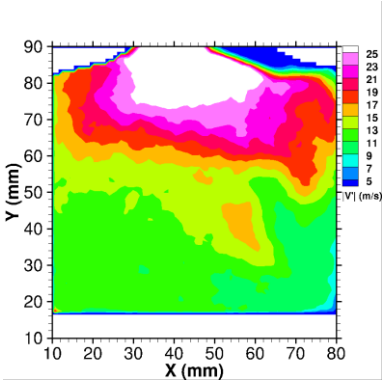
CAD = -178	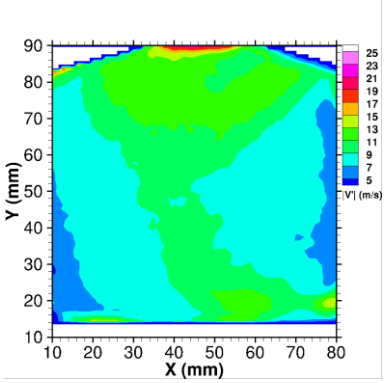	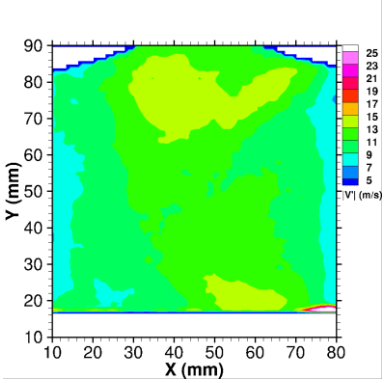	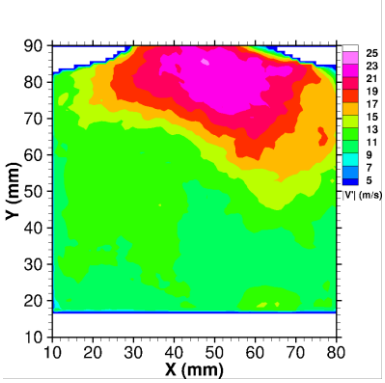

CAD = -130

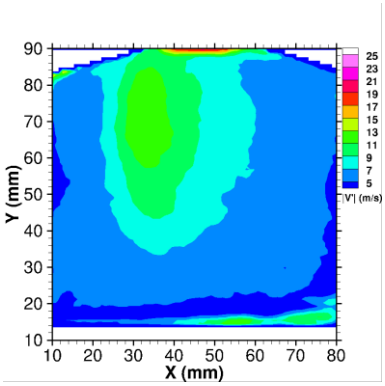

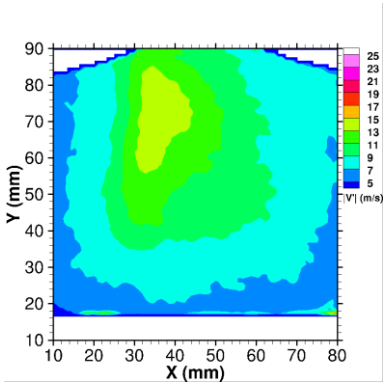

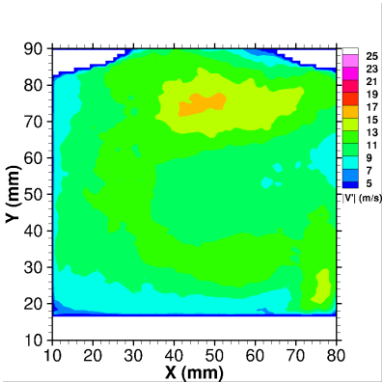

CAD = -106

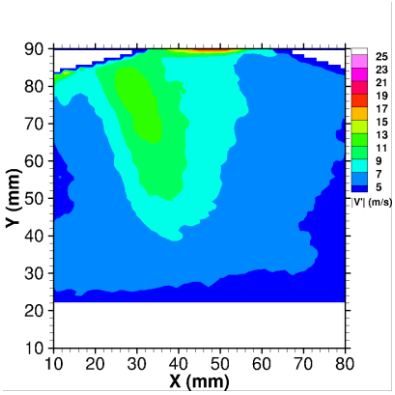

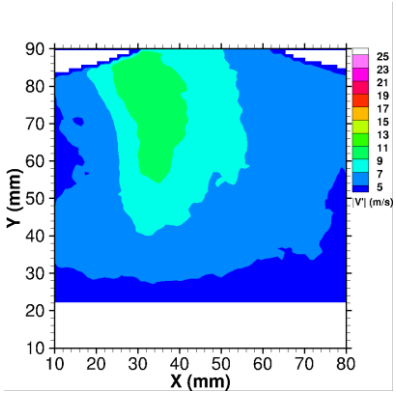

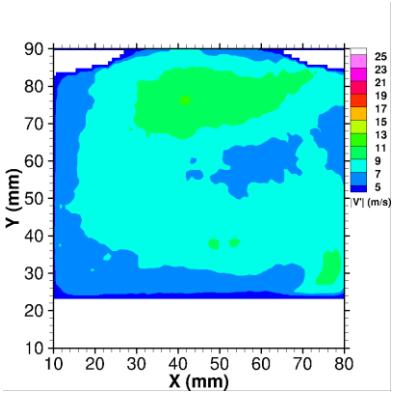

CAD = -82

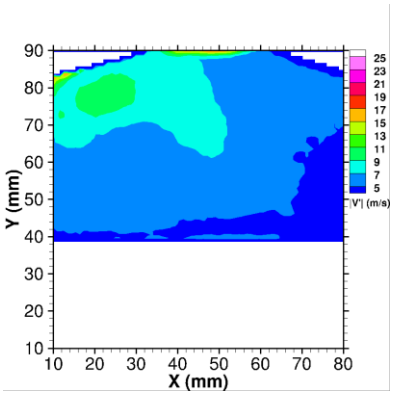

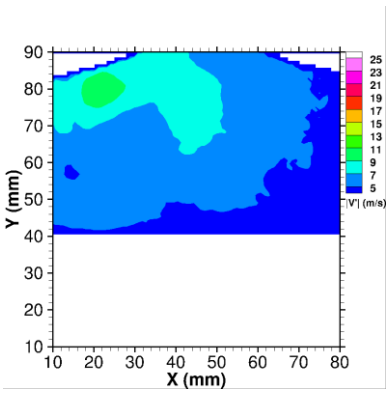

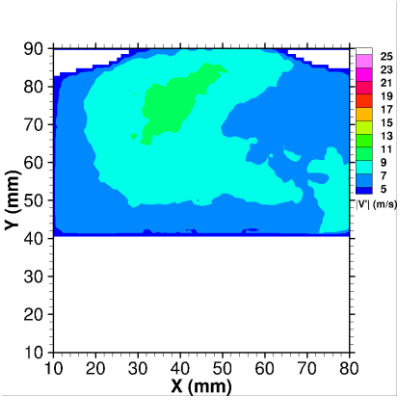

Annexe 2

- **Phase- averaged velocity fields from Tomo-PIV measurements at 2000 RPM**

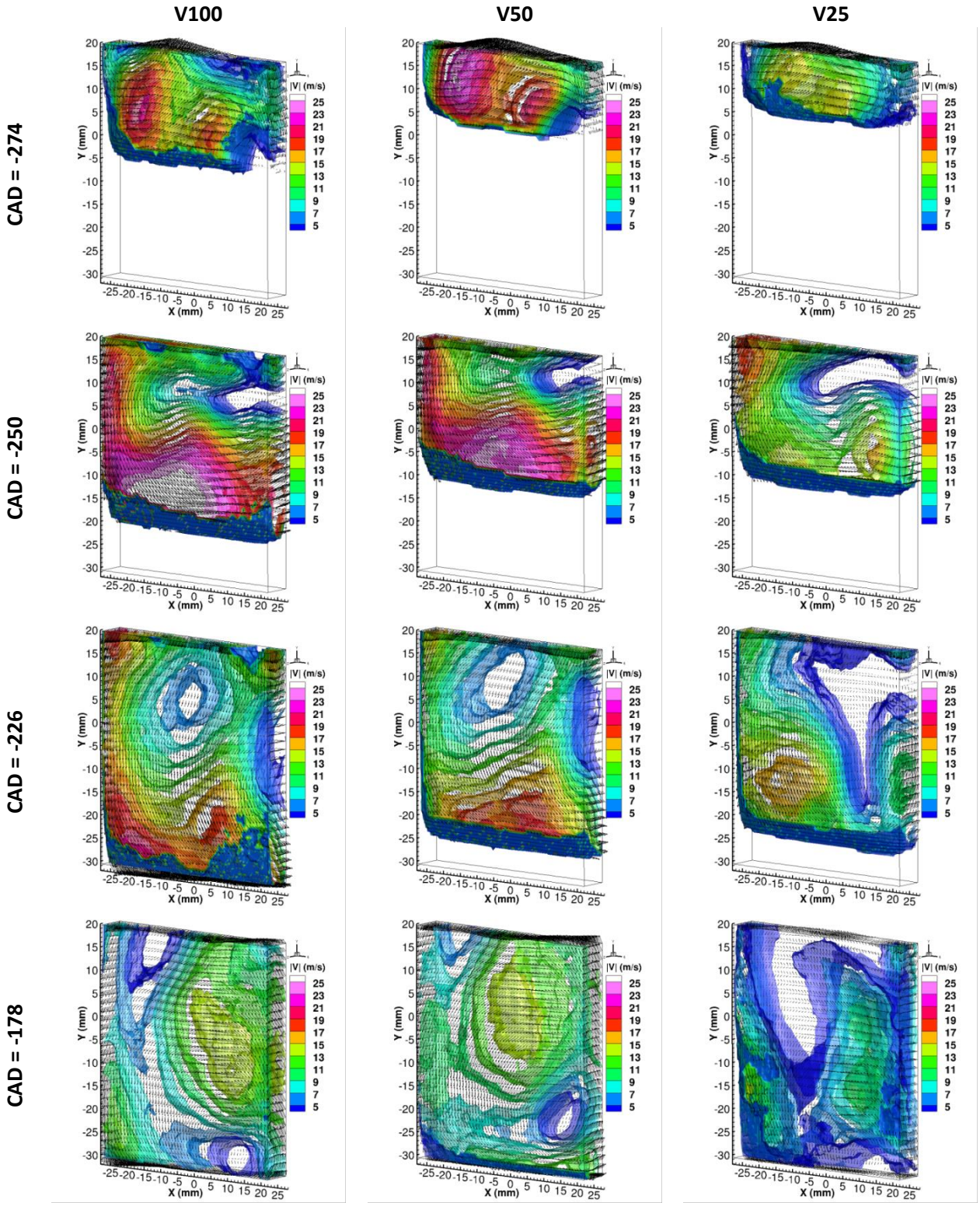

CAD = -130

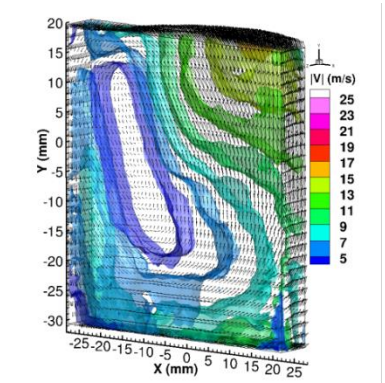

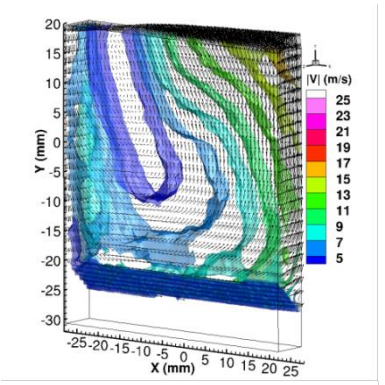

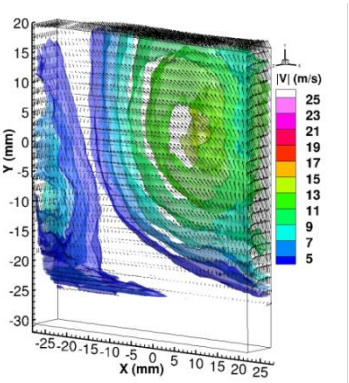

CAD = -106

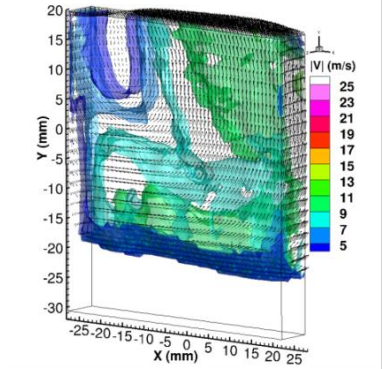

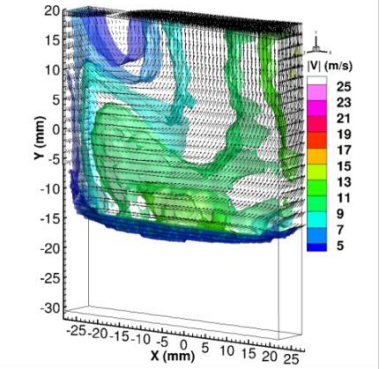

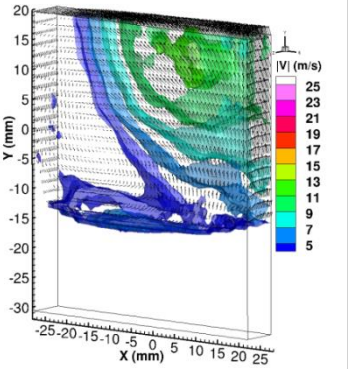

CAD = -82

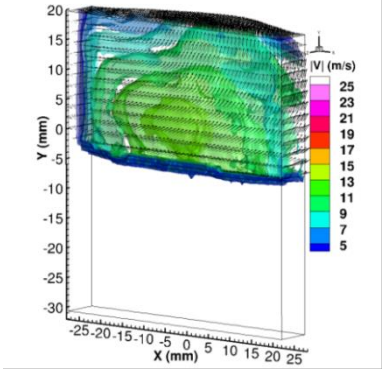

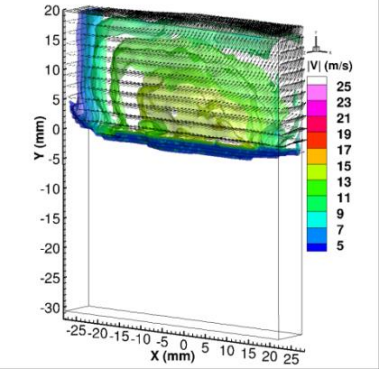

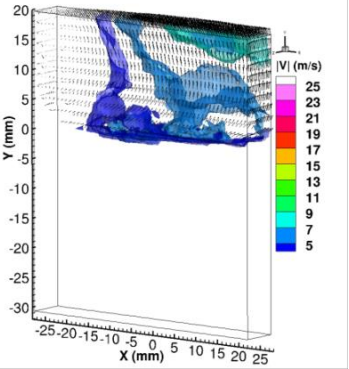

- **Phase- averaged velocity fields from Tomo-PIV measurements at 3000 RPM**

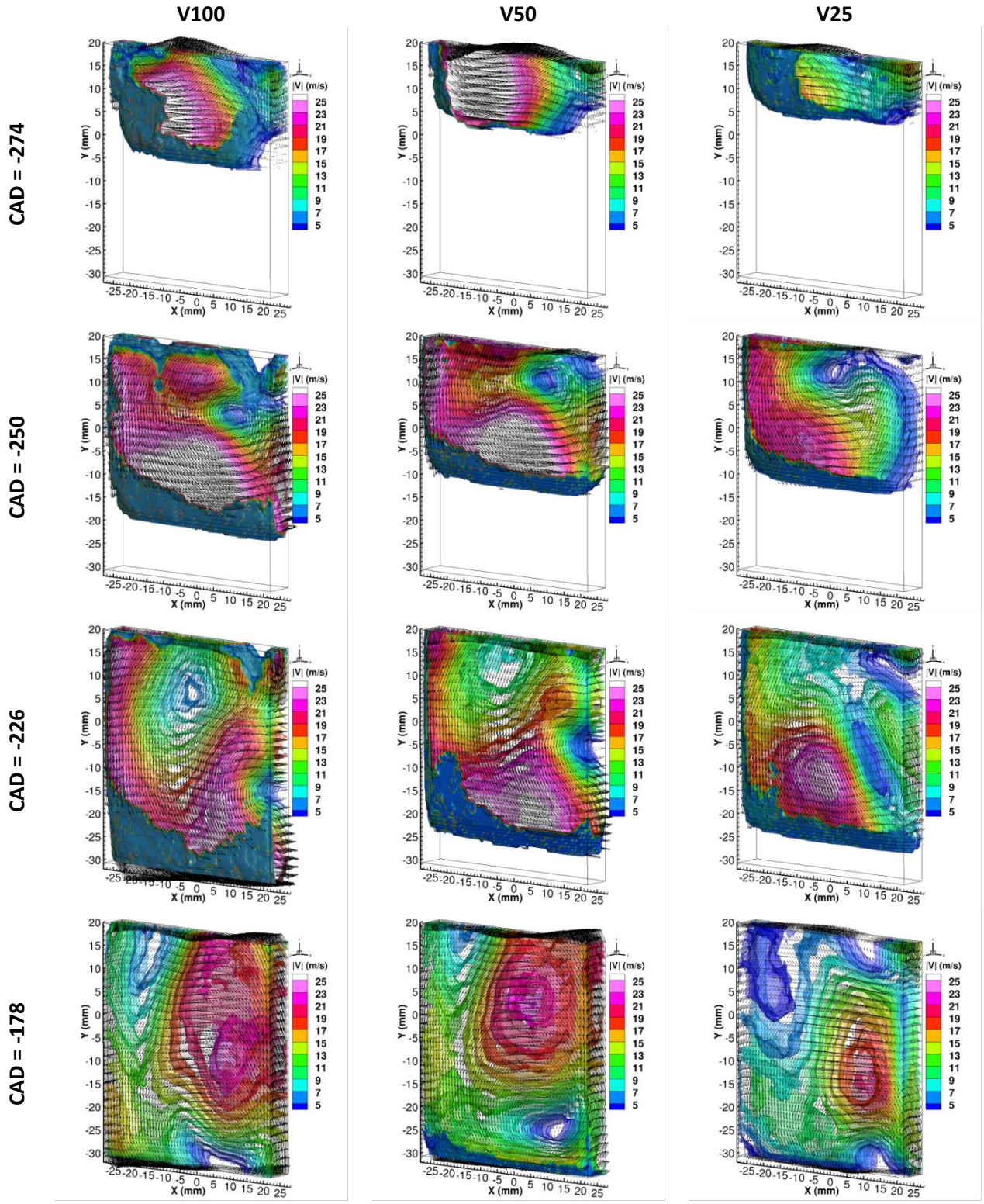

CAD = -130

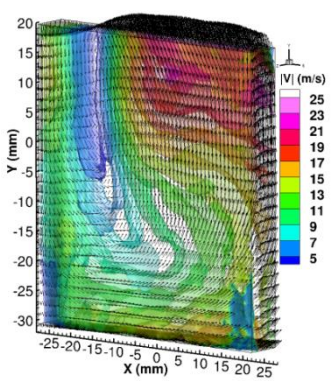

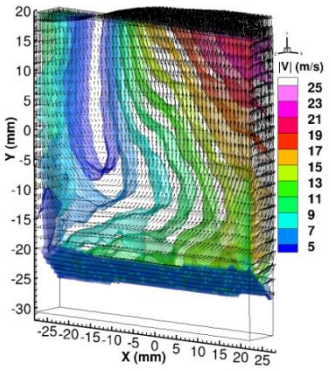

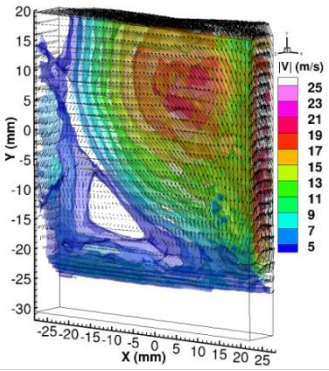

CAD = -106

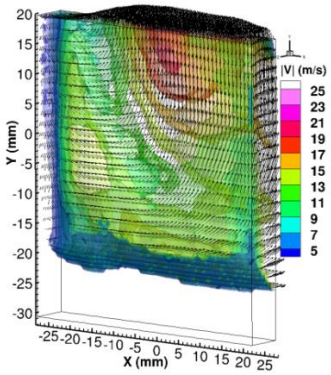

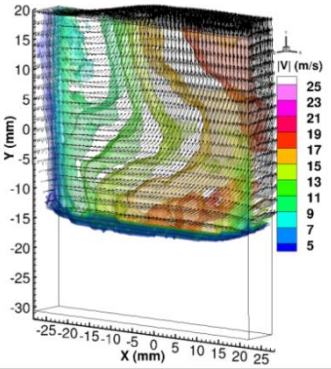

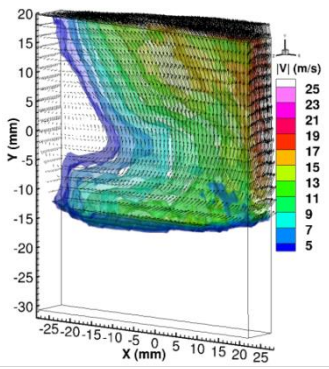

CAD = -82

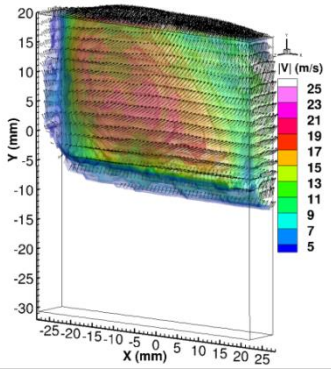

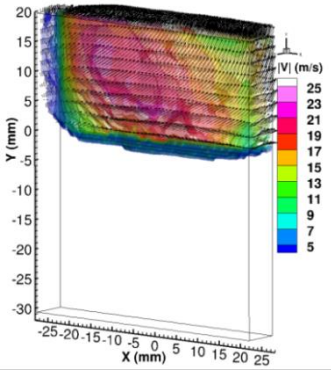

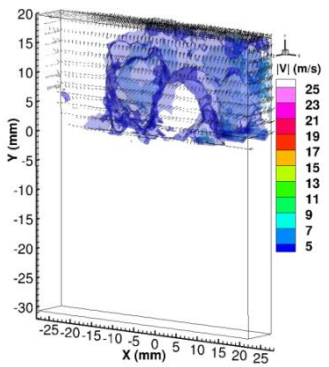

- **Phase-averaged velocity fluctuations from Tomo-PIV measurements at 2000 RPM**

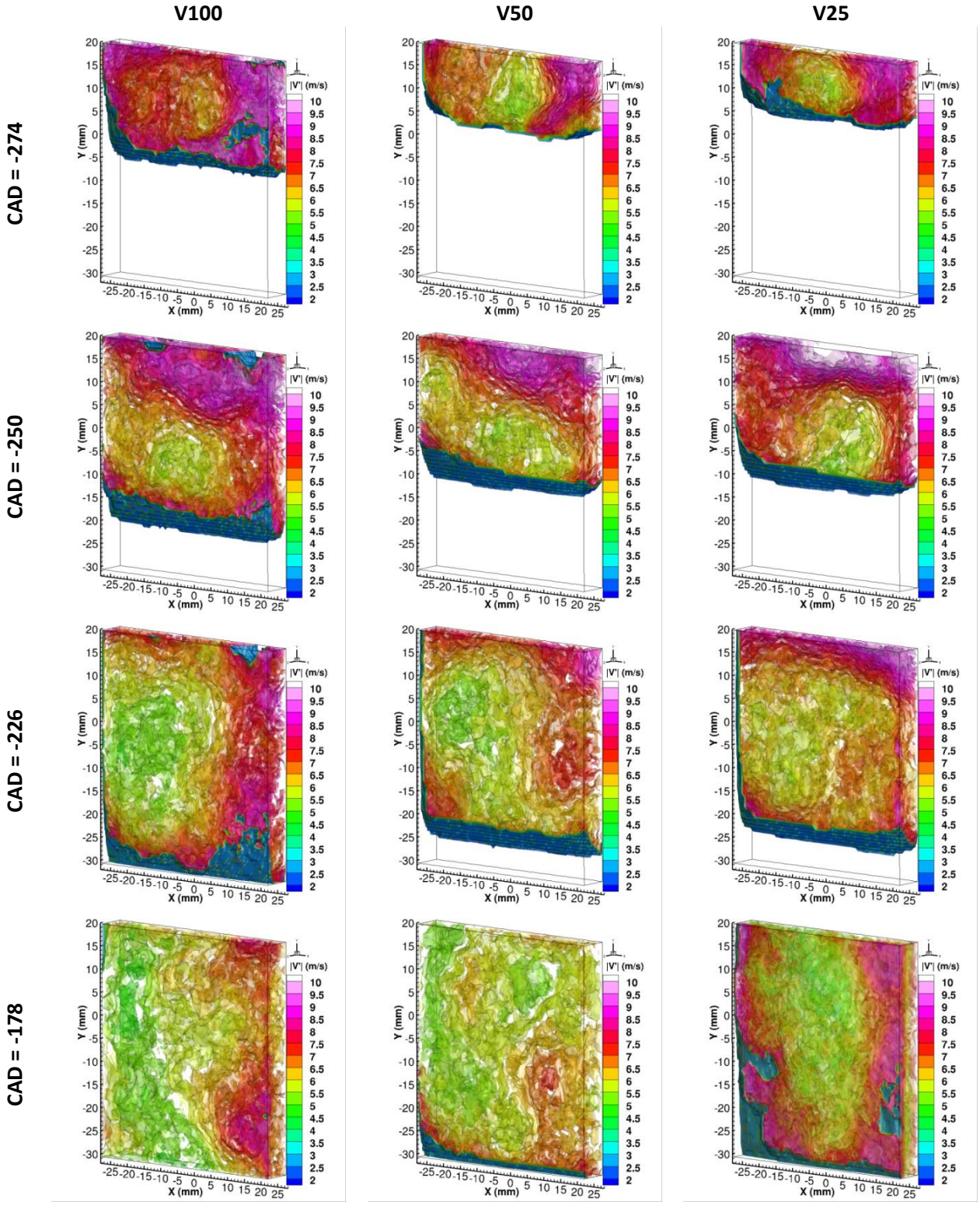

CAD = -130

CAD = -106

CAD = -82

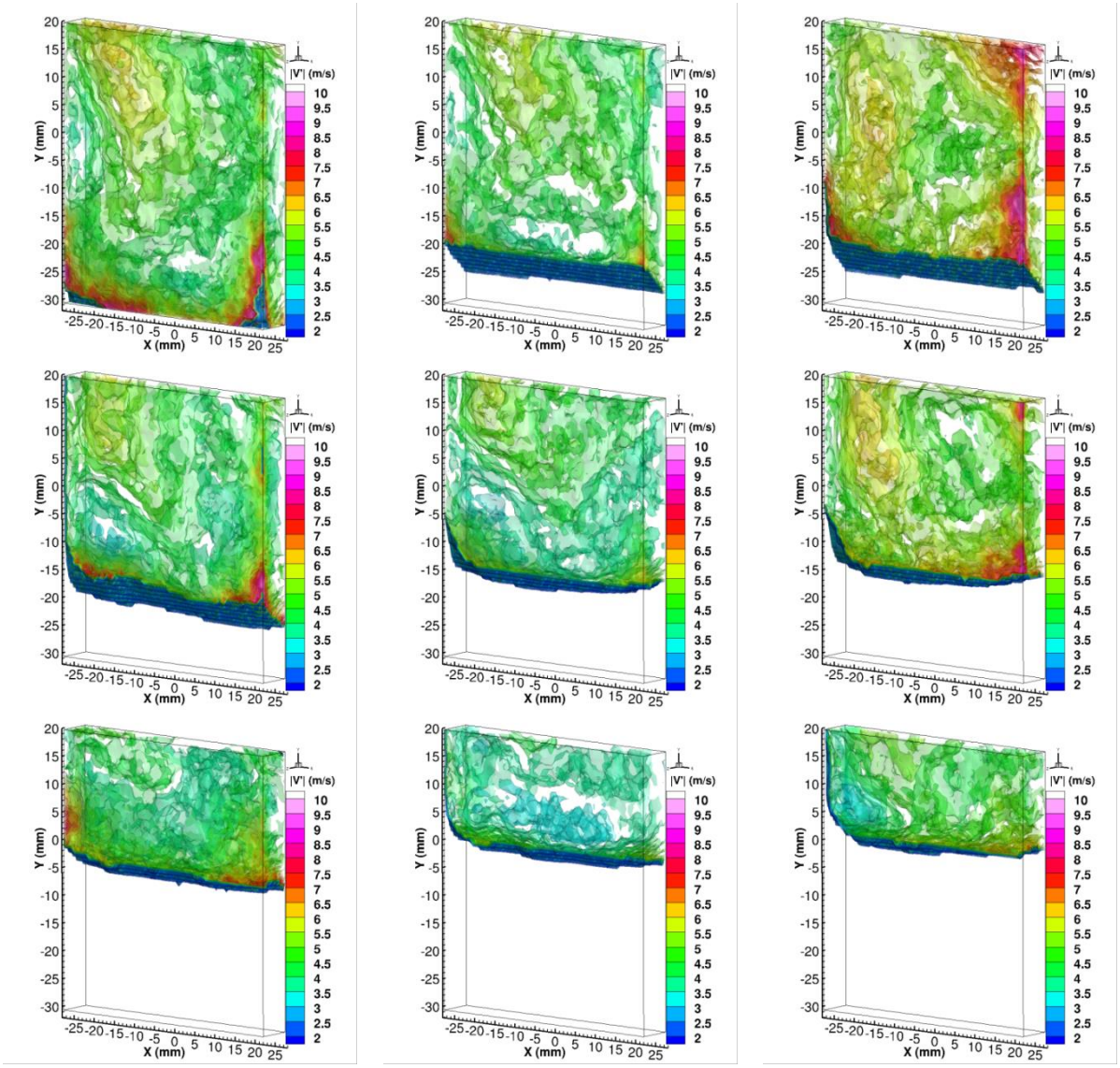

- **Phase-averaged velocity fluctuations from Tomo-PIV measurements at 3000 RPM**

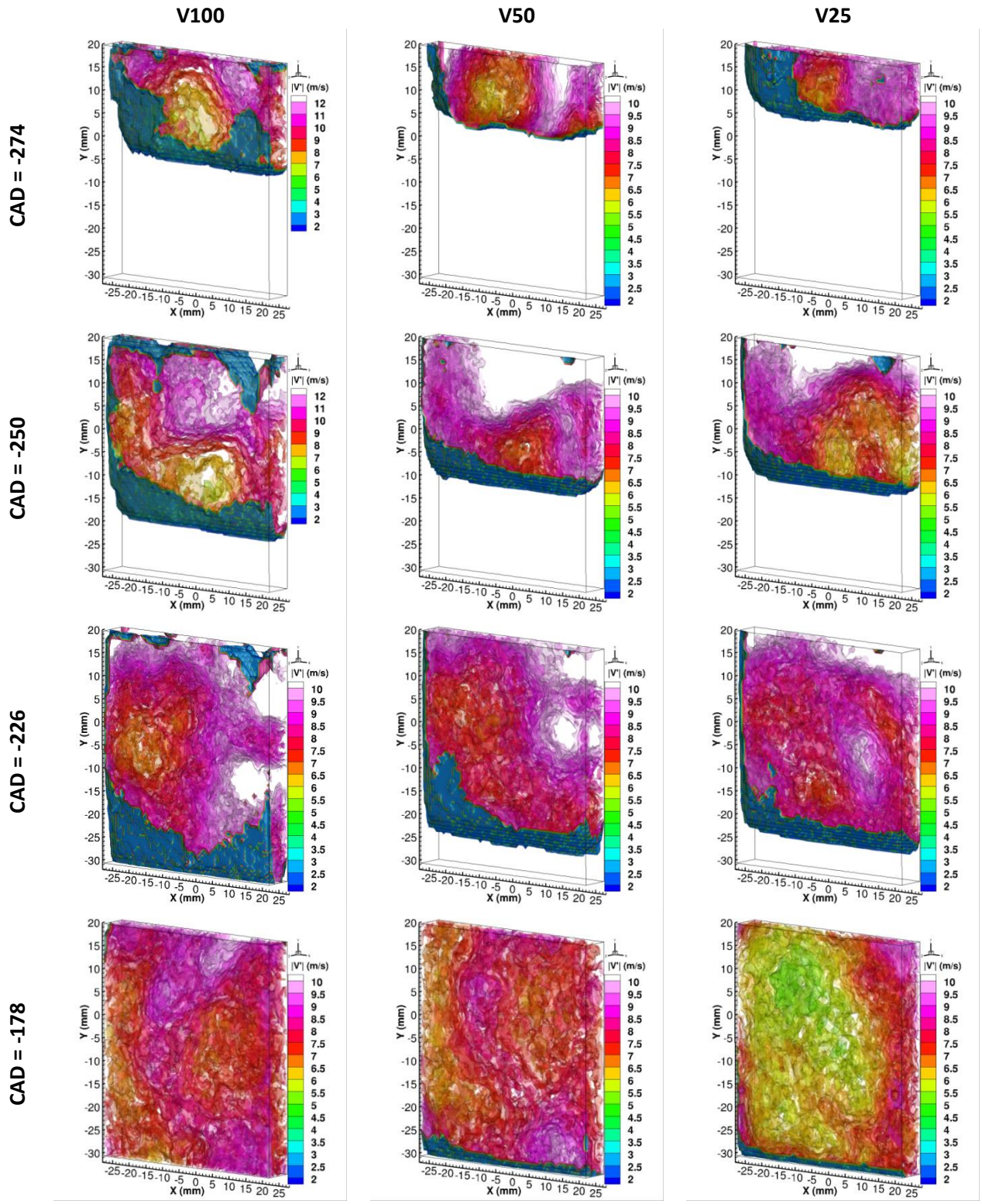

CAD = -130

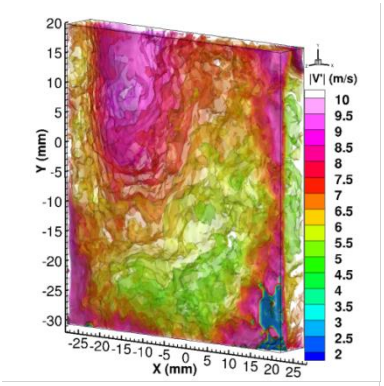

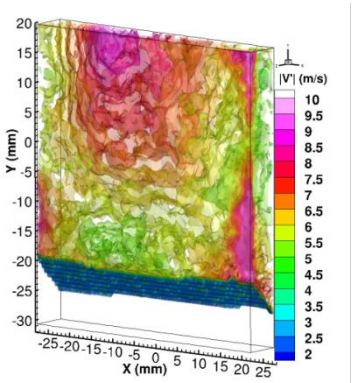

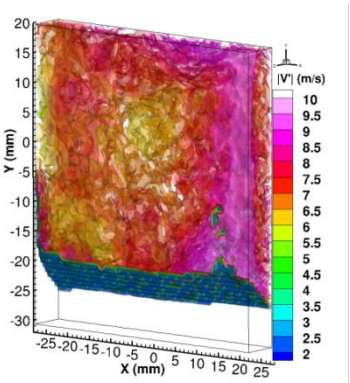

CAD = -106

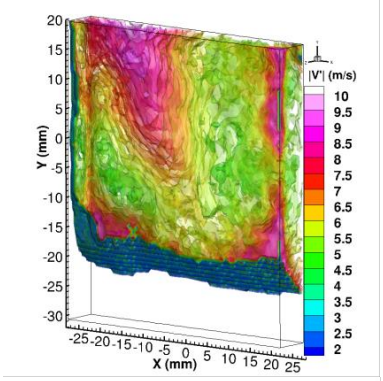

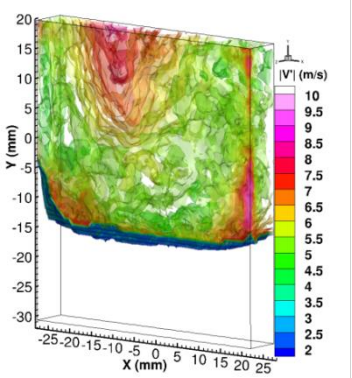

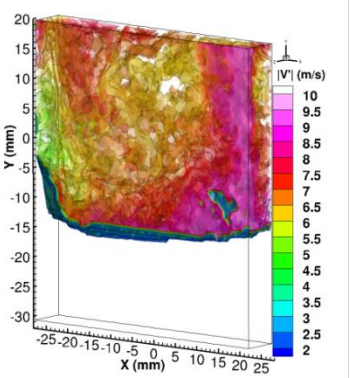

CAD = -82

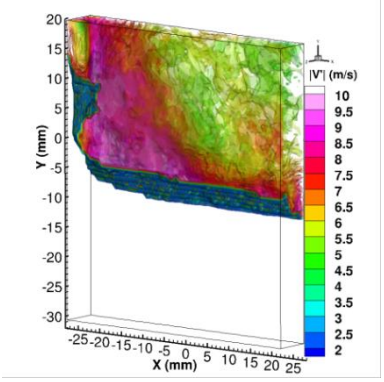

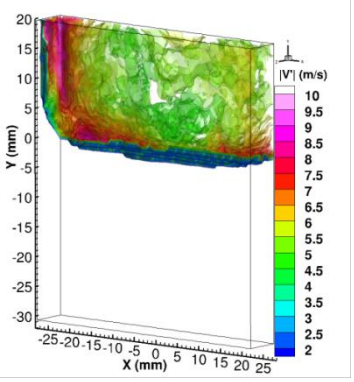

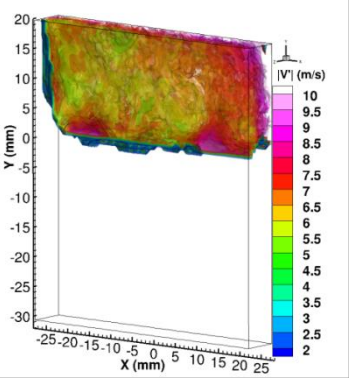

Annexe 3

➢ Z_0-plane average velocity with respect to inlet flow at 2000 RPM

Similarly to the 2D analysis, the three inlet cases are displayed at the considered rotational speed of 2000 RPM. The deduction made for V100 in §2.2.4.4 of the manuscript, where the 3D data was compared to 2D data, can be made for V50 and V25. In other terms, the three cases show the same engine flow characteristics as the 2D recorded data in this plane, more accurately in the common regions of measurements. This observation on the one hand validates furthermore the quality of our 3D tomographic measurements. On the other hand, it allows us to draw the same description about the inlet flow's influence on the aerodynamics in the tumble plane during intake and compression strokes.

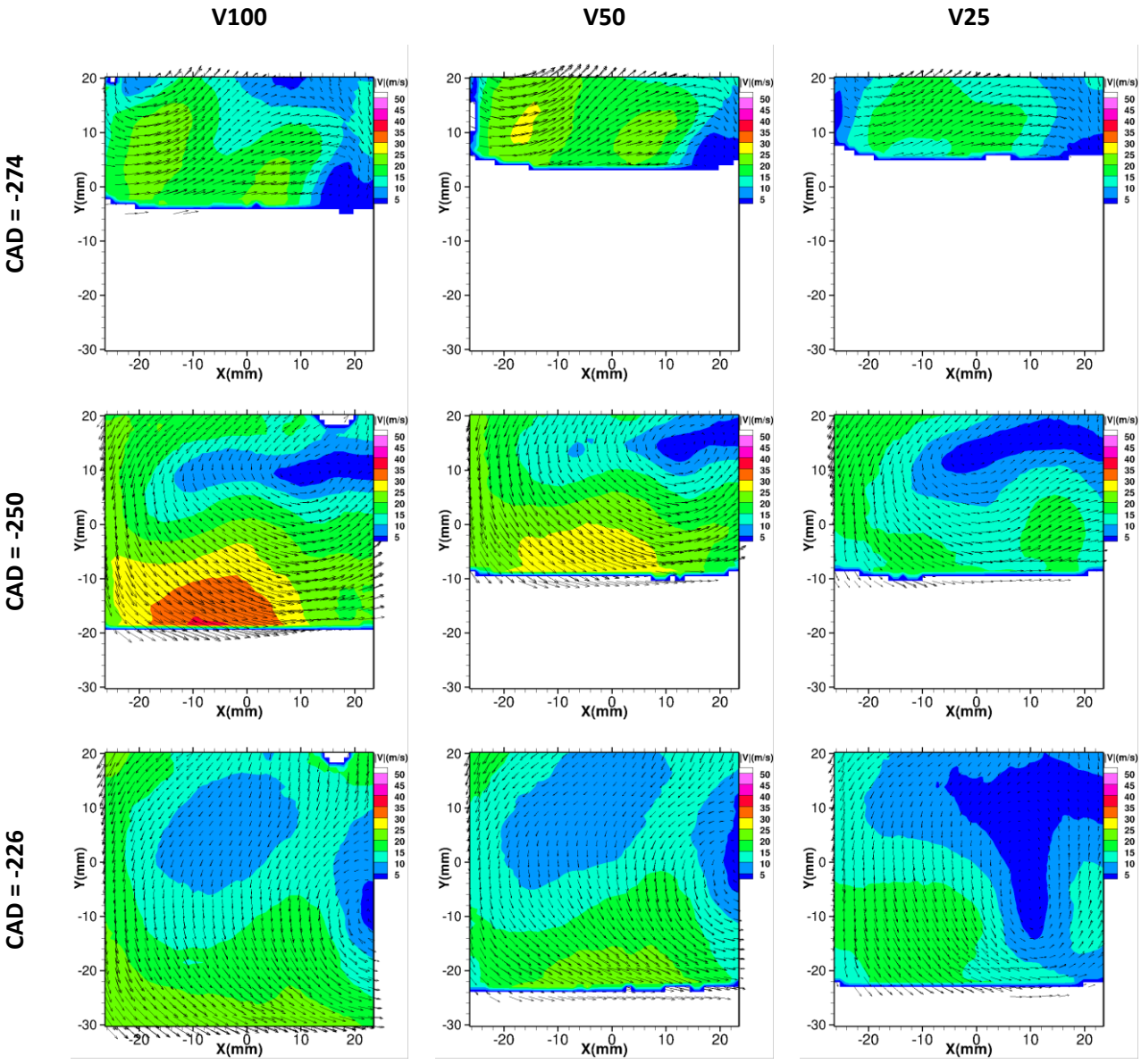

CAD = -178

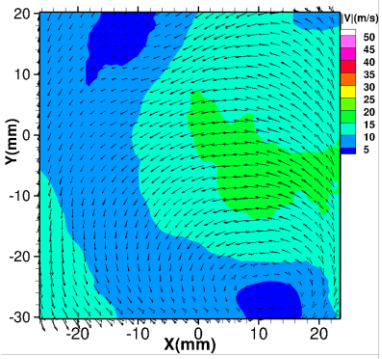

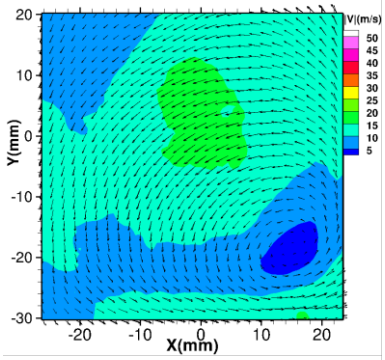

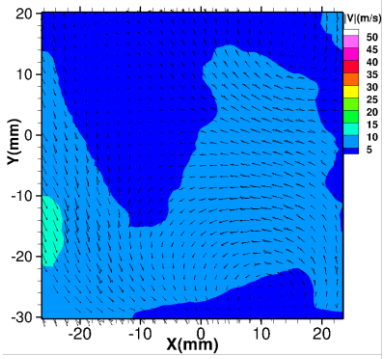

CAD = -130

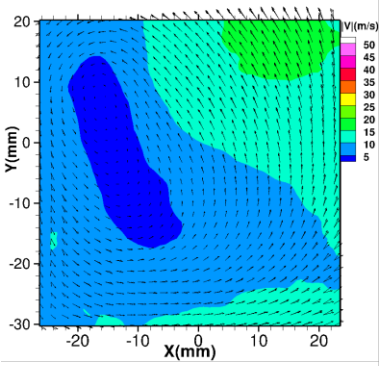

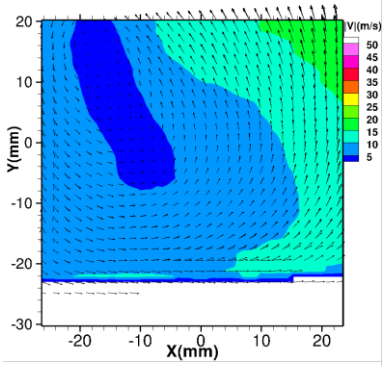

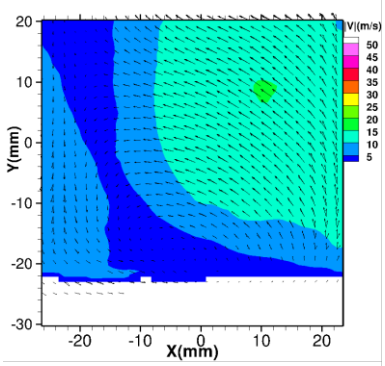

CAD = -106

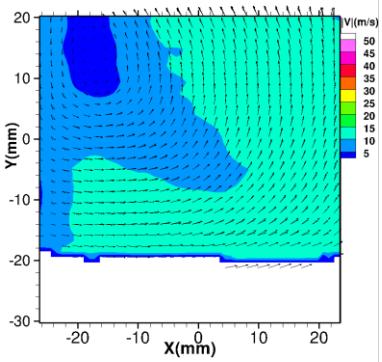

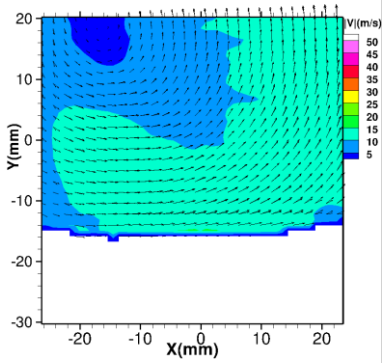

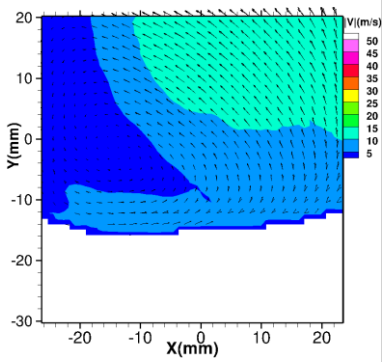

CAd = -82

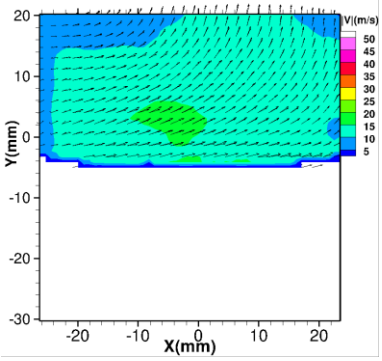

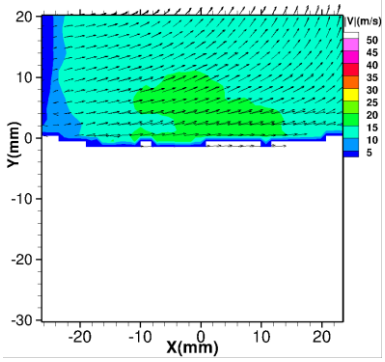

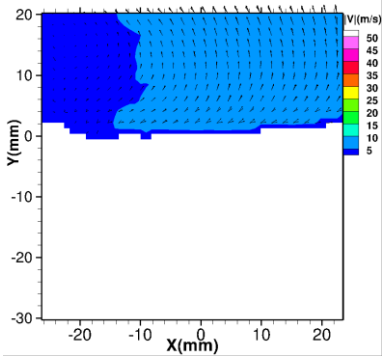

➢ Z_0-plane fluctuations from Tomo-PIV measurements at 2000 RPM

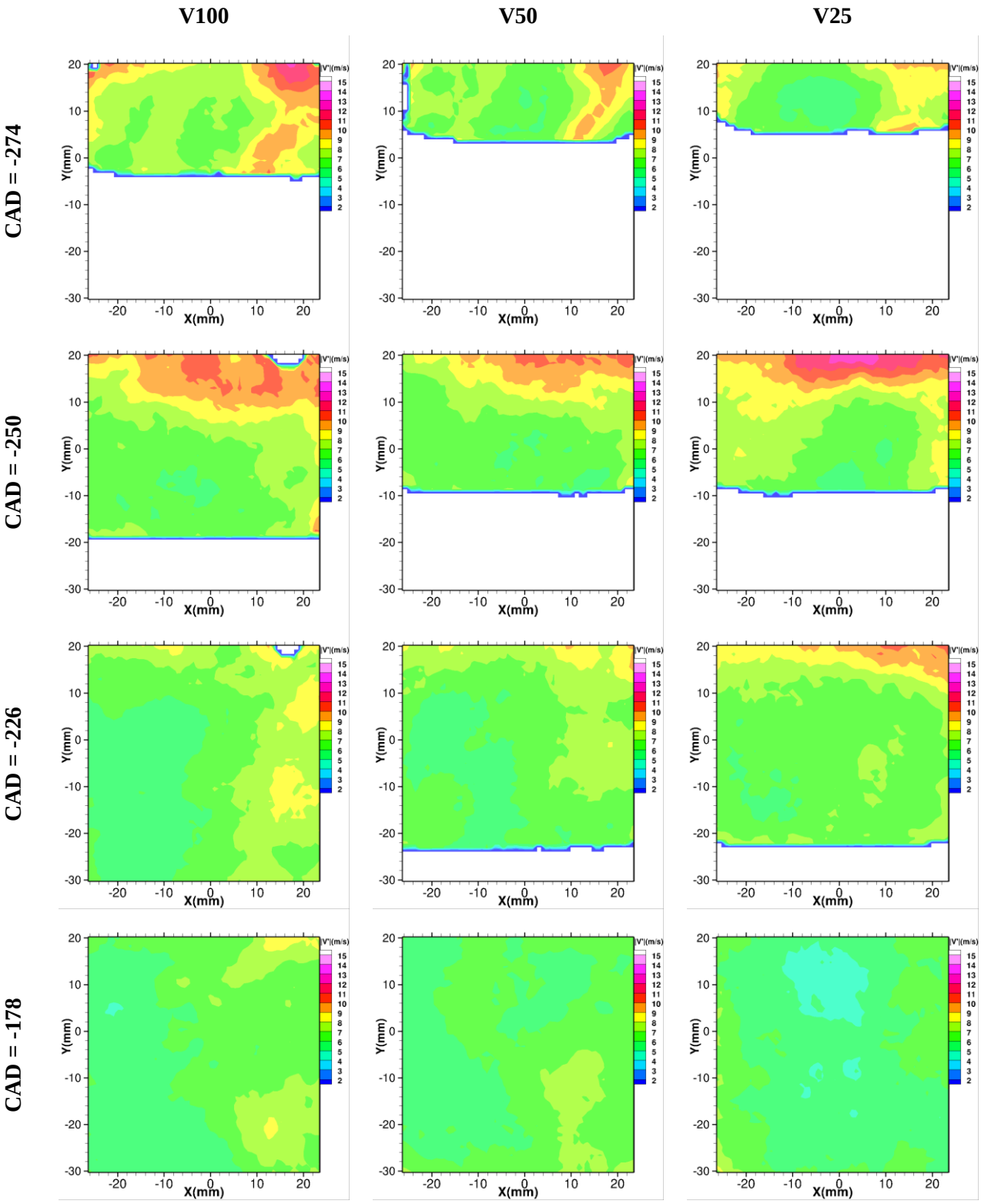

CAD = -130

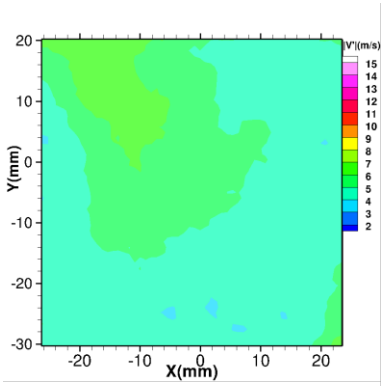

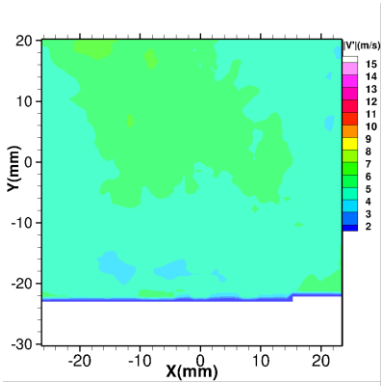

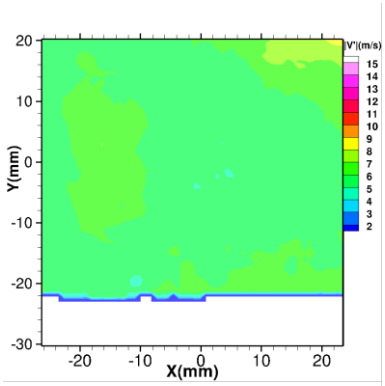

CAD = -106

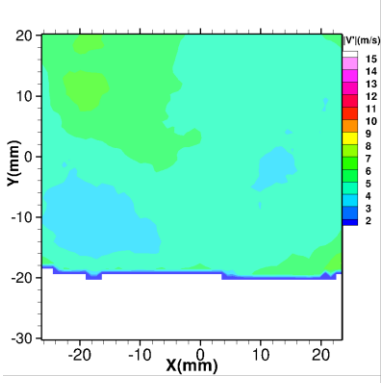

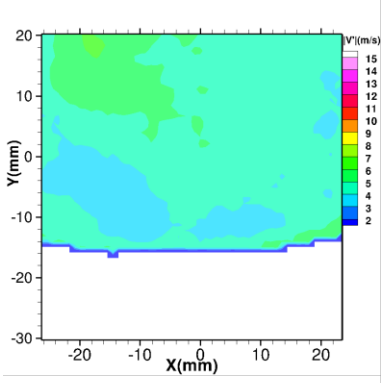

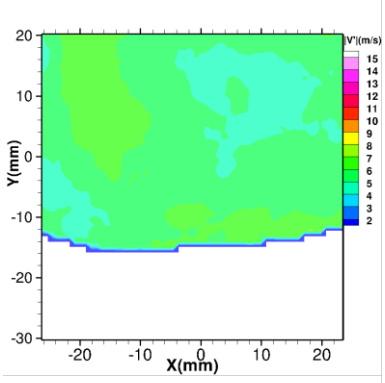

CAD = -82

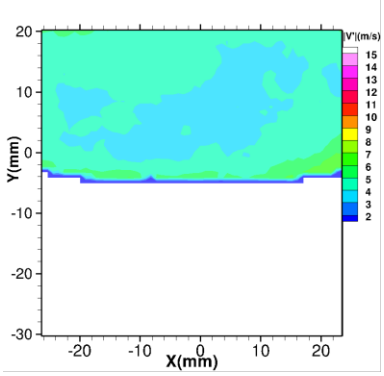

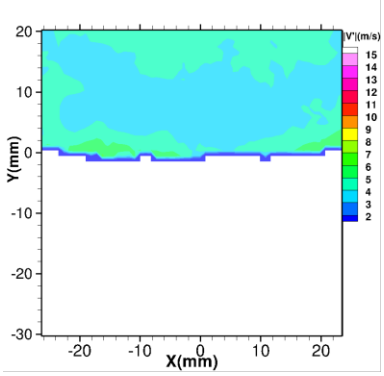

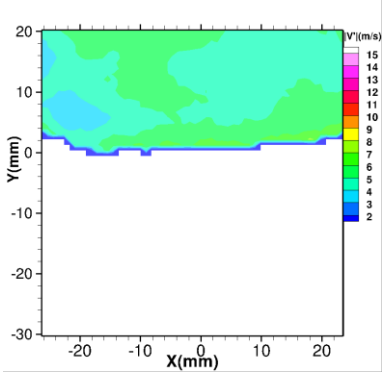

➢ Z0-plane average velocity with respect to inlet flow at 3000 RPM

Ensemble averaged velocity fields and fluctuations at Z_0-plane obtained from Tomo-PIV are shown for the three inlet cases at 3000 RPM. The same engine flow characteristics as the 2D recorded data in the common regions of measurements are again observed with the slightly smaller velocity magnitudes (§3.1).

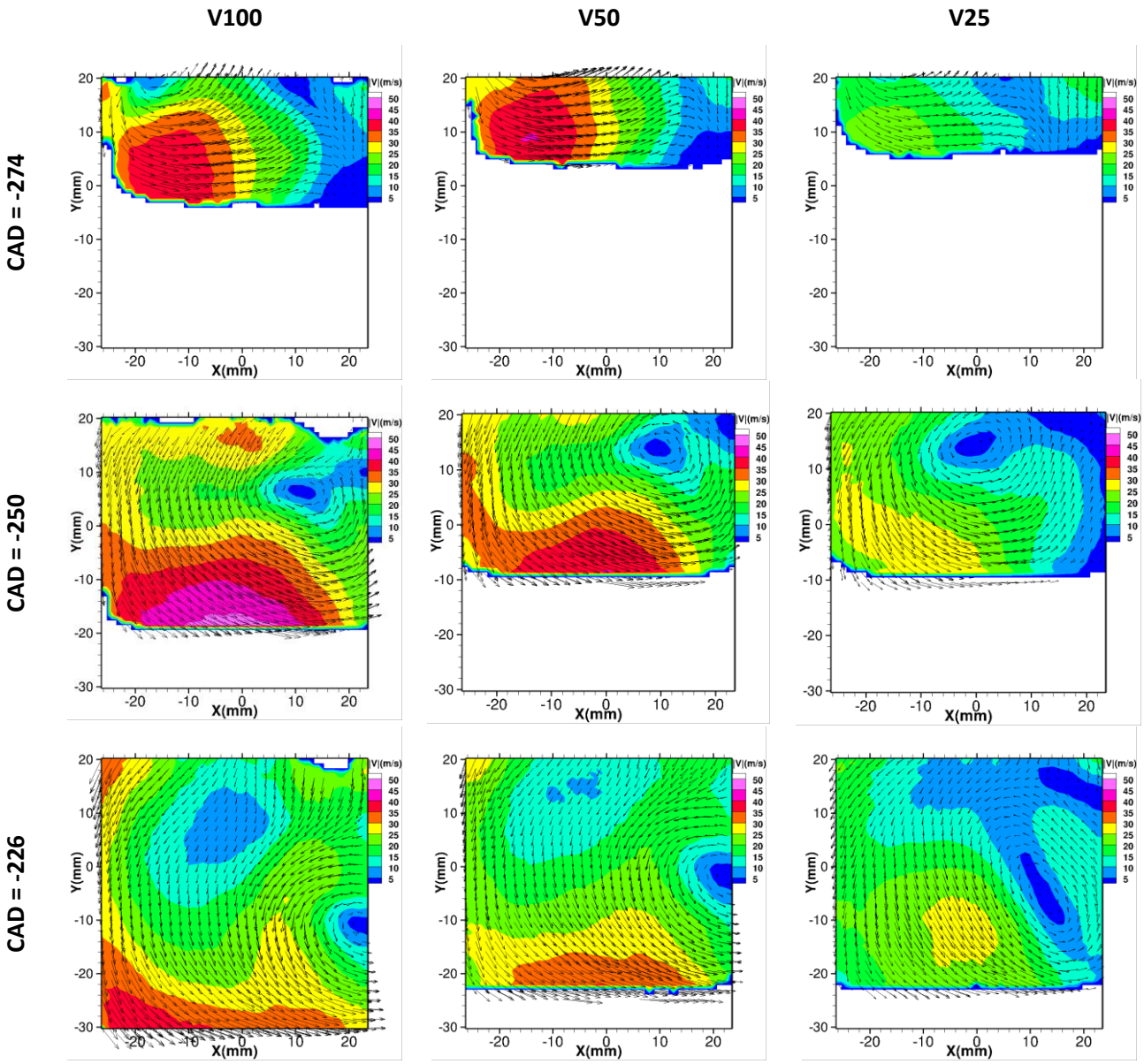

CAD = -178

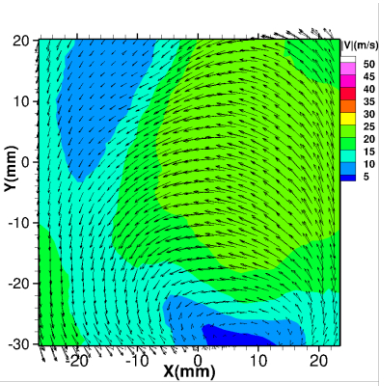

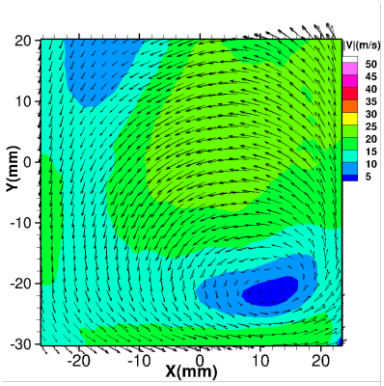

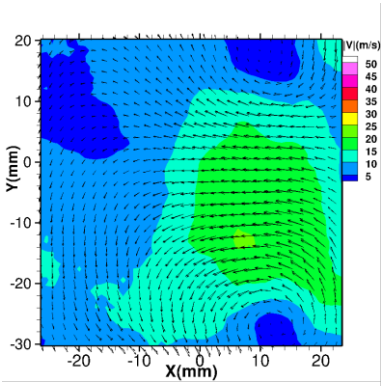

CAD = -130

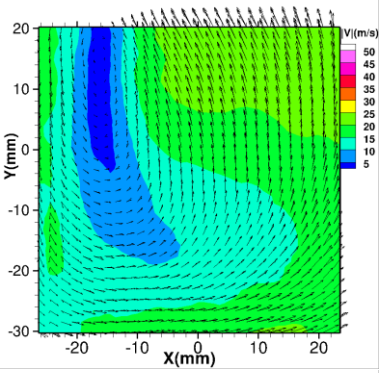

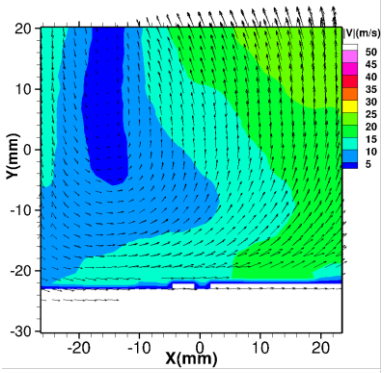

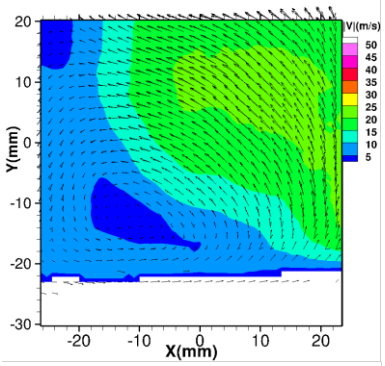

CAD = -106

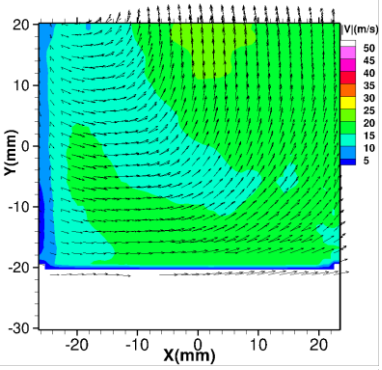

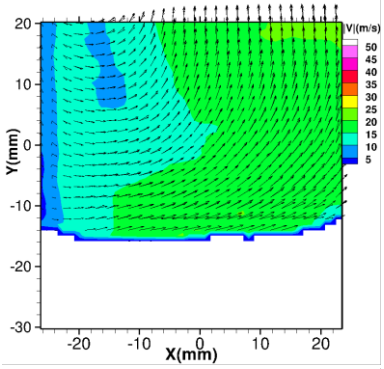

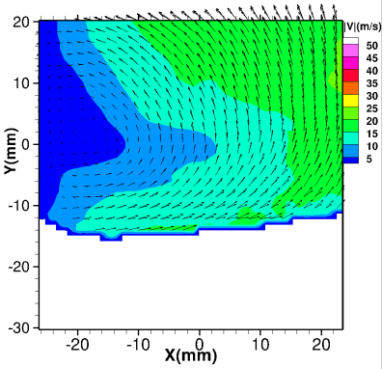

CAD = -82

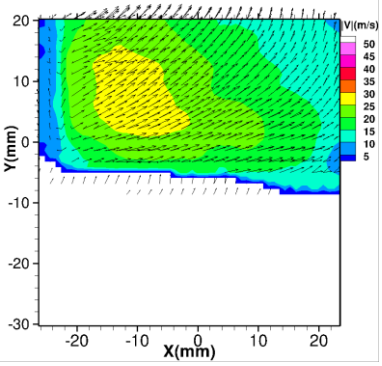

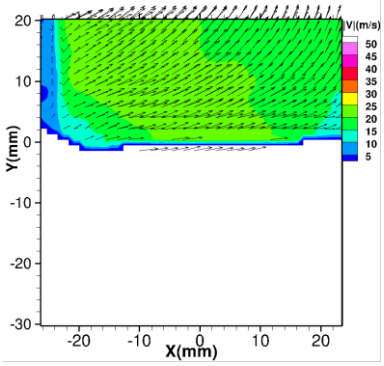

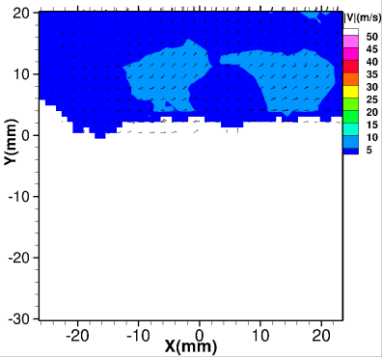

➢ Z_0-plane fluctuations from Tomo-PIV measurements at 3000 RPM

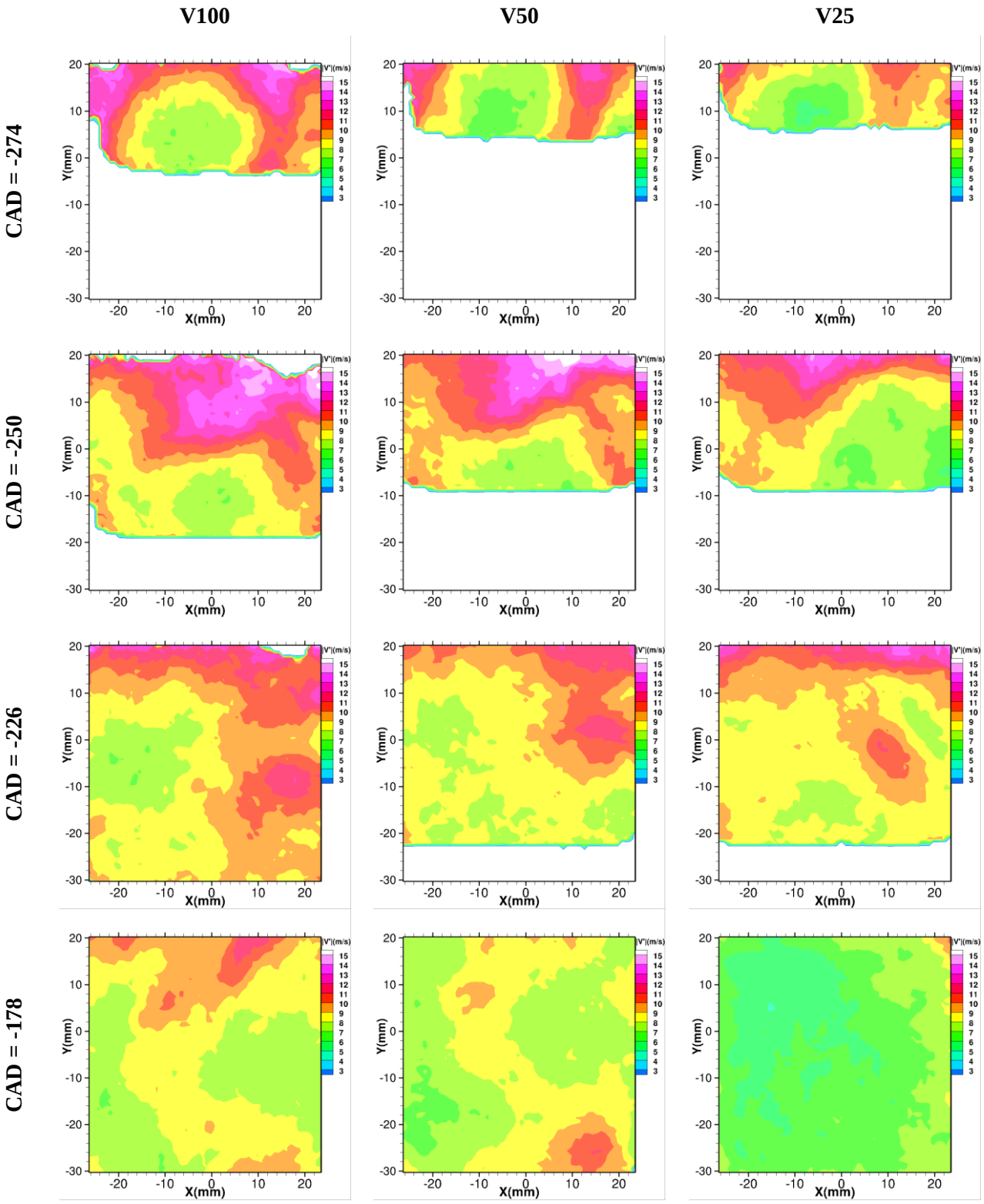

CAD = -130

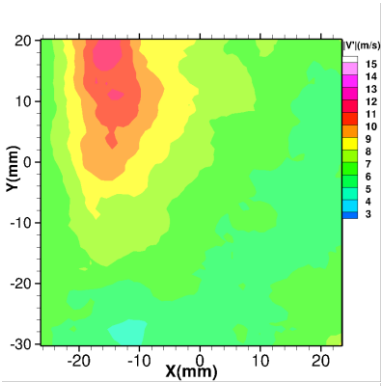

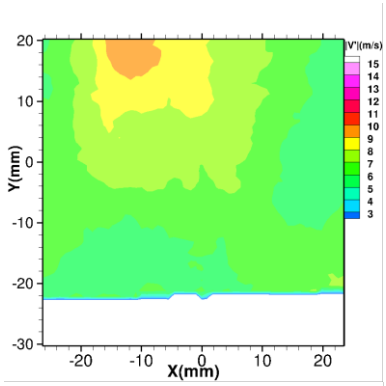

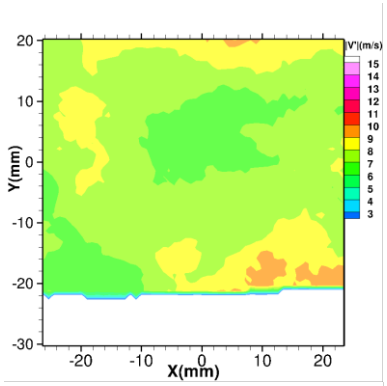

CAD = -106

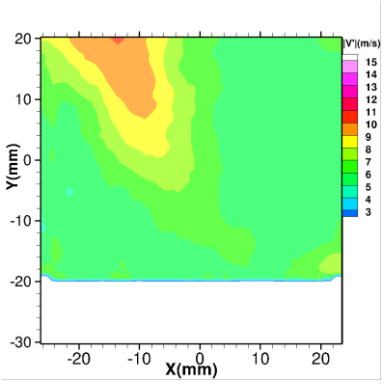

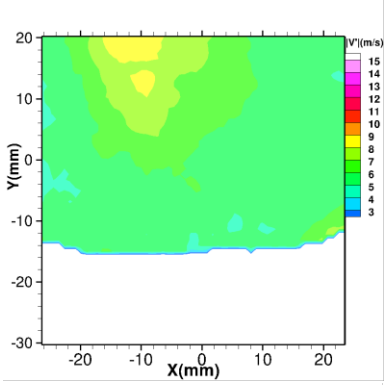

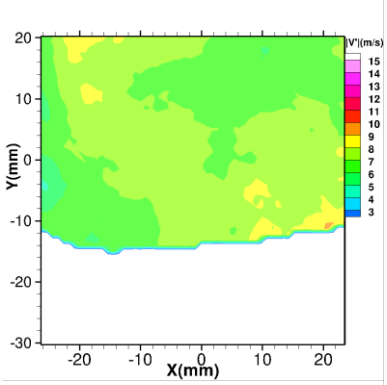

CAD = -82

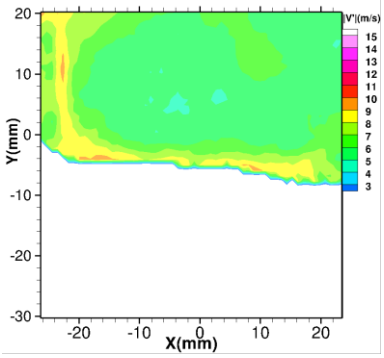

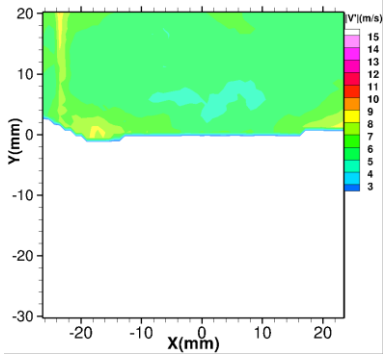

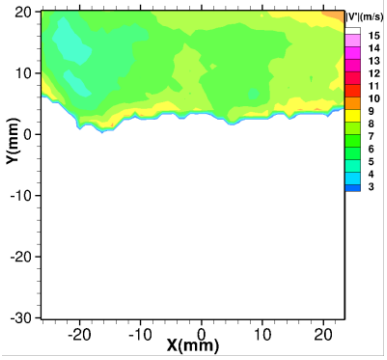

References

Abraham, P., Reuss, D., & Sick, V. (2013). High-Speed Particle Image Velocimetry Study of In-Cylinder Flows with Improved Dynamic Range. SAE International.

Arcoumanis, C., Bicen, A. F., & Whitelaw, J. H. (1982). Measurements in a Motored Four-Stroke Reciprocating Model Engine. *Journal of Fluids Engineering*, *104*(2), 235–241.

Arcoumanis, C., & Whitelaw, J. H. (1985). Fluid mechanics of internal combustion engines - a review. *International Symposium on Flows in Internal Combustion Engines-III*, *201*(1), 57–74.

Atkinson, C., Coudert, S., Foucaut, J.-M., Stanislas, M., & Soria, J. (2011). The accuracy of tomographic particle image velocimetry for measurements of a turbulent boundary layer. *Experiments in Fluids*, *50*(4), 1031–1056.

Baby, X. (2000). *Optimisation de l'aérodynamique interne dans un moteur a injection directe essence.* Institut National Polytechnique de Toulouse.

Basanta J., K. O. and K. N. (2013). Comparative study of camera calibration models for 3D particle tracking velocimetry. *International Journal of Innovative Computing, Information and Control*, *9*.

Bates, S. C. (1988). A Transparent Engine for Flow and Combustion Visualization Studies. SAE International .

Baum, E., & Peterson, B. (2012). Tomographic PIV measurements in an IC engine. *16th Int. Symp. on Applications of Laser Techniques to Fluid Mechanics*, (Lisbon, Portugal), 9–12.

Baum, E., Peterson, B., Surmann, C., Michaelis, D., Böhm, B., Hm, B., & Dreizler, A. (2013). Investigation of the 3D flow field in an IC engine using tomographic PIV. *Proceedings of the Combustion Institute*, *34*(2), 2903–2910.

Bode, J., Schorr, J., Krüger, C., Dreizler, A., & Böhm, B. (2016). Influence of three-dimensional in-cylinder flows on cycle-to-cycle variations in a fired stratified DISI engine measured by time-resolved dual-plane PIV. *Proceedings of the Combustion Institute*.

Borée, J., & Miles, P. C. (2012). In-Cylinder Flow. *Institut Pprime, Cnrs, Université De*

Poitiers.

Boutier, A. (2012). *Laser Velocimetry in Fluid Mechanics*. hermes-science.

Bowditch, F. W. (1961). A New Tool for Combustion Research A Quartz Piston Engine. SAE International .

Brücker, C. (1997). 3D scanning PIV applied to an air flow in a motored engine.pdf, *8*, 1480–1492.

Bücker, I., Karhoff, D. C., Klaas, M., & Schröder, W. (2012). Stereoscopic multi-planar PIV measurements of in-cylinder tumbling flow. *Experiments in Fluids*, *53*(6), 1993–2009.

Buschbeck, M., Bittner, N., Halfmann, T., & Arndt, S. (2012). Dependence of combustion dynamics in a gasoline engine upon the in-cylinder flow field, determined by high-speed PIV. *Experiments in Fluids*, *53*(6), 1701–1712.

Calendini, P. O., Duverger, T., Lecerf, A., & Trinité, M. (2000). *In-Cylinder Velocity Measurements with Stereoscopic Particle Image Velocimetry in a SI engine*. *SAE Technical Papers*.

Cao, Y., Thomas, L., Borée, J., & Guilain, S. (2014). Sensitivity Study of Cycle-to-Cycle Variation to Air Filling Parameters of a SI Engine, 7–10.

Chen, H., Reuss, D. L., & Sick, V. (2012). On the use and interpretation of proper orthogonal decomposition of in-cylinder engine flows. *Measurement Science and Technology*, *23*(8), 085302.

Cordier, L., & Bergmann, M. (2006). Réduction de dynamique par décomposition orthogonale aux valeurs propres (POD). *Ecole de Printemps OCET*, *7563*.

Cosadia, I., Borée, J., & Dumont, P. (2007). Coupling time-resolved PIV flow-fields and phase-invariant proper orthogonal decomposition for the description of the parameters space in a transparent Diesel engine. *Experiments in Fluids*, *43*(2–3), 357–370.

Daher, P., Lacour, C., Lefebvre, F., Domingues, E., Cessou, A., & Lecordier, B. (2016). Etude des variabilités cycliques dans le cylindre d'un moteur essence à injection directe par la PIV haute cadence Résumé. *Congrès Francophone de Techniques Laser, CFTL 2016, Toulouse, France*.

Dannemann, J, Pielhop, M. K. (2011). Cycle resolved multi-planar flow measurements

in a four-valve combustion engine. *Exp. Fluids*, 961–976.

Di Mare, F., & Knappstein, R. (2014). Statistical analysis of the flow characteristics and cyclic variability using Proper Orthogonal Decomposition of highly resolved LES in internal combustion engines. *Computers and Fluids*, *105*, 101–112.

Druault, P., & Chaillou, C. (2007). Use of Proper Orthogonal Decomposition for reconstructing the 3D in-cylinder mean-flow field from PIV data. *Comptes Rendus - Mecanique*, *335*(1), 42–47.

Druault, P., Guibert, P., & Alizon, F. (2005). Use of proper orthogonal decomposition for time interpolation from PIV data: Application to the cycle-to-cycle variation analysis of in-cylinder engine flows. *Experiments in Fluids*, *39*(6), 1009–1023.

Elsinga, G. E., Scarano, F., Wieneke, B., & van Oudheusden, B. W. (2005). Tomographic particle image velocimetry. *6th International Symposium on Particle Image Velocimetry*, 1–12.

Enaux, B. (2010). *Simulation aux Grandes Échelles d'un moteur à allumage commandé - Évaluations des variabilités cycliques*. Université de Toulouse - Institut National Polytechnique de Toulouse.

Espey, C., & Dec, J. E. (1993). Diesel Engine Combustion Studies in a Newly Designed Optical-Access Engine Using High-Speed Visualization and 2-D Laser Imaging. SAE International .

Falchi, M., & Romano, G. P. (2009). Evaluation of the performance of high-speed PIV compared to standard PIV in a turbulent jet. *Experiments in Fluids*, *47*(3), 509–526.

Floch, A. (1990). *Etude de la turbulence instationnaire dans une chambre de combustion à volume constant: Interaction avec la propagation d'une flamme allumée par étincelle*. Université de Rouen.

Fogleman, M. (2005). *Low-dimensional models of internal combustion engine flows using the proper orthogonal decomposition*. Cornell University.

Goryntsev, D., Sadiki, A., Klein, M., & Janicka, J. (2009). Large eddy simulation based analysis of the effects of cycle-to-cycle variations on air-fuel mixing in realistic DISI IC-engines. *Proceedings of the Combustion Institute*, *32 II*(2), 2759–2766.

Graftieaux, L., Michard, M., & Grosjean, N. (2001). Combining PIV, POD and vortex identification algorithms for the study of unsteady turbulent swirling flows. *Meas. Sci. Technol. Meas. Sci. Technol*, *12*(1201), 1422–1429.

Heywood, J. B. (1988). *Internal Combustion Engine Fundementals*. *McGrawHill series in mechanical engineering* (Vol. 21).

Holmes, P. J., Lumley, J. L., Berkooz, G., Mattingly, J. C., & Wittenberg, R. W. (1997). Low-dimensional models of coherent structures in turbulence. *Physics Reports*, *287*, 337–384.

Jarvis, S., Justham, T., Clarke, A., Garner, C. P., Hargrave, G. K., & Halliwell, N. A. (2006). Time Resolved Digital PIV Measurements of Flow Field Cyclic Variation in an Optical IC Engine. *Journal of Physics: Conference Series*, *45*(1), 38.

Johnston, S. C., Robinson, C. W., Rorke, W. S., Smith, J. R., & Witze, P. O. (1979). Application of Laser Diagnostics to an Injected Engine. SAE International .

Justham, T., Jarvis, S., Clarke, A., Garner, C. P., Hargrave, G. K., & Halliwell, N. a. (2006). Simultaneous Study of Intake and In-Cylinder IC Engine Flow Fields to Provide an Insight into Intake Induced Cyclic Variations. *Journal of Physics: Conference Series*, *45*, 146–153.

Kapitza, L., Imberdis, O., Bensler, H. P., Willand, J., & Thévenin, D. (2010). An experimental analysis of the turbulent structures generated by the intake port of a DISI-engine. *Experiments in Fluids*, *48*(2), 265–280.

Karhoff, D., Bücker, I., Klaas, M., & Schröder, W. (2013). Time-Resolved stereoscopic PIV measurements of cyclic variations in an internal combustion engine. *10TH Internationnal Symposium on Particle Image Velocimetry -PIV13*.

Kashdan, J., & Thirouard, B. (2011). Optical Engines as Representative Tools in the Development of New Combustion Engine Concepts. *Oil and Gas Science and Technology*, *66*(5), 759–777.

Kolář, V. (2007). Vortex identification: New requirements and limitations. *International Journal of Heat and Fluid Flow*, *28*(4), 638–652.

Kuo, T. W., & Reuss, D. L. (1995). Multidimensional port-and-cylinder flow calculations for the transparent-combustion-chamber engine. *Engine Modeling*, *23*, 19–29.

Lecordier, B. and Demare, D. and Vervisch, L.M.J. and Reveillon, J. and Trinite, M. (2001). Estimation of the accuracy of PIV treatments for turbulent flow studies by direct numerical simulation of multi-phase flow. *Measurement Science and Technology*, *9*, 1382–1391.

Lecordier, B. and Trinite, M. (2004). *Advanced PIV algorithms with image distortion*

validation and comparison using synthetic images of turbulent flow. Springer.

Lecordier, B. and Trinité, M. (2006). Accuracy assessment of image interpolation schemes for PIV from real images of particle. *13th Int Symp on Applications of Laser Techniques to Fluid Mechanics Lisbon, Portugal, 26-29 June, 2006*, 26–29.

Lecordier, B. (1997). *Etude de l'interaction de la propagation d'une flamme prémélangée avec le champ aérodynamique, par association de la tomographie laser et de la vélocimétrie par images de particules*. Université de Rouen.

Lee, D. W. (1939). A study of air flow in an engine cylinder. *Journal of Applied Physics*, *14*(8), 399.

Lemetayer, J. (2016). *Etude par PIV par fluorescence de l'interaction d'un spary avec un écoulement gazeux en aérodynamique contrôlée - Application à l'injection directe essence*.

Lengyel, I. (1995). *Caractérisation des échelles de longueur turbulentes dans la chambre d'un moteur à combustion interne*.

Liu, D., Wang, T., Jia, M., & Wang, G. (2012). Cycle-to-cycle variation analysis of in-cylinder flow in a gasoline engine with variable valve lift. *Experiments in Fluids*, *53*(3), 585–602.

Liu, K., & Haworth, D. C. (2011). Development and Assessment of POD for Analysis of Turbulent Flow in Piston Engines. *SAE Technical Paper*, 1–6.

Lumley, J. L. (1967). The Structure of Inhomogeneous Turbulence. *Atmospheric Turbulence and Wave Propagation, Nauka, Moscow*, 166–178.

Maly, R.R., Eberspach, G., & and Pfister, W. (1990). Laser Diagnostics for Single-Cycle Analysis of Crank Angle Resolved Length and Time Scales in Engine Combustion. *Second Int'l. Symp. on Diagnostics and Modeling of Combustion in IC Engines, JSME*, 399–404.

Marc, D., Boree, J., Bazile, R., & Charnay, G. (1997). Tumbling Vortex Flow in a Model Square Piston Compression Machine: PIV and LDV Measurements. SAE International .

Marko, K. A., Li, P., Rimai, L., Ma, T., & Davies, M. (1986). Flow Field Imaging for Quantitative Cycle Resolved Velocity Measurements in a Model Engine. SAE International .

Marvin, Charles F, J., & Best, R. D. (1932). Flame Movement and Pressure Development in an Engine Cylinder. *NACA Technical Report 399*, (Jan).

Miles, P. C. (2015). The History and Evolution of Optically Accessible Research. *Proceedings of the ASME 2014 Internal Combustion Engine Division Fall Technical Conference ICEF2014 October 19-22, 2014, Columbus, IN, USA*, 1–20.

Müller, S. (2012). Analysis of in-cylinder processes of an internal combustion engine with direct-injection using high-speed laser diagnostics.

Müller, S. H. R., Böhm, B., Gleißner, M., Grzeszik, R., Arndt, S., & Dreizler, A. (2010). Flow field measurements in an optically accessible, direct-injection spray-guided internal combustion engine using high-speed PIV. *Experiments in Fluids*, *48*(2), 281–290.

Murali Krishna, B., & Mallikarjuna, J. M. (2010). Comparative study of in-cylinder tumble flows in an internal combustion engine using different piston shapes-an insight using particle image velocimetry. *Experiments in Fluids*, *48*(5), 863–874.

Nobach. (2007). Review of Some Fundamentals of data processing, (x), 1337–1398.

Ölçmen, S. (2012). Comparative Analysis of Velocity Decomposition Methods for Internal Combustion Engines. *Open Journal of Fluid Dynamics*, *02*(03), 70–90.

Overbrüggen, T. van, Bahl, B., Dierksheide, U., Klaas, M., & Schröder, W. (2013). Tomographic PIV measurements in an IC engine, 1–7.

Pera, C., Knop, V., & Reveillon, J. (2015). Influence of flow and ignition fluctuations on cycle-to-cycle variations in early flame kernel growth. *Proceedings of the Combustion Institute*, *35*(3), 2897–2905.

Peterson, B., Baum, E., Ding, C.-P., Michaelis, D., Dreizler, A., & Böhm, B. (2016). Assessment and application of tomographic PIV for the spray-induced flow in an IC engine. *Proceedings of the Combustion Institute*.

Prasad, A. K. (2000). Stereoscopic particle image velocimetry. *Experiments in Fluids*, *29*(2), 103–116.

Rask, R. B. (1979). Laser Doppler Anemometer Measurements in an Internal Combustion Engine. SAE International .

Rassweiler, G. M., & Withrow, L. (1936). High-Speed Motion Pictures of Engine Flames. *Industrial & Engineering Chemistry*, *28*(6), 672–677.

Regan, C. A., Chun, K. S., & Schock, H. J. (1987). Engine flow visualization using a copper vapor laser. *Proceedings of SPIE - The International Society for Optical Engineering*, *737*, 17–27.

Reuss, D. L., Adrian, R. J., Landreth, C. C., French, D. T., & Fansler, T. D. (1989). Instantaneous Planar Measurements of Velocity and Large-Scale Vorticity and Strain Rate in an Engine Using Particle-Image Velocimetry. SAE International .

Ricardo, H. . (1927). Some Notes on Gasoline-Engine Development. *NACA Technical Memorandum*, *420*(I).

Richman, R. M., & Reynolds, W. C. (1984). The Development of a Transparent Cylinder Engine for Piston Engine Fluid Mechanics Research. SAE International .

Richter, M. (2008). Optical methods for combustion research. *Division of Combustion Physics, Lund University, Sweden*.

Scarano, F. (2012). Tomographic PIV: principles and practice. *Measurement Science and Technology*, *24*(1), 012001.

Scarano, F., & Poelma, C. (2009). Three-dimensional vorticity patterns of cylinder wakes. *Experiments in Fluids*, *47*(1), 69–83.

Semeraro, O., Bellani, G., & Lundell, F. (2012). Analysis of time-resolved PIV measurements of a confined turbulent jet using POD and Koopman modes. *Experiments in Fluids*, *53*(5), 1203–1220.

Sick, V., Drake, M. C., & Fansler, T. D. (2010). High-speed imaging for direct-injection gasoline engine research and development. *Experiments in Fluids*, *49*(4), 937–947.

Sirovich. (1987). Low-dimensional procedure for the characterization of human faces.

Stansfield, P., Wigley, G., Justham, T., Catto, J., & Pitcher, G. (2007). PIV analysis of in-cylinder flow structures over a range of realistic engine speeds. *Experiments in Fluids*, *43*(1), 135–146.

Steinberger, R. L., Marden, W. W., & Bracco, F. V. (1979). A Pulsed-Illumination, Closed-Circuit Television System for Real-Time Viewing of Engine Combustion and Observed Cyclic Variations. SAE International .

Sunnarborg, D. A. (2000). Quick release engine cylinder. Google Patents. Retrieved from

Thomas, L., Tremblais, B., & David, L. (2014). Optimization of the volume reconstruction for classical Tomo-PIV algorithms (MART, BIMART and SMART):

synthetic and experimental studies. *Measurement Science and Technology*, *25*(3), 035303.

Towers, D., & Towers, C. (2008). High-speed PIV: Applications in engines and future prospects. *Topics in Applied Physics*, *112*, 345–361.

Tropea, C., Alexander, L., & Foss, J. F. (2007). *Springer Handbook of Experimental Fluid Mechanics*. Springer.

Voisine, M., Thomas, L., Borée, J. and Rey, P. (2010). Structure and in-cycle evolution of an in-cylinder tumbling flow. *15th Int Symp on Applications of Laser Techniques to Fluid Mechanics Lisbon, Portugal, 05-08 July, 2010 - 1*.

Voisine, M., Thomas, L., Borée, J., & Rey, P. (2010). Spatio-temporal structure and cycle to cycle variations of an in-cylinder tumbling flow. *Experiments in Fluids*, *50*(5), 1393–1407.

Watts, S. S., & Lloyd-Evans, B. J. (1934). The measurement of flame temperatures in a petrol engine by the spectral line-reversal method.

Wieneke, B. (2008). Volume self-calibration for 3D particle image velocimetry. *Experiments in Fluids*, *45*(4), 549–556.

Willert, C. (1997). Stereoscopic digital particle image velocimetry for application in wind tunnel flows. *Measurement Science and Technology*, *8*(12), 1465–1479.

Willert, C. E. (2015). High-speed particle image velocimetry for the efficient measurement of turbulence statistics. *Experiments in Fluids*, *56*(1).

Willert, C. E., & Schröder, A. (2007). *Particle image velocimetry: New Developments and Recent Applications* (Vol. 112). Springer.

Withrow, L., & Rassweiler, G. M. (1931). Spectroscopic Studies of Engine Combustion. *Industrial & Engineering Chemistry*.

Witze, P. O. (1996). In-Cylinder Diagnostics for Production Spark Ignition Engines. *Unstead Combustion*, 333–368.

Zentgraf, F., Baum, E., Böhm, B., Dreizler, A., & Peterson, B. (2016). On the turbulent flow in piston engines: Coupling of statistical theory quantities and instantaneous turbulence. *Physics of Fluids (1994-Present)*, *28*(4), 045108.

Zhang, J., Tao, B., & Katz, J. (1997). Turbulent flow measurement in a square duct with hybrid holographic PIV. *Experiments in Fluids*, *23*(5), 373–381.

Résumé

Les mécanismes d'évolution spatio-temporelle des structures turbulentes instationnaires tridimensionnelles, et en particulier ceux rencontrés aux plus grandes échelles, sont à l'origine de phénomènes d'instabilité qui conduisent très souvent à une diminution de la performance des systèmes énergétiques. C'est le cas des variations cycle-à-cycle dans le moteur à combustion interne. Malgré les progrès substantiels réalisés par la simulation numérique en mécanique des fluides, les approches expérimentales demeurent essentielles pour l'analyse et la compréhension des phénomènes physiques ayant lieu. Dans ce travail de thèse, deux types de vélocimétrie par image de particules (PIV) ont été appliqués et adaptés au banc moteur optique du laboratoire Coria pour étudier l'écoulement en fonction de six conditions de fonctionnement du moteur. La PIV Haute Cadence 2D2C a permis d'abord d'obtenir un suivi temporel de l'écoulement dans le cylindre durant un même cycle moteur ainsi qu'identifier ces variations cycliques. La PIV Tomographique 3D3C a permis ensuite d'étendre les données mesurées vers l'espace tridimensionnel. La Tomo-PIV fait intervenir 4 caméras en position angulaire visualisant un environnement de géométrie complexe, confinée, ayant un accès optique restreint et introduisant des déformations optiques importantes. Cela a nécessité une attention particulière vis-à-vis du processus de calibration 3D des modèles de caméras. Des analyses conditionnées 2D et 3D de l'écoulement sont effectuées en se basant principalement sur la décomposition propre orthogonale (POD) permettant de séparer les différentes échelles de structure et le critère Γ permettant l'identification des centres des tourbillons.

Mots clés : Aérodynamique moteur, PIV haute cadence, PIV tomographique, Calibration 3D, Confinement, Mesures tridimensionnelles

Abstract

The unsteady evolution of three-dimensional large scale flow structures can often lead to a decrease in the performance of energetic systems. This is the case of cycle-to-cycle variations occurring in the internal combustion engine. Despite the substantial advancement made by numerical simulations in fluid mechanics, experimental measurements remain a requirement to validate any numerical model of a physical process. In this thesis, two types of particle image velocimetry (PIV) were applied and adapted to the optical engine test bench of the Coria laboratory in order to study the in-cylinder flow with respect to six operating conditions. First, the Time-Resolved PIV (2D2C) allowed obtaining a temporal tracking of the in-cylinder flow and identifying cyclic variabilities. Then tomographic PIV (3D3C) allowed extending the measured data to the three-dimensional domain. The Tomo-PIV setup consisted of 4 cameras in angular positioning, visualizing a confined environment with restricted optical access and important optical deformations. This required a particular attention regarding the 3D calibration process of camera models. 2D and 3D conditional analyses of the flow were performed using the proper orthogonal decomposition (POD) allowing to separate the different scales of flow structures and the Γ criterion allowing the identification of vortices centres.

Key words: Engine aerodynamics, High-speed PIV, Tomographic PIV, 3D Calibration, Confinement, Three-dimensional measurements